FACTORS AFFECTING EXTENSIONAL FLOW-INDUCED CRYSTALLIZATION IN HIGH DENSITY POLYETHYLENE

By

SHEENA JACOB
Bachelor of Science
Panjab University
Chandigarh, India
1984

Master of Science
Panjab University
Chandigarh, India
1986

Master of Science
Oklahoma State University
Stillwater, Oklahoma
1995

Submitted to the Faculty of the
Graduate College of the
Oklahoma State University
in partial fulfillment of
the requirements for
the degree of
MASTER OF SCIENCE
May, 2000

FACTORS AFFECTING EXTENSIONAL FLOW-INDUCED CRYSTALLIZATION IN HIGH DENSITY POLYETHYLENE

Thesis Approved:

Thesis Advisor

Dean of the Graduate College

ACKNOWLEDGEMENTS

I wish to express my gratefulness to Dr. D. A. Tree, research advisor, for his valuable guidance in making this thesis possible. It was a pleasure to work with him. His help, advise, and patience is greatly appreciated.

I would like to thank Dr. K. A. High, and Dr. M. S. High for serving on my committee, and for the advise and suggestions regarding research during the group-meetings.

I owe my sincere thanks to, Lindsay Mendes, for his willingness to help me anytime, for being considerate, and above all, for being my friend. My special thanks to Tsai Tsung Chieh and Madhav Kakani for their technical help and useful discussions on experimental and theoretical aspects of flow-induced crystallization. Thankyou Sergei, for encouraging me to complete what I began four years ago. Charles, thanks for the years of help with tools and pieces of equipment, that I needed time and again. Pat, Sarah and Amber, thanks for all your help with the office work concerning me.

I want to take this opportunity to thank Dr. Westhaus for the timely financial support during the last two semesters of research.

My heartfelt thanks go out to my loving parents and brother, George. Their faith in my aptitude in academics motivated me to come back to school. I thank them for their encouragement and support throughout my life, and especially for the frequent overseas phone calls that immensely helped me to keep my morale up.

My deepest gratitude goes out to my husband, Steve, daughter, Jessica and my eleven month old son, Troy. I dedicate this work to Troy, who patiently awaited my love and attention, while I worked to accomplish this degree.

TABLE OF CONTENTS

LIST OF TABLES

LIST OF FIGURES

CHAPTER I

INTRODUCTION

Polymers, in today's world, are being increasingly used, due to their numerous applications, and advantages over other materials. Polymeric materials are light weight, inexpensive, conform to different shapes, and exhibit properties such as strength, that can rival the corresponding properties in steel and other metals.[1] Since the melting temperatures of most metals are significantly higher than the melting temperatures of polymers, polymers can be molded into products at much lower temperatures than metals which saves energy. Polymers can also be used as electrical insulators. Since polymer products are corrosion resistant, and can display both rigidity and flexibility, polymers have replaced glasses in various applications. The wide ranging properties and applications of polymeric materials assure that polymers will continue to play an important role in our society.

A critical step in determining the properties of polymers is the processing operation. Each process imparts a unique thermal and rheological history to the polymeric material, which determines the microstructure in the polymer. The microstructure, in turn, is a key factor in determining the properties of finished polymeric materials. As a consequence, each process produces a product with distinct properties. The focus of this thesis is the relationship between processing and microstructure.

Polymeric materials can show a range of microstructures, as illustrated in Figure 1.1. At rest, in the melt or solution, flexible polymer molecules show the random coil configuration[2]. Two low energy conformations can be noted in commonly processed crystallizable polymers: helical or folded chain. These conformations, usually accompanied by amorphous regions, tend to be tough, but mechanically weak. Another conformation that can be induced by a flow field is the extended chain morphology. Extended chain crystals (ECC) are formed when the polymer chains deform and elongate under stress. The increase in orientation increases the tensile strength of the polymer. In the folded chain crystals (FCC), the chain folds act as crystal defects, decreasing the strength of the FCC in comparison with the strength of the ECC. Therefore, the knowledge of the different microstructures is crucial in the fabrication of a polymeric material.

A change in morphology can dramatically affect the properties of polymeric materials. For example[1], the tensile strength of commercial grade polyethylene, with the FCC morphology, is 1-7 GPa. Whereas, in the form of a drawn melt, the strength increases to 70 GPa. As a drawn gel fiber, the mechanical strength of polyethylene attains much higher values, 120 – 220 GPa, a range that includes the tensile strength of steel (210 GPa). The extended chain morphology is predominant in both drawn melt, and drawn gel fibers of polyethylene. Thus, the mechanical properties are a sensitive function of the morphology of a polymer.

The evolution of crystalline morphology in polymers could be simulated with the help of models. A model developed by Avrami,[3,4,5] describes the kinetics of crystallization from the amorphous melt of polymers. The model uses parameters such

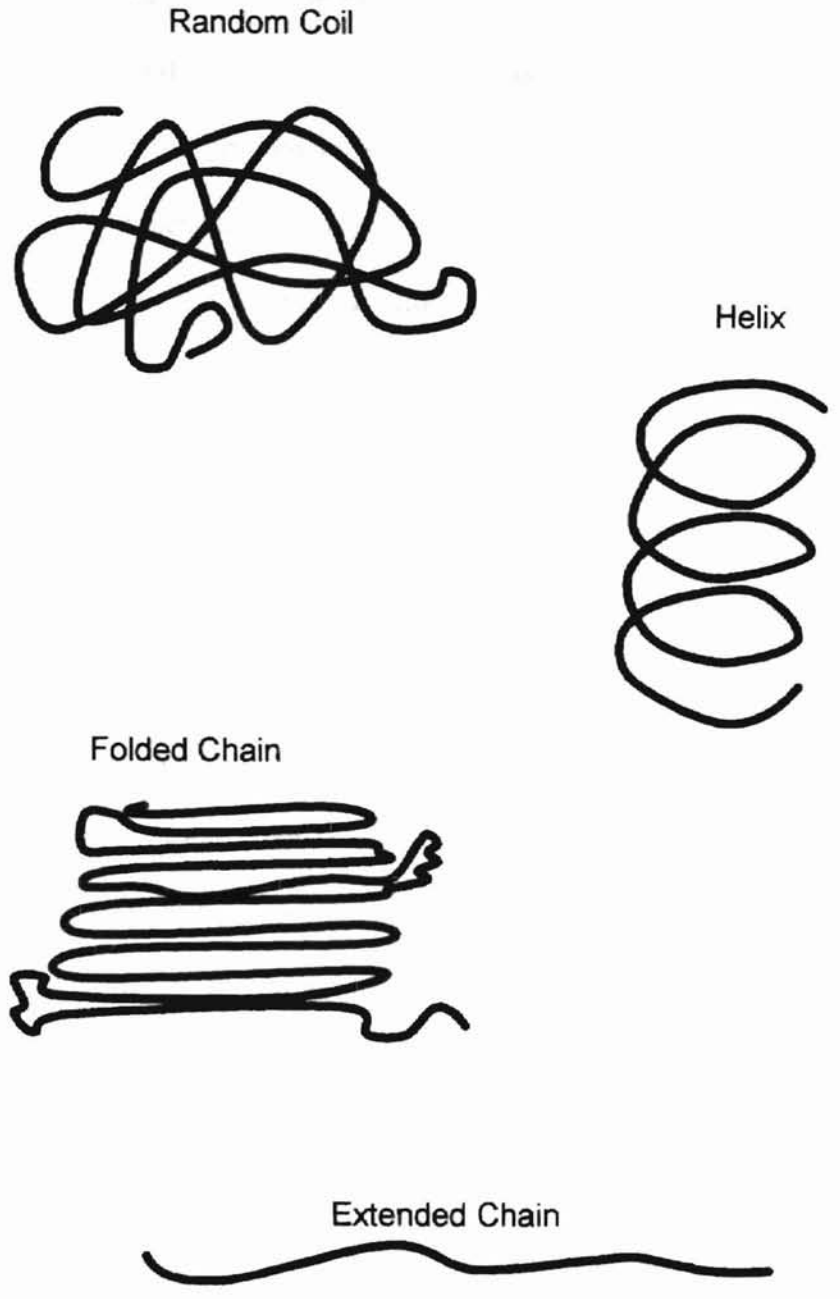

Figure 1.1 Random Coil, Helix, Folded Chain and Extended Chain Conformations [2]

as the number of nuclei in the pre-crystallization melt, the nucleation rate, and the growth rate to determine the crystallization kinetics. Although, originally formulated for crystallization in metals, the Avrami model has been successfully extended to the formation of the FCC morphology in polymers. However, the model has some difficulty in explaining flow-induced crystallization (FIC) kinetics.

A model to simulate extensional flow-induced crystallization from an amorphous polymer melt has been developed by Mendes.[6] The polymer molecules were represented by beads joined by massless rigid rods. The bead-rod chains in the amorphous melt were subjected to three forces: Brownian, hydrodynamic drag, and intermolecular forces. A time dependent probability distribution function (*pdf*) determined the probability of a bead in the amorphous melt occupying a crystal lattice site. The *pdf* being a measure of the crystallinity in the polymer, was used to study the kinetics of FIC.

Extensional FIC has been studied experimentally by Kakani.[7] Kakani used an optical train to observe birefringence in semicrystalline polymers. The intensity of the transmitted light during the formation of flow-induced crystals was recorded. The intensity data was used to calculate retardance. The proportionality between retardance and crystallinity was used to characterize the FIC kinetics of the polymer. However, Kakani's results were not quantitatively reproducible.

Birefringence and dichroism are optical phenomena by which crystallization in polymers could be observed. Kakani[7] used only birefringence to obtain information regarding FIC in the polymers. In this study, experiments were conducted using dichroism as well, so as to gain further insight into the kinetics of FIC.

This thesis discusses the theories and the assumptions required, and the results to characterize flow-induced crystallization in high density polyethylene. Theories regarding flow-induced crystallization, and the literature survey of progress in this field is discussed in Chapter II. Chapter III presents the experimental setup and procedures for conducting the experiment. The results are discussed in detail in Chapter IV. The conclusions of this study are presented in Chapter V. Further, Chapter V suggests approaches to future research.

CHAPTER II

BACKGROUND

This chapter reviews the relevant background for the study of quiescent and flow-induced crystallization in polymers. Concepts such as structural changes during crystallization, crystallization kinetics, and the optical phenomena of birefringence and dichroism, essential for this study, are explained in this chapter. Important experimental and theoretical developments in quiescent and flow-induced crystallization are also discussed.

§ 2.1 Polarization of Light

Polarized light can be discussed in terms of the electric field vector (**E**), the two components of **E** ($\mathbf{E}_x$ and $\mathbf{E}_y$), the optic axis, and the anisotropy of some materials. These terms are introduced in this section to lay a foundation for the discussion of dichroism and birefringence.

A light wave is depicted in Figure 2.1. Figure 2.1a shows that a light wave consists of the electric (**E**) and magnetic (**B**) field vectors, which are oriented in a direction perpendicular (or transverse) to the direction of propagation. Considering only the **E** field for simplicity, if the planes of the vibrations of the electric field vectors are

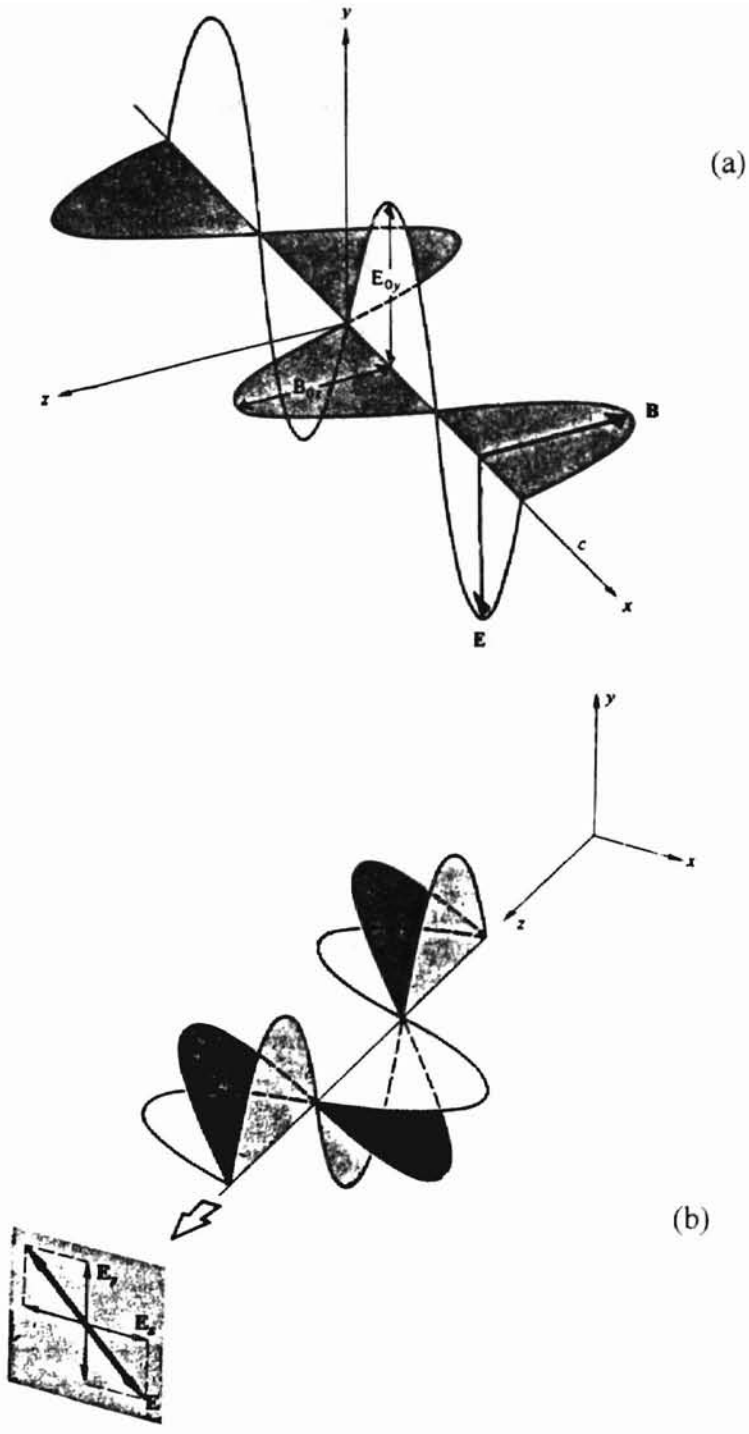

Figure 2.1 (a) Orthogonal E- and B- Fields (b) Plane Polarized Light[8]

oriented randomly, the light is said to be unpolarized. Conversely, if the electric vectors are all in one plane, the light is said to be plane polarized. Figure 2.1b shows that the plane of vibration contains the varying electric field vector, that can be resolved into its two mutually perpendicular components, $\mathbf{E}_x$ and $\mathbf{E}_y$. Interactions of both $\mathbf{E}_x$ and $\mathbf{E}_y$ with a material are indistinguishable along the optic axis, a direction within the material, about which the molecules are symmetrically arranged.

Polarizers transmit light waves with electric field vectors only in one plane while the waves in other planes are either reflected or absorbed. The ability to selectively transmit light originates from anisotropy in the microstructure of the polarizer. The polarization of light is based on four fundamental physical mechanisms: dichroism, birefringence, scattering, and reflection[8]. Since dichroism and birefringence were used in this study, only these two mechanisms are described in the following sections.

Dichroism and birefringence can be expressed mathematically by examining the refractive index of a medium, $\tilde{n}$. Using Maxwell's equations[9] of electromagnetic radiation propagating in a material, $\tilde{n}$ can be written as the sum of a real term, n and an imaginary part, $\imath n'$.

$$\underline{\underline{\tilde{n}}} = \underline{\underline{n}} + i\underline{\underline{n'}} \tag{2.1}$$

$\underline{\underline{n'}}$ in Equation (2.1), is called the extinction tensor, and is associated with the absorption of light in a material.

§ 2.1(a) Dichroism

Dichroism can be classified as being either conservative or consumptive. Conservative dichroism[10] refers to polarization due to scattering of light. Therefore, the light energy is conserved. Consumptive dichroism is defined as the selective absorption of light in all but one plane. Dichroism related to the extinction coefficient in Equation (2.1) is consumptive. Since scattering was negligible in the polymer melts used in this study, only consumptive dichroism is discussed in detail in this section.

The action of a dichroic material can be illustrated[11] using the following example of Polaroid E-sheet, which is a sheet of polyvinyl alcohol that has been stretched in one direction so as to align the long chain molecules. The sheet can be impregnated with iodine atoms, which attach themselves to the polymer molecules, and provide the sheet with sites of 'conduction' electrons. The linear molecules become conducting chains and are represented schematically as parallel lines in the polarizer in Figure 2.2.

In Figure 2.2, the molecules of the polarizer are oriented in the *y*-direction. If an unpolarized light beam is incident on Polaroid E-sheet, the *y*-component of the **E**-vibrations sets the 'conduction' electrons in oscillatory motion. Each vibrating electron constitutes a dipole source of electromagnetic energy which radiates in all directions. The **E**-vibrations of the electromagnetic radiation originating in the material are 180° out of phase with respect to the incident light. The superposition of the incident light with the beam generated by the conducting electrons leads to destructive interference. However, the 'conduction' electrons are not free electrons, and cannot readily move in the *x*-direction. Therefore, E_x remains unaltered as the light beam passes through the

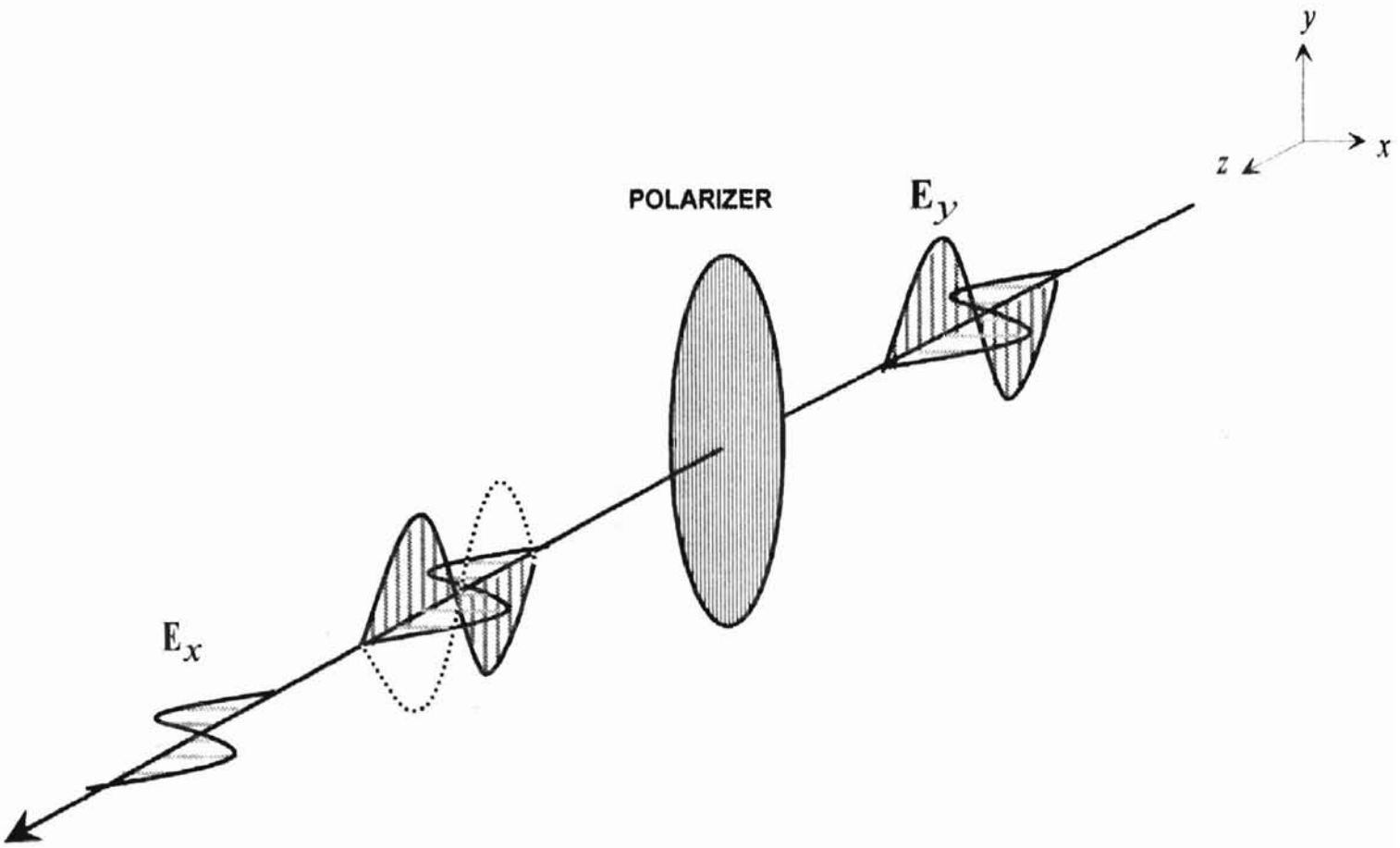

Figure 2.2 Action of a Dichroic Absorber [11]

sheet. Thus, the absorption of the incoming light and the subsequent emission leads to the polarization of light. This mechanism is called consumptive dichroism.

The efficiency of a dichroic absorber is a function of thickness, d, since the energy of the light wave, is gradually dissipated as the wave advances through the material. The expression for the attenuation of light intensity[11] is

$$I(x) = I_o \; e^{-\beta x} \tag{2.2}$$

where I_o is the incident intensity, β is the absorption coefficient, and x is the path length of the light.

§ 2.1(b) Birefringence

The effect of different speeds of light through an anisotropic material in different directions is called the birefringence[12]. Birefringence is caused by the asymmetry in the structure of certain materials. The asymmetry in the molecular arrangement leads to differences in the way the two components of the **E**-vector interact with the material, and the speed of light in the material becomes directionally dependent. Since the local refractive index is inversely proportional to the velocity of light, the refractive index also becomes directionally dependent.

An appropriate example[11] of a birefringent material is calcite ($CaCO_3$). The molecular structure of calcite is tetrahedral, as is shown in Figure 2.3a. The base of the tetrahedron consists of CO_3^{2-} as a triangular cluster. The Ca^{2+} cation is located at the apex. Incident light along the optic axis OA, passes unaffected through the crystal,

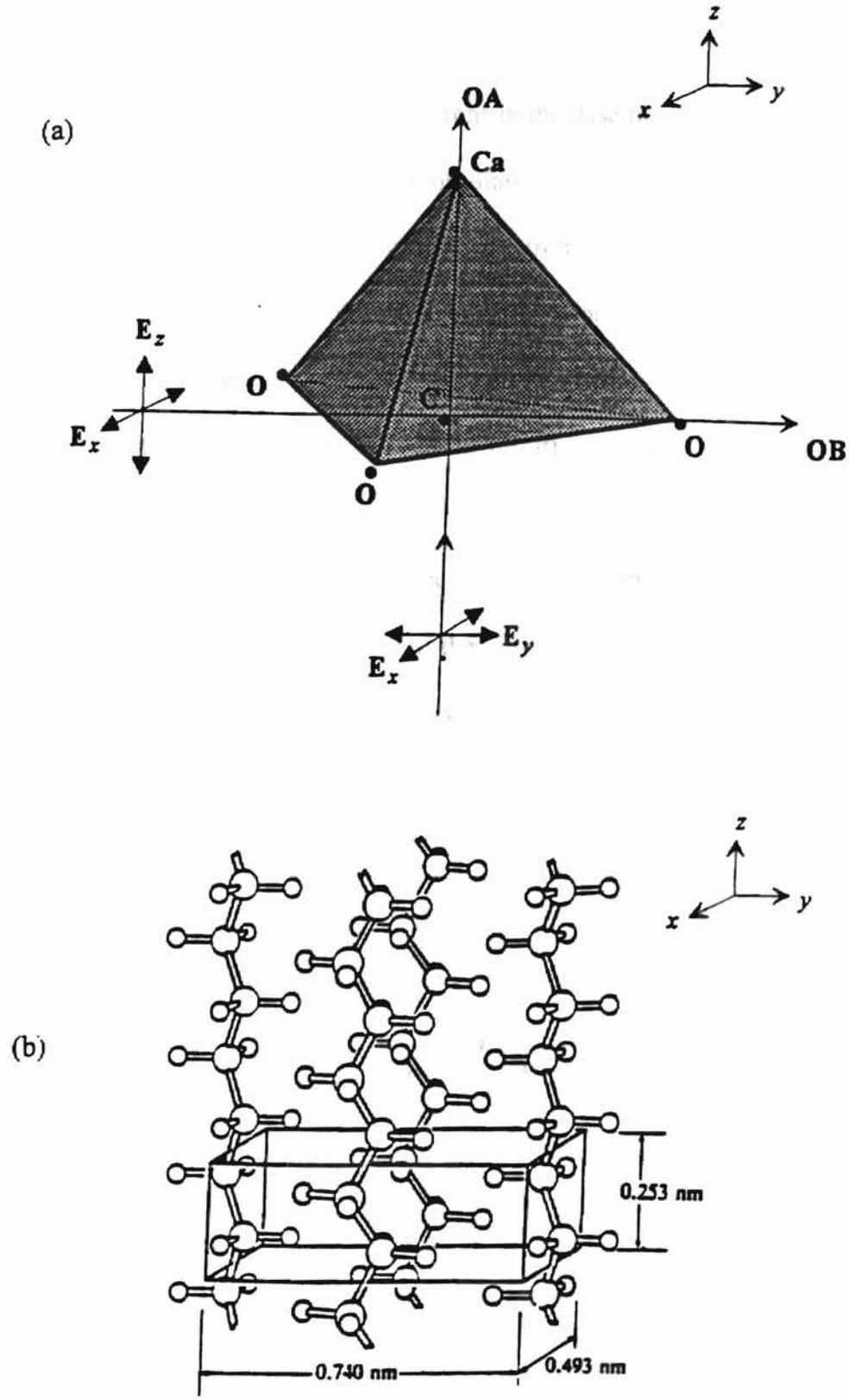

Figure 2.3 (a) Progress of Light Through a Molecular Unit of Calcite Crystal[11]
(b) Molecular Polyethylene Crystal

because E_x and E_y interact equally with the electrons in the base plane of the crystal. For light entering along OB, however, E_x causes oscillations in the plane of the base. E_z, which is perpendicular to the base plane with the electrons, has only weak interacions. The strong interaction of E_x with the electrons reduces the propagation speed, v_x, of E_x relative to the propagation speed, v_z, of E_z. Thus, $v_x < v_z$, and $n_x > n_z$. The asymmetry in the molecular structure of calcite gives rise to the birefringence observed.

Birefringence can also be observed in polymers. Figure 2.3b shows that a polyethylene crystal has an orthorhombic unit cell. For light propagating along the z-axis passing through the unit cell, E_x interacts with the electrons of closely spaced chains in the x-direction. Whereas, E_y interacts weakly with the electrons of the widely spaced chains in the y-direction. Therefore, $v_x < v_y$, or $n_x > n_y$, allowing the polyethylene crystal to be birefringent.

The phase difference between E_x and E_y is called the retardance and can be expressed in terms of the refractive indices n_x and n_y as[12]:

$$\delta = \frac{2\pi}{\lambda_o}\left(n_x - n_y\right)L = \frac{2\pi}{\lambda_o}(\Delta n)L \ , \qquad (2.3)$$

where λ_o is the wavelength in vacuum, L is the thickness of the polymeric sheet, and $\Delta n = n_x - n_y$, the birefringence.

Using Equation (2.1), the difference between birefringence and dichroism can be illustrated as follows. In a birefringent material which is not dichroic, the real part of the refractive indices are unequal in two orthogonal directions, while the corresponding imaginary part of the refractive indices are equal. In a dichroic, but non-birefringent material, however, the imaginary part of the refractive indices, rather than the real part,

are unequal in two orthogonal directions. The one property common to both the processes, however, is the asymmetry in structure along the direction of light propagation.

§ 2.2 Quiescent Crystallization

Quiescent crystallization of a polymer melt leads to the formation of crystals called spherulites. The microstructure of spherulites is affected by factors such as the temperature of crystallization, undercooling and the size and structure of the molecular chains present in the polymer. Induction time and the thickness are two other factors that influence the microstructure of the quiescently formed crystals.

Although several models successfully describe the kinetics of quiescent crystallization, no particular model considers all of the factors mentioned in the previous paragraph. A discussion of some of the models used to describe quiescent crystallization is presented in § 2.2(b), since many such models form the basis for the development of new theories of FIC, described in § 2.3.

§ 2.2(a) Microstructure of Semicrystalline Polymers

A large variety of stereochemically regular polymers solidify as spherulites. Structurally, spherulites are birefringent crystals which have spherical symmetry in the bulk of the substance [13]. Figure 2.4a shows a schematic diagram of a spherulite in which the spherulite is observed to be composed of lamellae growing radially outward. Within

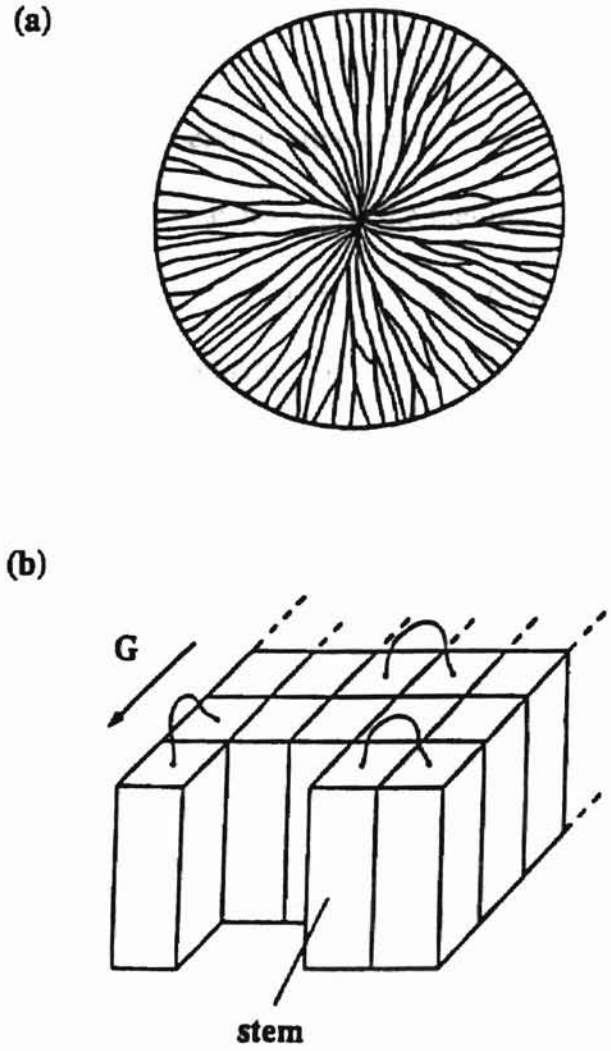

Figure 2.4 (a) Polymer Spherulite with Crystallite Fibrils[13] (b) Enlarged View of Tip of Spherulite Fibril; G (Growth Direction)

each lamella, the polymer chain segments resemble bricklaying as shown in Figure 2.4b. A given chain may fold several times before the crystallization process is completed. The noncrystalline chain folds and the loose chain ends constitute a part of the amorphous fraction of a semicrystalline polymer. Typically, polymer melts crystallizing under quiescent conditions show spherulitic structure.

The effects of temperature changes below the melting temperatureof a polymer, T_m, on polymer crystal morphology were observed by Vesely[14], using a transmission electron microscope (TEM). The formation of lamellar structure in polyethylene (PE) was noted, as the temperature dropped below the melting point (T_m). The density of the lamellae was observed to increase with the undercooling. Based on these observations, Vesely proposed that the molecular chains were randomly oriented in the melt state. "On cooling and in the presence of a nucleus, the chains organized themselves in the pattern of the nucleus. As the cooling continued, the cooler crystalline boundaries caused further condensation of the amorphous molecules. The lamellae propagated, forming ordered regions in the amorphous material, reducing the energy of the system"[14].

Vesely's observation confirmed the influence of another temperature below T_m, the crystallization temperature, T_c. Low values of T_c favored crystallization. Thus, crystallization depended on the temperature difference, T_m - T_c, or undercooling. Shroff *et al.*[15] proposed that undercooling strongly affects the nucleation and growth processes of polymer crystals. Shroff *et al.*[15] described the isothermal crystallization process as a concurrent process of nucleation and growth, with nucleation being a dominant factor near the melting point temperature. Shroff *et al.*[15] also made the observation that in

commercial grade polymers such as HDPE and LLDPE, undercooling determined the degree of crystallization.

The studies conducted by Vesely[14] and Shroff *et al.*[15] showed the formation of the folded chain morphology. However, Sutton *et al.*[16], observed the existence of extended chain morphology in the melt crystallization of three monodisperse paraffins, $C_{294}H_{590}$, $C_{246}H_{494}$ and $C_{198}H_{398}$.

Figure 2.5 shows the crystal growth rate as a function of the crystallization temperature[16] (T_c). As T_c was reduced from 145 °C (the temperature above T_m for all three samples), the growth rate increased followed by a decrease to a minimum (T_{min} = 124.5 ± 0.5°C), before a rapid rise. Observations using TEM showed that extended chain crystallization was predominant for $T_c > T_{min}$, resulting in the formation of coarse and highly birefringent aggregates of elliptic lamellae. However, as T_c was reduced below T_{min}, spherulitic crystals in which the molecules adopted a once-folded conformation, were formed. The minimum corresponded to the transition from the extended chain morphology to the spherulitic structure of the crystals.

From the observations presented, the following can be deduced. Although quiescent crystallization in polymers has been observed to form spherulites at temperatures below the melting point[14], there has been evidence of extended chain crystallization taking place below the melting point until a lower temperature, T_{min}, corresponding to a minimum crystal growth rate of a polymer.[16] Undercooling, a function of the crystallization temperature, T_c, and T_m, is another important variable, has been observed to affect the degree of crystallization[15].

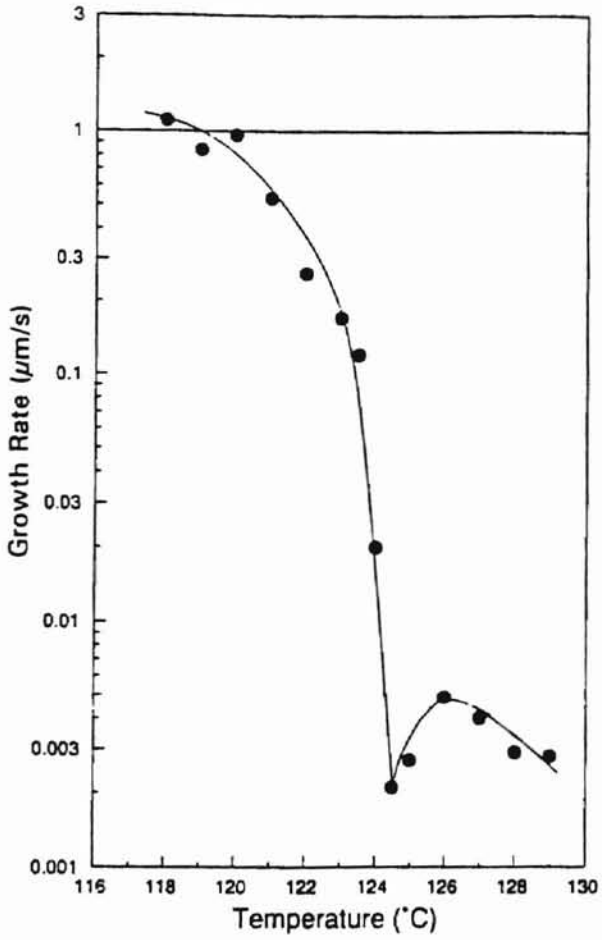

Figure 2.5 Variation in the Average Crystal Growth Rate[16] Versus Crystallization Temperature for $C_{294}H_{590}$

§ 2.2(b) Observations of Quiescent Crystallization

The typical observations regarding undercooling, crystallinity, induction time, and pressure effects, made during quiescent crystallization of polymers are discussed briefly in this section.

The effect of undercooling rates has been studied by Ding and Spruiell,[17] in polypropylene (PP). Figure 2.6a shows typical cooling curves. The temperature plateau (T_p) in each curve indicates when crystallization occurred. The temperature curves show that a higher rate of cooling leads to a lower temperature for the onset of crystallization. Ding and Spruiell also reported that lower crystallization temperatures resulted in lower values of crystallinity.

The relative crystallinity data of Ding and Spruiell[17] plotted against time is shown in Figure 2.6b. The data show three distinct regions. The first region is a lower plateau before crystallization began. The second region shows rapid crystal growth, which was attributed to primary crystallization. The third region shows an upper plateau where crystal growth is low or negligible. The duration of the second region corresponds with the duration of T_p in each cooling curve in Figure 2.6a.

Fu *et al.*[18] studied the crystallization of short chain branched metallocene polyethylene (SCBPE) and presented the relative crystallinity curve shown in Figure 2.7. The data at 105 °C and 110 °C show three regions that correspond to the regions in the Ding and Spruiell[17] data.

Ding and Spruiell[17] also observed that the radius of a spherulite increased linearly with time during most of the crystallization as is shown in Figure 2.8a. Therefore, Ding

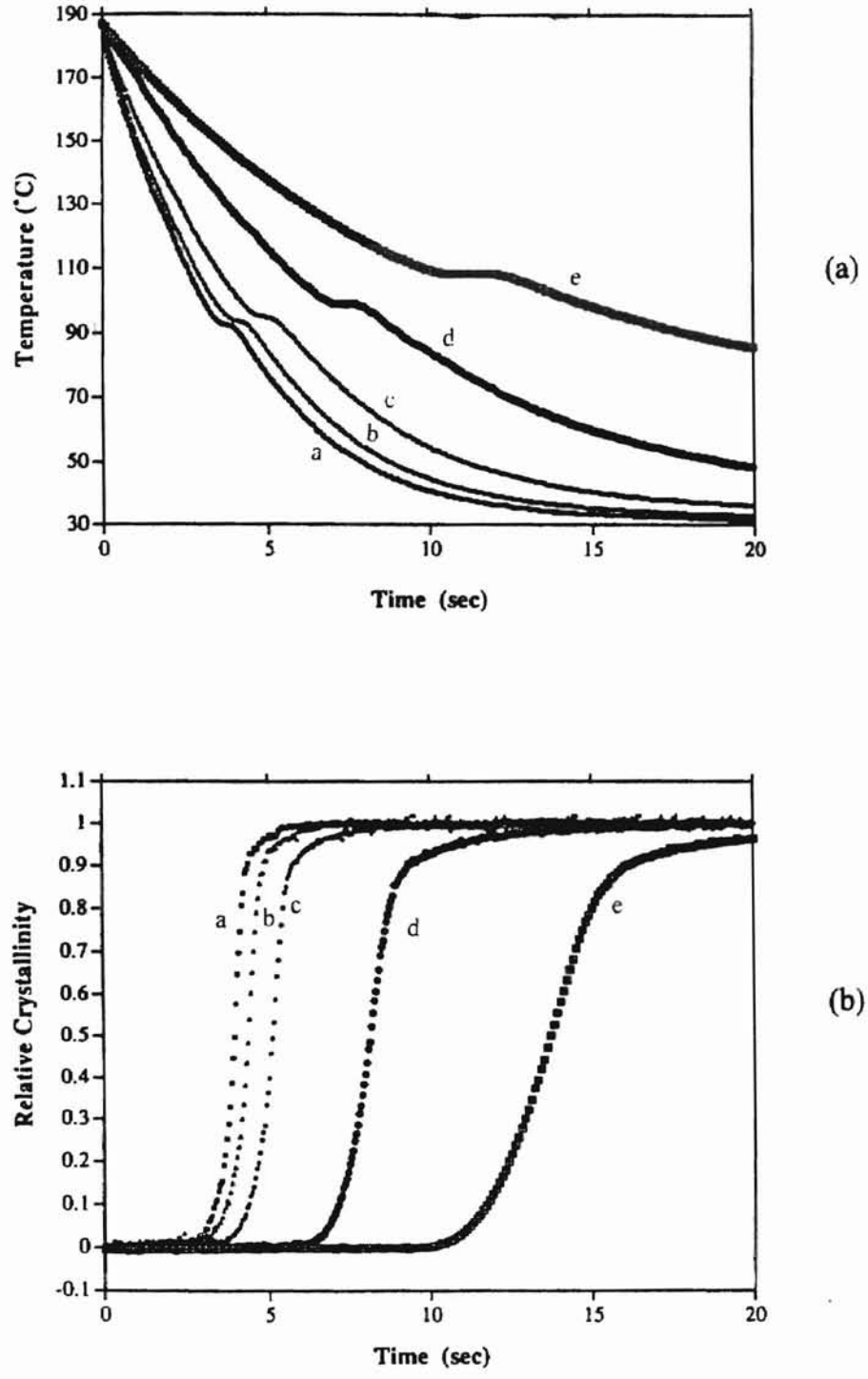

Figure 2.6 (a) Cooling Curves[17] (b) Relative Crystallinity Versus Time[17]

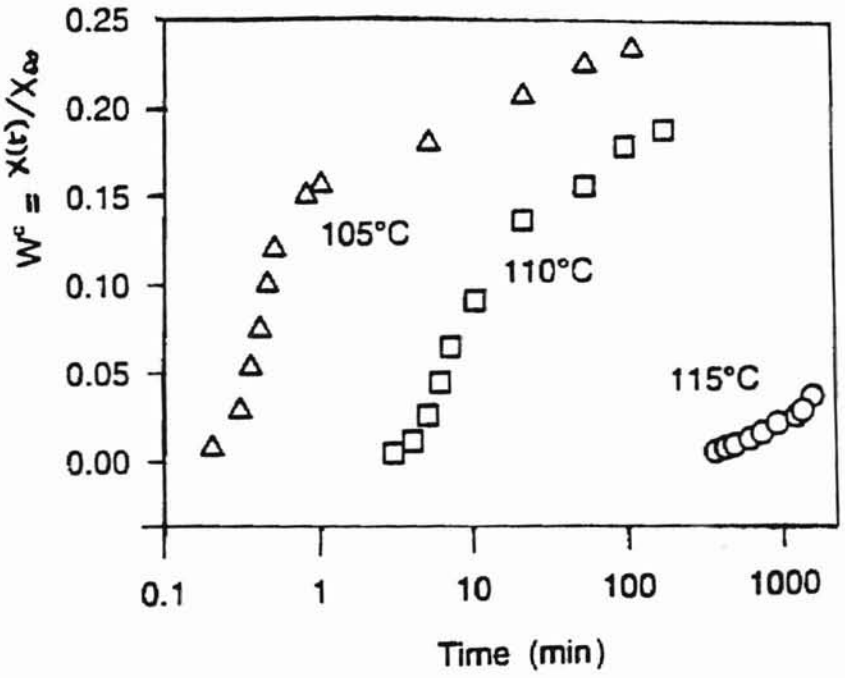

Figure 2.7 Increase in Crystallinity with Time at Different Temperatures[18]

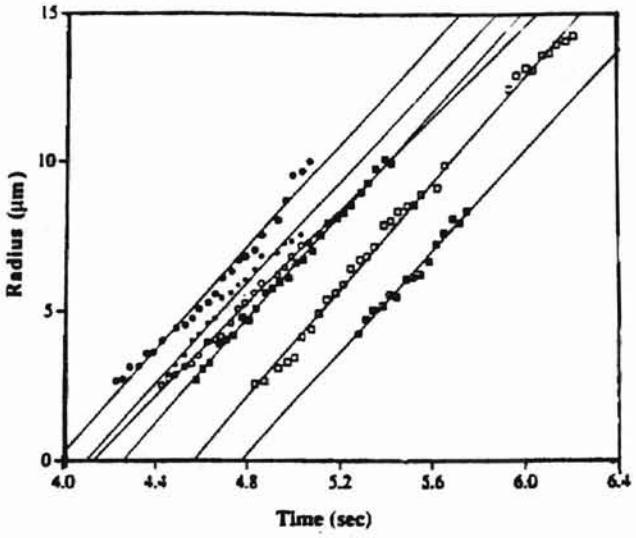

(a)

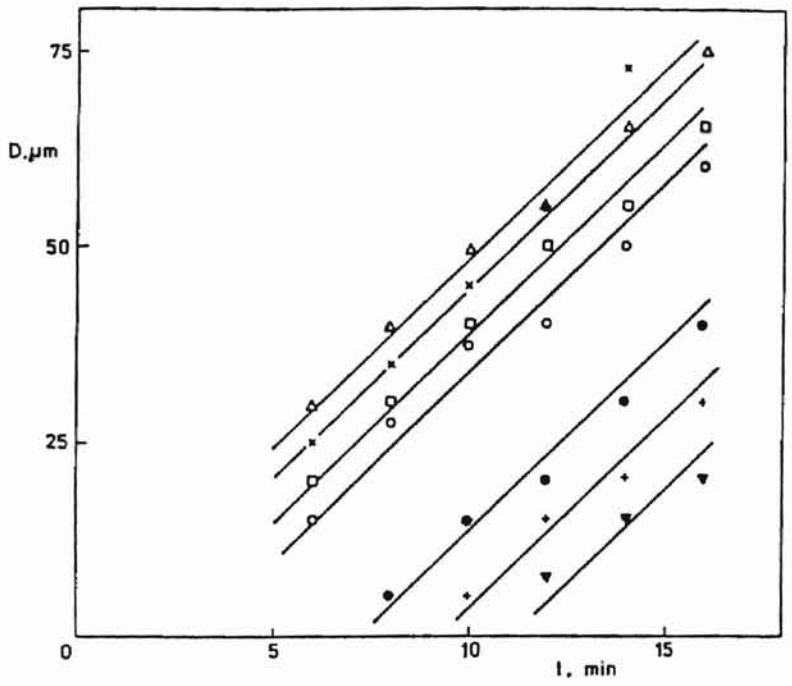

(b)

Figure 2.8 (a) Sherulitic Radius Versus Time[17]
(b) Increase in Spherulite Size with Time[19]

and Spruiell concluded that non-isothermal, quiescent crystallization showed a linear spherulitic growth rate, G. Binsbergen and De Lange[19] reached the same conclusion while isothermally crystallizing commercial PP at 135 °C. Figure 2.8b shows a linear growth in the spherulitic diameter with time according to Binsbergen and De Lange[19]. Wang and Liu[20], also observed a linear increase in the size of the crystal with time.

X-ray diffraction and DSC studies in polymer crystallization show the overall crystallization rate in bulk polymer specimens to be higher than the corresponding rate in thin films[21]. Conceptually, this observation can be related to the location of the center of the spherulites as shown schematically in Figure 2.9. In Figure 2.9, a thin slice in the bulk reveals that caps and sections of spheres whose centers are outside the slice are present along with spherulites that nucleate within the slice. On the other hand, a film of the same thickness as that of the slice, would only include the spherulites that nucleated within the slice. Therefore, a film of thickness, a, would show less crystallinity with respect to a slice in the bulk of a polymer melt.

Micrographs of PP crystallized from the melt[19], showed that, not all the spherulites started growing when the crystallization temperature, T_c, (135 °C) was reached. Figure 2.8a and b indicate that individual spherulites have different, so called, induction times.[17,19] The induction time was defined by Lednický and Muchová[19] as "the time period from the moment when crystallization temperature has been reached to the starting point of an individual spherulite growth." This concept is similar to the idea of an "incubation time", introduced by Lambrigger[22] as the time elapsed before the onset of crystallization after T_c is reached. Lednický and Muchová[19] proposed that a stable nucleus could be formed within the induction time, τ.

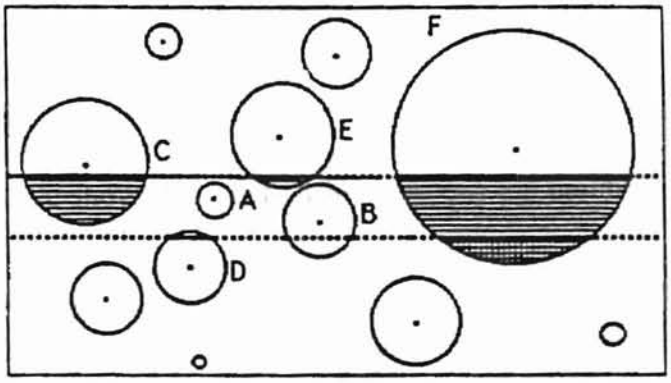

Figure 2.9 Spherulitic Growth in Bulk and in a Thin Slice of Polymer Melt[21]

Lednický and Muchová found that the induction time of iPP showed a monotonic increase with T_c as shown in Figure 2.10a. The two curves correspond to the values obtained from two identical experiments with iPP. Sakaguchi's[23] observation of the induction time for PET and copolymers of PET (TA-BA-8, TA-BA-16, TA-BS-8) show the influence of T_c on induction time, τ. Figure 2.10b, shows that τ decreases with T_c to reach a minimum value, following which, τ was observed to increase with T_c in agreement with the Lednický and Muchová [19] observation. Wang and Liu[20] studied the induction time for crystallization of polypropylene on carbon fibers as a function of temperature. Figure 2.10c shows the relationship between the number of nuclei and the time taken for the formation of an oriented layer of PP on the fibers, at different temperatures. The induction time for each curve was taken as the intercept of the curve on the time axis. The observations[20] showed that as temperature increased, so did the induction time.

Isothermal crystallization experiments under various pressure conditions were performed with PP, poly (polyethylene teraphthalate) (PET) and nylon 66 by He and Zoller[24]. He and Zoller[24] showed that although the melting temperature (T_m) and the crystallization onset temperature (T_o) increased linearly with pressure, undercooling to T_o ($\Delta T = T_m - T_o$) was not significantly affected by pressure variations as is illustrated in Figure 2.11a,b and c.

The observations cited in literature suggest that the major factors which influence quiescent crystallization are temperature and time. Higher cooling rates lead to lower values of T_c. Induction time is the time taken for the formation of a stable nucleus[17]. Induction time increases with temperature[19]. The size of each spherulitic crystal

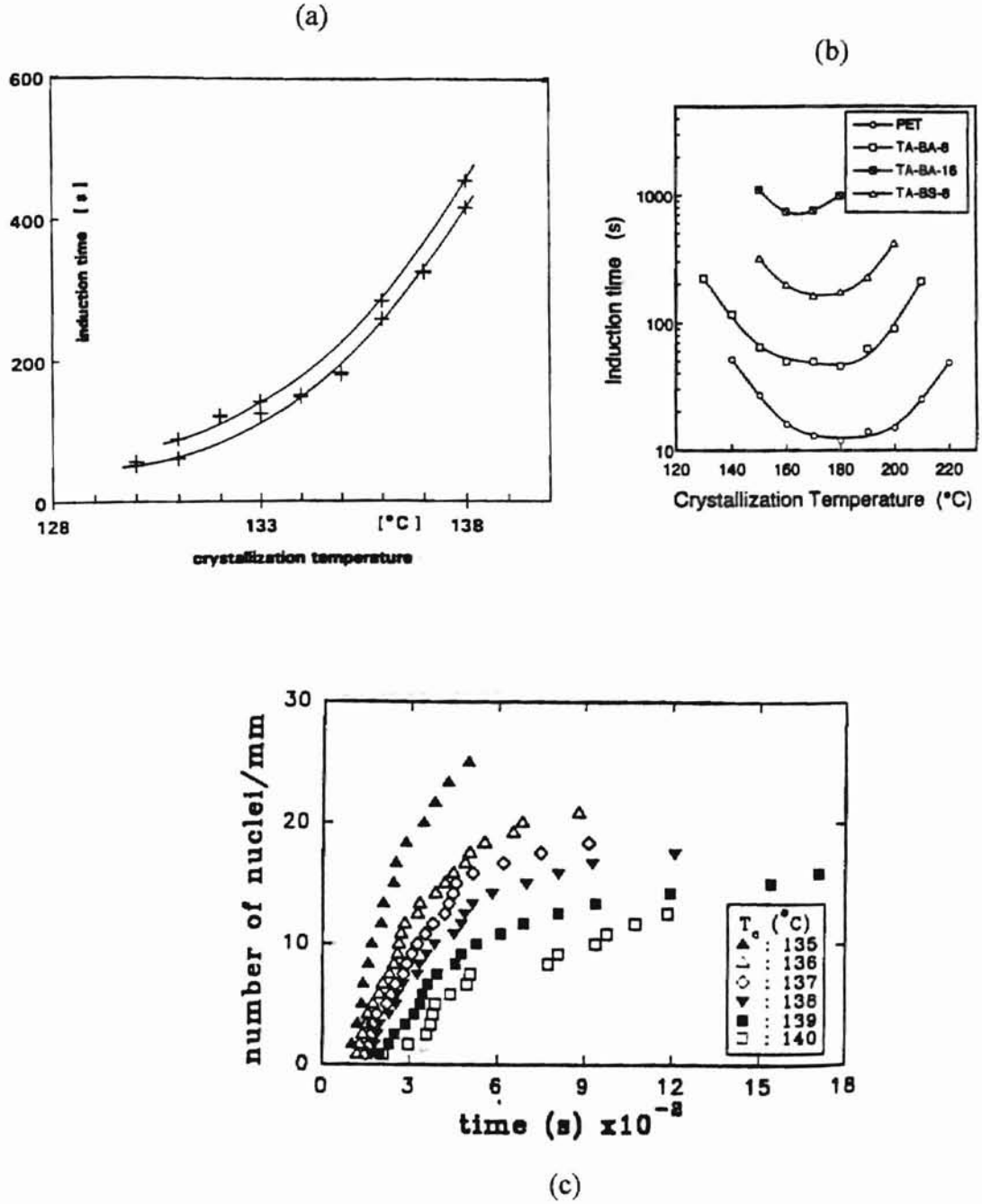

Figure 2.10 (a) Induction Time vs. Crystallization Temperature for Neat iPP[19]
(b) Temperature Dependence of Induction Time for PET and Copolymers[23]
(c) Nucleation Density[20] of PP at Different T_c's

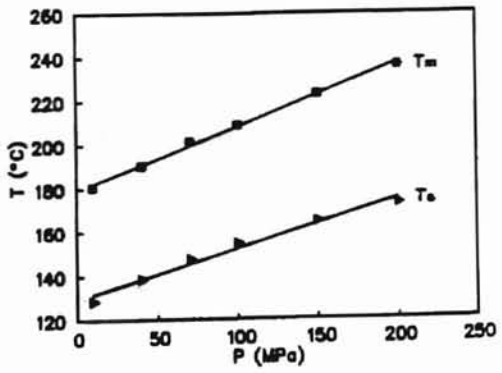

(a)

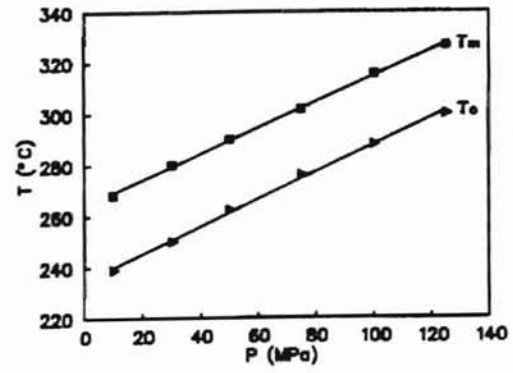

(b)

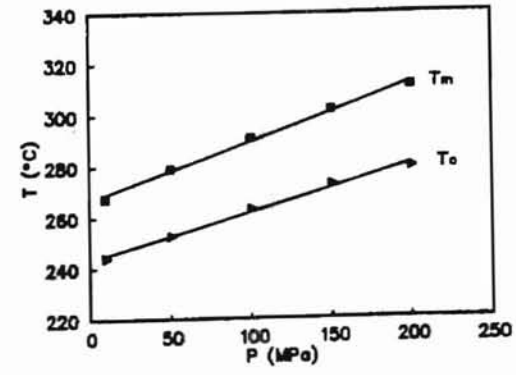

(c)

Figure 2.11 Melting Point and Crystallization Onset Temperature of (a) PP (b) PET and (c) Nylon 66, as a Function of Pressure[24]

increases linearly with time[20]. Crystallization in bulk is higher than in thin films[21]. Undercooling is independent of pressure[24].

§ 2.2(c) Modeling the Kinetics of Quiescent Crystallization

A model for isothermal, quiescent crystallization has been proposed by Avrami[3,4,5]. The Avrami model was developed for crystallization in metals. However, the model has also been used to describe crystallization in polymers.

The Avrami model[3,4,5] is based on the assumptions that potential nucleation sites called 'germ nuclei' exist in the melt, and that the rate of crystal growth, $G(t)$, is constant at a given temperature. The number of activated nuclei, or 'growth nuclei', $N'(t)$ is a fraction of the number of germ nuclei, $N(t)$, and determined by the frequency of activation, ν, of the germ nuclei to become the growth nuclei. The Avrami model assumes that the growing grains do not impinge upon one another. However, the Avrami model does account for potential nucleation sites consumed by growing crystals. The Avrami model also accounts for the possibility that crystal growth may be one dimensional (formation of rods), two dimensional (disk shaped growth), or three dimensional (spherulitic growth).

The Avrami model results in the Avrami equation:

$$ln\left[1-\xi(t)\right] = kt^{n} \tag{2.4}$$

where t is time, n is the Avrami exponent, k is the Avrami coefficient, and $\xi(t)$ is the relative crystalline volume fraction. The form of Equation (2.4) suggests that a plot of

$ln\{-ln[1-\xi(t)]\}$ as function of $ln(t)$ should be linear, with slope n and intercept $ln(k)$. Table 2.A illustrates how the values of n and k are functions of the dimensionality of crystal growth, the rate of crystal growth and the frequency of activation.

He and Zoller[24] studied crystallization of compressed PP and Nylon 66. Figure 2.12a shows the Avrami plots for crystallization in PP at a pressure of 100MPa. The n values estimated using the figure ranged between 1.3 and 1.7 for various values of T_c. At 200MPa, and different values of T_c, in Nylon 66, the same range of values of n was estimated indicating that the n values determined were independent of the crystallization temperature and pressure as is shown in Figure 2.12b and had non-integer values. The Avrami treatment of crystallization in PP by Ding and Spruiell[17] also showed (Figure 2.13a) that the n values are not affected by the crystallization temperature and that the values were non-integers. Sakaguchi's[23] studies on the kinetics of PET and copolymers of PET, showed supporting evidence of non-integer values of n, which had an average of 1.5 as is shown in Figure 2.13b.

The k values, were observed to be affected by temperature[24,17,23]. From Figure 2.12a and b, the Avrami plots by He and Zoller[24], the k values could be estimated. The k values estimated using Figure 2.12b were 0.12 at 282 °C, 0.03 at 284 °C and 0.005 at 288 °C, which showed that k was extremely sensitive to temperature, and decreased significantly after an increase in the temperature of only a few degrees. Figure 2.14a shows an exponential decay in the value of k with the plateau temperature, T_p discussed in § 2.2(b). Sakaguchi[23] also observed that k was very sensitive to temperature as shown in Figure 2.14b.

TABLE 2. A

n and k for Various growing Geometries and Nucleation Processes[51]

Dimension	Geometry	Fast Activation ($t\nu \ll 1$)		Slow Activation ($t\nu \gg 1$)	
		n	k	n	k
3	Sphere	3	$\frac{4\pi G^3}{3}\left(\frac{\overline{N}}{V_\infty}\right)$	4	$\frac{\pi G^3 \nu}{3}\left(\frac{\overline{N}}{V_\infty}\right)$
2	Disk	2	$\pi H G^2\left(\frac{\overline{N}}{V_\infty}\right)$	3	$\frac{\pi H G^2 \nu}{3}\left(\frac{\overline{N}}{V_\infty}\right)$
1	Rod	1	$\pi r^2 G\left(\frac{\overline{N}}{V_\infty}\right)$	2	$\frac{\pi r^2 G\ \nu}{3}\left(\frac{\overline{N}}{V_\infty}\right)$

* H: Height of the disk
** r: Radius of cross section

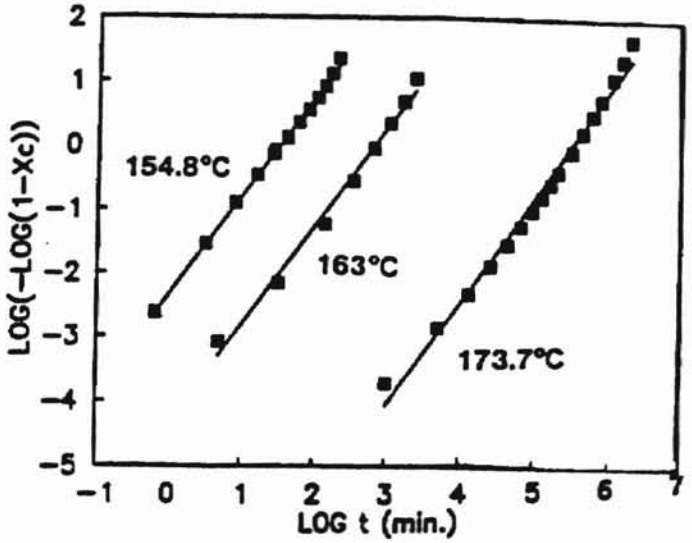

(a)

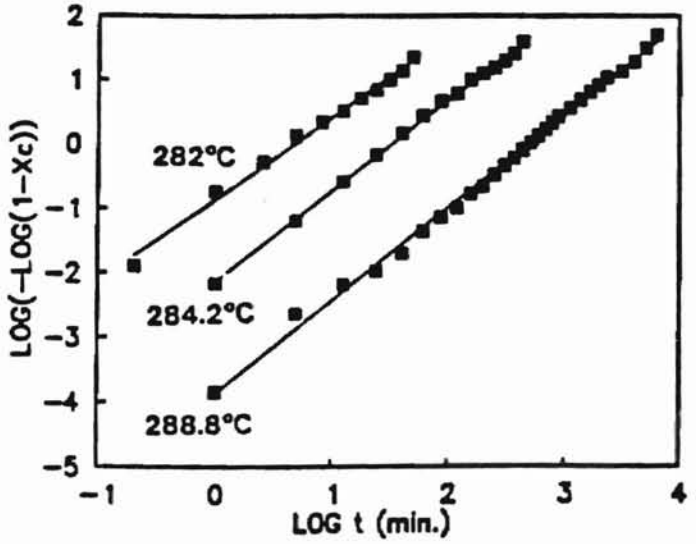

(b)

Figure 2.12 Avrami Plots at Various Temperatures[24]
(a) 100 MPa for PP (b) 200 MPa for Nylon 66

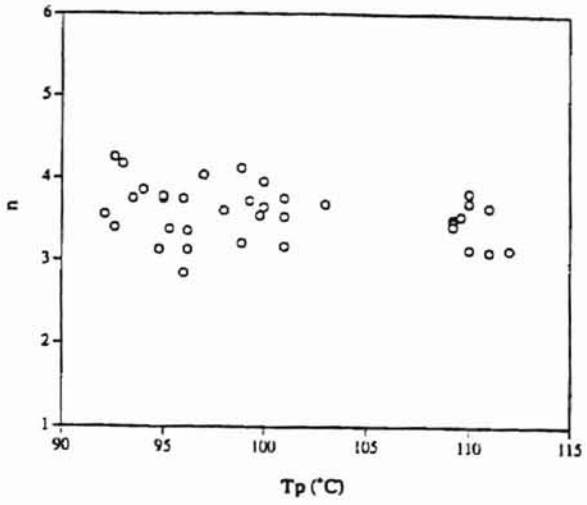

(a)

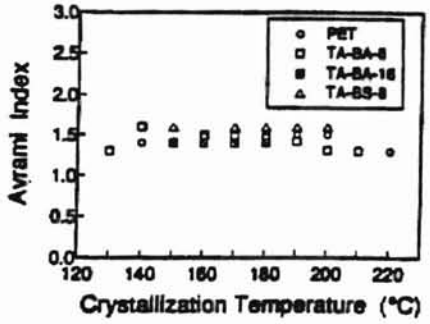

(b)

Figure 2.13 Avrami Exponents Versus Crystallization Temperature by (a) Ding and Spruiell[17] (b) Sakaguchi[23]

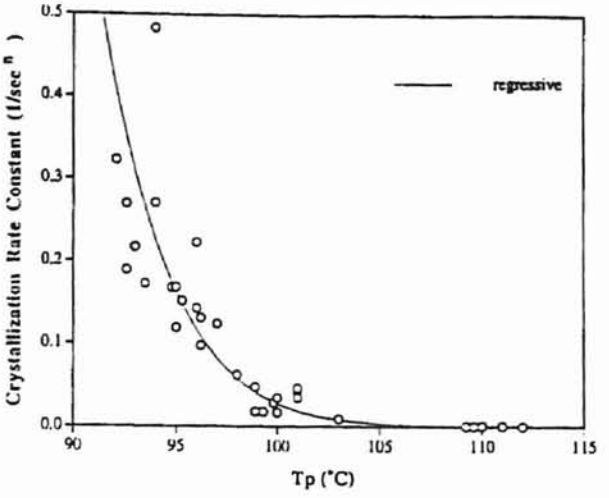

(a)

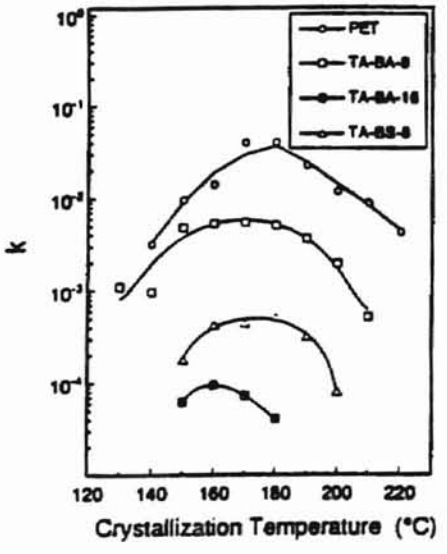

(b)

Figure 2.14 (a) Crystallization Rate Constant Versus T_c[17]
(b) k for PET and Copolymers under Isothermal Crystallization Conditions[23]

Application of the Avrami equation to SCBPE (branched metallocene polyethylene)[18], are shown in Figure 2.15a. The intermediate stage seen in Figure 2.6c was used to estimate the value of n which ranged between 2 and 4. The final stage yielded fractional values of n ($n < 0.5$). The values of n less than unity were attributed to secondary crystallization. Secondary crystallization as described by Fu *et al.*,[18] originates from the surface nucleation of the crystals formed during the primary stage of crystallization. The subsequent crystal growth takes place in the amorphous region trapped between the crystals formed during the primary stage of crystallization[18]. An Avrami plot with more than one linear section was also reported by Ding and Spruiell[17] as shown in Figure 2.15b. The section with a greater slope corresponded to the first and second regions in Figure 2.6b. The section with a smaller slope in Figure 2.15b corresponded to the third region in Figure 2.6b where slow crystallization began, after impingement of the spherulites. Ding and Spruiell[17] held secondary crystallization responsible for the slow crystallization. n values ranging between 3 and 4 were determined, using the first section of each curve in Figure 2.15b. Lambrigger[22] incorporated the concept of 'induction time', τ, to account for the non-integer values of n. Experiments performed Bukhina and Zorina[25] at crystallization temperatures of 170 K, 175 K, and 190 K, with polymethylsiloxane, compared well with the model[22] for n = 3.6, as shown in Figure 2.16. n was also shown as being independent of temperature[25].

The observations showed that the experimental data did not always conform to the Avrami model, and yielded varying and non-integer values of n. Therefore, modifications were made in the form of the Avrami equations to account for the noted

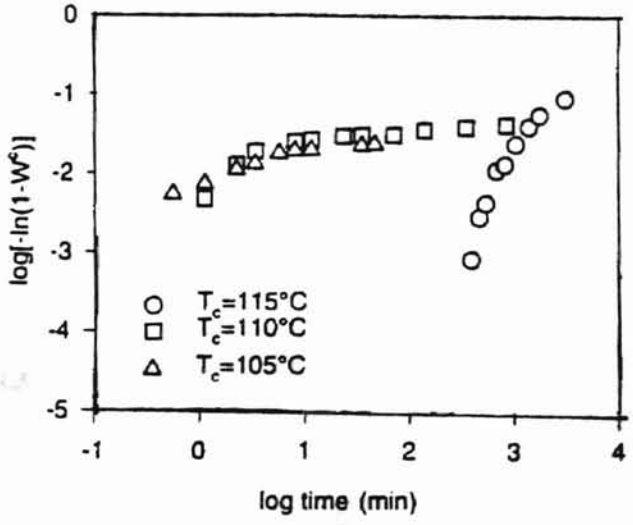

(a)

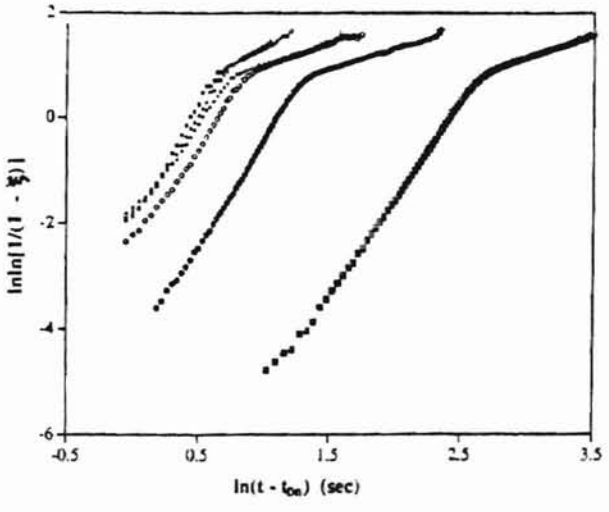

(b)

Figure 2.15 Avrami Plots for (a) SCBPE at Different Temperatures[18]
(b) PP During Non-Isothermal Crystallization[17]

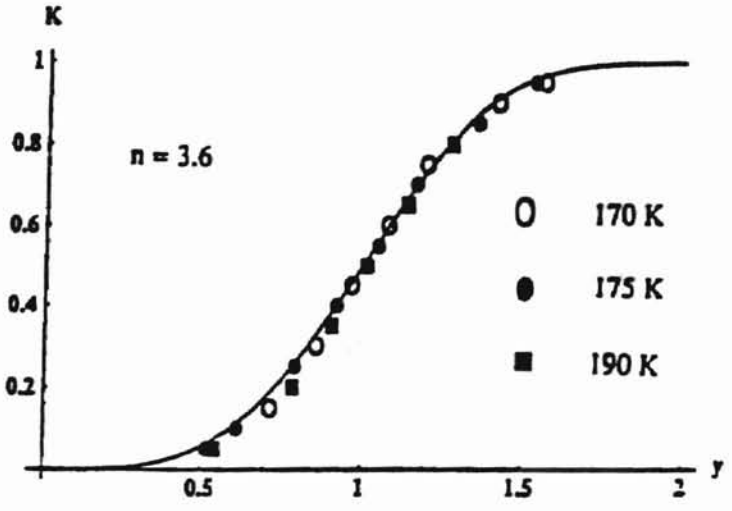

Figure 2.16 Experimental Verification of Lambrigger Model[25] using Polymethylsiloxane at Various T_c's

observations. Table 2.B summarizes the essential features of the models and the conclusions drawn from the models.

Lednický and Muchová[19] proposed that the non-integer values of n, which also changes during the course of measurement, was related to either instantaneous nucleation, or a constant nucleation frequency, in agreement with assumptions made by Ding and Spruiell[17]. However, in their analysis, Lednický and Muchová assumed that, induction time played an important role in determining n, rather than the secondary crystallization in the Ding and Spruiell[17] model. Hinrichs *et al.*[26] proposed that, the non-linear behavior of the Avrami plots resulted from slow time dependent rise in the local crystallinity, caused by secondary crystallization. Yet another model proposed by Schultz[21] based the non-linear effect of the Avrami equation on varying thickness of the crystallizing polymer sample. The smaller the thickness of the sample, the greater the deviation from the Avrami model.

In the present investigation, the induction time was not considered in the calculation of the n values, and hence, was not a controlling factor in the determination of the n values. However, there has been evidence of deviation from the Avrami model at locations of slow crystallization. Such locations were also associated with smaller thickness than the locations where the Avrami equation shows a straight line plot. Therefore, in this work, a particular factor that could influence the deviation from the Avrami theory has not been isolated. A further discussion of the non linear behavior of the Avrami plot is discussed in Chapter IV.

TABLE 2. B

Models Based On Avrami Model

MODEL BY	ASSUMPTIONS and MODIFICATIONS	CONCLUSIONS
Ding and Spruiell[17]	• Non-Isothermal Crystallization • Non-zero Nucleation rate	Severe impingement causes crystal growth restricted in certain directions resulting in non-integer values of n.
Lambrigger[22]	• Isothermal crystallization • Three-parameter Avrami equation: n, k, τ • Introduced dimensionless time functions, a and y	Developed two-parameter master curves: $I(a,n)$, $K(y,n)$, for $n>1$, and $n<1$, respectively. Experimental verification showed non-integral values of n.
Hinrichs *et al.*[26]	• Isothermal Crystallization • Time dependence of crystal growth • Overall crystallinity, a function of local crystallinity and change in crystal volume	Model explains non-linear behavior of Avrami plot $ln\{-ln[1-\xi(t)]\}$ vs. $\ln(t)$.
Janeschitz-Kriegl[53]	• Non-isothermal crystallization • Non-Isokinetic Crystallization • Description of cooing process by partial differential equation Functions φ_i of varying growth rate were introduced to provide information regarding growth geometry of crystals	Under rapid quenching of polymer melts, φ_i's could be used to determined that the number of activated nuclei increased with decrease in temperature.

Table 2.B continued...

MODEL BY	ASSUMPTIONS and MODIFICATIONS	CONCLUSIONS
Schultz[21]	• Isothermal Crytallization • Thickness (a) dependence on crystallization kinetics • Mathematical treatment of correction for thin films for homogeneously nucleated system	Developed modified Avrami equations for i) Radius, $R < a$; $a/G \geq t$ ii) $R > a$; $a/G < t$ For decreasing values of a/G the linear form of the Avrami equation yielded a curved line. For $a/G \rightarrow \infty$ the kinetics approached the Avrami model
Lednický and Muchová[19]	• Isothermal Crystallization • Induction time (τ) subtracted from time, t, in the Avrami equation • Individual spherulites have different τ	Existence of an overall τ about which the probability of nuclei generation is maximum. Determination of τ essential to obtain correct values of n, k. Non-integer values of n.

For non-isothermal crystallization, Janeschitz-Kriegl[53] proposed a model for crystallization in rapidly quenching polymers. Unlike other models discussed, G was a variable in this model. A brief sketch of the model is listed in Table 2.B.

Although, the Avrami treatment does not yield the expected integer values of the Avrami exponent, the model is widely used to characterize the kinetics of crystallization in polymer melts.

§ 2.2(d) Persistence of Anisotropy in UHMWPE

Most crystallization studies[74] conducted with conventional PE resins use samples with molecular weight (M_w) less than 300,000. In all such studies the quiescent melt was assumed to be totally amorphous, *i.e.*, free of any past history of mechanical treatment or influence of flow. However, experiments with ultra high molecular weight PE (UHMWPE) by Zachariades and Logan[27] showed that, the polymer ($M_w > 10^6$) was highly anisotropic even above its equilibrium melting point (T_m^o) and had a tendency to fibrillate. There have also been reports in the literature[27] which establish that the 'shish kebab' morphology of the solution drawn HDPE fibers exhibits birefringence at temperatures above 180 °C (~40 °C above T_m^o of the HDPE crystals)[27]. Wide angle X-ray analysis also showed evidence of order in UHMWPE[27].

Zachariades and Logan[27] melted HDPE powder ($M_w > 10^6$) at 145 °C and found that upon further heating, the powder particles formed clusters at 160 °C without losing their crystal structure. When the particles were placed between crossed polarizers, they

observed that the globular particles showed birefringence. The sample was then cooled and crystallized at 123 °C. Reheating of the sample displayed anisotropy at temperatures greater than 300 °C. The observed peculiar anomaly was attributed to slowly melting superheated crystals. In lower M_w polyethylene, superheating was observed up to no more than 10 °C above T_m^o. At this temperature, the polymer fused into an isotropic melt. Only UHMWPE showed the characteristic of being anisotropic in microstructure up to temperatures near 200 °C.

Evidence of molecular order in high molecular weight PE has also been observed by Bremner and Rudin[28] in proton magnetic resonance (NMR) spin-spin measurements on two commercial-grade polyethylene samples (M_w = 104,900 and 112,000) in the melt state. The samples were raised to 150 °C. For each sample, the NMR measurements showed that a large fraction of the melt exhibited longer relaxation time with respect to the rest of the melt. Thus, the NMR measurements exhibited strong evidence of the existence of compact ordered domains retained at temperatures above the melting point of the sample.

A plausible explanation for the observed order above the melting point temperatures has been provided by Bremner and Rudin[28]. In semicrystalline polymers with high molecular weight, crystalline segments may be trapped between firm entanglements. In such situations, raising the polymer temperature would expand the crystalline structure without disrupting the existing crystalline segments.

Aharoni *et al.*[28], studied UHMWPE melts using electron microscopy and found the radius of gyration of the molecules to be the same in the crystal phase as in the melt.

This led to the conclusion that crystallization process did not require large scale intermolecular disentangling or "reeling-in" of polymer segments. Therefore, in the melting process, the relative segmental densities in different regions of the polymer were retained.

The studies discussed show persistence of order in certain high molecular weight polyethylenes above melting point temperature. The discussion is significant in this investigation, since the materials used in this work were required to be completely amorphous above the melting temperature. High melt flow index (6.5) of the sample used here (HDPE) indicates that M_w was lower than the range discussed in this section and ensures the lack of order of the polymer chains in the melt state.

§ 2.3 Flow-Induced Crystallization

The term 'flow-induced crystallization' refers to the influence of an external flow field on polymers during phase transformation. The flow can be shearing, extensional or mixed. The resulting crystal is often strikingly different in morphology from the quiescently crystallized polymer. In the presence of an extensional flow field, for example, the randomly coiled molecules in a melt partially uncoil in an attempt to align themselves in the direction of the flow field[29]. The crystallization then proceeds much faster than quiescent crystallization, and the extended chain crystals formed have a higher degree of molecular orientation.

§ 2.3(a) Rheometers

Orientation in polymers can be generated by devices that are designed to induce a flow field. Such an instrument is called a rheometer if the instrument allows the flow field to be well characterized. While some rheometers generate a flow in a weakly birefringent matrix medium which contains the crystallizable polymer, others act directly on the polymer, inducing flow as well as orientation simultaneously. A brief description of rheometers is provided in the following section.

§ 2.3(a) *i.* Capillary Rheometer

Figure 2.17 shows a typical capillary rheometer (the Rheoscope 1000, manufactured by CEAST)[30]. The rheometer works on the principle of forcing the polymer melt through a capillary tube under high pressure. Flow-induced crystallization was initially discovered[31] and studied in a capillary rheometer.[32,33] However, the flow produced is inhomogeneous and direct observation of the crystallization process has never been achieved. Indirect measurements such as viscosity and first normal stress difference did not provide satisfactory insight into the process[32]. Capillary rheometers have been abandoned as means to study flow-induced crystallization.

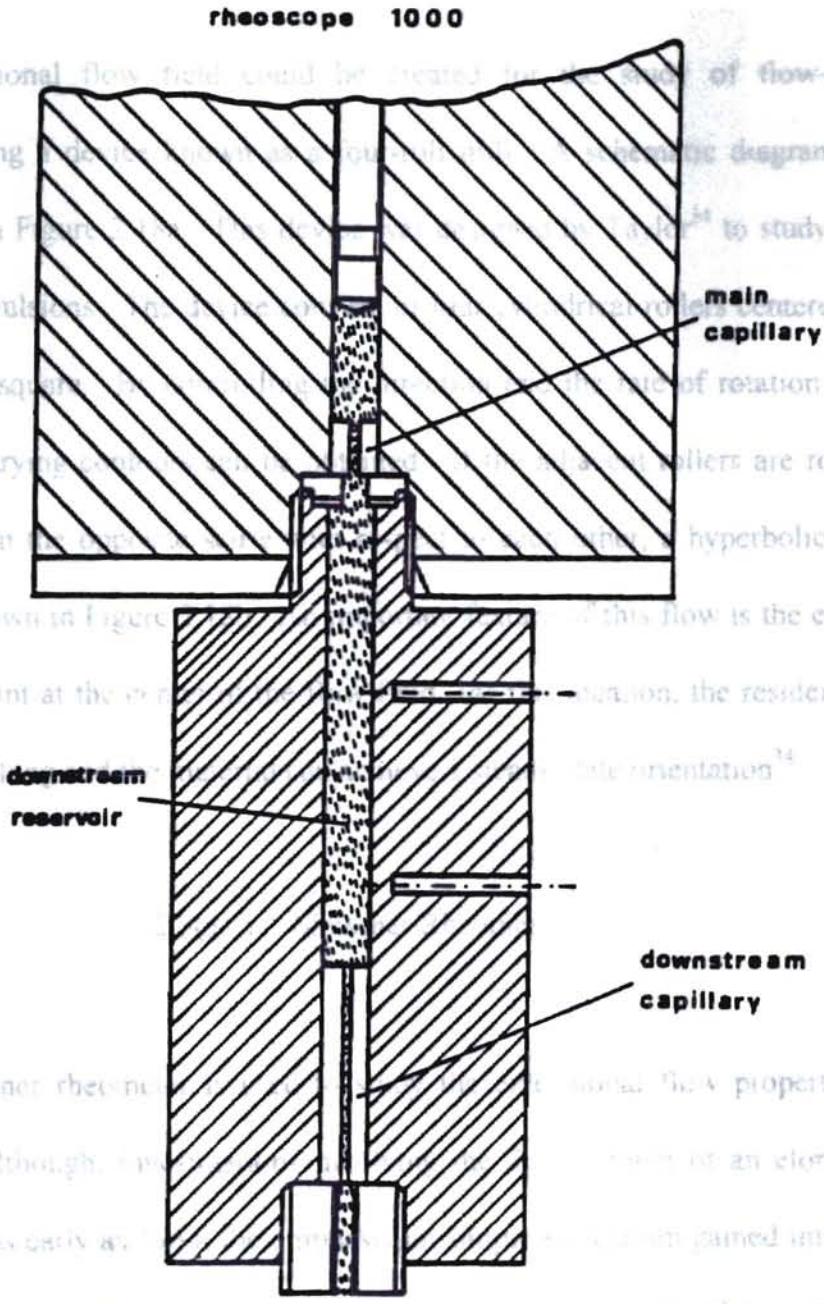

Figure 2.17 A Modified Capillary Rheometer[30]

§ 2.3(a) *ii.* Four-Roll Mill

An extensional flow field could be created for the study of flow-induced crystallization using a device known as a four-roll mill. A schematic diagram of the device is shown in Figure 2.18a. This device was designed by Taylor[34] to study droplet deformation in emulsions. The device consists of four cylindrical rollers centered at the four corners of a square. By controlling the direction and the rate of rotation of each roller, flows of varying contours can be obtained. If the adjacent rollers are rotated at equal speed, but in the opposite sense with respect to each other, a hyperbolic flow is produced as is shown in Figure 2.18b. An important feature of this flow is the existence of a stagnation point at the center of the flow field. At this location, the residence time for the material is long and the material can achieve a steady state orientation[34].

§ 2.3(a) *iii.* Meissner Rheometer

The Meissner rheometer is used to study the extensional flow properties of a polymer melt. Although, investigations involving the development of an elongational rheometer began as early as 1964, the emphasis on simple elongation gained importance in the late 1970s. Figure 2.19a shows a schematic representation of an extensional rheometer designed by Meissner[35]. Two rotary clamps Z_1 and Z_2 placed at a distance L_o from each other, clasped the sample which was a rod-shaped polymer melt of diameter d. The clamps were driven by a synchronous motor, M_1. The sample, which floated on the surface of a Silicone oil-bath, was elongated with a constant Hencky rate of strain. An

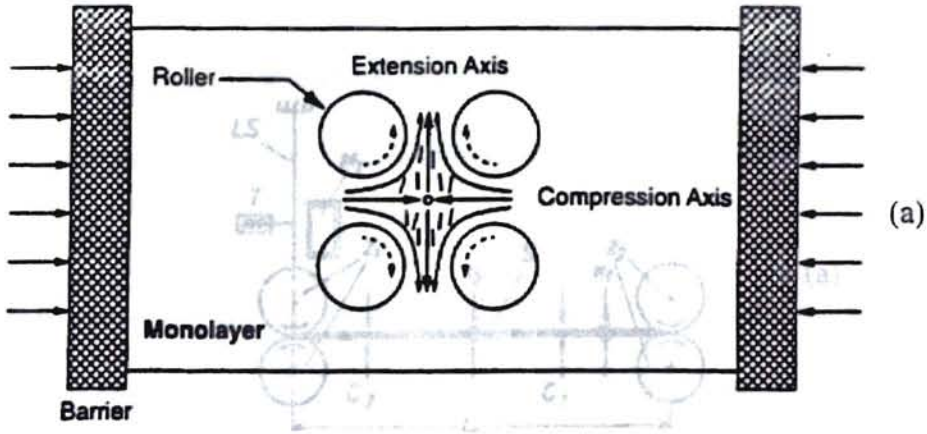

(a)

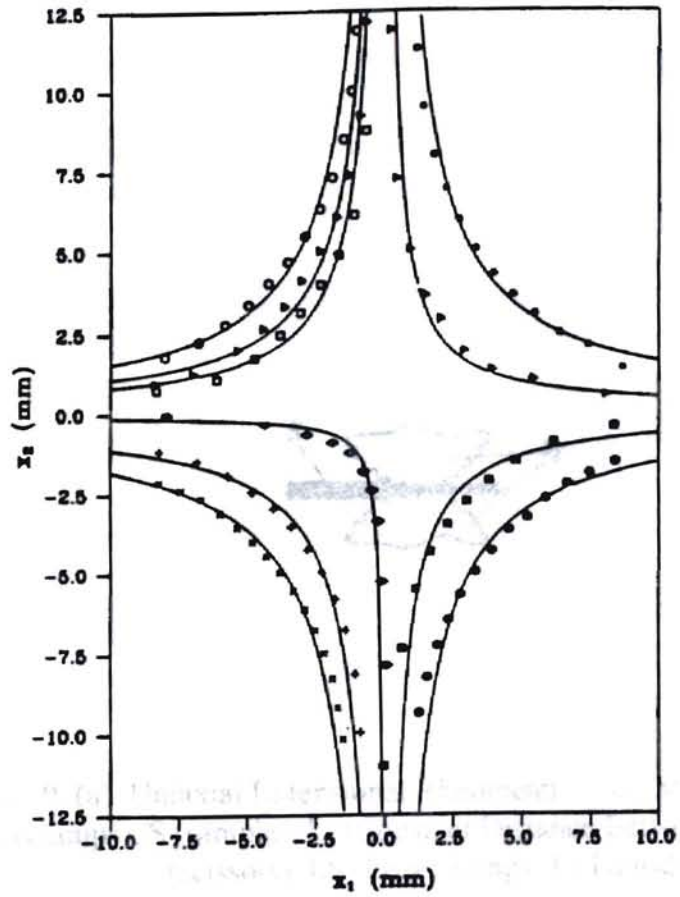

(b)

Figure 2.18 (a) Four-Roll Mill[34] (b) Hyperbolic Streamline[42] for LLDPE at 134 °C
x_1, x_2 (Orthogonal Coordinate Axis)

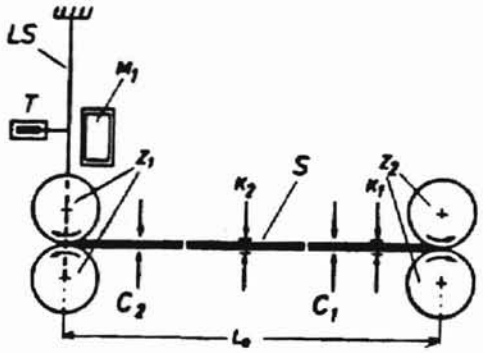

(a)

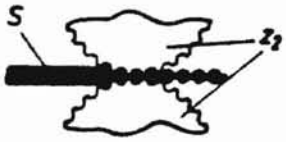

(b)

Figure 2.19 (a) Uniaxial Extensional Rheometer[35] (b) M_1 (motor), Z_1, Z_2 (clamps), S (sample), L_o (Constant Distance Between Rollers), C_1, C_2 (scissors), LS (Leaf Spring), T (Transducer)

important feature associated with the clamps is that, as material was continuously transported from the inside to the outside of the clamps, the formation of necking zones was precluded and the sample maintained a homogeneous cross section (Figure 2.19b). However, the operation of the rheometer required a constant temperature in the silicone oil bath ($\Delta T < 0.1$ °C).

The Meissner rheometer[35] is associated with certain experimental shortcomings. The rotational speed of the clamps is not completely transferred as local speed to the sample. The difference in the two speeds is ~10%. Another issue of concern is the interfacial tension between the sample and the supporting liquid. Finally, for short samples, the necking at the clamps induces an error in the true elongation of the sample.

§ 2.3(b) Experimental Techniques to Observe Flow-Induced Crystallization

In 1967, van der Vegt and Smit[31], reported the arrest of flow in polymer polypropylene melt in capillary tubes. They recognized the existence of a critical shear stress which lead to shear thickening, and eventually cessation of flow in polymeric melts in a capillary rheometer. The cessation of flow was attributed to the formation of a new crystal phase in the capillary tube. Following this unusual observation, additional experiments were performed to observe crystal structures and to measure related properties such as melting point, orientation, modulus, and transparency[36].

Southern and Porter[36], performed tests on high density polyethylene (HDPE) using a capillary rheometer. The temperature of the melt was held between 130 °C and 145 °C. The crystallization process occurred near the entrance of the capillary under

high pressure (≤ 1900 atm) and was marked by the cessation of flow. Subsequently the capillary was cooled to 110 °C and removed. The X-ray photographs of the crystal morphology revealed the presence of arcs, instead of concentric rings as in the case of quiescent crystallization. This was conclusive evidence of orientation in the polymer chains.

One of the most frequently encountered terms in the characterization of polymer chain orientation is the Hermann's orientation function, f, defined as

$$f = \frac{3\langle \cos^2 \phi \rangle - 1}{2} \quad , \tag{2.5}$$

where ϕ is the angle of orientation with respect to the flow (ϕ = 0, for maximum orientation). Southern and Porter found that as T_c in the capillary was raised, the melting point of the resultant crystals decreased as is shown in Table 2.C. The orientation function, f, was found to have decreased from 0.9 to 0.6, as T_c was increased. The experiment showed that high values of f corresponded to high values of the melting point of the crystal formed.

As an additional observation, Southern and Porter noted that the portion of the polymer extruded at the exit of the capillary was opaque because the light was scattered by randomly oriented folded chain segments. Whereas, the portion of the polymer inside the capillary which experienced flow-induced crystallization was transparent.

Titomanlio and Marrucci[30] discovered, while performing experiments with HDPE, that although elongational flow was observed by Southern and Porter[36] at the entrance of the capillary, shear flow dominated along the length of the capillary. A schematic diagram of capillary flow behavior is shown in Figure 2.20. Titomanlio and

TABLE 2. C

Melting Point as a Function of Rheometer Crystallization Temperature[87] by Differential Scanning Calorimetry*

Rheometer crystallization T_c, °C	T_m, ± 0.4 °C
136	140.1
137	140.0
138	140.0
139	140.0
140	138.8
142	139.0
144	138.8

*The samples were the 4-mm segments adjacent to the capillary entrance crystallized at a plunger speed of 5.0cm/min; scan rate, 5°C/min.

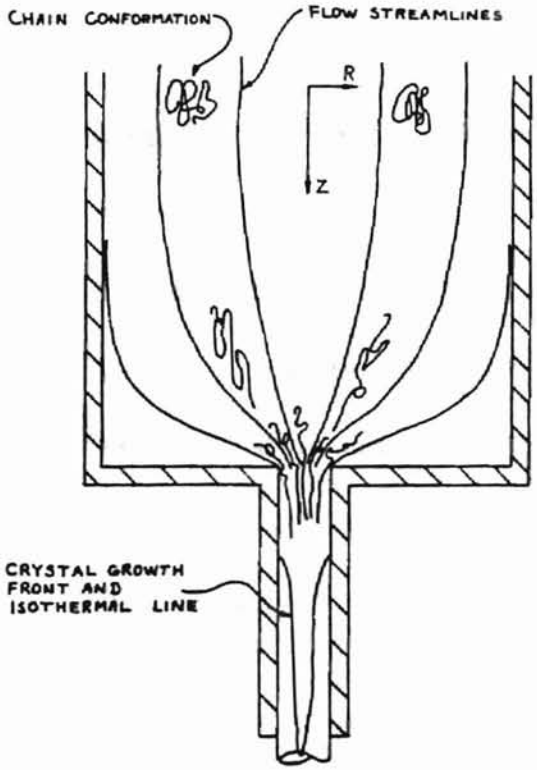

Figure 2.20 Capillary Flow Behavior[35]

Marrucci[30] proposed that away from the entrance of the capillary, shear-induced crystallization takes place over the layer(s) of crystals initially formed due to elongational flow.

A brief discussion on the concept of "precursors" will be useful in the discussion in the following paragraphs. A study on analysis of the orientation distribution of crystals by Krigbaum and Roe[37] showed that the probability of the formation of a stable nucleus with a particular orientation is proportional to a critical number of segments with that orientation. The formation of such oriented nuclei, could increase the probability of oriented crystallization. The initially formed oriented nuclei are termed as the precursors to further crystallization. Desai, and Abhiraman[38] experimentally showed that flow-induced orientation of poly(ethylene terephthalate) (PET) melts led to the orientation of precursors, and significantly increased rate of crystallization.

Short term shearing was studied by Eder, Janeschitz-Kriegl, and Liedauer[39] using PP which was extruded in a rectangular duct. Eder *et al.* observed that, while a polymer would take several hours to crystallize quiescently, it was possible to trace the shear-induced crystallization process as soon as the temperature was lowered a few degrees below the melting point. The crystal growth showed the value of the Avrami exponent of one. Using the DSC-pan photographs[39], Eder *et al.* proposed that, during the shear, nucleation of thin precursor sheets takes place, and after the cessation of flow, unidimensional crystal growth occurs over the thin sheets.

Jerchow and Janeschitz-Kriegl[40], in their study on shearing flows of *i*PP at high shearing rates and short durations, attributed the formation of highly oriented surface layers to the existence of thread-like precursors arranged parallel to the flow direction.

Away from the walls of the ducts, a fine grained layer, characteristic of lower shear rates, was observed to form. This layer, they believed, consisted of small spherulites, and collectively, did not show any birefringence.

An experimental technique was described by Sakellarides and McHugh[29] to produce oriented polymer fibers, by introducing needle-like obstructions in a film-extrusion die. These 'needles' effectively served the purpose of the 'precursors'. The 'needles' acted as nucleation sites which locally generated an extensional flow field, which in turn, induced a high degree of orientation in their neighborhood causing the formation of fibrillar crystallites in a much less oriented matrix. Micrographs of extruded blends of LLDPE and HDPE showed that the 'needles' induced crystallized structures which were composed of HDPE. The structures exhibited high birefringence and melting point elevation, indicating a high extensional orientation.

McHugh *et al.*[41] showed that self-reinforced polymers could be produced by oriented crystallization during melt flow at high temperatures. Crystallization in HDPE and PP films, extruded through a slit die equipped with optical windows, showed the presence of extended chain structures in the extrudate manifested as birefringence. Figure 2.21 illustrates the DSC scans of die-crystallized HDPE, at various positions within the die. The scans show increasing degree of crystallization from the core to the outer edge of the slit die extrudate.

McHugh, Guy, and Tree[42] used a four-roll mill to deform a cylindrical droplet of HDPE suspended in a LLDPE in the melt phase. The deformation of the droplet at T_c led to planar extensional flow-induced crystallization in HDPE. The transformation kinetics was studied with the aid of video imaging of the birefringence produced. A typical trend

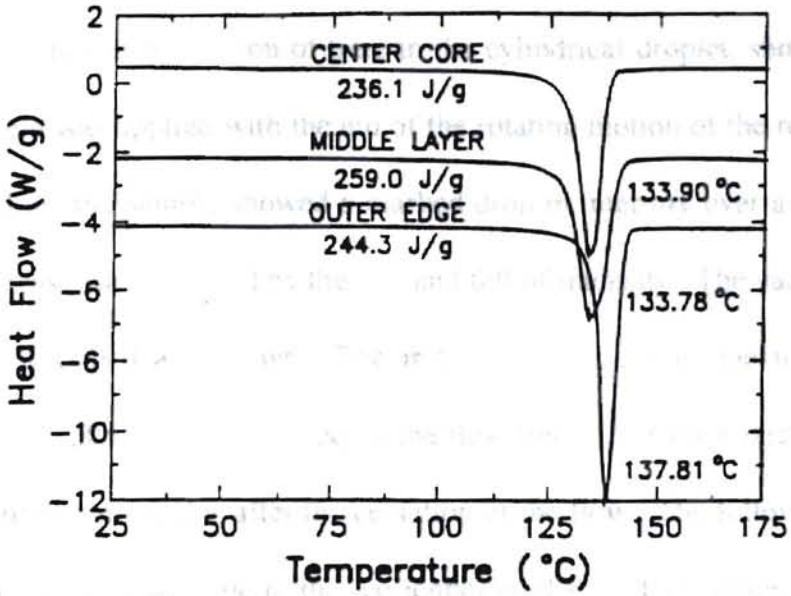

Figure 2.21 DSC Scans of Die-Crystallized PE Film[41]

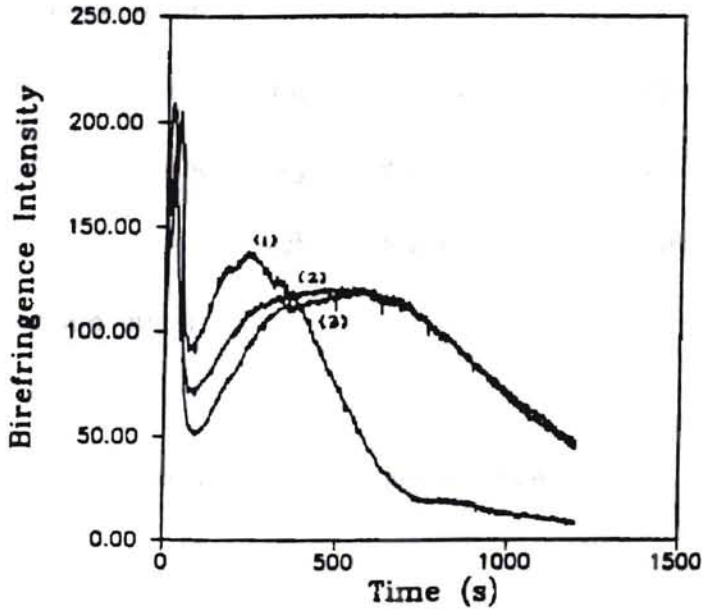

Figure 2.22 Droplet Phase (HDPE) Birefringence Intensity[47] at the Axial Positions T_c = 129.2 °C. $\dot{\varepsilon}$ = 0.031/s, Deformation Time = 50s

of variation in the intensity due to birefringence is given in Figure 2.22. The intensity due to the birefringence as a function of time in the cylindrical droplet, showed a sharp rise as the flow field was applied with the aid of the rotating motion of the rollers. After the cessation of flow, the sample showed a marked drop in intensity over a certain time interval. The decrease was followed by the rise and fall of intensity. The variation in the intensity can be described as follows. The initial sharp rise was due to the forced molecular orientation of the HDPE, caused by the flow field. The sharp decline was due to the relaxation of the molecules after the cessation of the flow. The following rise and fall in the intensity pattern was due to the reorientation of the HDPE molecules to form the ECC morphology, indicating the formation of flow-induced crystals. The curves labeled (1),(2) and (3) are the intensity curves for locations in order of their decreasing distance from the stagnation point.

DSC measurements, X-ray diffraction methods and birefringence studies of the crystals formed due to a flow show long range order in the crystals, unlike the folded chain crystals. Such crystals display stable low energy configurations corresponding to elevated melting point temperatures.

§ 2.3(c) Kinetics of Flow-Induced Crystallization

Crystallization kinetics of FIC is currently, a field of exploration. Several theories have been proposed which are applicable only to a limited group of polymers under certain constraints, such as temperature, pressure, strain and the rate of strain. Some of the relevant theories, analysis and results are presented in this section.

Desai and Abhiraman[38] studied the crystallization process in low- and high-speed melt-spun threadlines of PET. The experiments led Desai and Abhiraman to conclude that the Avrami exponent, n, decreased with an increase in the precursor orientation. The precursor orientation was observed to increase with the spinning rate of the PET fibers. The n values estimated using Figure 2.23 shows an increase in the values as the spinning rate decreases. This observation was interpreted as follows. For high spinning rates, the precursors were oriented along the direction of the drawing, as were the molecules in the melt close to the precursors. These molecules had the tendency to form crystals along the precursor orientation, and caused the values of the Avrami exponent to be close to unity. Whereas, lower spinning rates caused less orientation in the direction of the drawing, and consequently, less order in the crystal structure in the direction of the drawing, leading to $n > 1$.

Birefringence measurements to analyze the kinetics of seeded crystal growth in a tubular flow geometry of 0.01wt% solutions of PE in Xylene were studied by McHugh and Spevacek[43]. The crystallization kinetics were analyzed using a modified form of the Avrami equation. The modification was suggested by Eder *et al.*[39], who proposed the inclusion of a structure function, $\theta(v, t)$ which affected both nucleation and growth factors. The term $\theta(v, t)$, which shows both flow rate (v expressed in cm/min) and time dependency, is considered to be the probability that the nucleation and the growth processes occur as a result of transmission of stress to the precursor. In other words, in the absence of flow, precursor formation and hence crystallization are impossible. Equation (2.4) under the given conditions of flow rate and temperature can be written as

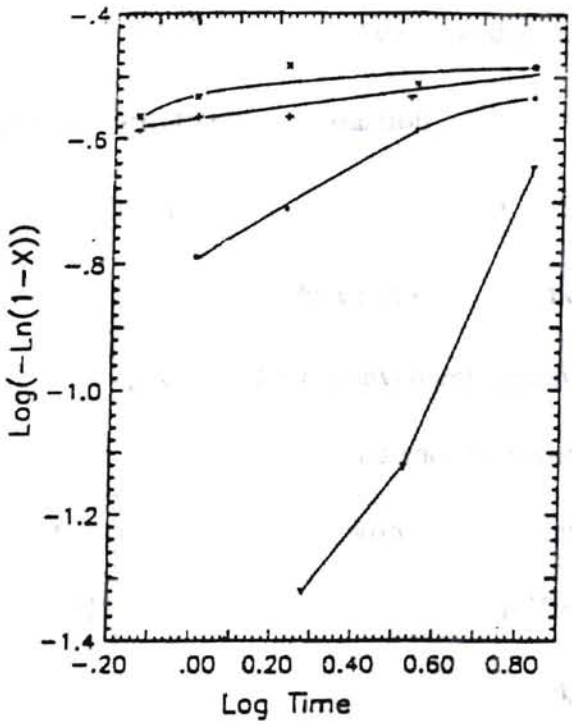

Figure 2.23 Avrami Plot for PET Filaments[38] at 150 °C

$$-ln\left[1-\xi(t)\right] = k' t^{n'} \quad , \tag{2.6}$$

where
$$k' = \left(\frac{f\rho_c}{\phi_\infty \rho_l}\right) Gv[\theta(v,t)]^2 \quad . \tag{2.7}$$

and
$$\theta(v) = 1 - a_o e^{-a_1 v} \quad . \tag{2.8}$$

In Equation (2.7), f includes geometrical parameters, and ρ_c and ρ_l are the densities of crystal and solution phase, respectively. In Equation (2.8), a_o = 47.7 and a_1 = 1.03 x10^{-3} min/cm. Figure 2.24a shows a typical Avrami plot with n' = 2, and k' = 8.3 X 10^{-5}/sec^2. Figure 2.24b shows the temperature dependence of k' for PE and PP samples.

Equation (2.6) may appear to be a convenient equation for this investigation, since in this work the kinetics of FIC was studied and the parameters n and k calculated. However, the assumption made in the theory proposed by Eder *et al.*[39] is different from the assumption in this work. $\theta(v, t)$ defined by Eder *et al.*[39] depends on a certain flow rate of the tubular flow of PE solution, whereas in this work, the flow is induced by stretching an HDPE melt sample. Therefore, the relevant parameter in this work becomes the rate of elongation, rather than the flow rate. Since the theory proposed by Eder *et al.*[39] is only valid in the presence of a flow rate, Equations (2.7) and (2.8) do not apply to this work.

§ 2.3(d) Experimental Work in FIC by Kakani[7]

The experimental work done by Kakani[7] to generate data to study crystallization kinetics of semicrystalline polymers such as HDPE and PP is of special importance to

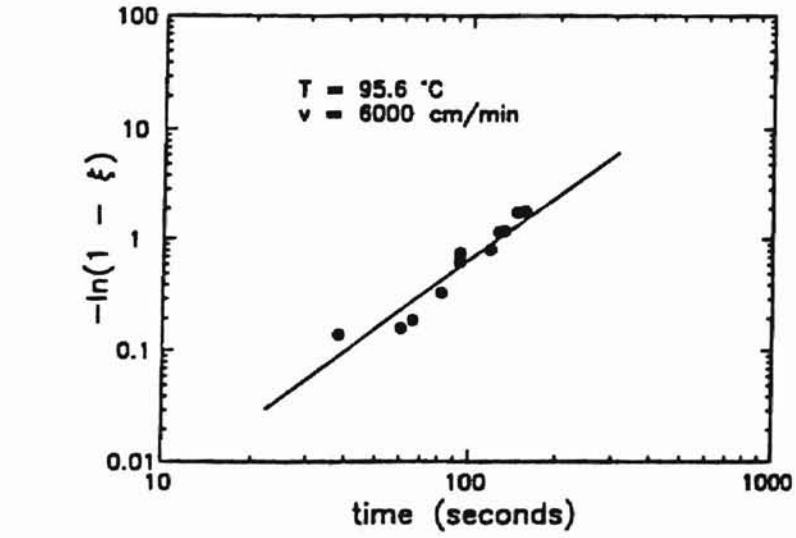

(a)

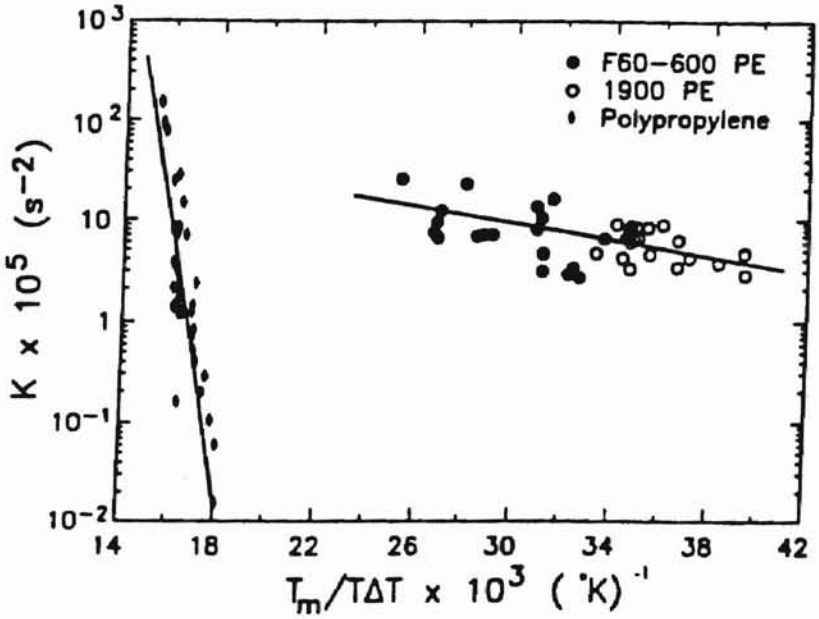

(b)

Figure 2.24 (a) Avrami Plot at 95.6 °C, $\dot{\varepsilon}$ = 6000 cm/min,[43] $n = 2$
(b) Temperature Dependence of k values for PE and PP on a Supercooling Plot

this work. Kakani observed the birefringence in polymer samples undergoing flow-induced crystallization. The birefringence varied according to the changing orientation of the molecules in the sample. The flow to induce crystallization in the polymer sample was generated by an extensional rheometer, a modified form of the Meissner rheometer.

§ 2.3(d) *i* Optical Train to Observe Birefringence

Figure 2.25 shows the optical train configured to observe birefringence[7]. The light source for the experiment was a 150 W Tungsten Halogen lamp. The emitted light passed through a light pipe, 0.9 cm in diameter. The end of the light pipe had a pin-hole opening to approximate a point source of light.

The pin hole opening was placed at the focal point of a biconvex lens with a focal length of 15 cm. A light filter (maximum transmission at 488 nm) was placed between the convex lens and the polarizer. The polarizer was oriented at 45° counterclockwise with respect to the vertical direction (the reference direction). An analyzer was oriented perpendicular to the polarizer and placed in the train such that a Silicone oil bath containing the sample could be situated between the polarizer and the analyzer. As the sample crystallized, the intensity of the light transmitted through the optical train varied and was observed with a black and white video camera and a monitor. The images were recorded with a VCR for later analysis.

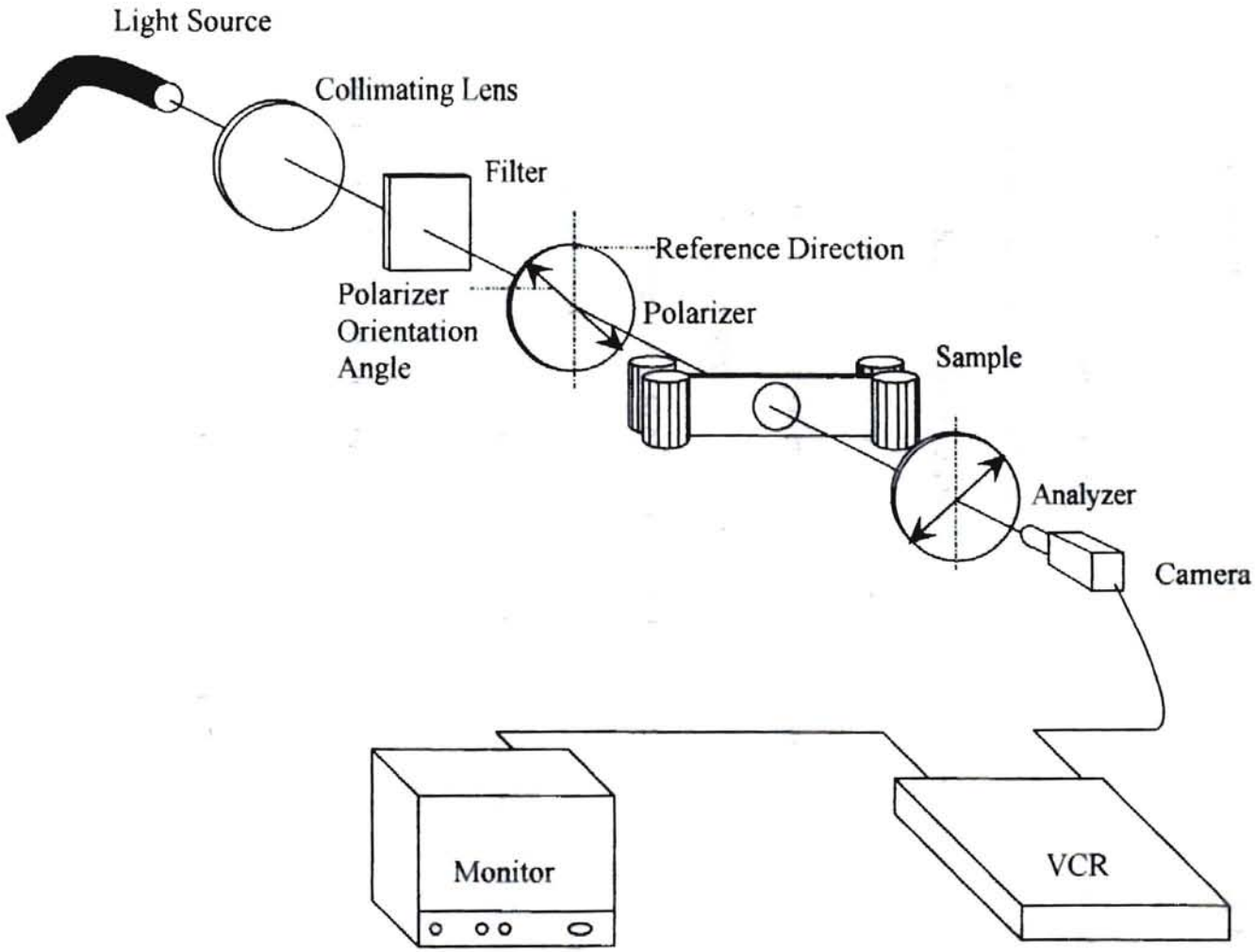

Figure 2.25 Optical Train to Study Flow-Induced Crystallization using Birefringence [7]

§ 2.3(d) *ii* The Extensional Rheometer

The major components of the rheometer, originally developed by Siddiquee[44], are shown in Figure 2.26a. The components include a stepper motor (part M), a system of pulleys and sprockets (part P which included parts A, B, C, D and F), shafts (labeled S), rotary clamps (labeled R), and a temperature controlled oil bath shown in Figure 2.26b. The sample was held in aluminum rotary clamps as shown in Figure 2.26a. The rotary lamps were attached to the lower ends of the four stainless steel shafts, and the pulleys and the sprockets were attached to the upper ends. The rollers were driven by the stepper motor through the system of pulleys and a belt. The system was designed such that the adjacent rollers would rotate in the opposite direction, but at the same speed. The effect of the mechanical system was to clasp and stretch the sample.

The clamps, with the sample in place, were lowered into the oil bath. The oil in the tank was a Silicone oil obtained from Dow Corning, and was used as a heat transfer medium and to support the molten polymer. Silicone oil, being transparent and of high boiling point (232 °C), was suitable for the experiment, since the maximum temperature required to conduct an experiment was 180 °C. The bath temperature was maintained by a temperature controller, which consisted of a temperature sensor, a heating element and a circulating pump. The tank containing the Silicone oil was 72 x 35 x 16 cm^3, and made of stainless steel. The tank was encased in a wooden housing with a 1.3 cm thick lining of glass wool between the wall of the tank and the wooden housing, which served as thermal insulation. The oil tank was placed in the optical path as indicated in Figure 2.25b. The transmission of light through the tank was facilitated by circular observation

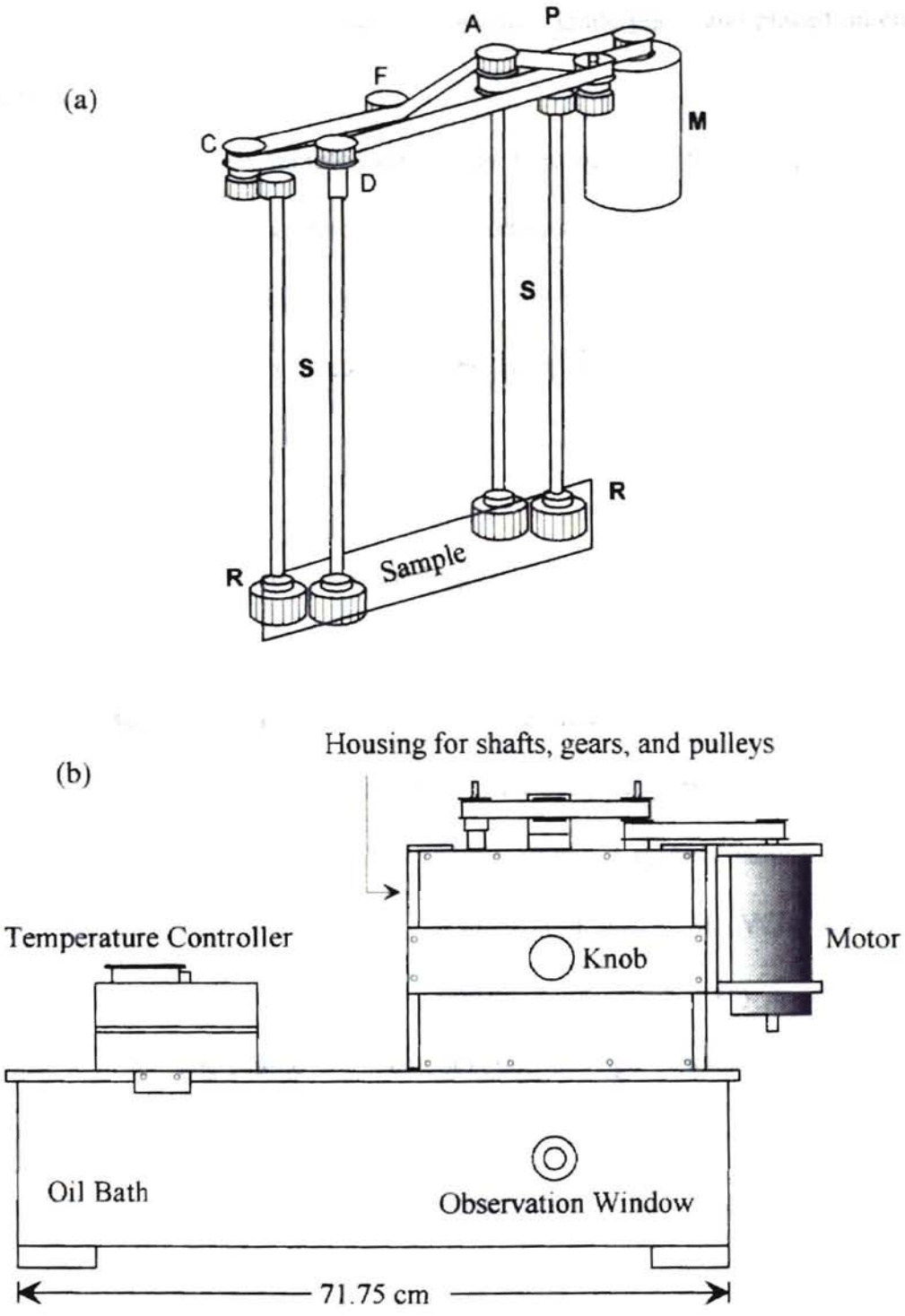

Figure 2.26 Extensional Rheometer (a) Strain Inducing Mechanism
(b) External View[7]

windows (2.5 cm in diameter), made of laboratory grade glass, and placed on either side of the tank.

The polymer melt sample, which was held between the clamps (schematically shown in Figure 2.26c), was stretched by the action of the motor. The stepper motor was controlled by a computer and could be programmed to give a desired velocity profile with respect to time. The details of the programming code have been given by Siddiquee[44] and Kakani[7].

§ 2.3(d) *iii* Data Acquisition and Digitization

The intensity of the emerging beam was detected by a black and white video camera at the rate of 30 frames/sec and stored on video tape. The video tapes were analyzed by replaying each tape. DT2853 Frame Grabber manufactured by Data Translations, Inc., was installed in a personal computer. The VCR signal sent to a program, created by Kakani[7], allowed a cursor to be placed at any desired point on the computer screen. The Frame Grabber converted the light intensity into pixel values at the position of the cursor. The pixel data were stored in a computer file for later analysis. Each sample was analyzed at four different points.

§ 2.3(d) *iv* Sample Preparation

Approximately 12 g of resin was compression molded to make a sample of dimensions 19.5 x 2.5 x 0.3 cm^3. During the course of his work, Kakani observed that

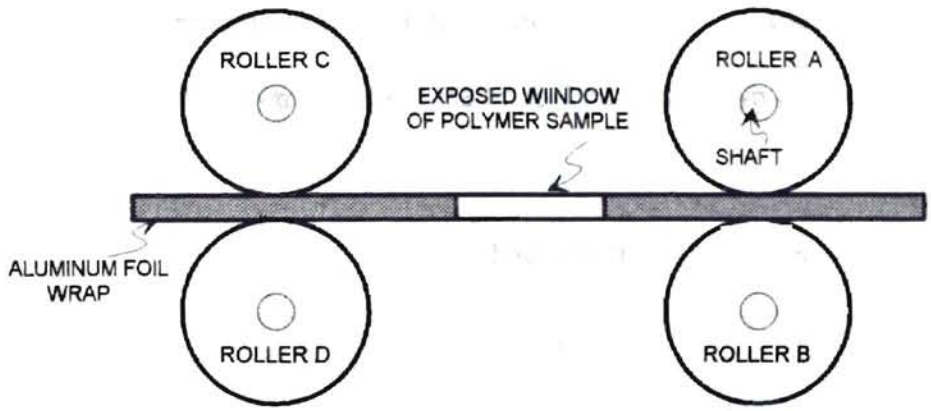

Figure 2.26 (c) The Sample Clamped by the Rollers

the sample in its melt state, tended to rise upward towards the surface of the oil, due to buoyancy of the polymer while in the oil. This destroyed the original dimensions of the sample. In order to solve the floatation problem, the sample was wrapped in aluminum foil. A window of dimensions 1 x 2 cm^2 was cut out from the aluminum foil wrap. Figure 2.27 shows the dimensions of the sample and the exposed window along with the vertical and the horizontal axes. To facilitate splitting of the foil upon application of the extensional flow-field, scalpel marks were made from the corners of the window extending to the upper and lower edges of the sample. The exposed area of the sample was now positioned so as to intercept the optical path as shown in Figure 2.25.

§ 2.3(d) *v* Experimental Procedure

In the experimental procedure followed by Kakani[7], the polarizer and the analyzer were set parallel to each other. The sample was heated to a 2-5 °C above the melting point temperature, T_m. The sample became transparent above T_m. The polarizer and the analyzer were then set perpendicular to each other and the sample was allowed to cool to the crystallization temperature, T_c. For the HDPE sample (crystallization in HDPE is the subject of discussion in this work), T_c was set at 124.6 °C. The elongational flow field was applied 20 minutes after the commencement of the cooling process.

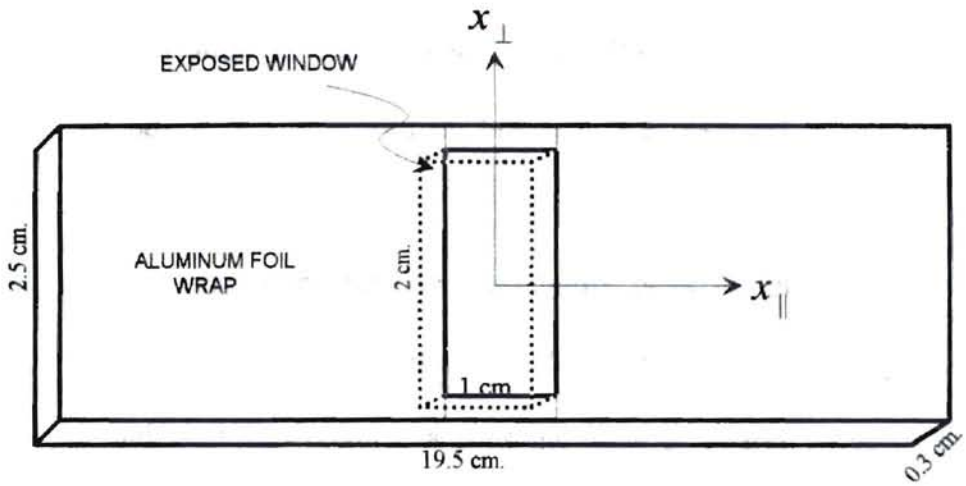

Figure 2.27 Sample Dimensions and Axes

§ 2.3(d) *vi* Observations and Results

Figure 2.28a shows a typical intensity profile observed by Kakani[7]. The four plots are the intensity curves for four locations on the sample chosen at random. The initial constant low intensity drops further, indicating the onset of quiescent crystallization. When the flow is applied, forced alignment of the molecules in the flow direction, and the subsequent relaxation at the cessation of the flow results in the sharp spike in intensity. This behavior is followed by birefringence observed due to flow-induced crystallization.

Figure 2.28b shows the relative crystallinity plots for the locations in Figure 2.28a. The relative crystallinity increased rapidly with time during the initial stage of crystallization, and gradually attained a constant value at a large value of time. The corresponding Avrami plots are shown in Figure 2.28c. Although the plots $ln\{-ln(1-\xi)\}$ versus $ln(t)$ should yield a straight line, the plots demonstrated a non-linear trend as was observed by other research groups.[17,18,26,38] The values of n and k were estimated using the best fit for the Avrami plots. The n were found to be non-integral ($\sim 0.5 \pm 0.2$) and less than 1, and the k values were between 0.006 and 0.95. The results obtained, however could not be reproduced. Therefore, in this investigation, the question of reproducibility has been addressed.

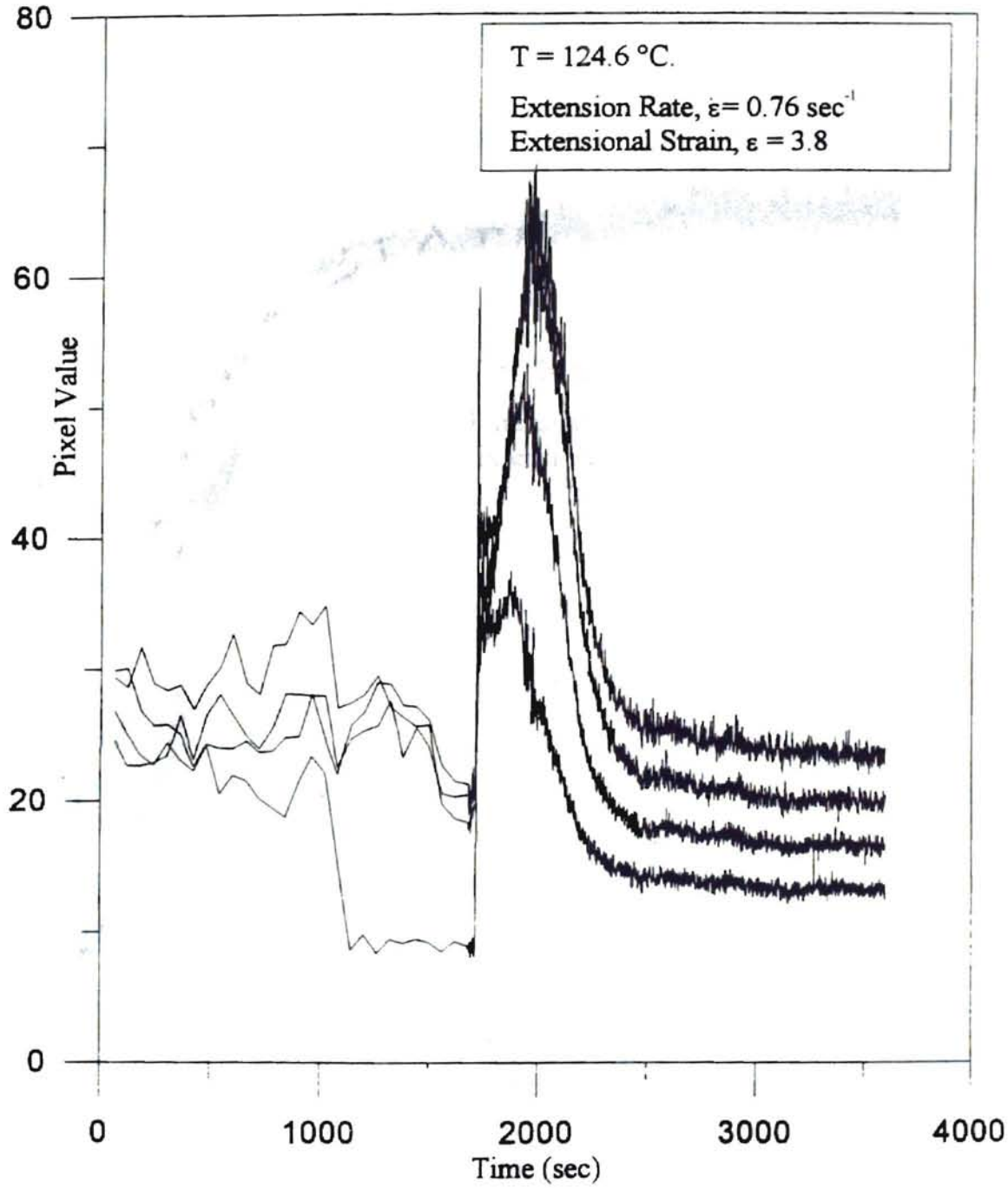

Figure 2.28 (a) Pixel Value Versus Time for HDPE[7] at $\dot{\varepsilon} = 0.76$ /s, $\varepsilon = 3.8$

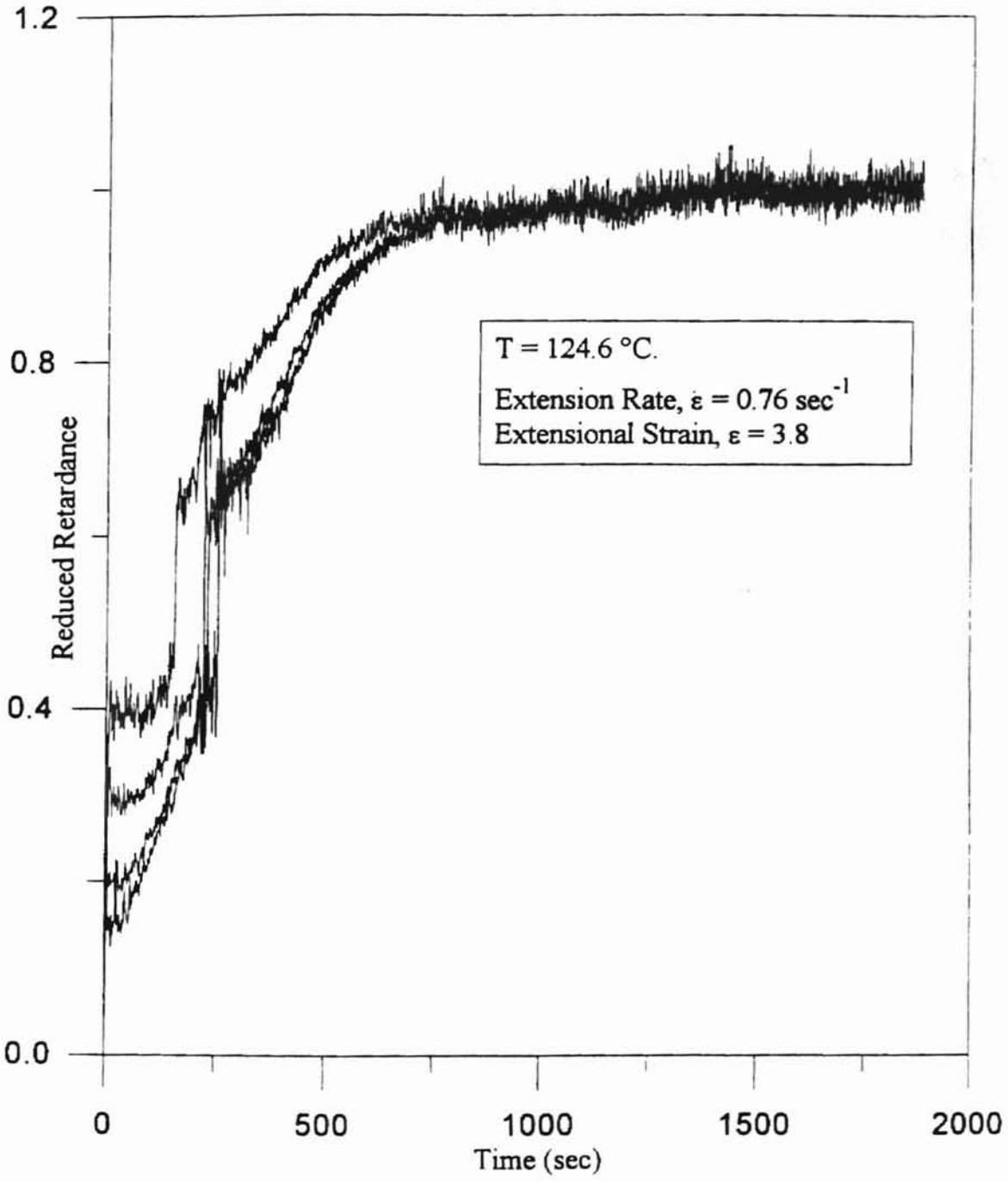

Figure 2.28 (b) Reduced Retardance Versus Time for HDPE[7] at $\dot{\varepsilon} = 0.76$ /s, $\varepsilon = 3.8$

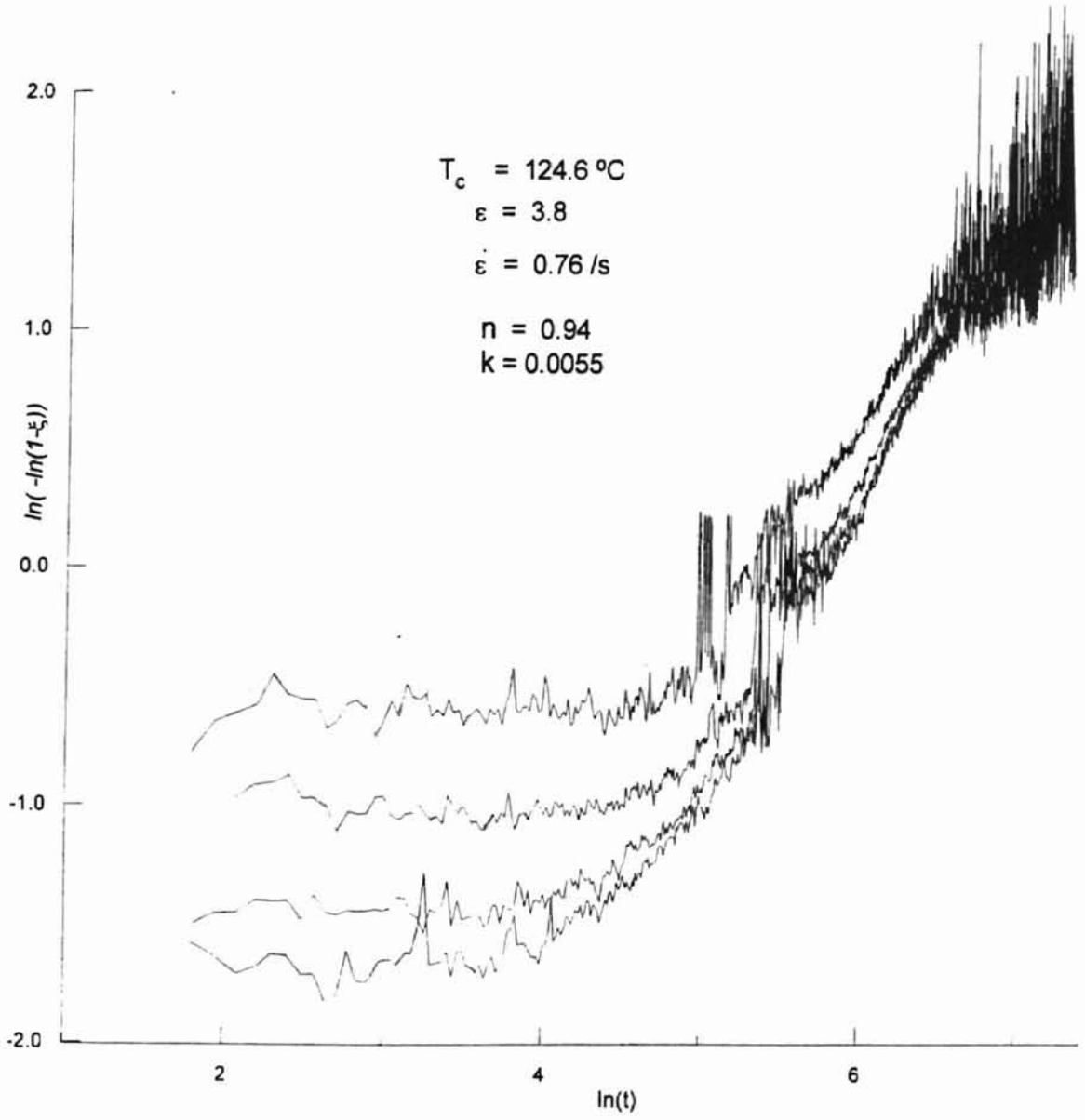

Figure 2.28 (c) Avrami Plot for HDPE[7] at $\dot{\varepsilon} = 0.76$ /s, $\varepsilon = 3.8$

§ 2.3(e) Predictive Model of FIC by Mendes[6]

The most relevant model of FIC pertaining to this investigation is the model developed by Mendes[6] for uniaxial extensional flow-induced crystallization. The simulations developed closely represented the experiments performed in this work. Figure 2.29a shows a schematic of the model for a crystallizing extended chain. The mass of each polymer chain is represented as beads connected with massless rigid rods. The so called 'bead-rod' model is extensively discussed by Bird *et al.*[45]. The schematic shows a partially crystallized molecule, with a fraction, represented by the bead A, in the amorphous state. The motion of the bead in the amorphous phase is influenced by Brownian, and interactive molecular forces. An additional force, the hydrodynamic drag force is introduced by an externally generated flow, and acts upon the bead in the amorphous phase. A detailed description of the forces and constraints on the molecule has been given by Tsai[46]. A space-time dependent probability distribution function (pdf), determines the probability of the bead occupying the nearest available lattice site shown in Figure 2.29a as an open circle.

Determining the value of ψ, the pdf, requires the development of a diffusion equation. The diffusion equation for the configurational probability distribution for the system in Figure 2.29a is given by

$$\frac{\partial}{\partial t}\left(\frac{\psi}{\sin\theta}\right) = \frac{\partial}{\partial \underline{u}} \cdot \left[\underline{\underline{\kappa}} : \underline{u}\underline{u}\underline{u} - \underline{\underline{\kappa}} \cdot \underline{u} + \frac{1}{12\lambda kT}\frac{\partial \Gamma}{\partial \underline{u}} + \frac{1}{12\lambda}\frac{\partial}{\partial \underline{u}} \right]\left(\frac{\psi}{\sin\theta}\right) \quad , \quad (2.9)$$

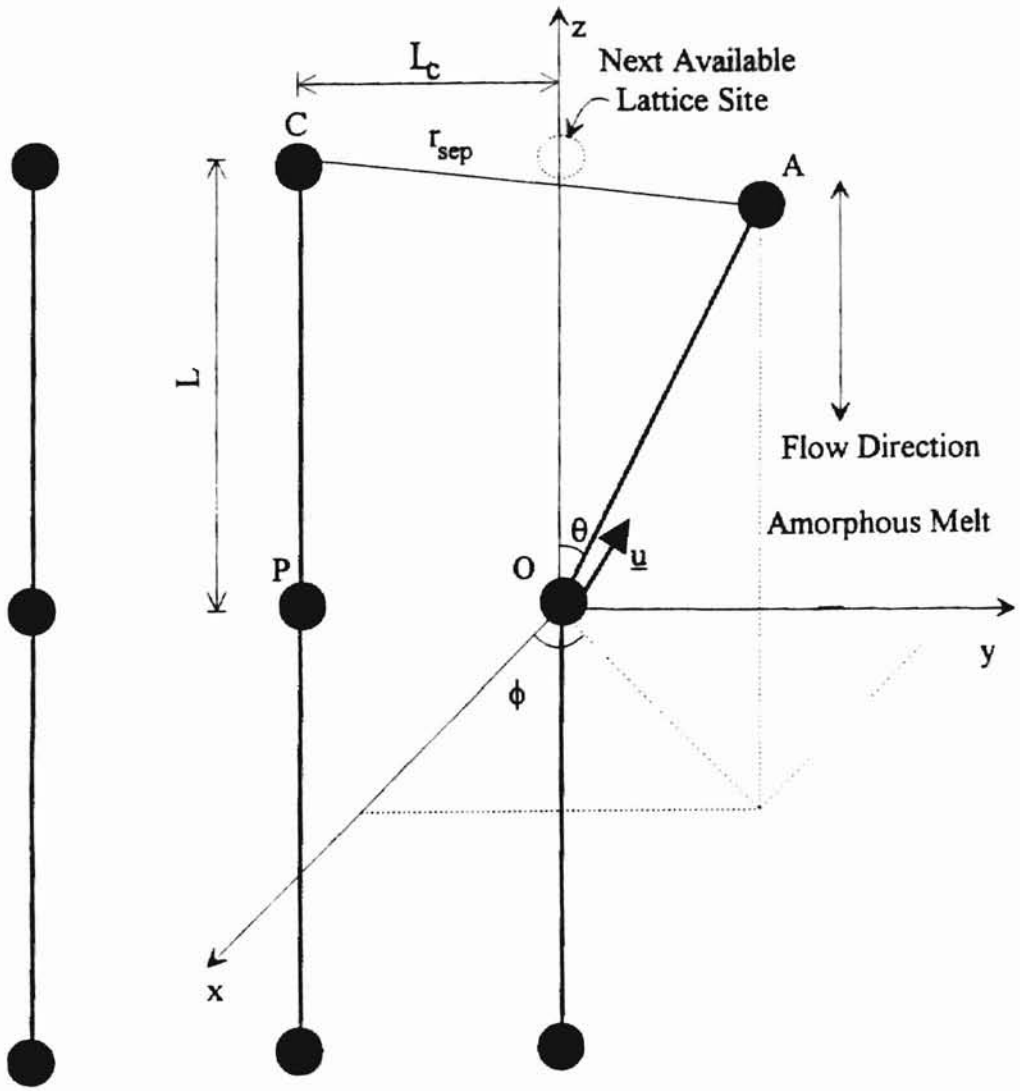

Figure 2.29 (a) Dumbbell Model for a Growing Extended Chain Crystal[6]

where, λ is the relaxation time constant, k is the Boltzman constant (not to be confused with the Avrami coefficient), $\underline{\underline{\kappa}}$ is the transpose of the velocity gradient tensor, and Γ is the potential due to the attractive force between the beads. The simulation of FIC generated a set of values of ψ at various instants of time. For crystal growth to take place, the polar angle, θ, was required to be small enough for bead A to occupy the empty lattice site. This condition corresponds to large values of the pdf at θ approaching 0°.

The integral of ψ at small values of θ represents the volume fraction of crystal. Figure 2.29b shows the result of a simulation run at 124.6 °C. The material was deformed at 0.2 sec^{-1} for 3 sec and then held without further deformation. Time $t = 0$ corresponds to the end of the deformation. The ordinate is the normalized crystallized volume fraction. The initial value of the crystalline volume fraction is non-zero, indicating that some crystallinity developed during the deformation. The following rapid increase is due to the flow-induced orientation and the intermolecular force of attraction which influences bead A such that the probability of the bead occupying the vacant lattice space increases. A comparison between the retardance curves obtained experimentally by Kakani in Figure 2.28b, and Figure 2.29b show a striking qualitative match.

§ 2.3(f) Dichroism and Flow-Induced Crystallization

Bushman and McHugh[47] studied the anisotropy in crystallized HDPE using dichroism. A cylindrical droplet was stretched along the direction of the flow in a four-

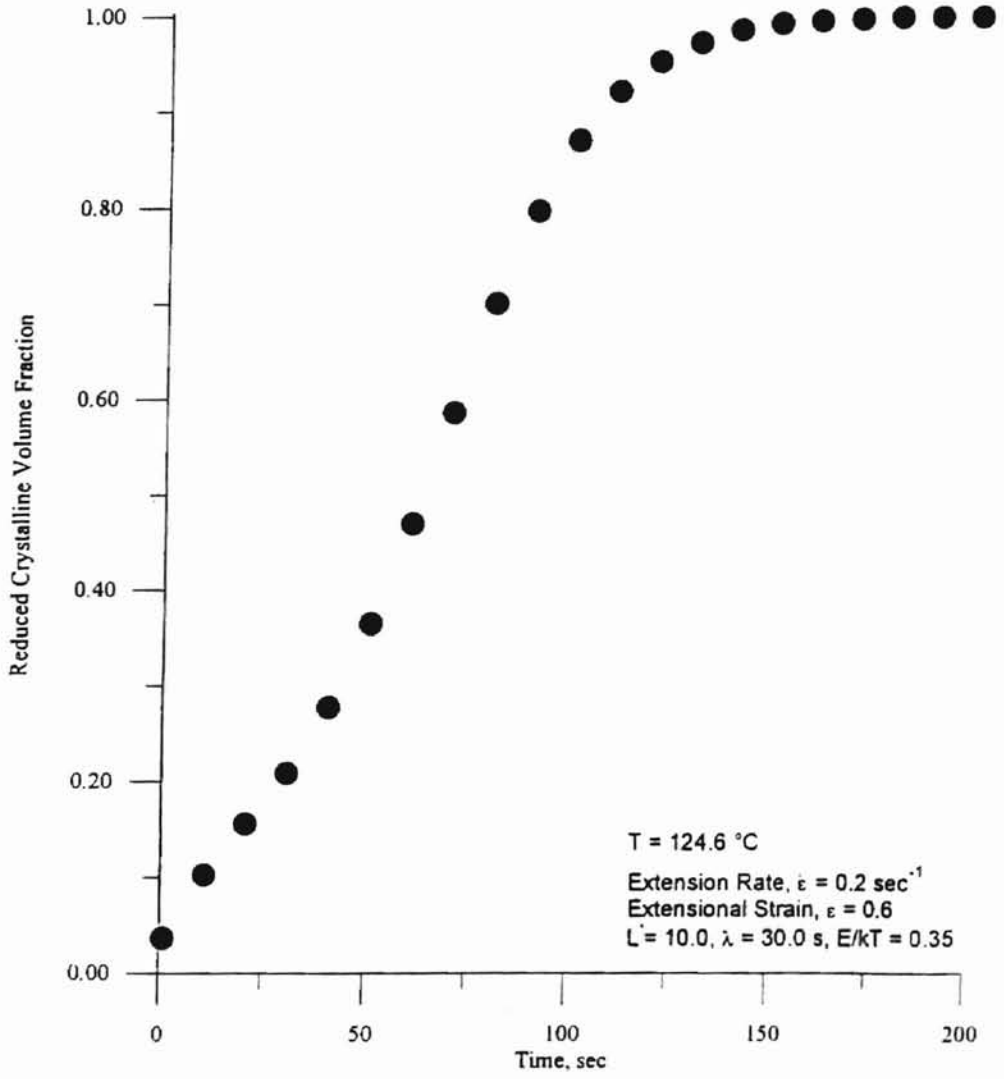

Figure 2.29 (b) Normalized Crystalline Volume Fraction Versus Time[6]

roll mill. The optical train for the experiment is shown in Figure 2.30a. The polarizer P_1 is removed when exclusive dichroism measurements are required. The Cartesian coordinates, in the laboratory frame of reference are represented by x_1, x_2, and x_3, respectively. P_2 was oriented at 90°, and P_3 at 0° with respect to x_1.

The droplet was deformed in the x_1 direction. As a result of the deformation, the molecules aligned along x_1, allowing the transmission the electric field vibrations in the x_2 direction. Since x_2 and the polarization axis of P_2 are parallel, the intensity of the transmitted light along path B would become $I_o/2$, in the limit of perfect alignment of all the molecules in the x_1 direction. Figure 2.30b shows pixel values as a function of time, for path A, at various points along the deforming droplet. Initially, there is no orientation and the transmitted intensity along path A would be $I_o/2$. With the deformation of the sample in the x_1 direction, the sample would act as polarizer. The orientation of the changing polarization axis of the sample with respect to P_3 would cause the polarization angle to increase from 0°, which would explain the slight but noticeable decline of the transmitted intensity during the deformation. As the molecules relax after the cessation of the deformation, the intensity shows a small increase followed by a drastic decline due to dichroic action of the molecules that would now attempt to align themselves along x_1.

The expression for transmission according to Bushman and McHugh[47] is

$$T = \frac{I}{I_o} = \frac{exp(-A_e)}{2}(\cosh\kappa - \sinh\kappa\cos 2\alpha) \quad , \qquad (2.10)$$

where I is the instantaneous light intensity, κ is the extinction measure of the light intensity as the light passes through the material, A_e is the absorbance, and α is the angle

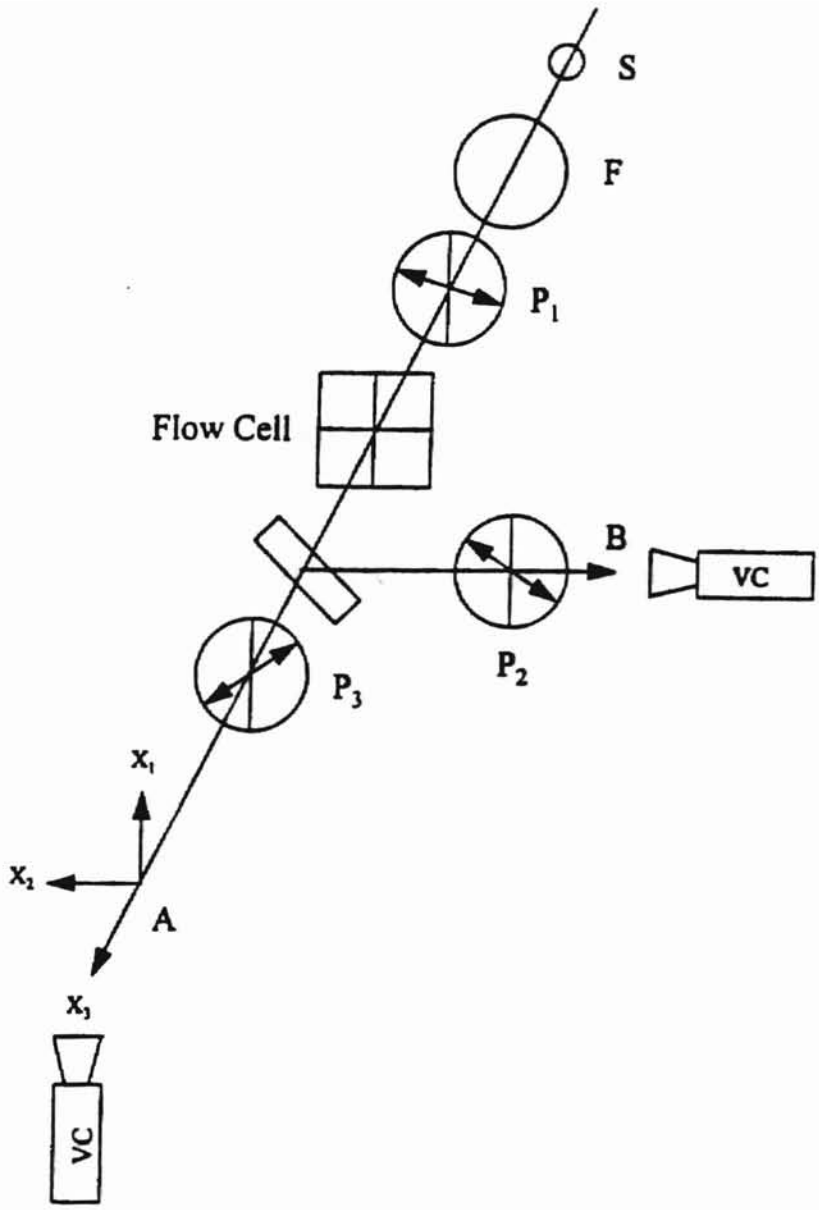

Figure 2.30 (a) Optical Train to Observe Dichroism[47]; S (Light Source), P_i (Polarizers), F (Filter), VC (Video Camera), x_1 (Reference Axis)

between x_1 and P_i (i = 2, 3). From Equation (2.10), the values of κ, and A_e were evaluated for $\alpha = 0°$ or 90° as:

$$\kappa = \frac{1}{2}\ln\left(\frac{I_B}{I_A}\right) \tag{2.11a}$$

$$A_e = \frac{1}{2}\ln\left(\frac{4I_B I_A}{I_o I_o}\right) \tag{2.11b}$$

where I_o is the unpolarized incident light on the sample. κ is defined as:

$$\kappa = \frac{2\pi L(n_2' - n_1')}{\lambda_o} \quad , \tag{2.12}$$

where n'_1 and n'_2 are the imaginary part of refractive indices in the x_1 and x_2 directions, respectively, and L is the thickness of the sample at the cessation of flow. Figure 2.30c shows the difference between n'_1 and n'_2 with time[11] at three locations from the stagnation point of the sample. The location farthest away from the sample shows the greatest values of (n'_1-n'_2). Correspondingly, the transmittance, T, decreases as shown in Figure 2.30b.

Friedenberg *et al.*[34] also studied flow-induced anisotropy using dichroism. The samples under study were polymers at the interface of air and water, namely phthalocyaninatopolysiloxane (PcPS). A schematic of PcPS is shown in Figure 2.31a. PcPS is a rigid hairy-rod polymer of cofacially stacked phthalocyanine rings joined by a polysiloxane backbone and grafted at the periphery with C_8 alkyl chains. A monolayer of PcPS has the property of strong polarized absorption, especially when the **E**-vector of the incident light is in the plane of the phthalocyanine ring. A four-roll mill was used to create the flow which oriented the rod-like molecules of the monolayer at a uniform

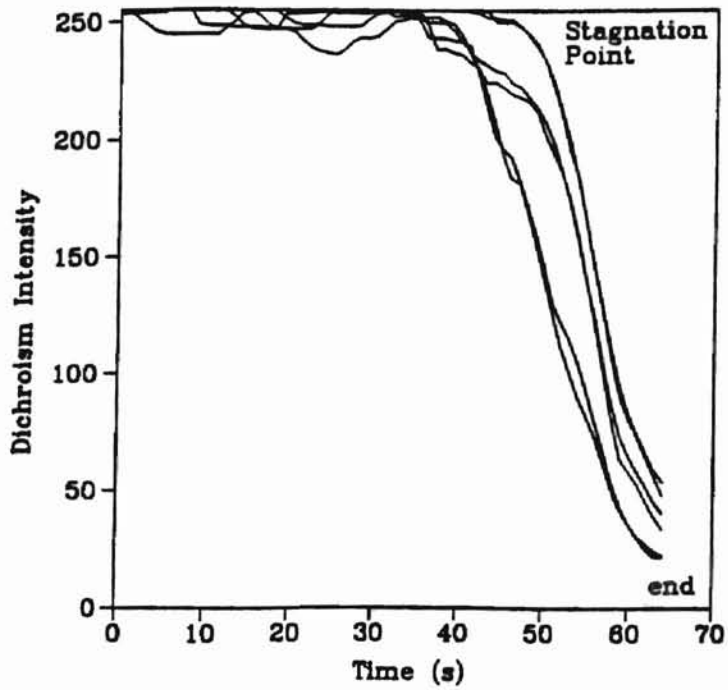

(b)

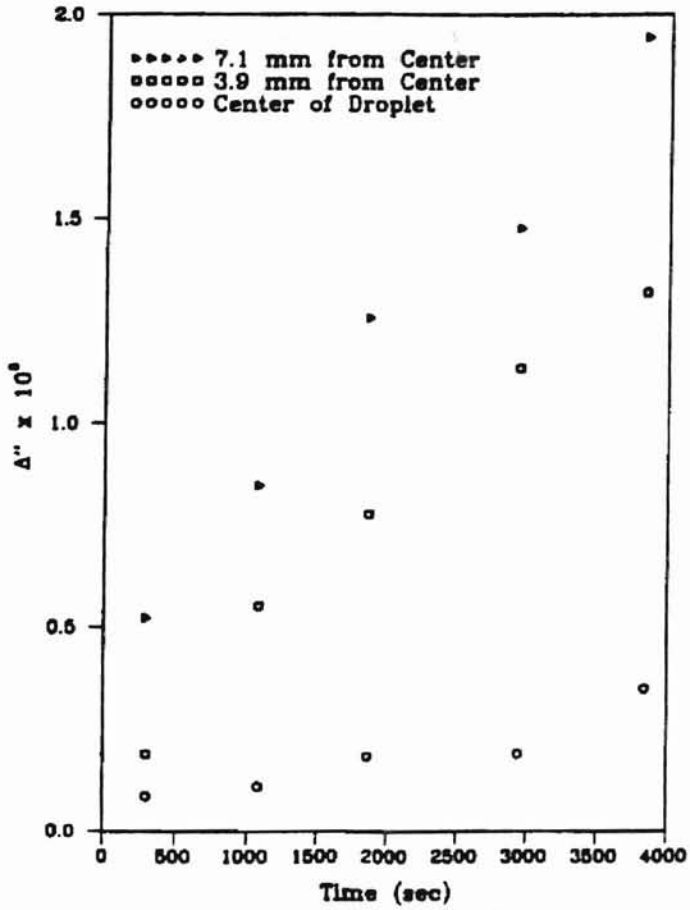

(c)

Figure 2.30 (b) HDPE Droplet Phase Intensity[47] at 129.2 °C; $\dot{\varepsilon} = 0.034/s$
(c) Extinction Versus Time of HDPE at 133.2 °C, $\dot{\varepsilon} = 0.032/s$

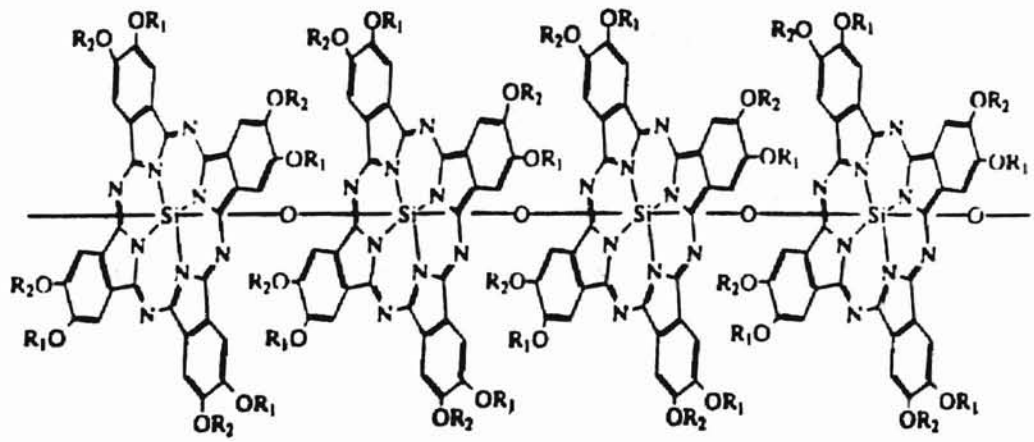

Figure 2.31 (a) Chemical Structure of Phthalocyaninatopolysiloxane[34] (PcPS); $R_1 = CH_3$; $R_2 = C_8H_{17}$

flow-rate, $\dot{\epsilon}$. The source of light was a 543nm He-Ne laser. The intensity of the light transmitted through the monolayer was monitored with a photodiode submerged in the water trough.

Figure 2.31b shows the relationship between the extinction and strain rate. Friedenberg *et al.*[34] observed that when the strain rate was greater than 0.02/sec, the rod-like PcPS molecules were completely aligned in the flow field, which led to the conclusion that high a rate of strain results in large a relaxation time that is greater than the characteristic time (reciprocal of the strain rate) of the flow. Below 0.02/sec, the anisotropy decreased as the flow weakened. The flow was observed to compete with the relaxation process over this time scale. From this experiment, an approximate value of the relaxation time could be deduced.

Figure 2.31c shows the variation of extinction with time. This experiment was performed for a periodic flow reversal with the four-roll mill. A strain rate of 0.05/sec was applied and the rods were allowed to reach a steady state of alignment before the flow was reversed. With the reversal of flow, the average orientation angle of the PcPS rods were switched by 90°, causing the optical anisotropy to pass through a minimum. Following the minimum, the dichroism increased strongly indicating an alignment along the flow and reached steady-state value. This experiment shows that the PcPS molecules can be completely aligned along the direction of the flow at large values of rate of strain (>0.02/sec).

The topics that have been discussed thus far, form the basis of the present investigation. From the information in the literature regarding polymer crystallization, it is evident that a standard formulation of the crystallization kinetics has yet to materialize.

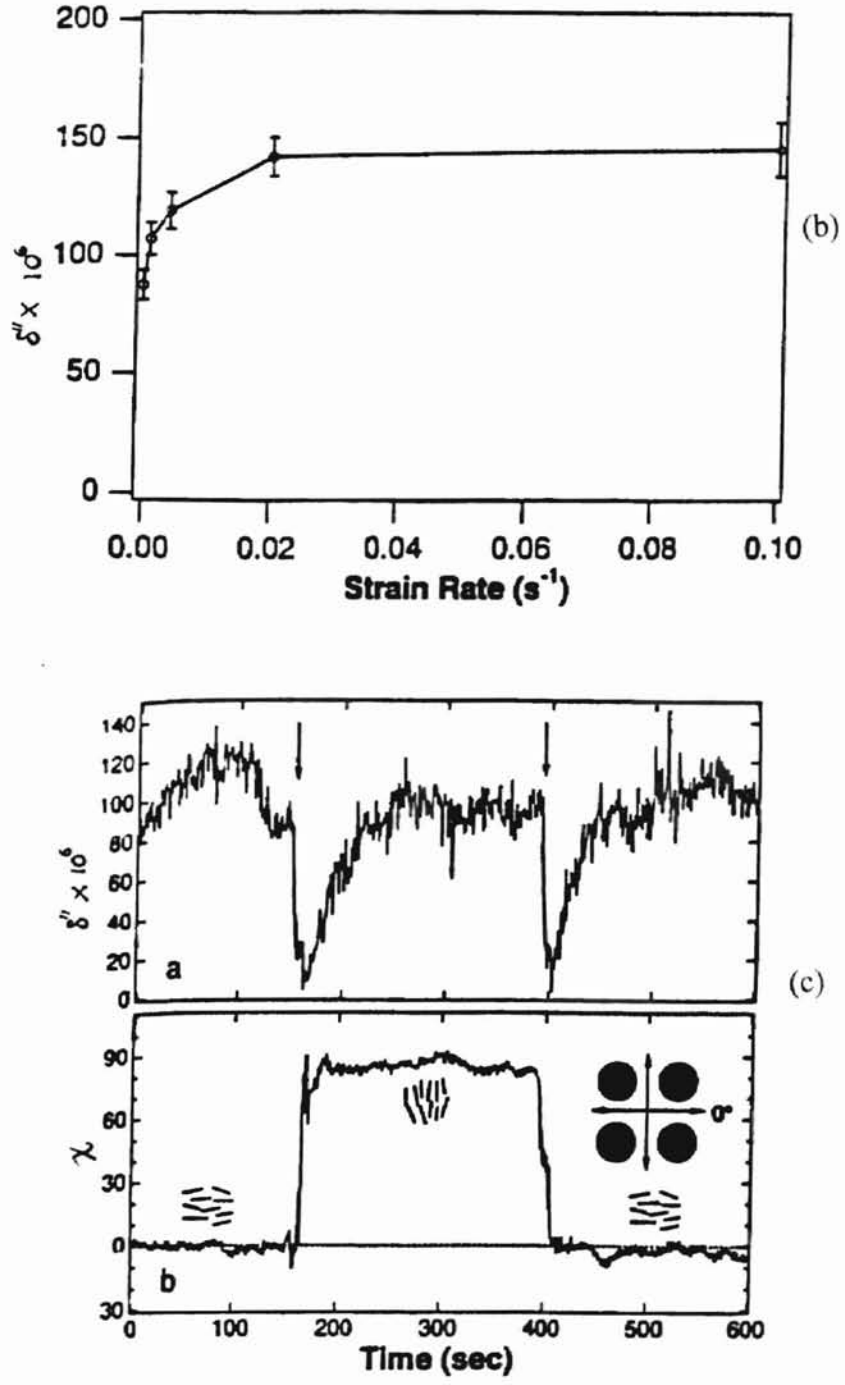

Figure 2.31 (b) Dependence of Extinction on Strain Rate for PcPS Monolayer[34]
(c) Orientational Response to Flow Reversal ; χ (Orientational Angle)

However, the experimental work over three decades, has produced a collection of valuable theories and results regarding the crystallization process and the kinetics involved.

CHAPTER III

EXPERIMENTAL PROCEDURES AND METHODS OF ANALYSIS

This chapter contains a discussion of the experimental setup and the techniques used to investigate extensional, flow-induced crystallization. The data analysis techniques to determine the crystallization kinetics are also described. Experiments were conducted to observe the birefringence in HDPE melts undergoing well characterized uniaxial deformations. The assumptions used in Kakani's method[7] of data analysis were examined, and an improved technique was developed. A new setup and procedure to observe the dichroism, and a method of analysis for the dichroism data were also developed.

§ 3.1 Experimental Setup

The experimental apparatus used to observe the birefringence pattern during flow-induced crystallization in polymers has been described in § 2.3(c.1)(*i*). The apparatus could be configured to observe either birefringence or dichroism. The extensional rheometer described in § 2.3(c.1).(*ii*) was used to generate the flow for the FIC study. A brief description of the materials used in this study is also given in this section.

§ 3.1(a) Optical Train to Observe Dichroism

The optical train to observe dichroism is shown in Figure 3.1. The optical train, from the light source to the sample, was identical for the observation of both dichroism and birefringence. However, in the dichroism configuration the light emerging from the sample was split into two beams of equal intensity. The beam labeled A, passed through the analyzer, as in the birefringence measurements, and through a system of prisms before reaching the camera. Beam B was diverted by a system of prisms around the analyzer and then into the camera. Therefore, on the video monitor, two images were formed of the same area of the sample. Beam A in Figure 3.1 typically displayed a low intensity (pixel values ranging between ~10 and 20). The intensity of beam B was not attenuated by the analyzer, and normally exceeded the detection range of the camera (pixel values greater than 255) before the onset of crystallization. Birefringence data was obtained from beam A and dichroism data was obtained from beam B.

§ 3.1(b) Materials

The material which was primarily used in this study was a HDPE resin from Quantum Chemical Corporation (LS 6601-00). Two other resins used were polystyrene (STYRON 687) from Dow Plastics, and a high density polyethylene from BASF, Ludwishafen, Germany. All of the resins were originally in the form of pellets The manufacturer-supplied physical properties of the Quantum HDPE are listed in Table 3.A.

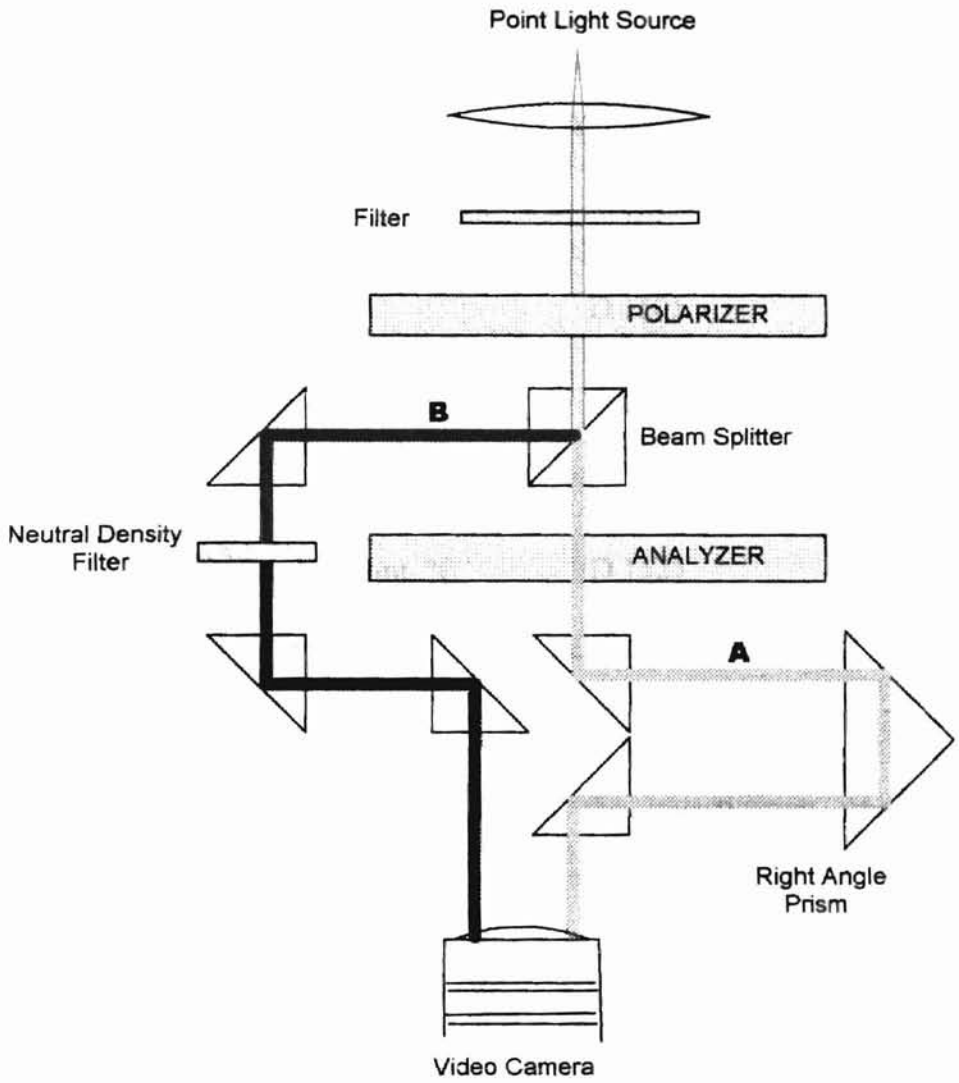

Figure 3.1 Optical Train to Observe Dichroism

TABLE 3.A

Physical Properties[48] of Quantum HDPE Resin LS 6601-00

	ASTM Test	
ASTM Type, Class, Category	D 1248	III A 3
Melt Index, g/10 min.	D 1238	6.5
Density, g/cm^3	D 1505	0.952
Tensile Strength, @ Break, psi	D 638	4,000
Elongation, @ Break, %	D 638	1,000
Tensile Impact, $ft\text{-}lbs/in.^3$	D 1822	34
Vicat Softening Point, °C	D 1525	126
Hardness, Shore D	D 2240	67

The most widely used material in the investigation was a high density polyethylene resin from Quantum.

§ 3.2 Procedure to Obtain Intensity Data

The sample was prepared and covered with aluminum foil as described in §2.3(c.1)(*iv*). The polarizer and the analyzer were set at 45° in the counterclockwise direction with respect to the horizontal axis. At room temperature, the sample was opaque to the incident light.

By making repeated measurements of the temperature at which the samples became transparent, the effective melting point of the HDPE was determined to be ~132 °C. To ensure the absence of any crystallinity, the sample was raised to 134 °C (~2 °C above melting point of the sample) and held at this temperature for 1.5 min. From the value of the melt index (6.5 g/10 min) of the HDPE sample, it can be deduced that the molecular weight of the sample was less than 10^6 amu. Therefore, raising the temperature of the sample used in this work to 2 °C above the melting point, would have been sufficient to make the sample completely amorphous.

The thermostat was then reset to 124.6 °C. The thermocouple for the temperature controller was placed 0.5 cm away from and level with the lower edge of the sample. A display panel gave the temperature in °C with an accuracy of ± 0.1 °C. A fairly constant cooling rate was observed (cooling rate will be discussed further in § 3.3(a.3)). 14-15 minutes of cooling decreased the temperature in vicinity of the lower edge of the sample to 124.6 ± 0.2 °C. Upon reaching 124.6 °C, the sample was maintained at this temperature.

At the onset of phase change from the amorphous melt state to the crystalline state. the sample began to darken. The sample became completely opaque within approximately 2-3 minutes. Using this indication as the apparent onset of quiescent crystallization, the compumotor was switched on. The PC was set to command-execution mode through the X-language commands. The analyzer was reset to 90° with respect to the polarizer, and the preprogrammed command statements were executed. The sample was stretched under the influence of the elongational flow, provided by the

rotating rollers. The transmitted intensity was observed on the monitor and recorded by the VCR, for three hours.

§ 3.3 Analysis of Intensity Data

Analyzing the intensity variations due to the birefringence in the sample was the key to obtaining results. Depending on the assumptions made during the analysis, different results could be obtained. Kakani's method of analysis yielded markedly different results for identical experiments. The differences were found to be due to certain assumptions made by Kakani, which caused the inconsistency in the results. This section presents a discussion on the assumptions, and a modified method of analysis which was used in this investigation.

Figure 3.2 illustrates the intensity pattern obtained due to the birefringence in a typical experiment. The four intensity plots correspond to four locations selected from the top to the bottom on the exposed region of the sample, respectively. The initial drop in the intensity at $t < t_A$ was due to the cooling process of the melt, which caused the onset of crystallization, manifested by the sample becoming opaque. At the onset of crystallization, indicated by the lowest values of the intensity, the analyzer was set at 90° with respect to the polarizer.

At time t_A the elongational flow field was applied, marked as **A**, for all four intensity curves. A spike in the intensity followed by the subsequent drop was caused by the orientation of molecules due to the flow field and the subsequent relaxation of the molecules after the cessation of the flow. The intensity then rises and falls due to flow-

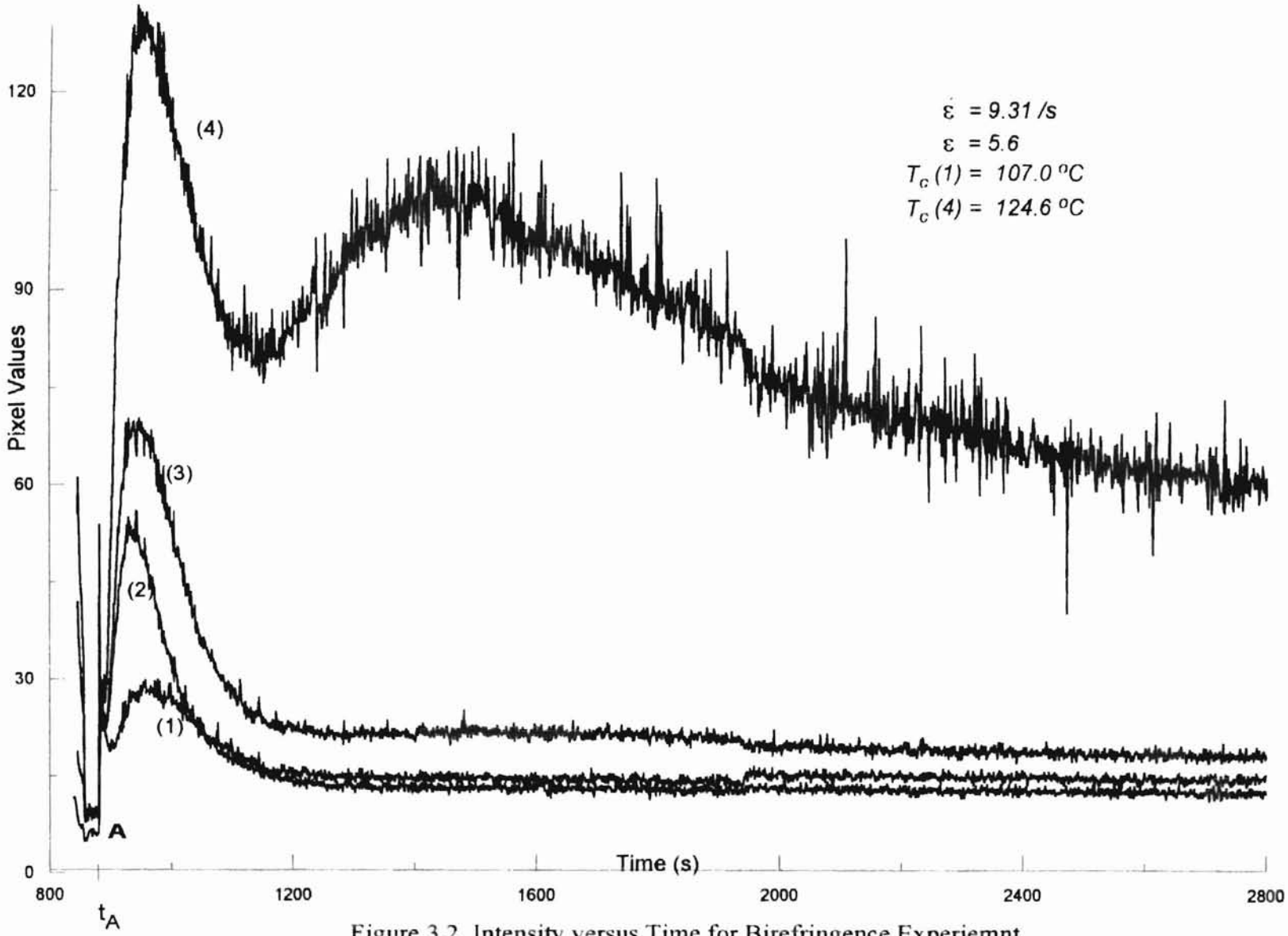

Figure 3.2 Intensity versus Time for Birefringence Experiemnt

induced crystallization causing the sample to be birefringent. This behavior of the intensity pattern is related to the sine functional dependence of the intensity on the retardation. The rise and fall in the intensity pattern continued until no further crystallization took place, beyond which the intensity remained constant. For the curves labeled (1), (2), and (3), the flow-induced crystallization took place for a shorter duration than for the curve labeled (4), where the crystallization process continued for a much longer time and showed more than one maximum in the intensity curve. The reasoning for the difference in the magnitudes of the four intensity plots will be discussed in Chapter IV.

The retardance, δ, for the optical train described in § 2.3(c)1.(*i*) can be expressed in terms of the transmitted intensity as

$$\delta = 2sin^{-1}\sqrt{\frac{I(t)}{(I_o/2)}} \quad , \tag{3.1}$$

$I(t)$ being the instantaneous intensity. $I_o/2$ is the transmitted intensity with the axis of the polarizer and the analyzer parallel to each other when the sample was in the melt state.

Applying Equation (3.1) to the intensity data, the plots in Figure 3.3 were obtained. The figure shows that for each curve, the retardance initially increased and at large times attained a constant value. Although the trend of the retardance was the same at every location on the sample, the values of δ_∞ corresponding to large times t_∞, varied from one location to another on the sample. Therefore, the curves were normalized with respect to δ_∞ to cause them to overlap as shown in Figure 3.4.

From Equation (2.3), the retardance was seen to be proportional to the birefringence caused by crystallization. The retardance is proportional to the volume of

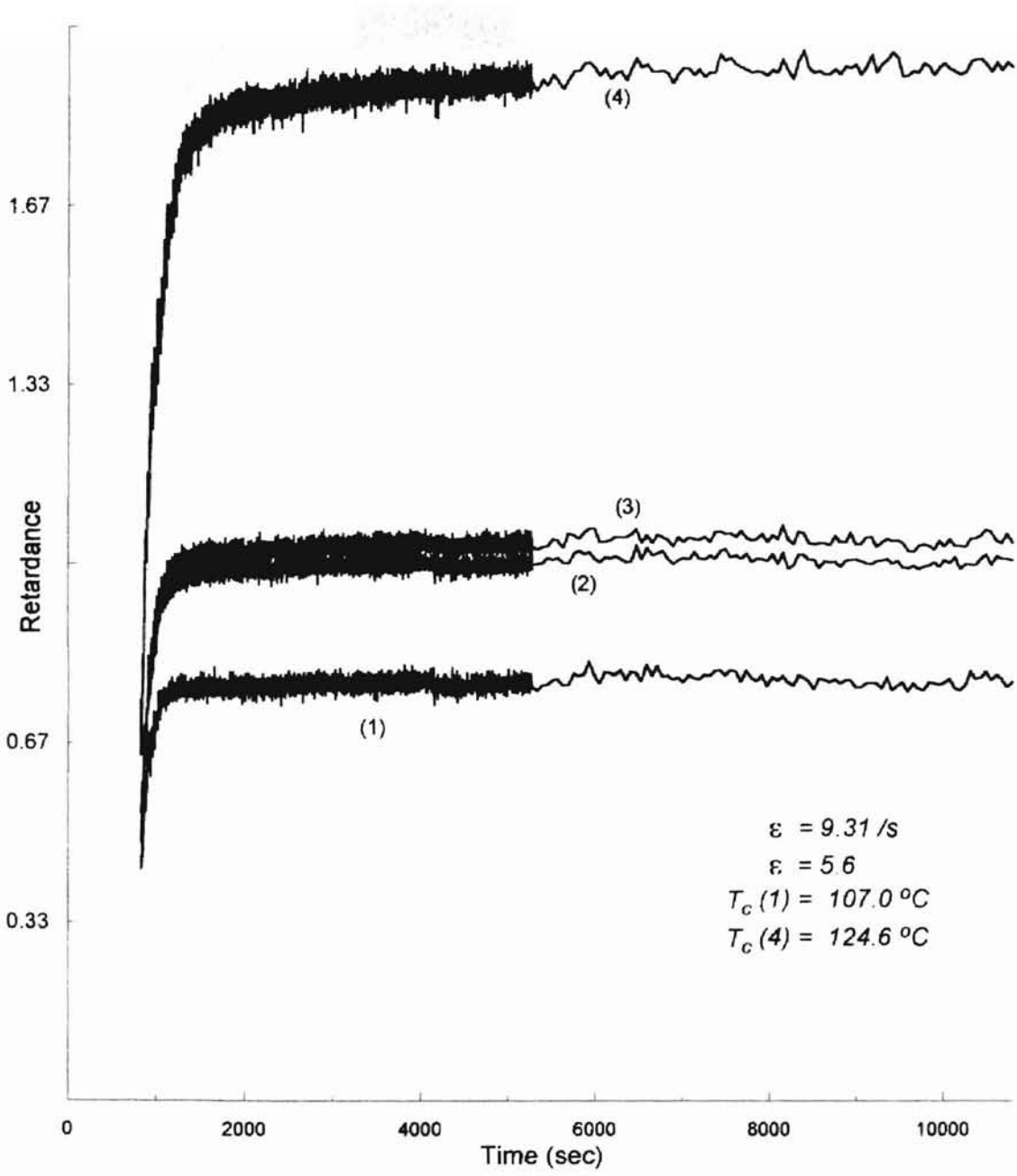

Figure 3.3 Relative Retardance Versus Time

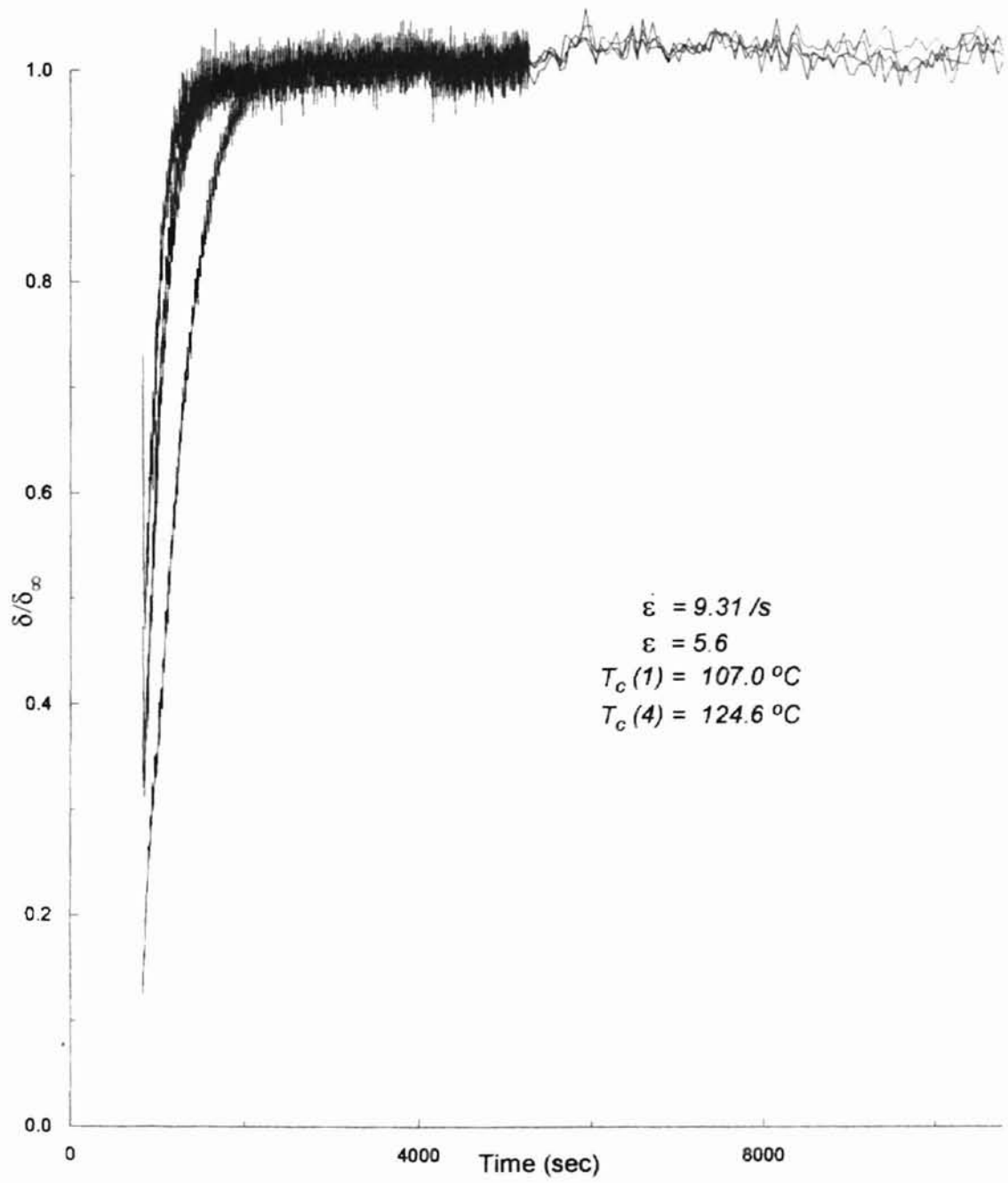

Figure 3.4 Relative Retardance Versus Time for Data in Figure 3.3

the crystallized sample. Therefore, the ratio δ/δ_∞ can be assumed as being equal to relative crystallinity or the crystallized volume fraction of the sample, $X_c(t)/X_\infty$ or $\xi(t)$ in Equation (2.4). The Avrami equation, Equation (2.4), could then be rewritten as

$$\frac{\delta(t)}{\delta_\infty} = 1 - e^{-kt^n} \quad . \tag{3.2}$$

§ 3.3(a) Kakani's[7] Assumptions

Kakani[7] followed the procedure described in § 2.3(c.1)(*v*). The assumptions made by Kakani[7] to simplify the analysis are discussed here.

§ 3.3(a.1) Analyses of the Intensity Profiles

The normalized or relative retardance is given by

$$\frac{\delta}{\delta_\infty} = \frac{\sin^{-1}\left(\sqrt{\frac{I(t)}{(I_o/2)}}\right)}{\sin^{-1}\left(\sqrt{\frac{I(t_\infty)}{(I_o/2)}}\right)} \tag{3.3}$$

In Kakani's method,[7] the ratio of intensities in Equation (3.3) were expressed as the ratio of normalized intensities:

$$\frac{\delta(t)}{\delta_\infty} = \frac{\sin^{-1}\sqrt{\frac{I(t)-I_{min}}{I_{max}-I_{min}}}}{\sin^{-1}\sqrt{\frac{I(t_\infty)-I_{min}}{I_{max}-I_{min}}}} \quad , \tag{3.4}$$

where, I_{max} and I_{min} are the maximum and the minimum pixel values on the intensity curve, respectively. The saturation value δ_∞ at infinite time was determined from the plot of $\delta(t)$ versus time, t. δ/δ_∞ versus time was re-plotted for data from the various locations under simultaneous observation.

Equation (3.1) interpreted as Equation (3.4) was used by Kakani to calculate the time-dependent retardance. The results obtained were affected by the use of Equation (3.4) in the following manner:

(i) The typical intensity data, such as in Figure 3.5, showed that during the undercooling of the sample, the initial intensity was nearly constant for ~ 1000 sec (12-15 minutes). Before the flow field was applied, however, the intensity began to decline. Light scattered by nucleating sites accounted for the fall in intensity and indicated the onset of crystallization. However, according to Equation (3.4), $\delta = 0$ for the minimum intensity, incorrectly suggesting that the sample was amorphous at time t_A as shown in Figure 3.6.

(ii) Figure 3.7 shows a normalized intensity curve calculated using Equation (3.4), and a reduced intensity curve obtained from the data for the curve labeled (4) in Figure 3.2. Reduced intensity in this text refers to Equation (3.3). The reduced intensity curve is thus a scaled-down representation of the original intensity curve. In Kakani's method, however, normalization was performed in parts. Prior to reaching I_{max}, the value of I_{min} in Equation (3.4) was the lowest intensity value, but for the latter part of the curve after I_{max} was reached, I_{min} was the intensity value at t_∞. As a result the intensity values ranged from 0 to 1, and the slopes of the intensity curve differed considerably from the slopes of the curve labeled (4) in Figure 3.2. Since the intensity curve was crucial in determining

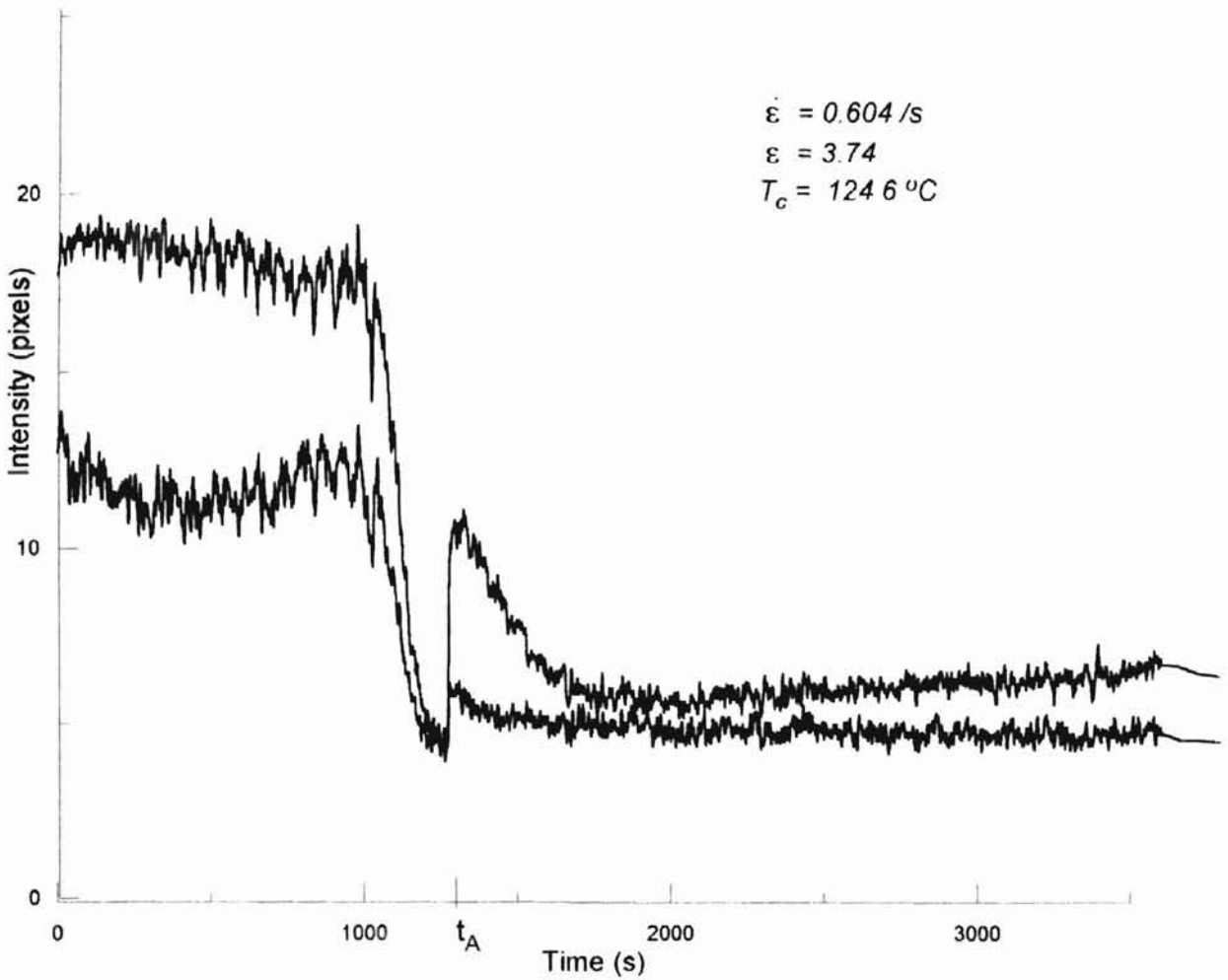

Figure 3.5 Intensity vs. Time Around the Onset of Crystallization

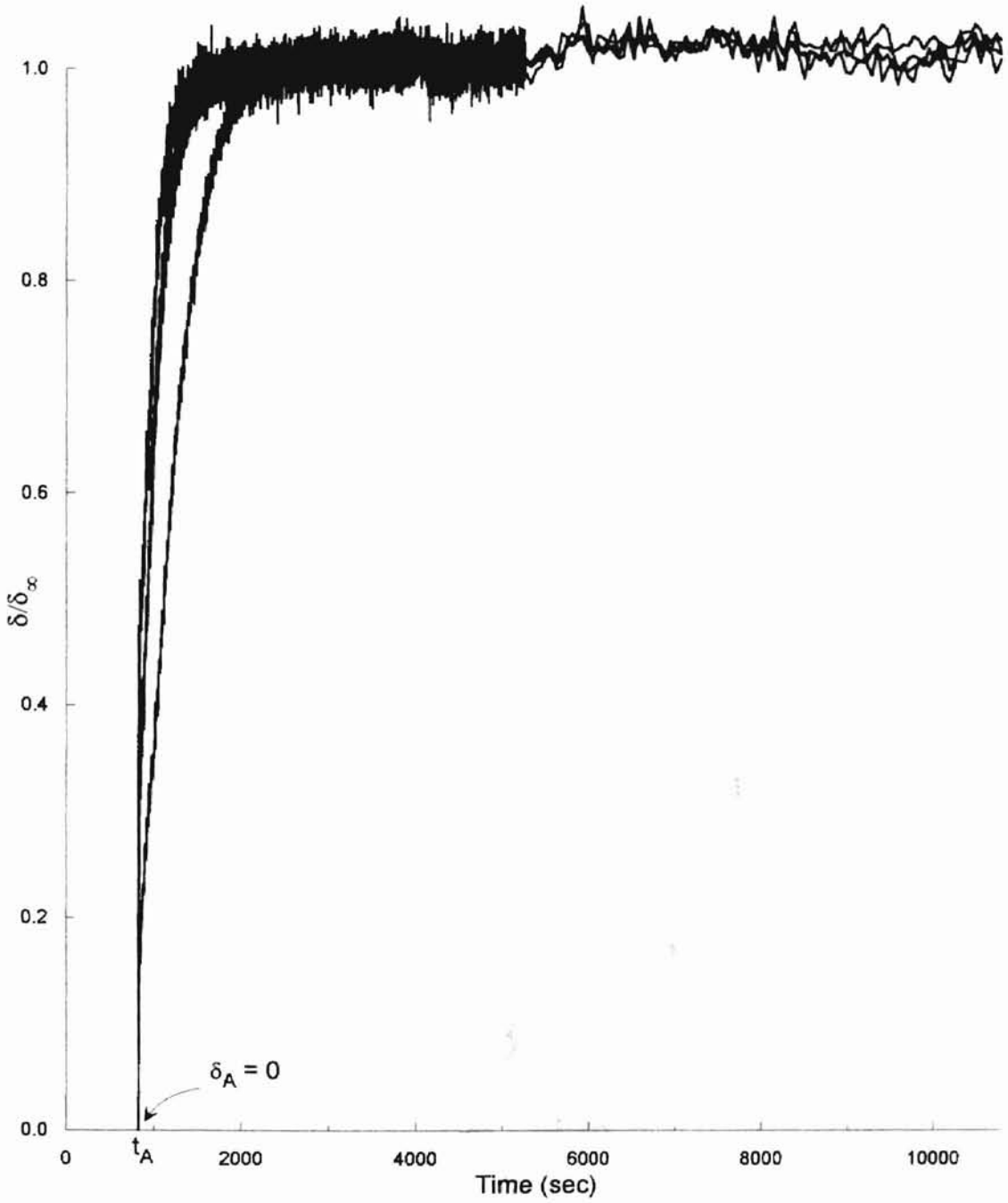

Figure 3.6 Relative Retardance Versus Time Using Kakani's Method[32]

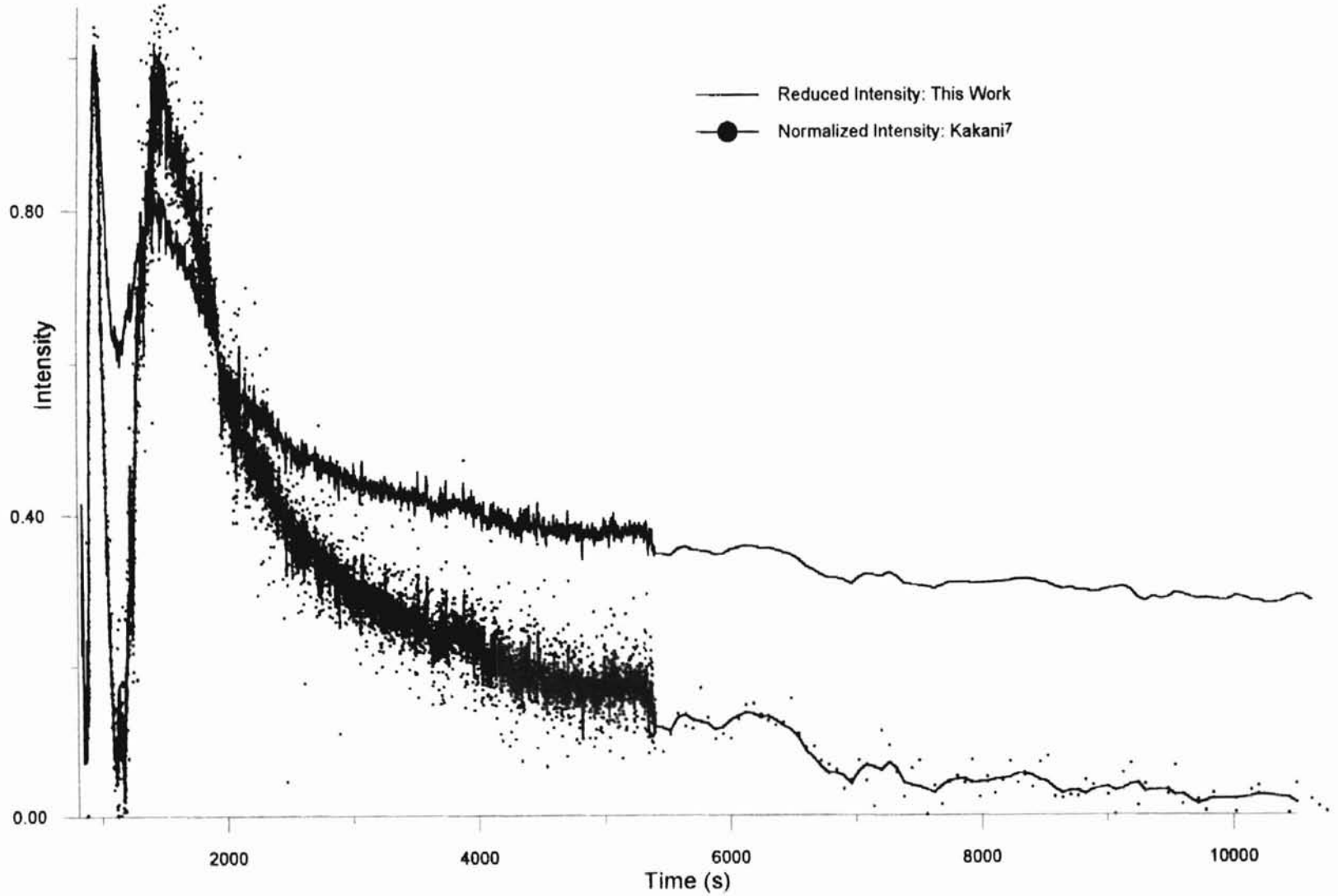

Figure 3.7 Normalized and Reduced Intensity Versus Time

the retardance values, the normalized curve would yield results different from the reduced curves as shown in Figure 3.8.

(iii) Intensity typically ranged between 10 and 100 pixel values (approximately). The maximum possible pixel value was 255. In most cases, a value 255 could be reached for an intensity lower than $I_o/2$. Therefore the pixel value of 255 may represent an intensity lower than $I_o/2$. From Equation (3.4), $I(t) = I_{max}$ would correspond to $\delta = 180° = \pi$ radians. Whereas for $I_{max} = 100$, Equation (3.1) could be interpreted as

$$\delta = 2sin^{-1}\left(\sqrt{\frac{100}{255}}\right) \qquad \text{at} \quad I(t) = I_{max} = 100. \tag{3.5}$$

In Equation (3.5) the pixel value $I_o/2$ is taken to be 255 as a conservative assumption. Thus $\delta = 77.54° \cong (0.43)\pi$ radians. The value of retardance corresponding to I_{max}, in this case, would be ~43% of the δ value obtained using Kakani's method.

For the optical train shown in Figure 2.24, the maximum transmitted intensity that can be attained is:

$$I_{max} = \frac{(I_o/2)}{4}. \tag{3.6}$$

A derivation of Equation (3.6) is given in Appendix A1. Substituting for I_{max} in Equation (3.1), the following result is obtained:

$$\delta = 2sin^{-1}\left(\sqrt{\frac{I_{max}}{I_o/2}}\right) = 2sin^{-1}\left(\sqrt{\frac{1}{4}}\right) = 60° \ . \tag{3.7}$$

From Equation (3.7), the maximum attainable value of δ can be interpreted as a method to calculate the maximum possible value of $I_o/2$. The value of I_{max} from the intensity data can be substituted in Equation (3.7) to obtain the value of $I_o/2$. However,

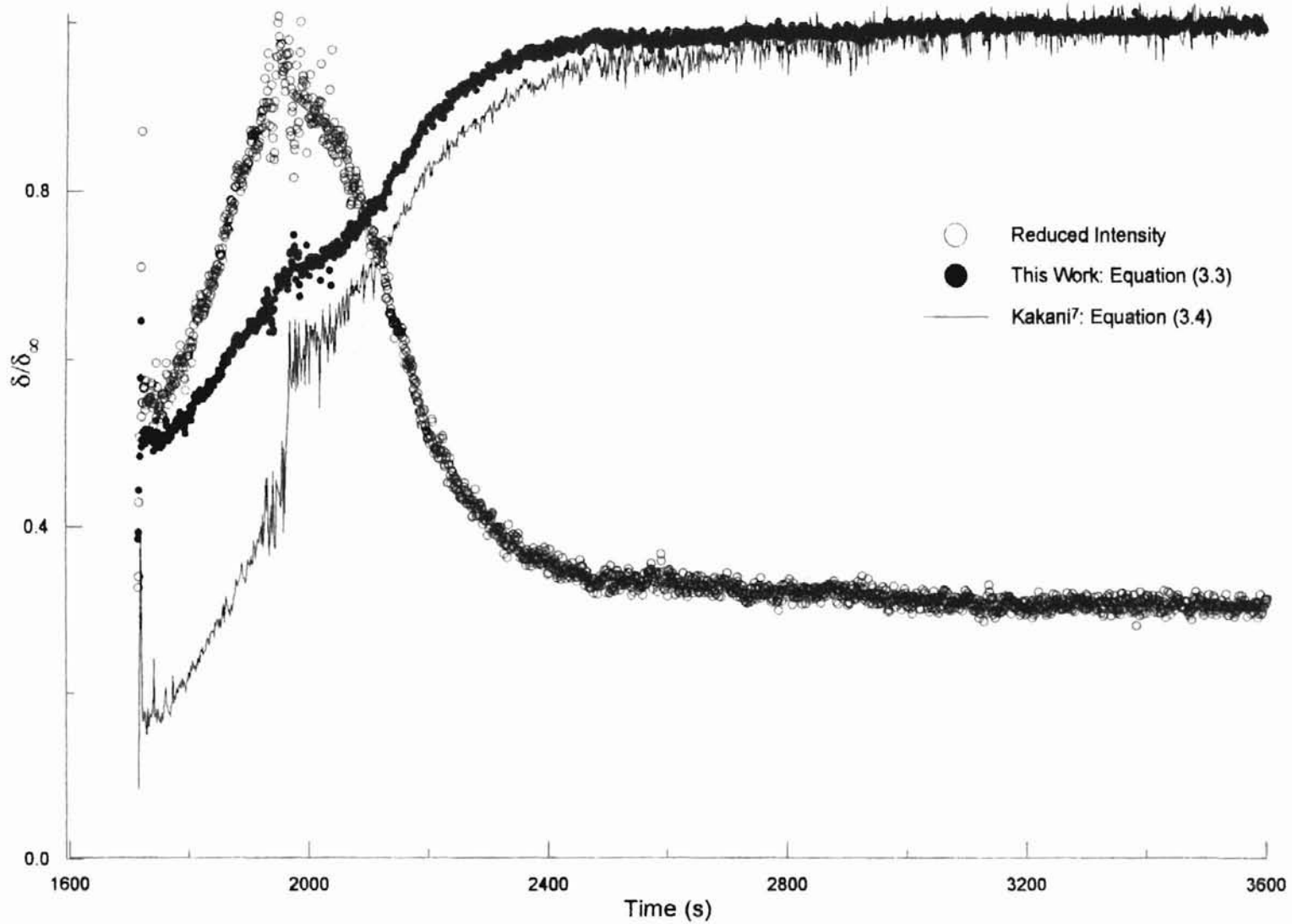

Figure 3.8 Comparison Between Retardance Data from This Work and Kakani's Work[7]

as a word of caution, $\delta = 60°$ was obtained assuming a perfect alignment of polymer molecules along the $x_{\|}$ axis (Appendix A1). Therefore, a less than perfect alignment of the polymer chains would lead to values less than 60° for the retardance, which will affect the value of I_{max}, rather than $I_o/2$. Since the determination of the exact alignment of the polymer chains requires a high resolution CCD camera, Equation (3.7) was not used to calculate $I_o/2$ in this investigation.

In the present investigation the pixel value for $I_o/2$ was taken as 280. The reasoning for this choice was based on the following argument. With the polarizer and the analyzer aligned parallel to each other, the intensity of the source was gradually increased from the minimum value and the corresponding pixel values were observed. The observed data was plotted as shown in Figure 3.9. The curve was extrapolated to obtain the pixel value corresponding to the maximum source intensity. The curve-fit was a fourth order polynomial and gave 280 as the maximum pixel value. When the observed data are fit a straight line, the pixel value corresponding to the maximum intensity is 297. Table 3.B illustrates that the values of $I_o/2$ ranging from 255 to 300 has only a small effect in the third significant figure. Therefore, the value 280 obtained from the best fit curve was chosen as the value of $I_o/2$ in this investigation.

The purpose of Equation (3.7) in this investigation is to demonstrate that $\delta = 180°$ obtained by Kakani[7] using Equation (3.4) was incorrect. Thus Kakani's interpretation of intensity results in large values of retardance causing a discontinuous jump from $\delta(I_{max})$ to the next value in the plot of δ versus t(sec). On the other hand, the latter interpretation gave a smoothly varying curve (Figure 3.8).

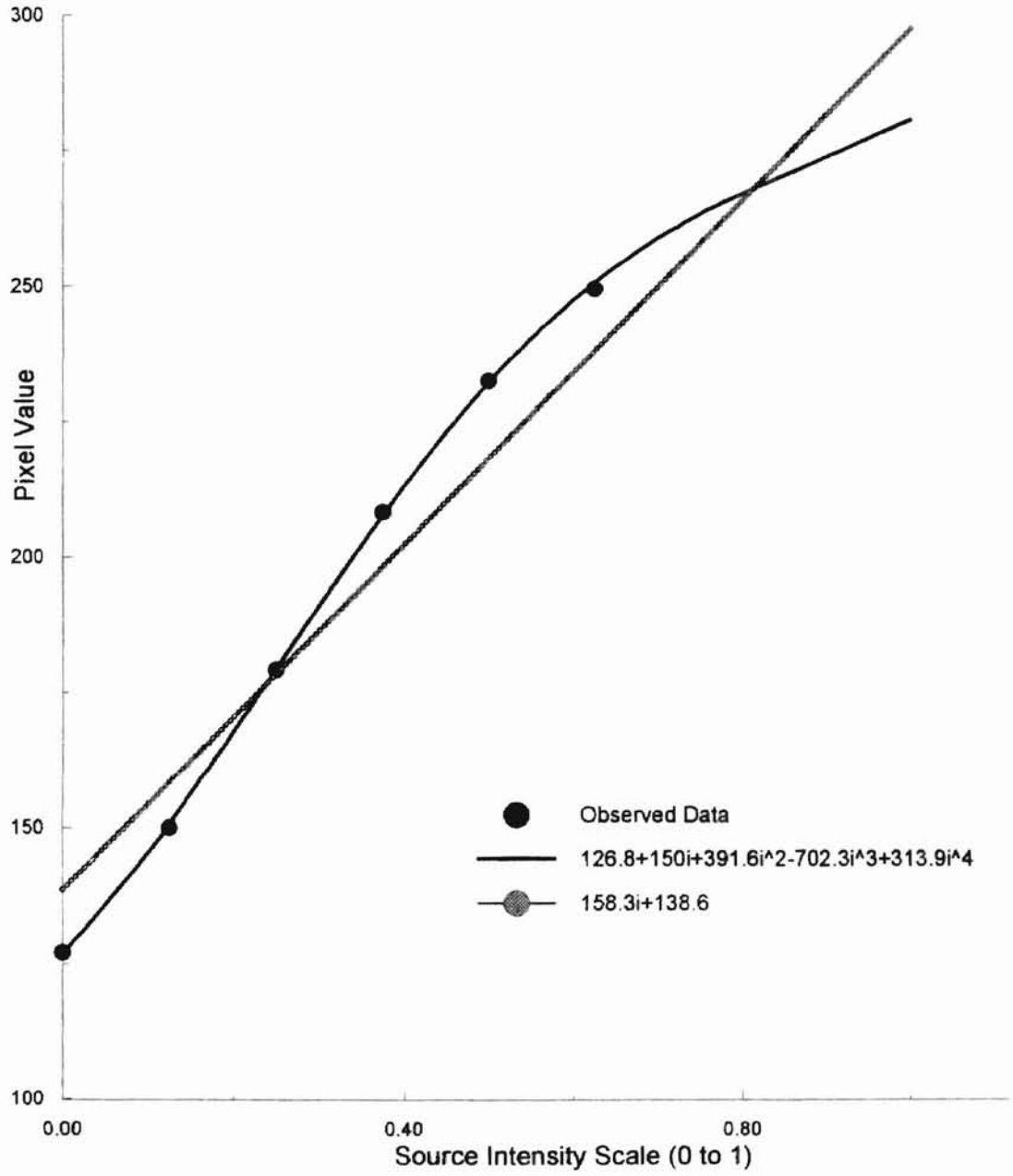

Figure 3.9 Plot to Determine the Pixel value corresponding to $I_o/2$

TABLE 3.B

Normalized Retardance for Two Values of $I_o/2$ at I_{max}

I_{max}	Normalized Retardance (δ)		
	$I_o/2$=255	$I_o/2$=280	$I_o/2$=300
60	0.722383	0.7232566	0.7238401
70	0.7207006	0.7217602	0.7224653
80	0.7189458	0.7202069	0.7210427
90	0.7171121	0.718592	0.7195686
100	0.7151919	0.7169107	0.7180392
110	0.7131765	0.7151568	0.7164503
120	0.7110555	0.7133238	0.7147967
130	0.7088166	0.711404	0.713073
140	0.7064453	0.7093881	0.7112727
150	0.7039236	0.7072657	0.7093881
160	0.7012291	0.705024	0.7074109
170	0.6983339	0.7026476	0.7053303
180	0.6952012	0.7001175	0.7031345
190	0.6917818	0.6974099	0.7008084
200	0.6880073	0.6944945	0.6983339

*Shaded area depicts the frequently observed range of I_{max} -values

The Avrami equation (2.4), written in the linear form is

$$ln\left(-ln\left\{1-\frac{\delta(t)}{\delta_\infty}\right\}\right) = ln(k) + n(ln\ t) \quad . \tag{3.8}$$

Using Kakani's method the plot of $ln\{-ln(1 - \delta(t)/\delta_\infty)\}$ vs. $ln(t)$ showed a discontinuity as shown in Figure 3.10, while the new method yielded a continuous curve.

§ 3.3(a.2) Conducting the Experiment

In Kakani's[7] method, the polarization axis of the polarizer and the analyzer were set at 90° with respect to each other at the onset of crystallization. Crossing the polarization axes led to significantly low transmittance. Consequently, the time of the onset of crystallization could not be determined. The flow-field was applied 20 minutes after the temperature reached 124.6 °C.

Studies conducted in the present work indicated that quiescent crystallization set in 12-15 minutes after the cooling process began. In Kakani's method, crystallization leading to the formation of folded chain crystals must have been taking place for over 5 minutes at the time the flow was applied. Thus, an uncertainty was introduced in the calculation of the parameters n and k which characterize flow-induced crystallization kinetics.

§ 3.3(a.3) Temperature Gradient Along the Sample Height

In Kakani's work[7], the entire sample was assumed to be at the same temperature at any given time. Therefore, the thermostat reading of 124.6 °C was considered to be

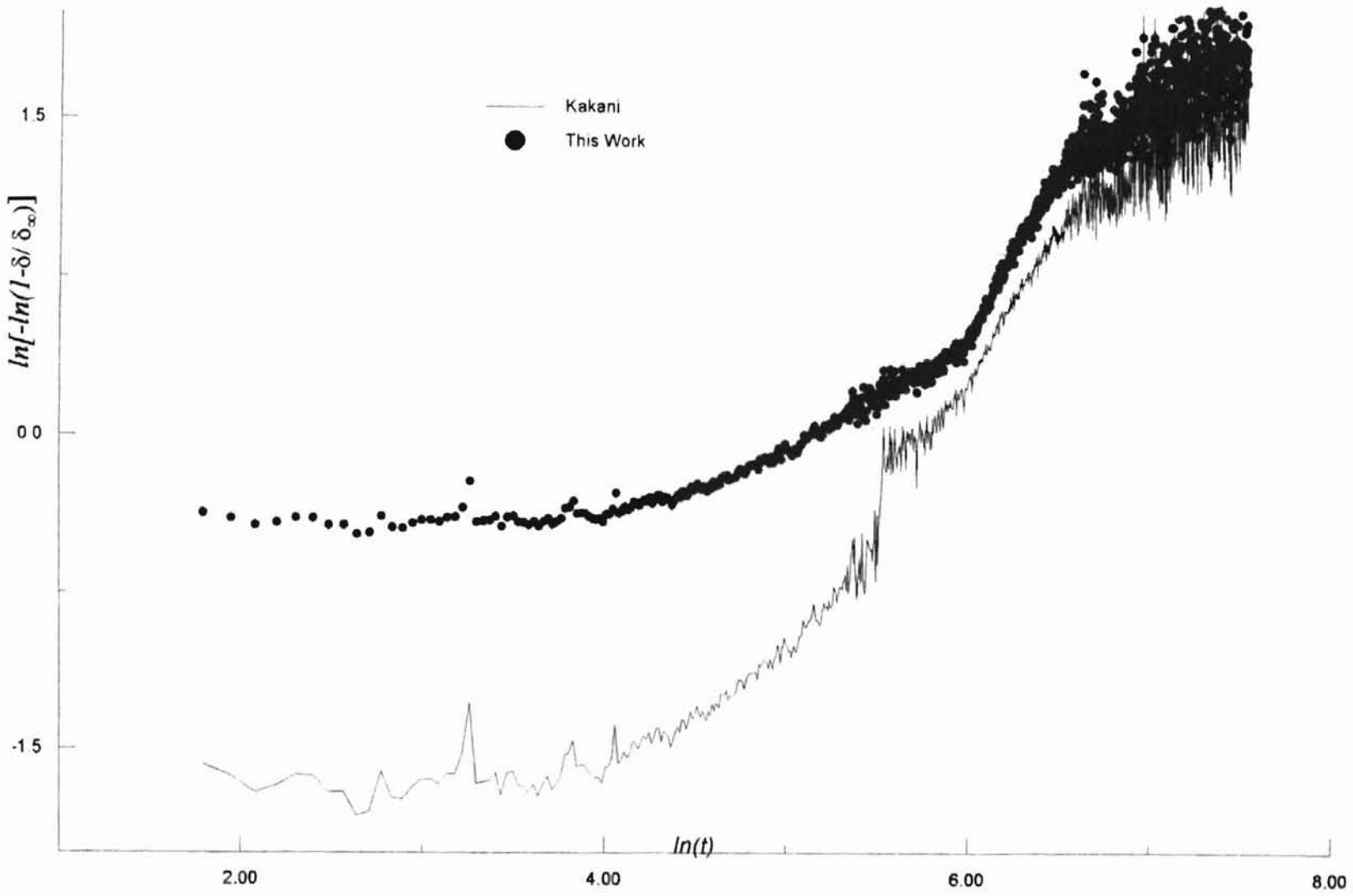

Figure 3.10 Avrami Equation in Comparison with Kakani's Method[32]

the crystallization temperature of the sample as a whole. However, in this work, the temperature measurements showed a marked difference at various points along the height of the sample.

Figure 3.11 shows the thermal history of quenching at four uniformly spaced locations along the height of the sample. The thermocouple was placed 0.5 cm away from the sample. The room temperature for the data shown was 26-27 °C. The thermal data shows the equilibrium temperature to be different at each location on the sample. The equilibrium temperature was the crystallization temperature, T_c at each location. The quench from the initial temperature ranged from 9.9 to ~ 10.5 °C for the location (2), (3) and (4). However, location (1), close to the upper edge of the sample, showed a larger quench of ~ 13.0 °C. The figure shows the time duration of the quench for all four locations to be approximately the same, 16-17 minutes. Therefore, the cooling rates differed from the top of the sample (0.78 °C/min), to the bottom of the sample (0.61 °C/min).

At a room temperature of 21-22 °C, a range from 107 °C at the top of the sample (near the surface of Silicone oil), to 124.6 °C at the bottom edge of the sample (2.8 cm below the surface of the oil) can be noted from Figure 3.12. The quenching time was observed to be 14-15 minutes as shown in Figure 3.13. The undercooling, from 134 °C, and the rate of cooling were 27 °C and ~ 1.9 °C/min respectively, near the top edge, and 9.4 °C and ~ 0.7 °C/min respectively, near the lower edge of the sample. Figure 3.11 and Figure 3.13 display near constant cooling rates, although each case was under a different room temperature. The data in Figure 3.11, clearly show that the thermal history was not

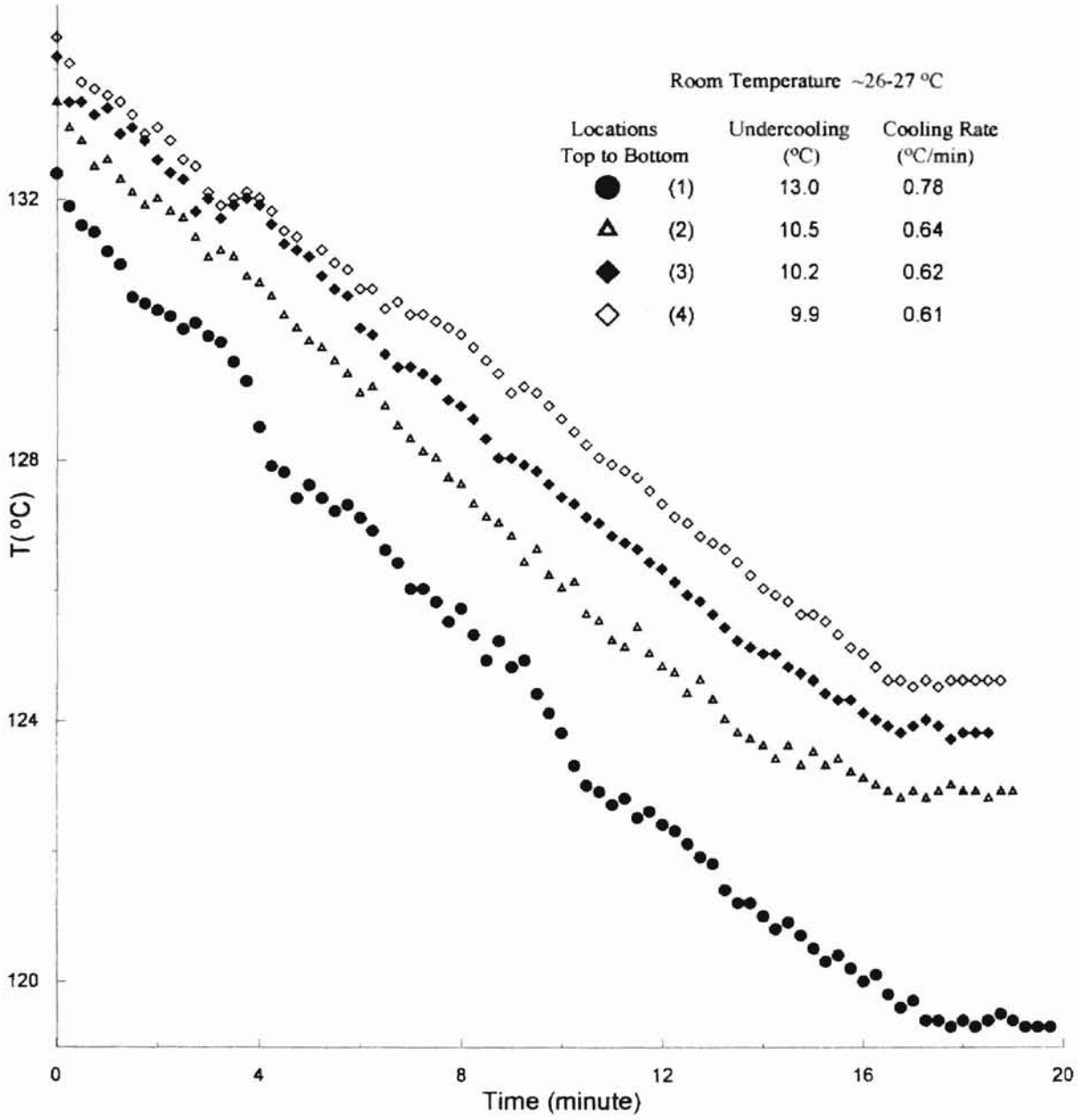

Figure 3.11 Thermal History of Sample in the Quenching Process at Four Locations Along Height

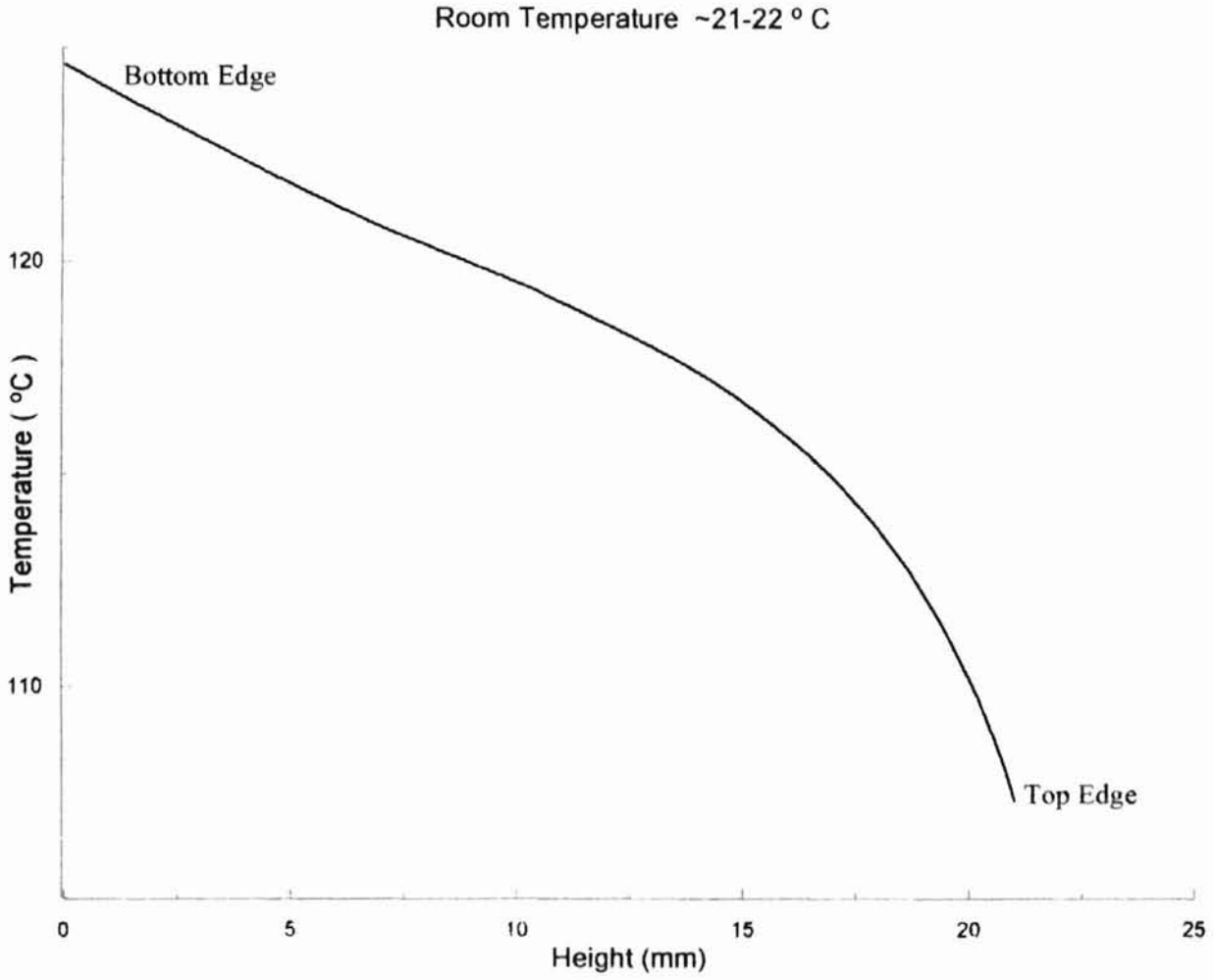

Figure 3.12 Equilibrium Crystallization Temperature Along Sample Height

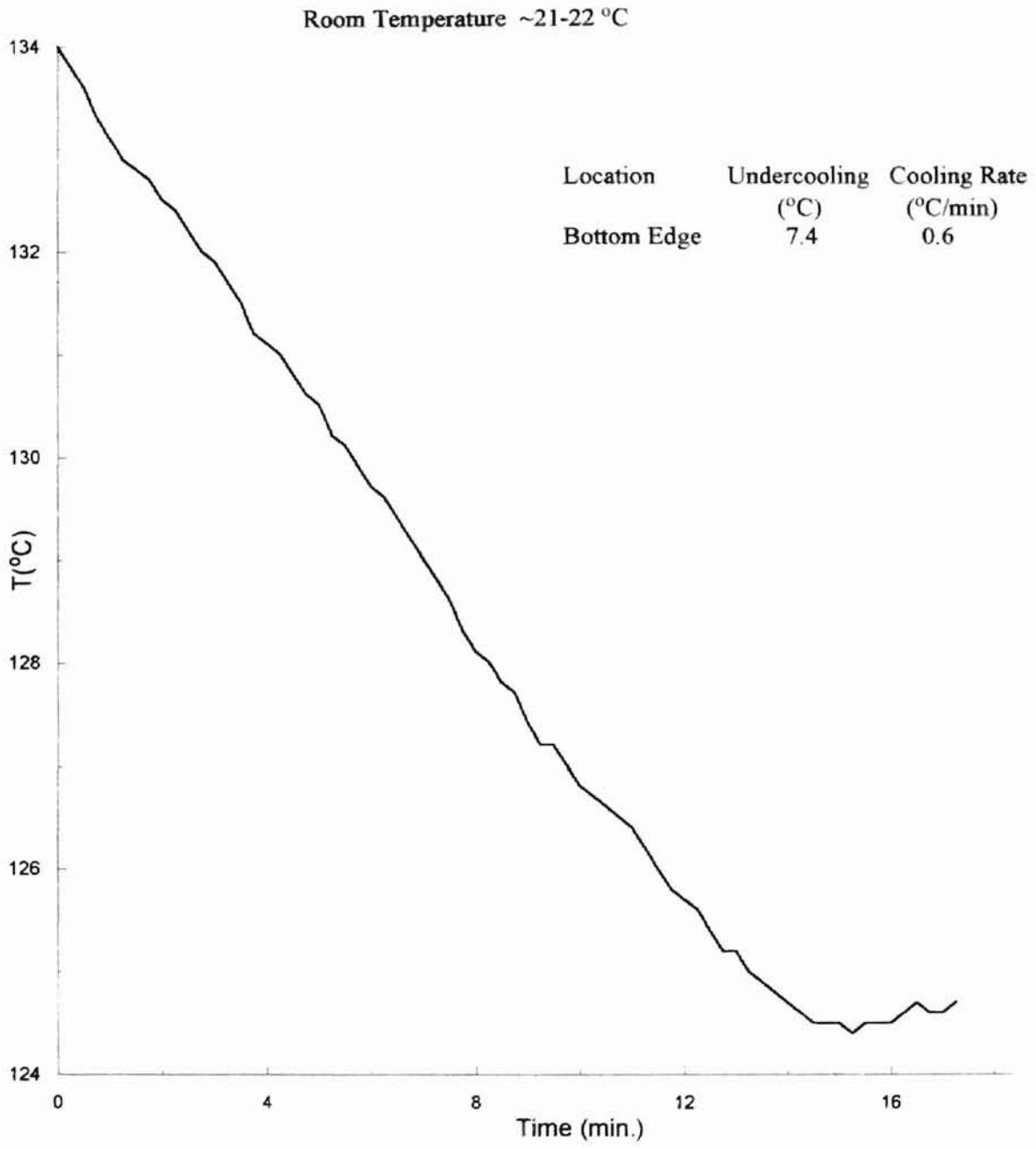

Figure 3.13 Quenching Temperature of Oil Bath Near the Base of Sample as a Function of Time

uniform from the top to the bottom of the sample. However, the room temperature becomes a variable in the cooling process, and the undercooling and the rate of cooling are functions of the room temperature.

Figure 3.14 shows the relative retardance with time for two locations on the sample: location (1) near the upper edge, and location (4), near the lower edge of the sample, respectively. For the curve labeled (1), rapid and large undercooling below the melting point resulted in crystallinity reaching the maximum value within a short duration (~1200 sec). At location (4), the smooth rise of the curve indicates a slow increase in crystallinity. The maximum value of retardance was reached over ~8000 sec. The significant difference of the undercooling ($\Delta T = T_m - T_c$) and the rate of cooling along the height of the sample, could be the cause of differences in the rates of crystallization at various locations on the sample.

The Avrami curves for the data in Figure 3.14 showed a straight line for location (1) in Figure 3.15, leading to the conclusion that the Avrami equation holds well for large undercooling (~ 27°C) over a given time duration (~ 14-15 minutes). Curve (4) in Figure 3.15 shows a non-linear behavior. The undercooling for this location was ~ 9.4°C within the time interval of ~ 14-15 minutes.

§ 3.3(a.4) Effect of Thickness on Retardance

The changing thickness of the sample stems from the observation of upward migration of the sample towards the surface of the oil bath due to the buoyancy of sample in Silicone oil. A schematic representing the sample thickness at the cessation of the

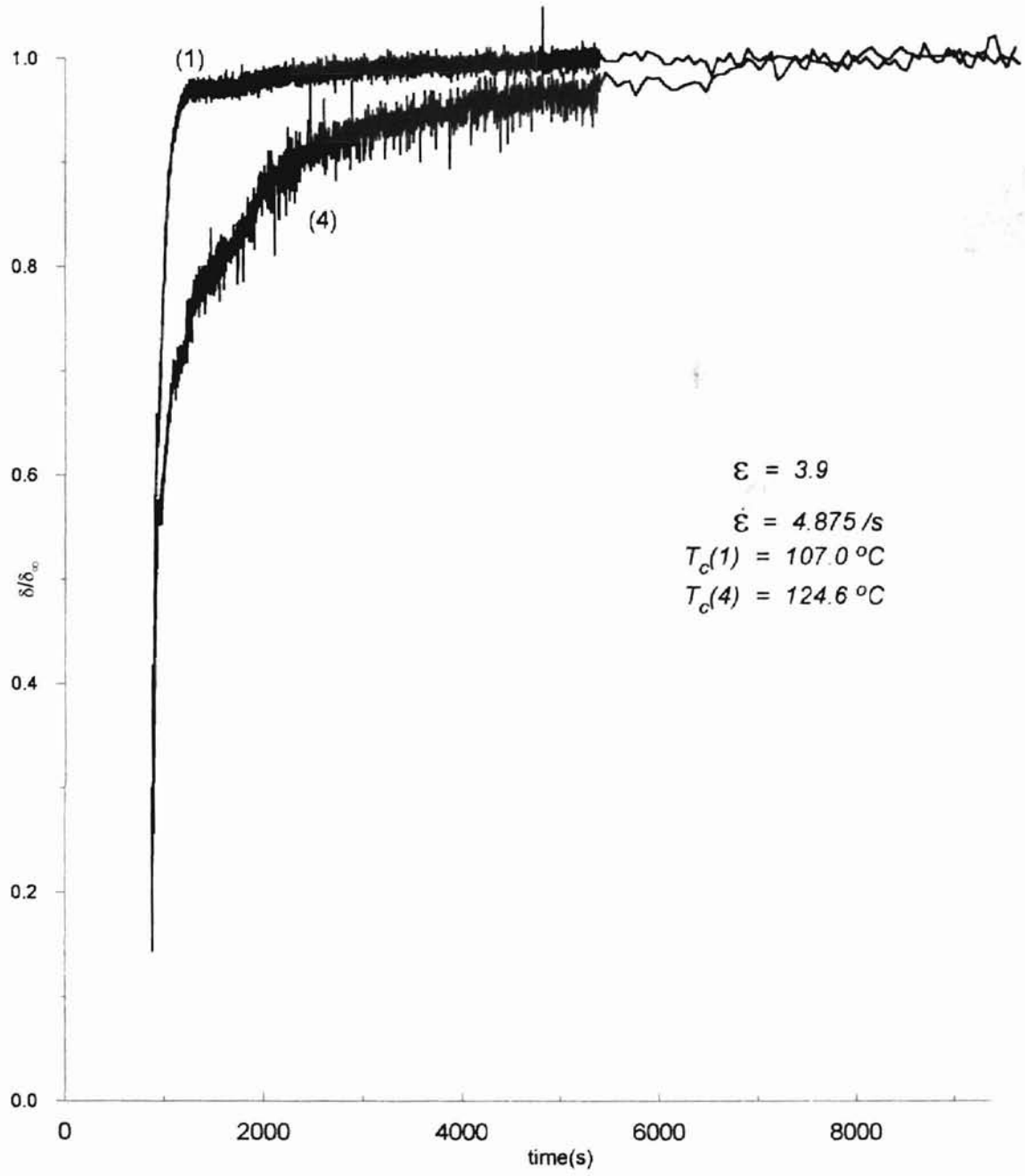

Figure 3.14 Relative Retardance at the Upper Edge (1) and the Lower Edge (4), respectively of the Sample

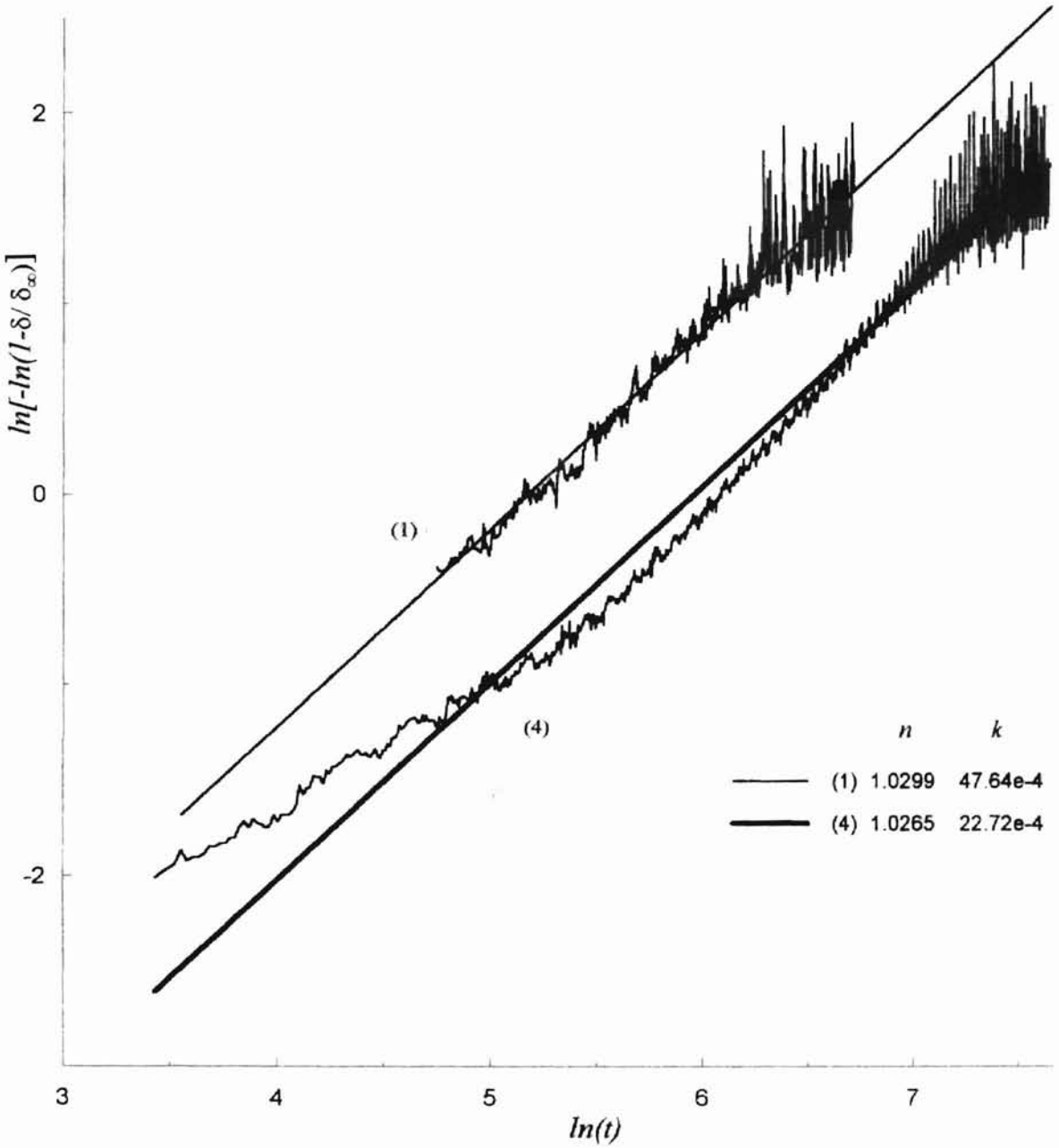

Figure 3.15 Linear Form of Avrami Equation for Data in Figure 3.14

applied flow and at t_∞ is shown in Figure 3.16. During the initial stage after the flow field was applied, when the sample was not fully crystallized, the gradual upward movement continued, until the sample was fully crystallized. In some samples, as the experiment proceeded, the lower portion of the sample became thin and film-like, and eventually broke. These observations led to the investigation of how thickness could affect the observation of FIC.

Using Equation (2.3), δ/δ_∞ could be expressed as:

$$\frac{\delta}{\delta_\infty} = \frac{(2\pi / \lambda)\Delta nL}{(2\pi / \lambda)\Delta n_\infty L_\infty} = \left(\frac{\Delta n}{\Delta n_\infty}\right)\left(\frac{L}{L_\infty}\right) \tag{3.9}$$

Equation (2.3) shows that $\delta = \delta(\Delta n, L)$. If the thickness L were assumed to be constant during the course of the experiment, δ could be freed from the spatial dimensions by normalizing the δ-curve. Relative retardance could then be written as

$$\frac{\delta}{\delta_\infty} = \frac{\Delta n}{\Delta n_\infty} \; . \tag{3.10}$$

whence all four curves will coincide with one another. However, a careful observation of Figure 3.4 shows that the $\delta(t)/\delta_\infty$ curves do not overlap. Therefore, $\delta(t)/\delta_\infty$ could be a function of both L and Δn. The thickness effect was disregarded in Kakani's method of analysis.

§ 3.3(a.5) Determination of Rate ($\dot{\varepsilon}$) and Total Strain (ε)

In Kakani's investigation, the values of $\dot{\varepsilon}$ and ε were determined as follows. The length of the window (l_o) on the sample was 1 cm. Upon application of the flow-field,

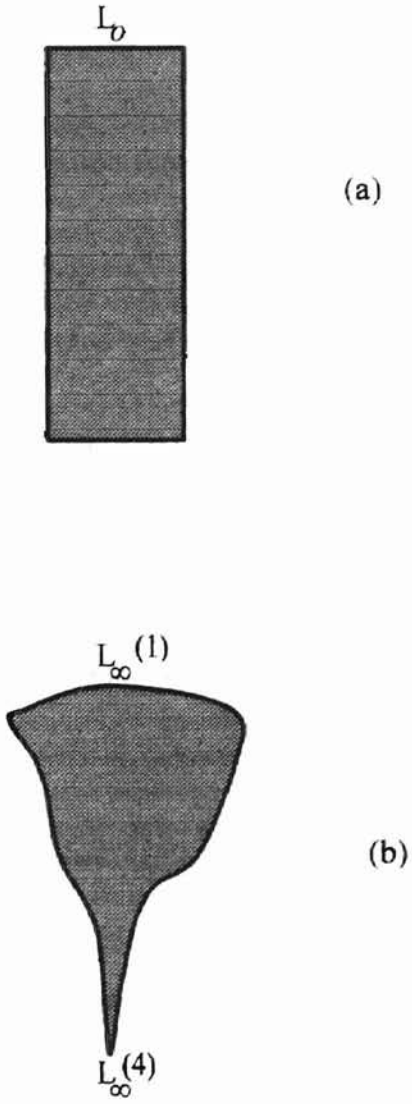

Figure 3.16 Typical Cross Sectional View of the Sample Thickness (L); (a) At the Cessation of Flow (b) At Infinite Time; (1)Top Edge, (4)Bottom Edge

the sample elongated to its final length (l). The actual total strain experienced by the sample was:

$$\varepsilon = \frac{l - l_o}{l_o} \quad . \tag{3.11}$$

Assuming a constant rate of elongation throughout the rotation of the rollers, the rate of strain can be written as

$$\dot{\varepsilon} = \frac{\varepsilon}{t} \quad . \tag{3.12}$$

where t is the time of the elongation obtained from the X-Language commands. However, t was observed to be greater than the value specified by the X-Language commands (further discussion is in Chapter IV). Therefore, in this investigation, the actual value, t_{actual}, was used in the calculation of $\dot{\varepsilon}$ and ε.

§ 3.3(b) Improved Methods of Experimentation and Analysis

The assumptions made by Kakani[7] included: linear form of the Avrami equation, a uniform thermal history throughout the sample, uniform thickness of the sample before and after deformation, and a constant rate of deformation of the sample during the application of the flow field. In many cases, the assumptions could not be justified. Based on the examination of the assumptions, new experimental and analysis techniques were developed.

§ 3.3 (b.1) Data Analysis Using the New Method

The linear form of the Avrami Equation was used by Kakani[7]. A plot of $ln\{-ln(1-X_c(t)/X_{c\infty})\}$ vs. $ln(t)$ was expected to yield a straight line. However, due to the reasons discussed in § 3.3, the curve was non linear as shown in Figure 3.17a,b,c,d. Therefore, the straight line did not approximate the data especially for the initial 30 minutes after the strain was applied, since the time interval between the data points for the initial 30 minutes was 1 minute, and was reduced to 1 second after the 30 minutes.

The method used in this investigation did not employ the linearization approach. The Avrami Equation can be written in non-linear form as:

$$1-\frac{\delta}{\delta_\infty}=e^{-kt^n} \quad . \tag{3.13}$$

The left side of Equation (3.13) was plotted using the experimentally obtained data, whereas the right side was an expression that could be used to fit the curve obtained from the data. Suitable values of n and k could thus be determined.

§ 3.3(b.2) Reduction of Temperature Gradient

A constant temperature profile could be obtained by covering the equipment with an insulating material capable of withstanding temperatures up to 140 °C; *e.g.*, glass-wool, wood, cork board, etc. The temperature profile in Figure 3.18 shows that, after a housing of insulation was constructed over the pulley-roller shaft system, the temperature variation from the top of the sample to the bottom was reduced to less than 2.0 °C.

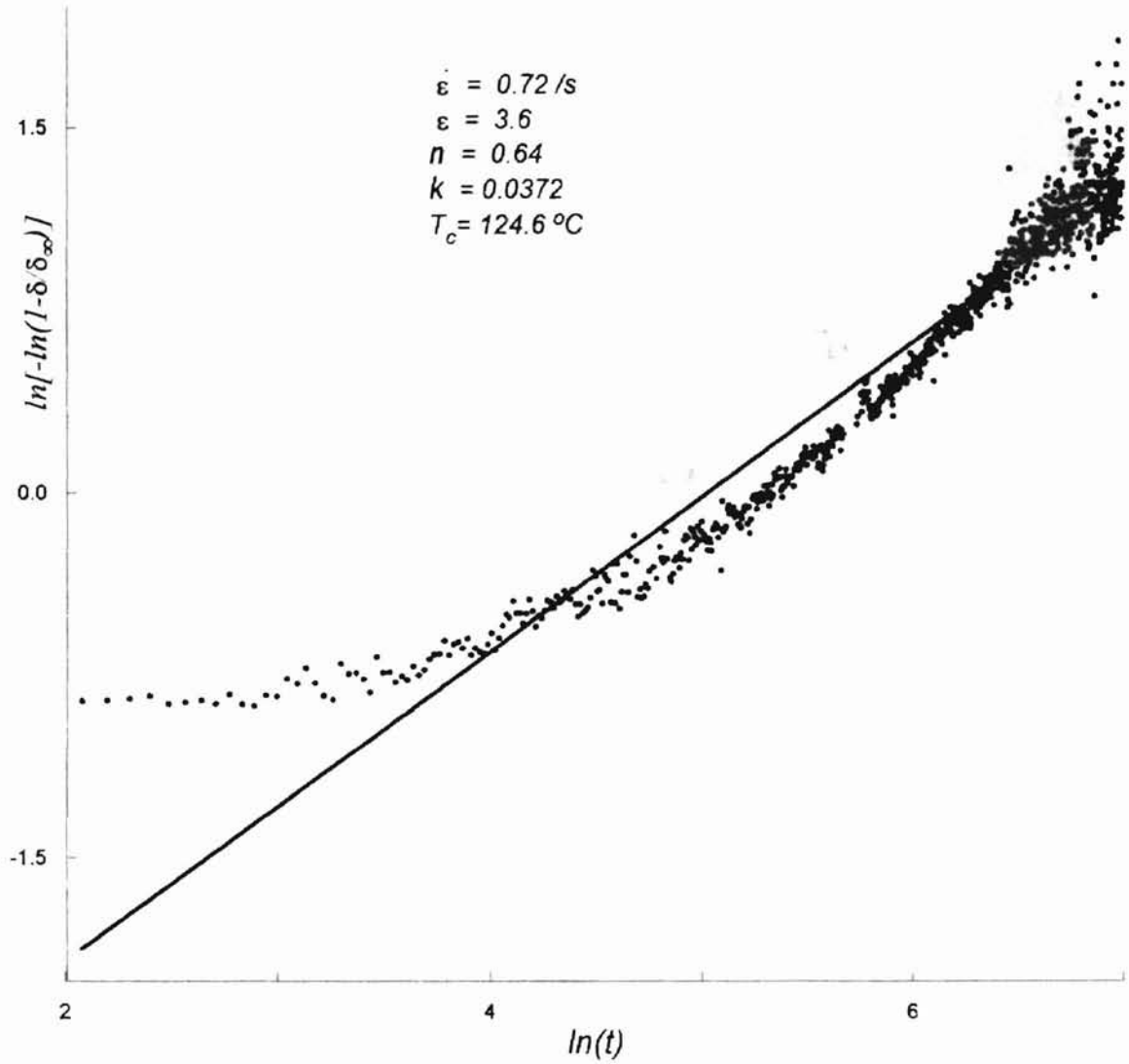

Figure 3.17a Weighted Linear Form of Avrami Equation; Location (1)
Obtained From Figure D2 [7]

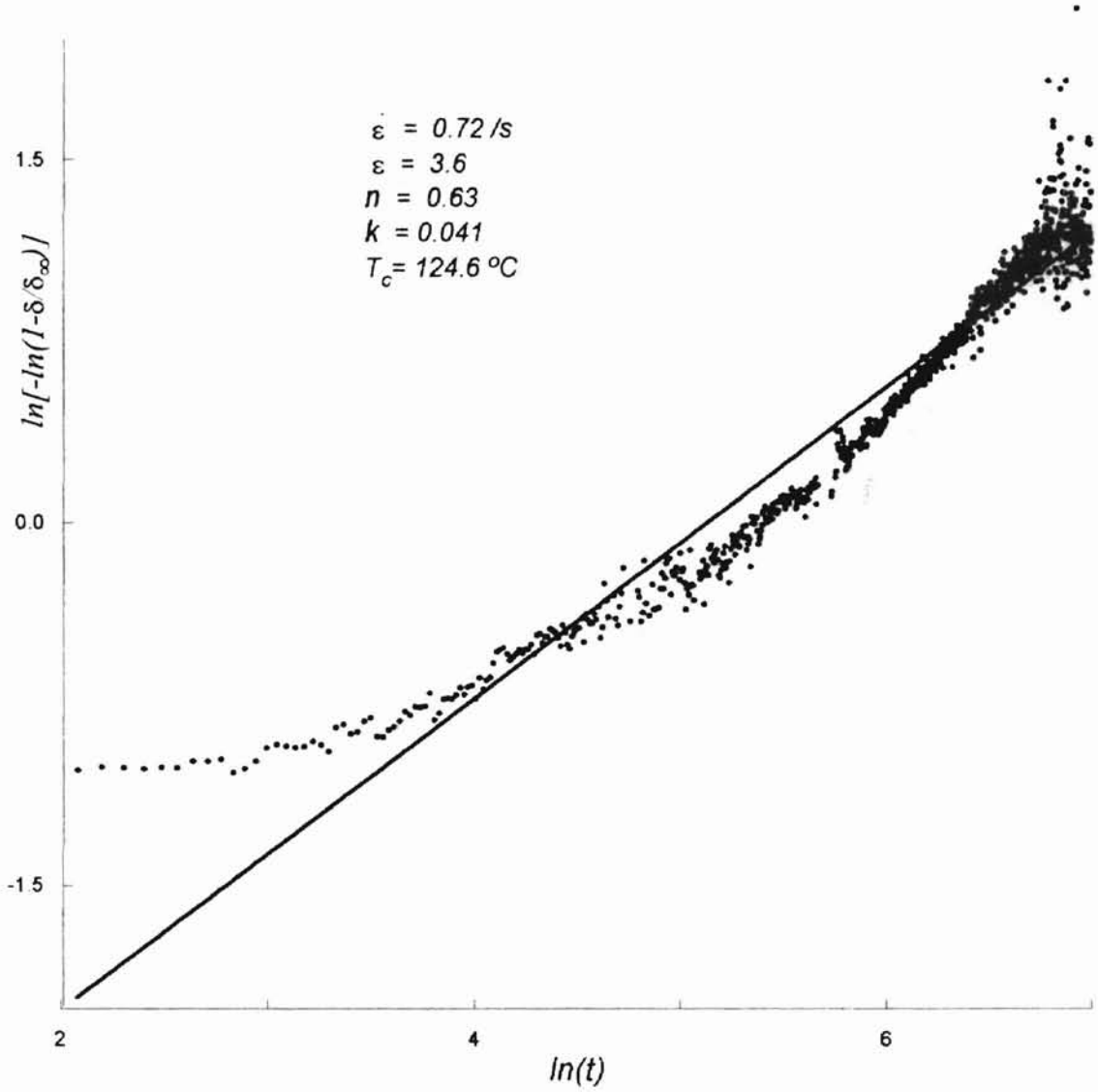

Figure 3.17b Weighted Linear Form of Avrami Equation; Location (2)
Obtained From Figure D2[7]

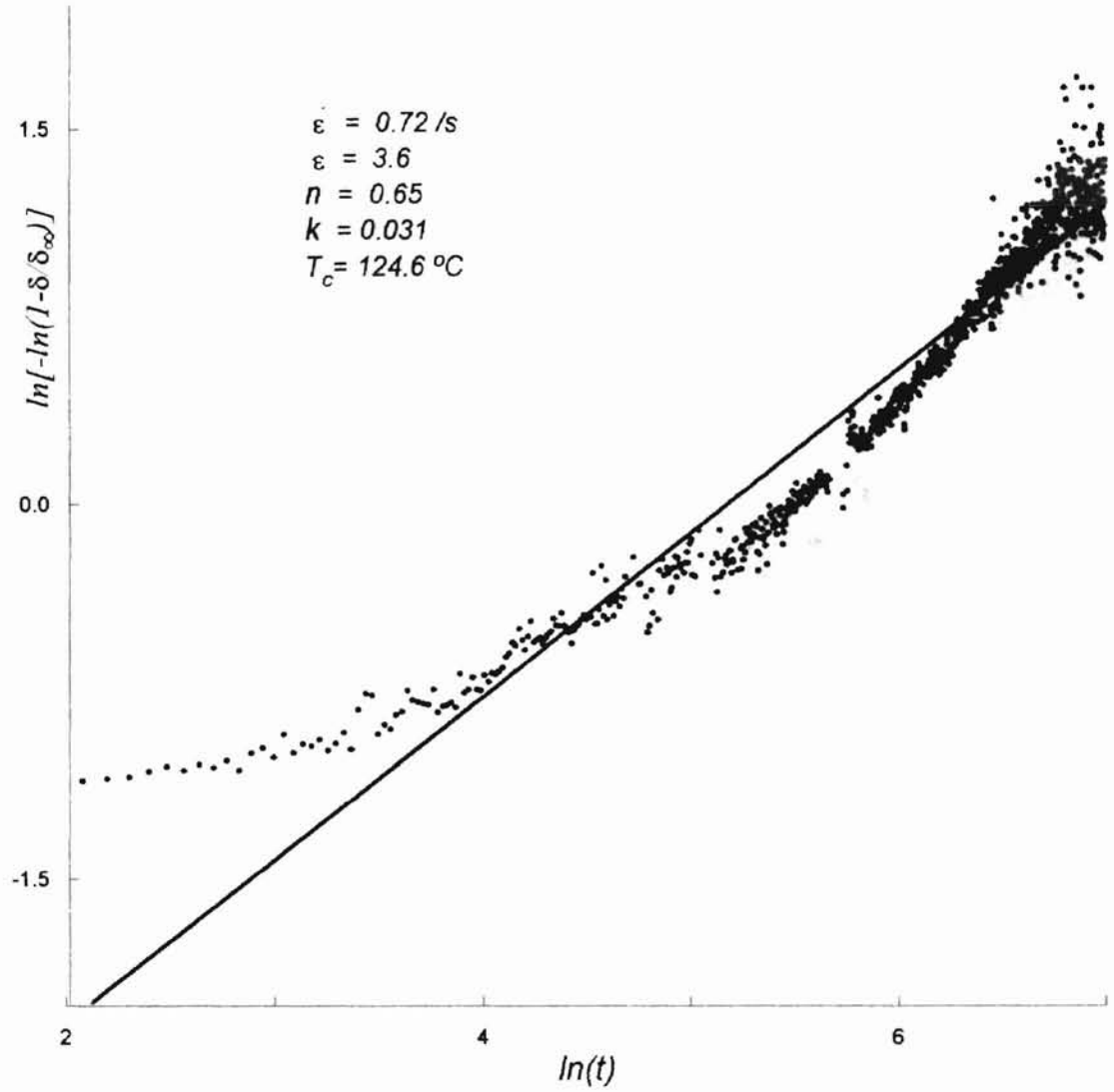

Figure 3.17c Weighted Linear Form of Avrami Equation; Location (3) Obtained From Figure D2 [7]

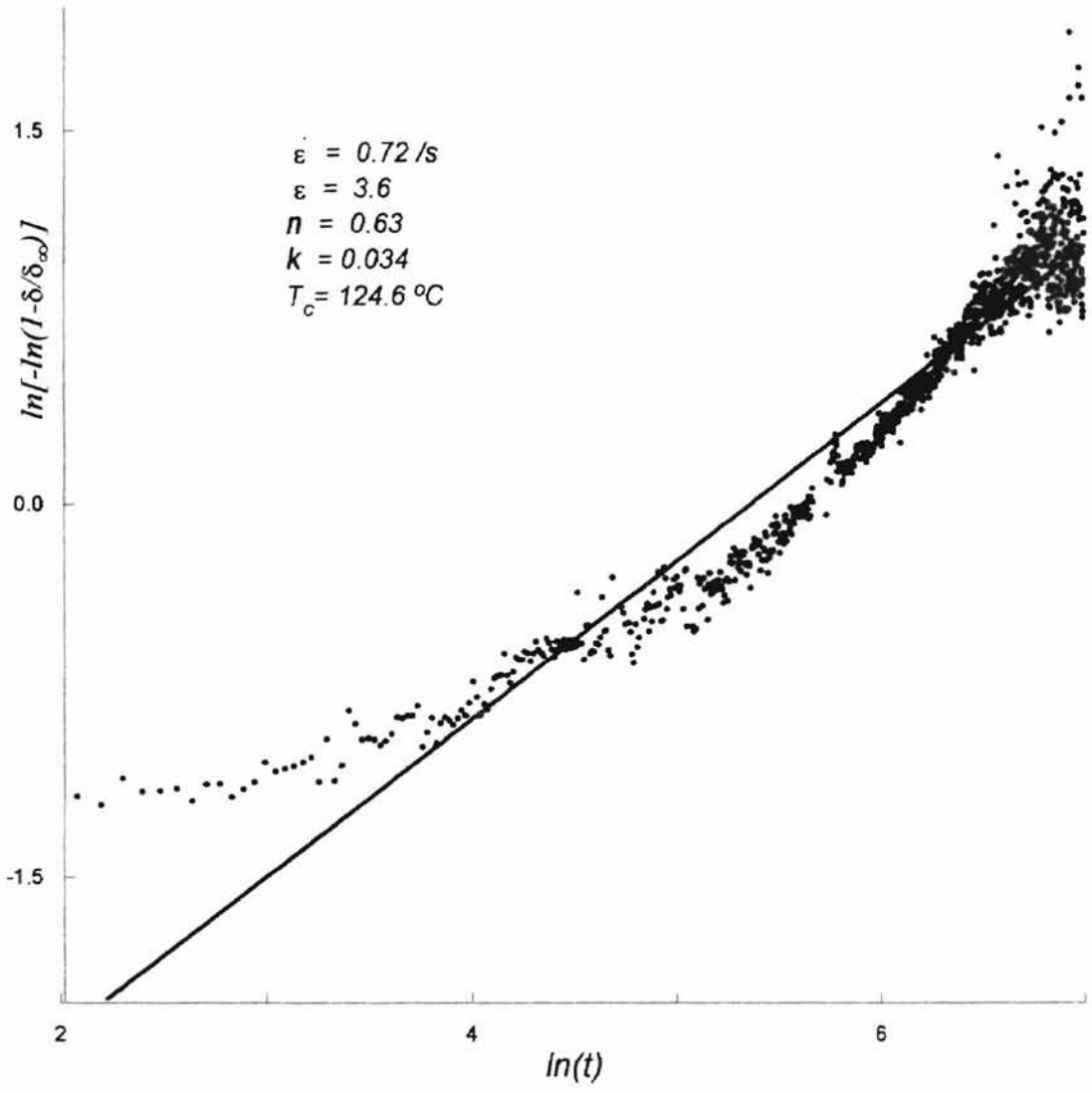

Figure 3.17d Weighted Linear Form of Avrami Equation; Location (4)
Obtained From Figure D2 [7]

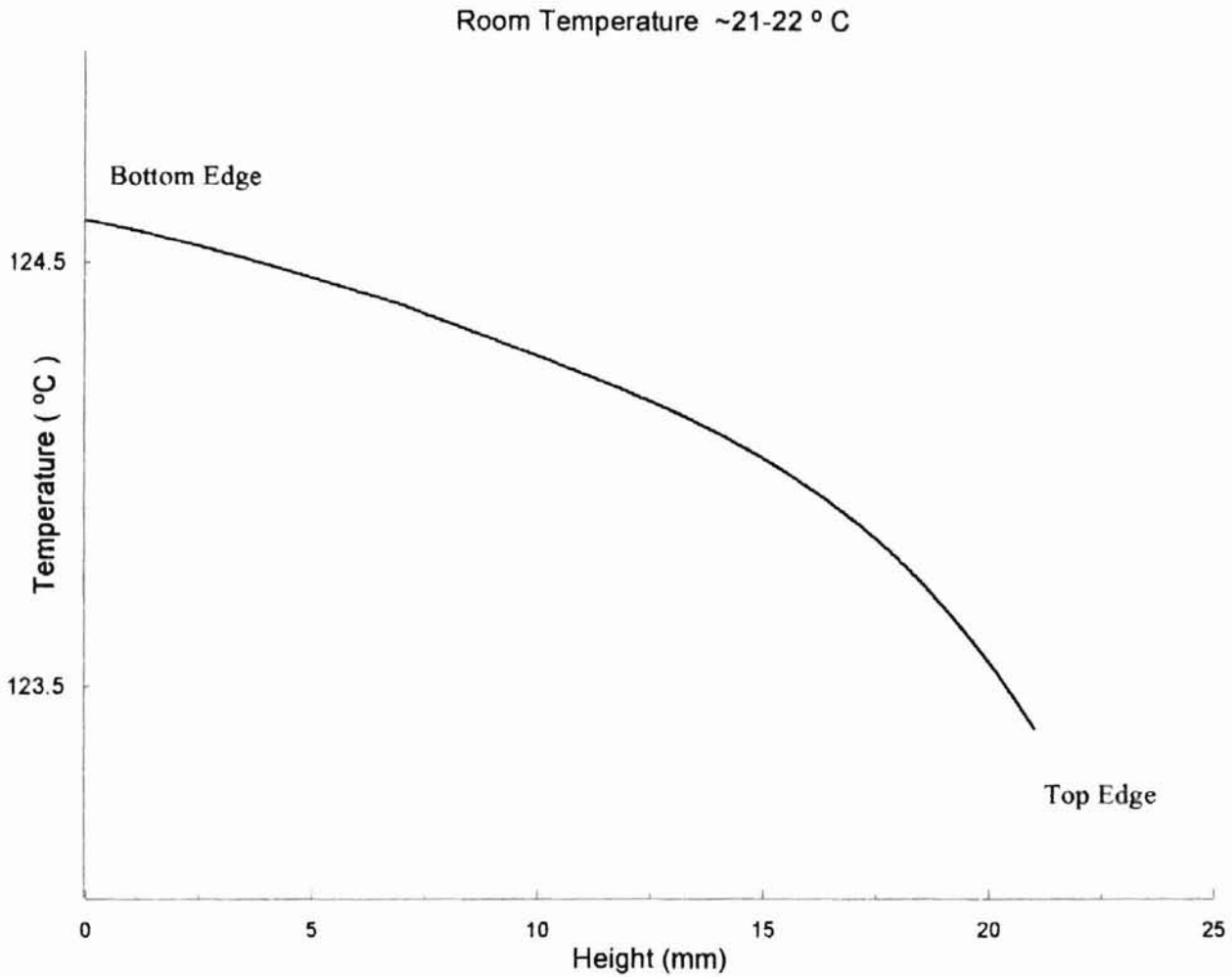

Figure 3.18 Equilibrium T_c Along Sample Height With Insulation over Sample Housing

§ 3.3(b.3) Analysis of Thickness Change

A procedure to check the dependence of δ/δ_∞ on thickness has been developed. The main assumptions essential for the procedure are stated below:

i) If L varies, the change occurs during a certain time interval, the upper limit of which is t_∞.

ii) $\underset{t \to t_\infty}{Lim} \quad \Delta n = \Delta n_\infty$, where Δn is the birefringence of the sample as defined in Equation (2.3).

iii) $\frac{I_o}{2} = 255$, a conservative lower limit; $t_\infty = 4000\,\text{sec}$, most birefringent action is observed within this interval;

iv) $$I = I\left(t, L, L_\infty\right); \tag{3.14a}$$

v) $$L = L_o e^{-\alpha_{L1} t} + L_\infty\left(1 - e^{-\alpha_{L2} t}\right); \tag{3.14b}$$

where L_o is the thickness at $t = 0$, L_∞ is the thickness at $t = t_\infty$, and α_{L1}, α_{L2}, are the characteristic time constants in the empirical exponential equations.

The choice of form of Equation (3.14b) was made by considering two simultaneous processes. At the onset of FIC, the effect of the original thickness, L_o, dominated. However, with time, the thickness changed such that at t_∞, the thickness attained its final value of L_∞. Therefore, a decrease in the effect of L_o should be accompanied by an increasing effect of the final thickness. Moreover, the rates at which the two processes took place had to be consistent with the observed retardance data,

which was exponential in nature. Thus, the instantaneous value of the thickness, L, was expressed as the sum of two exponential curves, as shown in Equation 3.14b. The rate of decrease in the effect of L_o was described by the time constant, α_{L1} , while the opposing effect was characterized by the time constant, α_{L2} . Other forms, such as linear forms describing the simultaneous effects were also tested. However, such forms did not give the best description of the retardance data. Hence, the choice of the form of Equation 3.14b over other forms.

A plot of thickness change with time is shown in Figure 3.19. (The required data for the plot was taken Table 4.G in Chapter IV). Location (4) shows the expected curve decrease in thickness. At location (1), although the final value shows an increase in thickness with respect to the initial value, the initial steep rise cannot be explained. However, since Equation (3.14b) when used to fit the original intensity data (Equation 3.14a) showed remarkable agreement with the data, Equation (3.14b) has been used in this investigation as a measure of change in thickness of the sample during FIC.

vi) $$\Delta n = \Delta n_{\infty}\left(1 - e^{-\alpha_n t}\right) \quad , \tag{3.14c}$$

α_n being the characteristic time constant for the exponential equation. Equation (3.14c) is also an empirical equation. In this case, the birefringence approached its final value at t_{∞} . Once again, Equation (3.14c) best described the retardance data over the other forms considered.. Equation (3.14c), when combined with Equation (3.14b) in Equation (3.9) was well in agreement with the experimental data of the δ/δ_{∞} curve. The intensity can now be rewritten as:

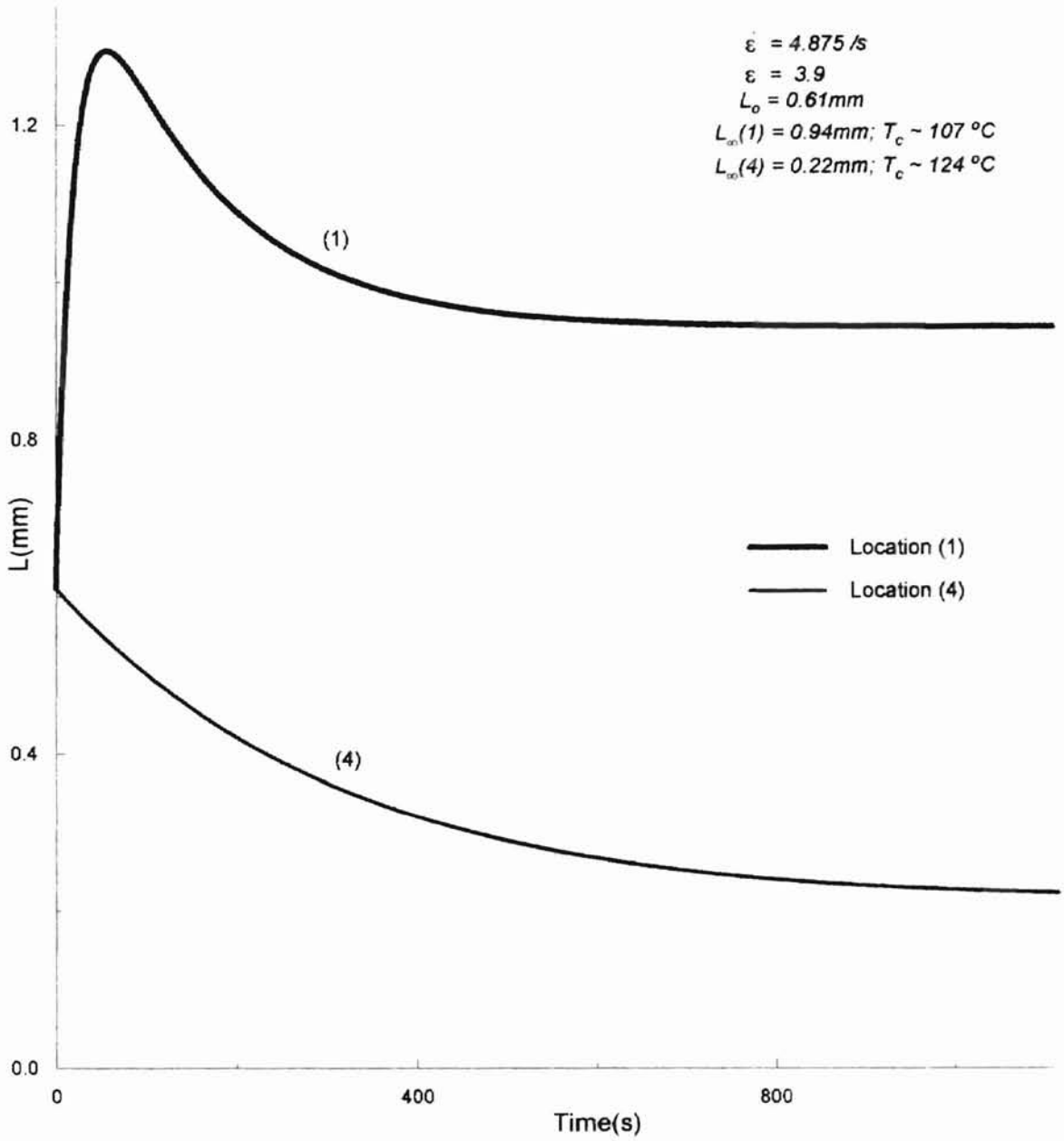

Figure 3.19 Thickness of Sample at the Top (1) and bottom (4) with Time
Data Obtained From Table 4.H, Chapter IV

$$I = I(t,\ \Delta n,\ \alpha_{L1},\ \alpha_{L2},\ \alpha_n,\ L/L_\infty),$$

where
$$\frac{L}{L_\infty} = \frac{L_O}{L_\infty} e^{-\alpha_{L1} t} + \left(1 - e^{-\alpha_{L2} t}\right). \qquad (3.14b')$$

Equation (3.14b') is important in determining the change in thickness with time during FIC.

Combining Equation (3.3) and Equation (3.9), the following equation can be obtained:

$$sin\left[\left(sin^{-1}\sqrt{\frac{I_\infty}{I_o/2}}\right)\left(\frac{\Delta n}{\Delta n_\infty}\right)\left(\frac{L}{L_\infty}\right)\right] = \sqrt{\frac{I}{I_o/2}} \quad . \qquad (3.15)$$

Using trigonometry for small angles, the sine of a small argument can be approximated by the argument itself. Therefore, for small values of $\sqrt{\frac{I_\infty}{I_o/2}}$, $sin^{-1}\sqrt{\frac{I_\infty}{I_o/2}} \approx \sqrt{\frac{I_\infty}{I_o/2}}$.

Equation (3.15) can now be rewritten as:

$$sin\left[\left(\sqrt{\frac{I_\infty}{I_o/2}}\right)\left(\frac{\Delta n}{\Delta n_\infty}\right)\left(\frac{L}{L_\infty}\right)\right] = \sqrt{\frac{I}{I_o/2}} \quad . \qquad (3.16)$$

Substituting for $(\Delta n/\Delta n_\infty)$ and (L/L_∞) in Equation (3.16) and rearranging,

$$I = \frac{I_o}{2} sin^2\left[\sqrt{\frac{I_\infty}{I_o/2}}\left(1 - e^{-\alpha_n t}\right)\left(\frac{L_o}{L_\infty} e^{-\alpha_{L1} t} + \left(1 - e^{-\alpha_{L2} t}\right)\right)\right] \quad . \qquad (3.17)$$

The quantity in the last set of curved brackets in Equation (3.17) is the right hand side of Equation (3.14b'). An algorithm developed to determine L/L_∞ is shown in Figure 3.20. Each intensity curve was obtained by recording the pixel values with time, at a particular location on the sample chosen at random. Four simultaneous equations of the form of Equation (3.17), with different sets of values of I and t, were solved to obtain the four unknown values, α_{L1}, α_{L2}, α_n, and L/L_∞ respectively, for each intensity curve, using

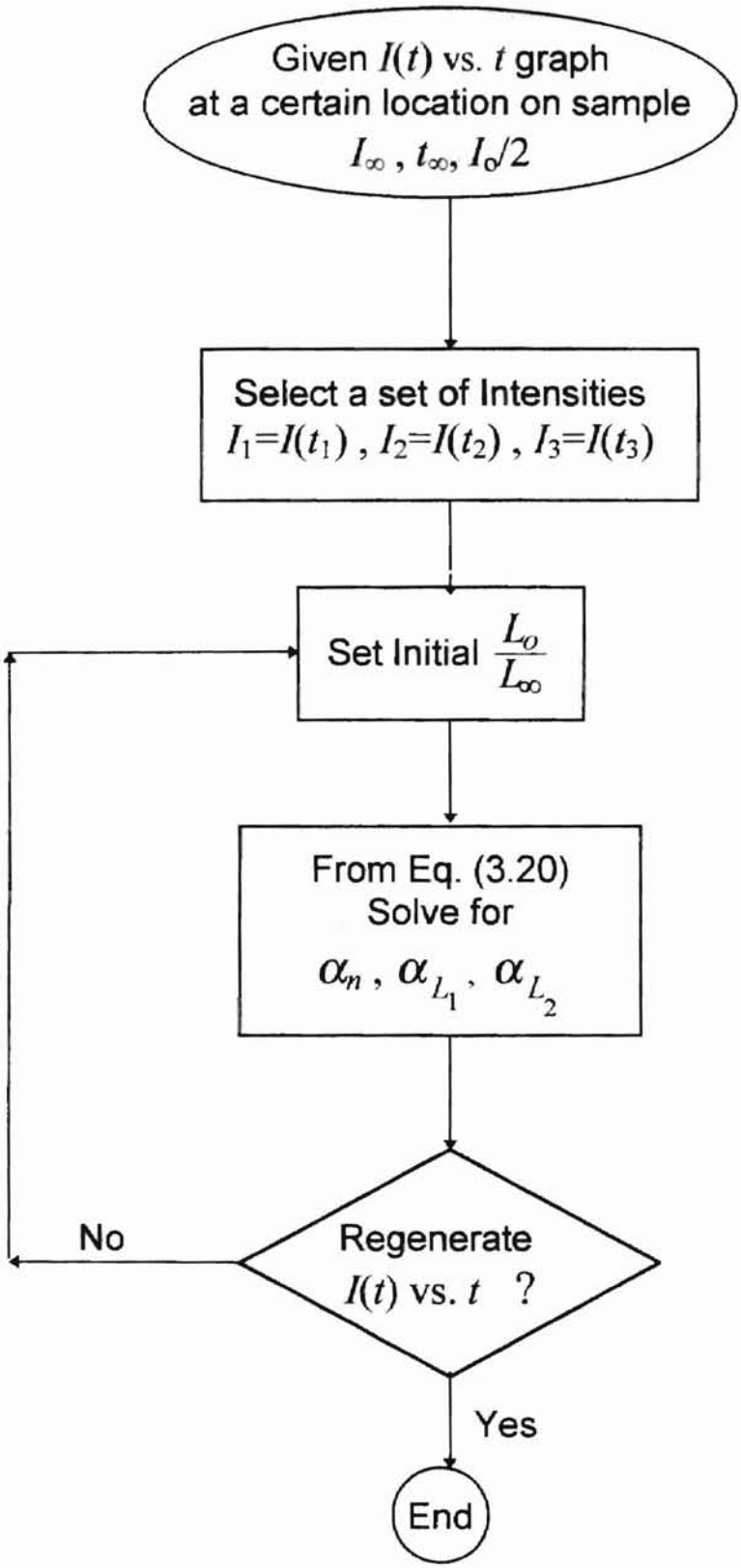

Figure 3.20 An Algorithm to determine the Change in the Local Thickness, L(t) of the Sample

MathCad. The $I(t)$ vs. t curves for each location were regenerated using these parameters, as a measure of check for the validity of Equation (3.17). For values of L/L_∞ other than unity, a change in thickness during the course of the experiment can be inferred. Different values of L/L_∞ corresponding to different sites on the same sample would also suggest a non uniform deformation of the sample under the influence of a flow field. Equation (3.9) could be rewritten as:

$$\frac{\Delta n}{\Delta n_\infty} = \frac{\delta / L}{\delta_\infty / L_\infty} \quad . \tag{3.17}$$

Substituting for L, Equation (3.17) becomes:

$$\frac{\left(\delta / \delta_\infty\right)}{\left(\frac{L_o}{L_\infty}\left(e^{-\alpha_{L1}t}\right)+\left(1-e^{-\alpha_{L2}t}\right)\right)} = \left(\frac{\Delta n}{\Delta n_\infty}\right) \quad , \tag{3.18}$$

where δ/δ_∞ could be obtained from the experimental data. The right hand side of Equation (3.18) is independent of spatial terms and is solely due to birefringence. The elimination of the thickness factor should now cause the $\Delta n/\Delta n_\infty$ curves to overlap.

Although determination of the local thickness as a function of time is useful in the analysis of crystallization kinetics, the procedure has not been adopted for all the experiments performed for this investigation. However, the method has been applied to data from one of the experiments. The procedure further leads to obtaining useful information regarding the relaxation time and induction time, as is demonstrated in Chapter IV.

§ 3.3(b.4) Strain Rate ($\dot{\varepsilon}$) and Total Strain (ε)

In this investigation, the total deformation and the rate of deformation experienced by the sample were determined. Although the X-Language commands specified the rotational distance and the angular velocity of the rollers, the actual measurements of strain and rate of strain did not involve these two given specifications. This section includes the derivation of formulae to calculate $\dot{\varepsilon}$ and ε, using the X-Language input commands, and a method to measure the actual $\dot{\varepsilon}$ and ε.

§ 3.3(b.4) (*i*) $\dot{\varepsilon}$ and ε from X-Language Commands

The parameters predefined using the X-Language commands, for the rotation of the compumotor were, the rotational distance, the angular speed, and the time of rotation. D, was the number of steps to be taken by a roller. There were 25,000 steps/revolution. The angular speed, V, of the roller was measured in revolutions/sec. The time, t, taken by a roller to cover D number of steps was expressed in seconds. The execution of the commands were in accordance with the equation

$$D = V\,t\,(25{,}000)\,. \tag{3.19}$$

Assuming no-slip condition between the roller and the sample, the linear velocity experienced by the sample, at the point of contact between the roller and sample, $v_{\|}$, along the $x_{\|}$ axis, could be obtained from the angular velocity of the roller of radius r, as

$$v_{\|} = 2\,\pi\, r\, \mathrm{V} \quad . \tag{3.20}$$

The portion of the sample under the foil adhered to the foil and had the same velocity as the material in contact with the rollers. The resulting strain was experienced only by the material in the window. The strain experienced by the exposed area of the sample along $x_{\|}$ was defined as

$$\varepsilon(t) = \frac{l(t) - l_o}{l_o} \quad , \tag{3.21}$$

where $l(t)$ was the instantaneous length of the window during the flow. The rate of strain is

$$\dot{\varepsilon} = \frac{d\varepsilon(t)}{dt} \quad . \tag{3.22}$$

Substituting for $\varepsilon(t)$ from Equation (3.21) into Equation (3.22),

$$\dot{\varepsilon} = \frac{1}{l_o}\frac{dl(t)}{dt} \quad . \tag{3.23}$$

In Equation (3.23), dl/dt can be replaced by $2v_{\|}$:

$$\dot{\varepsilon} = \frac{2v_{\|}}{l_o} \quad . \tag{3.24}$$

Substituting for $v_{\|}$ from Equation (3.20) into Equation (3.24) yields

$$\dot{\varepsilon} = \frac{4\pi r \mathrm{V}}{l_o} \quad . \tag{3.25}$$

The measured radius of the roller was 2.86 cm and taking l_o was 1cm, $\dot{\varepsilon}$ becomes

$$\dot{\varepsilon} = (35.94)\mathrm{V} \quad . \tag{3.26}$$

The total linear strain can be calculated using Equation (3.26) and Equation (3.22) as:

$$\varepsilon = \int_0^t \dot{\varepsilon} dt = \int_0^t (35.94) \mathrm{V} dt = \frac{35.94}{25000} \cdot \frac{\mathrm{D}}{\mathrm{t}} \int_0^t dt = \frac{35.94}{25000} \cdot \frac{\mathrm{D}}{t} \cdot \mathrm{t} \quad .$$

Further simplification leads to

$$\varepsilon = (1.44 \times 10^{-3})\mathrm{D} \quad . \tag{3.27}$$

From Equation (3.26) and Equation (3.27), it can be noted that $\dot{\varepsilon}$ was a function of the roller speed, and the total strain, ε, was dependent on the number of steps through which a roller rotated.

§ 3.3(b.4) (*ii*) Actual $\dot{\varepsilon}$ and ε

The actual total strain experienced by the sample (not the same as obtained from X-Language commands) was:

$$\varepsilon_{actual} = \frac{l - l_o}{l_o} \quad . \tag{3.28}$$

The rate of strain can be written as

$$\dot{\varepsilon}_{actual} = \frac{d\varepsilon}{dt} = \frac{\varepsilon_{actual}}{t_{actual}} \quad . \tag{3.29}$$

where t_{actual} is the actual time of the elongation. To determine ε_{actual} using Equation (3.28), the length l of the window of exposure on the sample was measured after the experiment was performed[7]. This procedure has been observed to yield values that are different from ε in Equation (3.27). Consequently the values of $\dot{\varepsilon}$ (Equation (3.26)) and $\dot{\varepsilon}_{actual}$ also differ from each other. Since ε and $\dot{\varepsilon}$ could be determined from the X-

Language commands without actually measuring the sample, it would be reasonable to rename them as ε_{th} and $\dot{\varepsilon}_{th}$ respectively. Differences between the theoretical values and those determined experimentally will be discussed in Chapter IV.

§ 3.4 Observation of Flow-Induced Crystallization using Linear Dichroism

Although, HDPE is clearly birefringent at 488 nm., the polymer may also be dichroic at the same wavelength. In Kakani's study of FIC, only birefringence was utilized. Since the sample displays strong birefringence, it becomes difficult to isolate birefringence from dichroism for this sample. For this reason, the optical train was modified as was described in § 3.1(a) to give both birefringence and dichroism.

Transmittance for the optical path including the polarizer and the analyzer (beam A) is given by[1] :

$$\frac{I_b}{I_o} = \frac{e^{-A_e}}{4}\left(\cosh \kappa - \cos \delta\right)\sin^2[2(\alpha - \chi)] \quad . \tag{3.30}$$

The optical path without the analyzer (beam B) yields the transmittance[1] expressed as

$$\frac{I_d}{I_o} = \frac{e^{-A_e}}{2}\left(\cosh \kappa - \sinh \kappa \cos[2(\alpha - \chi)]\right) \quad , \tag{3.31}$$

where A_e is the absorbance, and κ is a quantity similar to retardance δ, called the extinction coefficient. A_e and κ can be written as

$$A_e = \frac{\pi L}{\lambda_0}\left(n'_{\perp} + n'_{\parallel}\right) \tag{3.32a}$$

and $$\kappa = \frac{\pi L}{\lambda_0}\left(n'_{\perp} - n'_{\parallel}\right) \quad , \tag{3.32b}$$

where n' is the imaginary term of the complex refractive index. I_b and I_d are the intensities of beams A and B, respectively. In equations (3.30) and (3.31) α is the angle between the optic axis of the sample and the polarization axis, and χ is the angle between the x-axis of the reference frame (in this case the frame of the laboratory in Cartesian coordinates) and $x_{\parallel}$ of the sample. In the present work, $\alpha = 45°$; $\chi = 0°$.

Using Equation (3.30) and (3.31), the following equations can be obtained:

$$A_e = ln\left(\frac{(cos\delta)/2}{\frac{1}{(I_o/2)}\left(\frac{I_d}{2} - I_b\right)}\right) \tag{3.33}$$

$$\kappa = ln\left\{\frac{B \pm \sqrt{B^2 - 4}}{2}\right\} \quad , \tag{3.34}$$

where $$B = 2e^{A_e}\left(\frac{\left(I_b + \frac{I_d}{2}\right)}{(I_o/2)} + cos\ \ \delta\right) \quad .$$

Derivation of Equation (3.33) and (3.34) from Equation (3.30) and (3.31) is given in APPENDIX A2. As A_e and κ are functions of time dependent intensities (I_b and I_d) and retardance δ, Equation (3.33) and (3.34) could give time dependent profiles of A_e and κ.

In the case of birefringence, retardance, δ is a measure of the difference in the real part of refractive indices, whereas κ is the measure of difference in the imaginary part of the refractive indices. In the analysis of the data obtained from experiments using

dichroism, κ is plotted as a function of time, just as δ was plotted as a function of time in the birefringence measurements.

§ 3.4 Conclusion

The experimental setup coupled with the new methods to analyze the data, were utilized, for a better understanding of flow-induced crystallization kinetics. A preliminary study of dichroism in HDPE was also conducted. The methods discussed in this chapter were implemented, and the results are presented in Chapter IV.

CHAPTER IV

RESULTS AND DISCUSSION

This chapter presents the analysis of the experimental data and a discussion of the results obtained. Kakani's[7] data were re-analyzed using the modified method of data analysis, described in Chapter III. A series of experiments were performed according to the new experimental procedure. The results obtained showed consistency in the values of the Avrami exponents. A comparison of the results obtained with those from the model proposed by Mendes[6] showed qualitative agreement. Experimental observations of FIC using linear dichroism are also presented.

§ 4.1 Characterization of FIC

Isothermal, flow-induced crystallization can be characterized by determining the values of n and k under specified experimental conditions. Temperature and undercooling play an important role, since k is a function of temperature. The thickness of the sample affects the retardance and consequently the values of n and k. Strain (ε) and the rate of strain ($\dot{\varepsilon}$) do not appear in the calculation for n and k. However, every

FIC experiment has a specified set of ε and $\dot{\varepsilon}$ and hence their influence on n and k. In this section, the factors affecting FIC and the results obtained are discussed.

§ 4.1(a) n and k Values Using the New Method

Kakani's intensity data[7] for nineteen runs were re-analyzed. The results are shown in Table 4.A. APPENDIX B contains the corresponding Avrami plots. The values of ε, $\dot{\varepsilon}$ and t in Table 4.A are shown as reported by Kakani[7]. The values for each run in Table 4.A were determined from the X-Language commands. As discussed in Chapter III, the values of ε, $\dot{\varepsilon}$ and t have significant errors.

Kakani observed birefringence at four locations chosen at random on the sample. In Table 4.A, the locations are labeled as (1), (2), (3) and (4). However, the Avrami exponents (n) and coefficients (k) shown in Table 4.A were determined using the new method described in § 3.3 (b.1). The n values were found to be close to, or slightly greater than 1. For most runs, the k values were consistent within a given experiment. However, since the temperature at each location was not reported,[7] it is difficult to ascertain the consistency in the k values throughout the sample.

In Kakani's method of data analysis, the n and k values were an average over all four of the locations. In order to draw a comparison with Kakani's data, the n and k values in Table 4.A, determined using the new method, were also averaged. The results are listed in Table 4.B. Kakani's n values were less than one, typically ranging from ~0.2 to ~0.9. However, the Avrami theory predicts the values of n must be greater than or

TABLE 4.A

The Avrami Exponent and Index, at Random Locations on the Sample Obtained by Re-Analyzing Kakani's[7] Data

Experimental Run[7]	Location on the sample	Avrami Exponent n	Avrami Coefficient $k \times (10^4)$ $\{sec^{-n}\}$
D1	(1)	1.42	2.5
$\varepsilon = 3.80$	(2)	1.42	2.5
$\dot{\varepsilon} = 0.76$ / sec	(3)	1.42	2.5
t = 5.00 sec	(4)	1.42	2.5
D2	(1)	1.30	5.0
$\varepsilon = 3.60$	(2)	1.30	5.0
$\dot{\varepsilon} = 0.72$ / sec	(3)	1.30	5.0
t = 5.00 sec	(4)	1.30	5.0
D3	(1)	1.12	8.0
$\varepsilon = 2.90$	(2)	1.12	8.0
$\dot{\varepsilon} = 0.29$ / sec	(3)	1.12	8.0
t = 10.0 sec	(4)	1.12	8.0
D4	(1)	1.30	15
$\varepsilon = 3.40$	(2)	1.30	15
$\dot{\varepsilon} = 1.70$ / sec	(3)	1.30	15
t = 2.00 sec	(4)	1.30	20
D5	(1)	1.10	20
$\varepsilon = 3.35$	(2)	1.00	25
$\dot{\varepsilon} = 1.68$ / sec	(3)	1.00	18
t = 1.99 sec	(4)	1.10	19
D6	(1)	1.00	15
$\varepsilon = 3.20$	(2)	1.00	24
$\dot{\varepsilon} = 0.32$ / sec	(3)	1.00	24
t = 10.0 sec	(4)	1.00	28
D7	(1)	1.20	32
$\varepsilon = 4.0$	(2)	1.15	39
$\dot{\varepsilon} = 4.00$ / sec	(3)	1.15	39
t = 1.00 sec	(4)	1.15	33
D8	(1)	1.35	17
$\varepsilon = 3.30$	(2)	1.33	28
$\dot{\varepsilon} = 3.00$ / sec	(3)	1.35	20
t = 1.00 sec	(4)	1.35	22
D9	(1)	1.00	12.5
$\varepsilon = 3.20$	(2)	1.00	12.5
$\dot{\varepsilon} = 0.16$ / sec	(3)	1.00	12.5
t = 20.0 sec	(4)	1.00	12.0

Table 4 A continued....

D10	(1)	1.00	35
$\varepsilon = 4.06$	(2)	1.00	35
$\dot{\varepsilon} = 0.21/\text{sec}$	(3)	1.00	35
t = 19.3sec	(4)	1.00	25
D11	(1)	1.35	2.0
$\varepsilon = 3.60$	(2)	1.35	2.0
$\dot{\varepsilon} = 0.16/\text{sec}$	(3)	1.35	2.0
t = 22.5 sec			
D12	(1)	1.00	35
$\varepsilon = 3.80$			
$\dot{\varepsilon} = 3.80/\text{sec}$			
t = 1.00 sec			
D13	(1)	1.00	35
$\varepsilon = 2.47$			
$\dot{\varepsilon} = 3.36/\text{sec}$			
t = 0.74 sec			
D14	(1)	1.38	3.0
$\varepsilon = 2.25$	(2)	1.34	2.5
$\dot{\varepsilon} = 3.38/\text{sec}$	(3)	1.36	3.0
t = 0.67 sec	(4)	1.36	3.0
D15	(1)	1.00	90
$\varepsilon = 3.61$	(2)	1.00	150
$\dot{\varepsilon} = 4.51/\text{sec}$			
t = 0.80 sec			
D16	(1)	1.00	4.5
$\varepsilon = 3.00$	(2)	1.25	2.5
$\dot{\varepsilon} = 5.97/\text{sec}$	(3)	1.25	2.7
t = 0.50 sec			
D17	(1)	1.50	2.4
$\varepsilon = 2.37$	(2)	1.50	3.0
$\dot{\varepsilon} = 3..95/\text{sec}$	(3)	1.45	2.4
t = 0.60 sec			
D18	(1)	1.10	9.5
$\varepsilon = 3.03$	(2)	1.10	8.5
$\dot{\varepsilon} = 6.06/\text{sec}$	(3)	1.10	8.5
t = 0.50 sec	(4)	1.10	8.5
D19	(1)	1.10	15
$\varepsilon = 2.44$	(2)	1.05	19
$\dot{\varepsilon} = 4.06$ sec	(3)	1.05	19
t = 0.60 sec	(4)	1.05	17

TABLE 4.B

Comparison of the n and k Values Obtained by Kakani's[7] Method and the Improved Method

Experiment[7]	Kakani's		New		ε	$\dot{\varepsilon}$ (s^{-1})	t(s)
	n	$k \times 10^4$ (sec^{-n})	n	$k \times 10^4$ (sec^{-n})			
D1	0.94	60	1.42	2.50	3.80	0.76	5.00
D2	0.57	600	1.30	5.00	3.60	0.72	5.00
D3	0.37	2200	1.12	8.00	2.90	0.29	10.0
D4	0.27	4800	1.30	16.3	3.40	1.70	2.00
D5	0.50	600	1.05	20.5	3.35	1.68	1.99
D6	0.67	200	1.00	22.8	3.20	0.32	10.0
D7	0.19	7400	1.16	35.8	4.00	4.00	1.00
D8	0.19	7700	1.35	21.8	3.30	3.30	1.00
D9	0.46	900	1.00	12.4	3.20	0.16	20.0
D10	0.42	1600	1.00	32.5	4.06	0.21	19.3
D11	0.69	150	1.35	2.00	3.60	0.16	22.5
D12	0.84	140	1.00	35.0	3.80	3.80	1.00
D13	0.79	170	1.00	35.0	2.47	3.36	0.74
D14	0.47	1200	1.36	2.90	2.25	3.38	0.67
D15	0.29	4600	1.00	120	3.61	4.51	0.80
D16	0.24	7800	1.17	3.20	3.00	5.97	0.50
D17	0.45	1600	1.48	2.60	2.37	3.95	0.50
D18	0.22	9500	1.10	8.80	3.03	6.06	0.50
D19	0.76	150	1.06	17.5	2.44	4.06	0.60

equal to 1 (Table 2.A). The values of k reported by Kakani show a wide range of values, ranging over two orders of magnitude. Whereas, the k values obtained from the new method range over less than one order of magnitude. Tables 4.A and 4.B demonstrate that the new method of analysis gives more consistent and reasonable values of n and k than were obtained with Kakani's method.

In this investigation, the onset of quiescent crystallization was observed to begin after ~12 to ~15 minutes of the cooling process. Whereas, in Kakani's method, the onset of crystallization was disregarded and the strain was applied after 20 minutes of undercooling. The values n in Table 4.A, being greater than 1, may indicate a combination of quiescent (two or three dimensional crystallization) and linear flow-induced (one dimensional) crystallization.

An additional set of fifteen experiments were performed. The flow was applied as soon as the sample was observed to be completely dark. In this set of experiments, the temperature gradient along the height of the sample was the same as in Kakani's experiments (Table 4.A). Therefore the crystallization temperature at each location on the sample was different. The values of n and k were determined with materials discussed in § 3.3. The true values of ε and $\dot{\varepsilon}$ were determined. The locations for observation of birefringence were chosen along the height of the sample as is listed in Table 4.C. The results are shown in Table 4.D. The graphs of this set of experiments are included in APPENDIX C.

The n values in Table 4.D are close to unity indicating linear crystal growth in the sample. Within a given experiment, the k-values showed an increase from the top to the bottom of the sample. Sakaguchi's[23] observation of change in k values with the

TABLE 4.C

Locations of Data Acquisition from Top of the Sample

Experimental Run	Height of the Sample = 20 mm. (mm)			
	(1)	(2)	(3)	(4)
1	3	7	11	16
2	3	8	12	16
3	5	10	13	16
4	4	10	12	16
5	2	6	11	16
6	3	8	13	16
7	3	7	12	17
8	3	6	9	15
9	7	11	13	15
10	3	6	9	11
11	3	7	10	13
12	2	6	10	12
13	3	7	12	17
14	2	7	11	12
15	3	7	9	15

TABLE 4.D

Characterizing Flow-Induced Crystallization using the Avrami Coefficients

Experimental Run APPENDIX C	Location on the sample from top to bottom (mm)	Avrami Exponent n	Avrami Coefficient $k \times (10^4)$ (sec^{-n})
1	3	0.95	33.0
$\varepsilon = 3.74$	7	0.95	48.0
$\dot{\varepsilon} = 0.604$ / sec	11	0.95	60.0
t = 5.5sec	16	0.93	100
2	3	0.93	55.0
$\varepsilon = 3.03$	8	0.93	45.0
$\dot{\varepsilon} = 0.658$ / sec	12	0.93	65.0
t = 4.5 sec	16	0.93	54.0
3	5	1.00	8.00
$\varepsilon = 2.71$	10	1.00	8.00
$\dot{\varepsilon} = 0.774$ / sec	13	1.00	7.00
t = 3.5 sec	16	1.00	7.00
4	4	0.95	30.0
$\varepsilon = 2.62$	10	0.95	30.0
$\dot{\varepsilon} = 0.749$ / sec	12	0.95	20.0
t = 3.5 sec	16	0.95	30.0
5	2	0.77	40.0
$\varepsilon = 3.38$	6	0.77	40.0
$\dot{\varepsilon} = 3.073$ / sec	11	0.77	55.0
t = 1.1 sec	16	0.77	65.0
6	3	1.00	50.0
$\varepsilon = 3.07$	8	1.00	50.0
$\dot{\varepsilon} = 4.386$ / sec	13	1.00	55.0
t = 0.7 sec	16	1.00	60.0
7	3	0.80	100
$\varepsilon = 3.14$	7	0.80	65.0
$\dot{\varepsilon} = 6.826$ / sec	12	0.70	320
t = 0.46 sec	17	0.70	250
8	3	1.00	52.0
$\varepsilon = 3.52$	6	1.00	55.0
$\dot{\varepsilon} = 7.040$ / sec	9	1.00	55.0
t = 0.5 sec	15	0.80	120

Table 4 D continued...

Experimental Run APPENDIX C	Location on the sample from top to bottom	Avrami Exponent n	Avrami Coefficient $k \times (10^4)$ (sec^{-n})
9	7	1.00	48.0
$\varepsilon = 3.35$	11	1.00	25.0
$\dot{\varepsilon} = 1.117$ / sec	13	0.90	42.0
t = 3.0 sec	15	0.80	70.0
10	3	0.90	20.0
$\varepsilon = 3.18$	6	0.85	30.0
$\dot{\varepsilon} = 1.223$ / sec	9	0.80	60.0
t = 2.6 sec	11	0.75	150
11	3	0.85	71.0
$\varepsilon = 2.85$	7	0.70	150
$\dot{\varepsilon} = 6.196$ / sec	10	0.70	100
t = 0.46 sec	13	0.70	100
12	2	1.39	12.0
$\varepsilon = 3.90$	6	1.39	11.0
$\dot{\varepsilon} = 4.875$ / sec	10	1.39	10.0
t = 0.8 sec	12	1.39	8.00
13	3	0.90	25.0
$\varepsilon = 2.72$	7	0.90	25.0
$\dot{\varepsilon} = 0.777$ / sec	12	0.90	25.0
t = 3.5 sec	17	0.90	30.0
14	2	0.75	75.0
$\varepsilon = 3.81$	7	0.75	75.0
$\dot{\varepsilon} = 5.687$ / sec	11	0.75	85.0
t = 0.67 sec	12	0.75	100
15	3	0.90	95.0
$\varepsilon = 4.07$	7	0.90	60.0
$\dot{\varepsilon} = 5.814$ / sec	9	0.90	50.0
t = 0.7 sec	15	0.90	65.0

crystallization temperature, T_c, can be noted in Figure 2.13(b). An increase in the values of k was observed with temperature, typically within the same order of magnitude, until a critical value of T_c was reached. This the trend observed in Table 4.D for k values. The critical value of T_c, however, has not been investigated in this work.

A set of eight experiments was performed with the temperature variation minimized to ~ 1.0 - 2.0 °C from the top to the bottom of the sample. The methods described in Chapter III were used to determine ε, $\dot{\varepsilon}$, t, n and k. Table 4.E summarizes the results of this set of experiments. APPENDIX D illustrates the intensity and Avrami plots of the experiments. The results showed that as for the series in Table 4.D, $n \sim 1$ for experiments in Table 4.E, indicating that the Avrami exponent is independent of temperature. The k-values in each experiment were consistent with one another within the same order of magnitude. However, within a particular sample, the values of k were observed to show an decrease from the top to the bottom.

From the three set of experiments listed in Table 4.A, Table 4.D, Table 4.E, respectively, the following conclusion can be drawn. The Avrami exponent is independent of temperature and is $\cong$ 1. The k values are consistent within a given experiment, especially when the sample is well insulated (Table 4.E). Therefore, k values are sensitive to temperature.

A factor that has not been considered in Table 4.A, Table 4.D and Table 4.E is thickness variations along the height of the sample. Schultz[21], through his model, expressed that thin samples show a lower rate of crystallization, which in turn was interpreted as being responsible for lower values of k.[23] This proposal of how the k values can be affected by a thickness change in the sample may have implications on the

TABLE 4.E

The Values of Avrami Coefficients and Exponents for Experiments with a Reduced Temperature Gradient

Experimental Run APPENDIX D	Location on the sample from top to bottom	Avrami Exponent n	Avrami Coefficient $k \times (10^4)$ (sec^{-n})
1	(1)	0.95	8.0
$\varepsilon = 6.20$	(2)	0.95	7.0
$\dot{\varepsilon} = 7.75/sec$			
$t = 0.8 sec$			
2	(1)	0.95	60.0
$\varepsilon = 5.98$	(2)	0.95	60.0
$\dot{\varepsilon} = 7.47/sec$	(3)	0.95	50.0
$t = 0.8 sec$	(4)	0.95	50.0
3	(1)	0.95	20.0
$\varepsilon = 6.95$	(2)	0.95	20.0
$\dot{\varepsilon} = 7.72/sec$	(3)	0.95	50.0
$t = 0.9 sec$	(4)	0.95	30.0
4	(1)	1.00	200
$\varepsilon = 5.63$	(2)	0.98	180
$\dot{\varepsilon} = 7.04/sec$	(3)	0.98	150
$t = 0.8 sec$	(4)	0.98	120
5	(1)	1.00	50.0
$\varepsilon = 5.50$	(2)	0.90	45.0
$\dot{\varepsilon} = 3.24/sec$	(3)	0.90	40.0
$t = 1.7 sec$			
6	(1)	1.00	15.0
$\varepsilon = 6.25$	(2)	1.00	15.0
$\dot{\varepsilon} = 3.47/sec$	(3)	1.00	15.0
$t = 1.8 sec$	(4)	1.00	15.0
7	(1)	0.95	20.0
$\varepsilon = 6.67$	(2)	0.95	20.0
$\dot{\varepsilon} = 3.34/sec$	(3)	0.99	20.0
$t = 2.0 sec$	(4)		
8	(1)	0.90	130
$\varepsilon = 5.87$	(2)	0.90	200
$\dot{\varepsilon} = 3.26/sec$	(3)	0.90	175
$t = 1.8 sec$	(4)	0.90	150

inconsistency in k values from experiment to experiment. The following section is a discussion on non-uniform deformation and will explore the changes in k values with the thickness of the sample.

§ 4.1(b) Non-Uniform Deformation

One of the factors of prime importance in determining the crystallization kinetics from the experiments is the effect of thickness (L), since the retardance is proportional to the local thickness of the sample (Equation (2.3)). In this section, the validity of the method proposed in § 3.3(b.3) is examined using an experiment (Run **12**) from Table 4.D. Thereafter, the possible applications of the thickness analysis such as, the calculation of n and k values, the induction time and the initial rate of crystallization, are explored in § 4.1(c).

A note can be made regarding the selection of an experiment from Table 4.D rather than Table 4.E. In the experiments listed in Table 4.D the samples were not well insulated compared to the samples for the experiments in Table 4.E. However, the time taken to observe the onset of crystallization in the latter case was longer (~17-30 minutes) than in Experiments listed in Table 4.D (~12-15 minutes). This indicates that the melt state persisted for a longer period in the experiments in Table 4.E. The density of HDPE melt being lower than the density of Silicone oil in the bath caused the sample to rise towards the surface, even after the crystallization temperature of 124.6 °C was reached. Therefore, in many cases, the bottom edge of the sample gradually rose during the course of the experiments. Thus, samples could not retain their original rectangular

shape as in the samples for Table 4.D. Hence, the choice of an experiment from Table 4.D rather than from Table 4.E

Table 4.F lists the thickness measurements in 15 flow-induced crystallized samples, listed in Table 4.D. The thickness was measured using a micrometer. L_o is the calculated thickness in the case of uniform deformation of the sample. For the four locations (1), (2), (3) and (4) from the top to the bottom of the sample, the thickness was observed to have decreased. This section shows the effect of thickness on the data analysis.

Using the algorithm shown in Figure 3.17, four simultaneous equations of the form of Equation (3.17) were solved to obtain values of the four unknowns L_o/L_∞ , α_n , α_{L1} , and α_{L2} shown in Table 4.G. The values obtained were used as initial values for the process of non-linear regression to regenerate the intensity curves obtained from the experimental data. Figures 4.1a, b, c, d show that the curves can be regenerated. The regeneration of the intensity curves supports the use of Equation (3.17) to represent the observed intensity data. Table 4.G indicates that the thickness is not a constant of the experiment and that the deformation is non-uniform.

The time-dependent expression for the thickness

$$\frac{\left(\delta / \delta_\infty\right)}{\left(\frac{L_o}{L_\infty}\left(e^{-\alpha_{L1}t}\right)+\left(1-e^{-\alpha_{L2}t}\right)\right)} = \left(\frac{\Delta n}{\Delta n_\infty}\right) \quad , \tag{3.18}$$

should demonstrate that the elimination of the thickness factor would now cause the $\Delta n / \Delta n_\infty$ curves to overlap. However, the curves, $\Delta n / \Delta n_\infty$ vs. t, did not coincide, as shown in Figure 4.2, indicating non-uniformity due to factors other than thickness. Two of the

TABLE 4.F

Thickness of the Sample from Top to Bottom Numbered in Ascending Order

Experimental Run	Measured Thickness at four Locations on the Sample (cm.) Shown in Table 4.C				ε	L_o at the Cessation of Flow (cm.)
	(1)	(2)	(3)	(4)		
1	0.274	0.137	0.145	0.102	3.74	0.063
2	0.140	0.071	0.038	0.051	3.03	0.074
3	0.155	0.122	0.066	0.061	2.71	0.081
4	0.130	0.070	0.05	0.03	2.62	0.083
5	0.030	0.160	0.07	0.02	3.38	0.069
6	0.074	0.071	0.051	0.031	3.07	0.074
7	0.076	0.061	0.071	0.023	3.14	0.073
8	0.097	0.071	0.058	0.023	3.52	0.067
9	0.064	0.061	0.038	0.023	3.35	0.069
10	0.280	0.100	0.050	Film	3.18	0.072
11	0.120	0.060	0.090	Film	2.85	0.078
12	0.086	0.071	0.061	0.023	3.90	0.061
13	0.060	0.090	0.060	0.050	2.72	0.081
14	0.070	0.080	0.060	Film	3.81	0.062
15	0.292	0.150	0.102	0.043	4.07	0.059

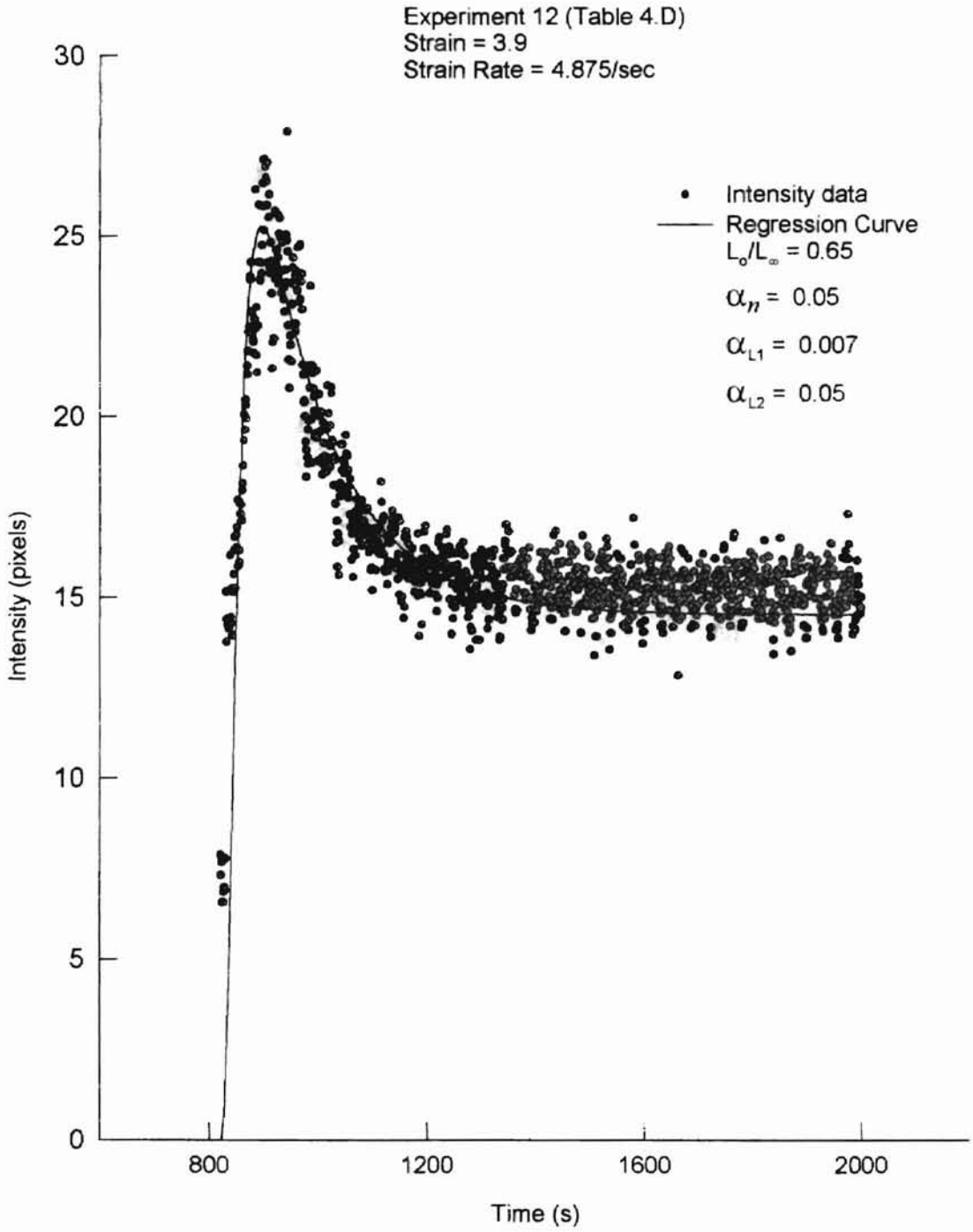

Figure 4.1(a) Regenaration of the Intensity Data by Non-Linear Regression at Location (1)

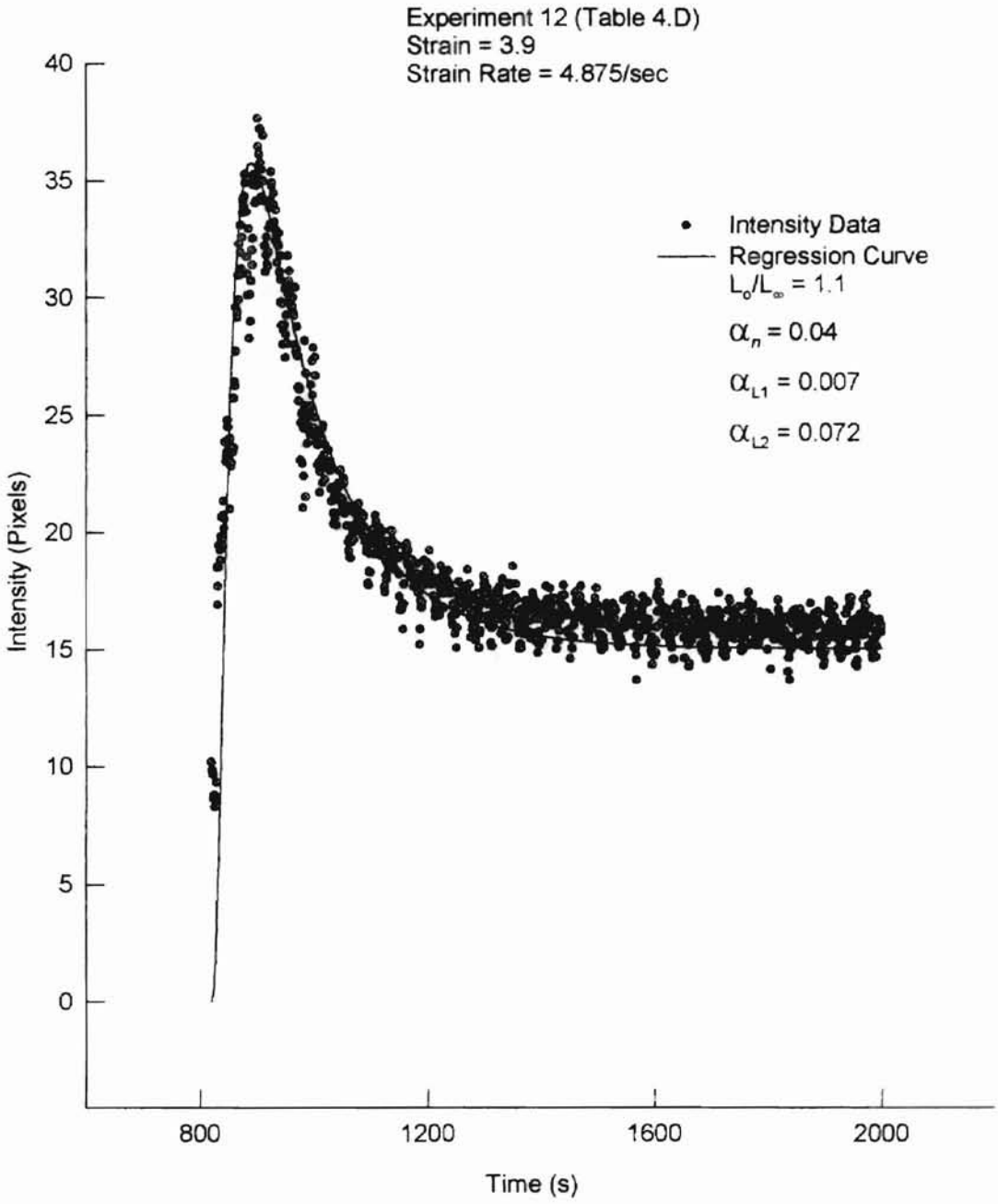

Figure 4.1(b) Regenaration of the Intensity Data by Non-Linear Regression at Location (2)

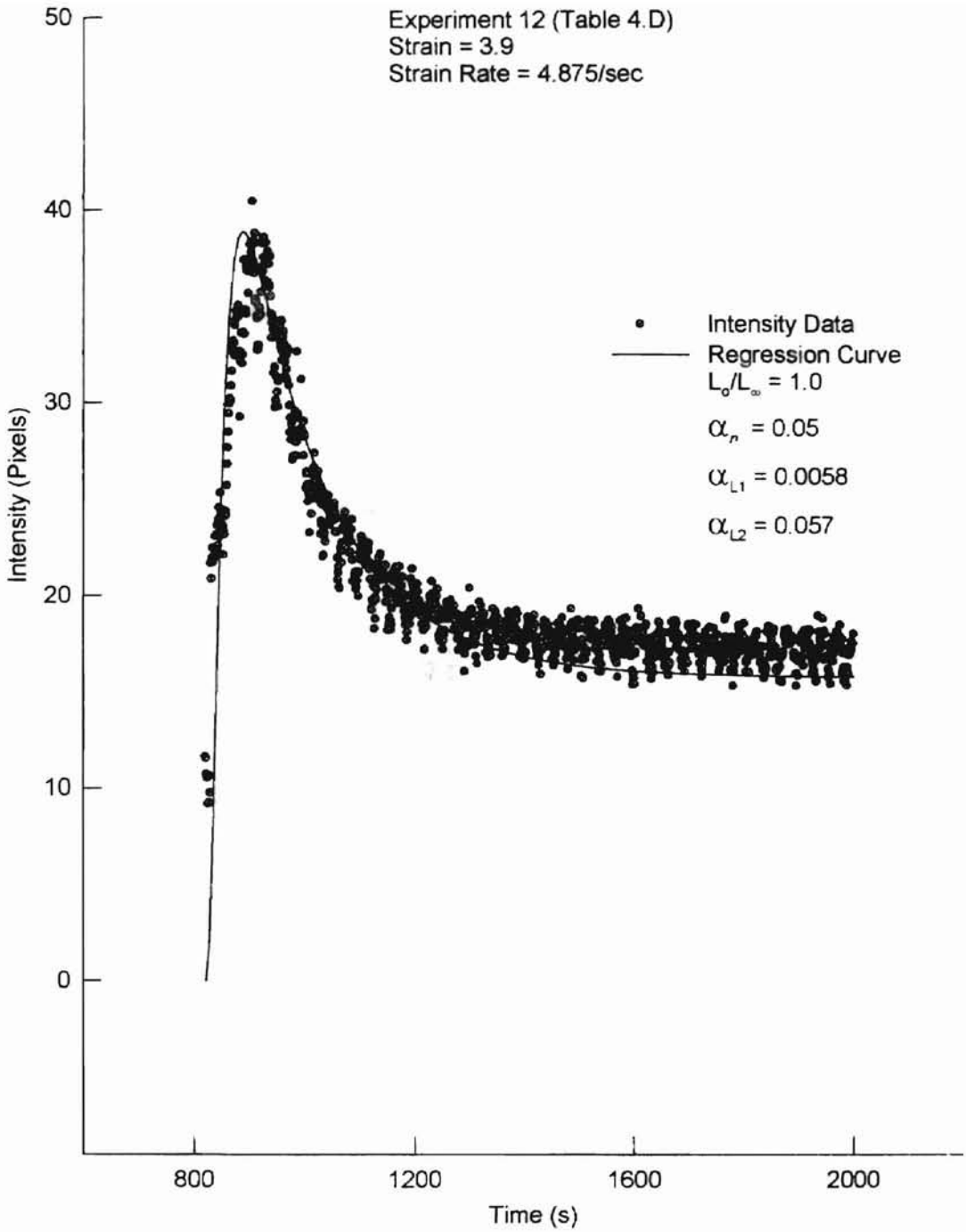

Figure 4.1(c) Regeneration of the Intensity Data by Non-Linear Regression at Location (3)

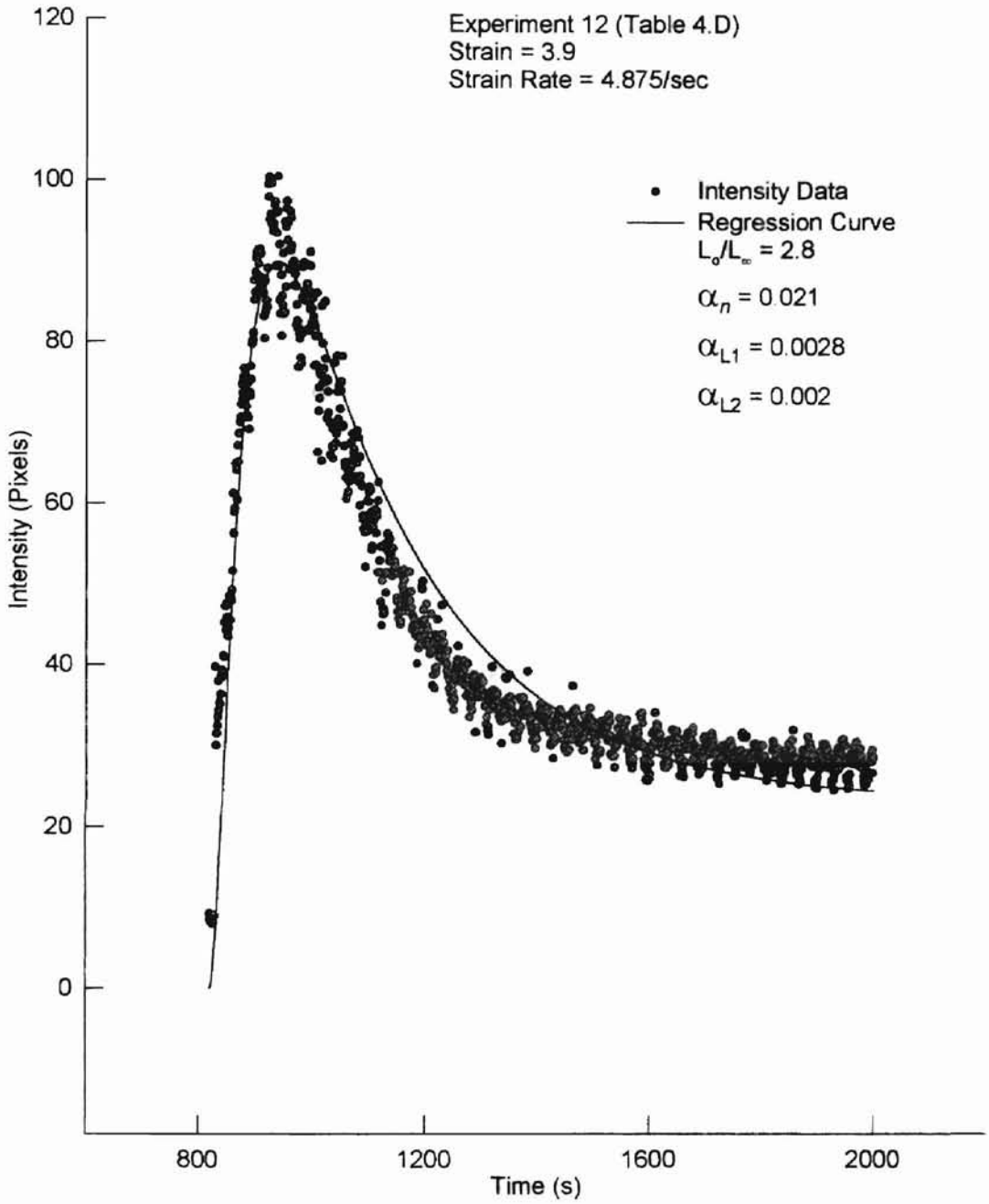

Figure 4.1(d) Regeneration of the Intensity Data by Non-Linear Regression at Location (4)

factors responsible for the non-overlap could be identified as the rates of undercooling and the temperature gradient after reaching the crystallization temperature along the height of the sample.

In this investigation, the lower part of a stretched sample was found to be thin and film-like, whereas the upper part had larger thickness varying from sample to sample. All experiments showed that the thickness of the sample was larger at the top than at the bottom as is indicated in Table 4.C.

TABLE 4.G

Values of Parameters to Reproduce Intensity Patterns for Plots in Figure 4.4a, b, c, d for Experiment **12** (Table 4.D, APPENDIX C)

Plot→	Intensity-(1)*	Intensity-(2)	Intensity-(3)	Intensity-(4)
L_o/L_∞	0.65	1.10	1.00	2.80
α_n	0.0500	0.0400	0.0500	0.0210
α_{L1}	0.0070	0.0070	0.0058	0.0028
α_{L2}	0.0500	0.0720	0.0570	0.0020
Thickness (Qualitative)	Increased by factor of 1.5	Slightly decreased	≈ Constant	Decreased by factor of 3

*The labels (1), (2), (3), (4) represent the locations on the sample from the top to the bottom.

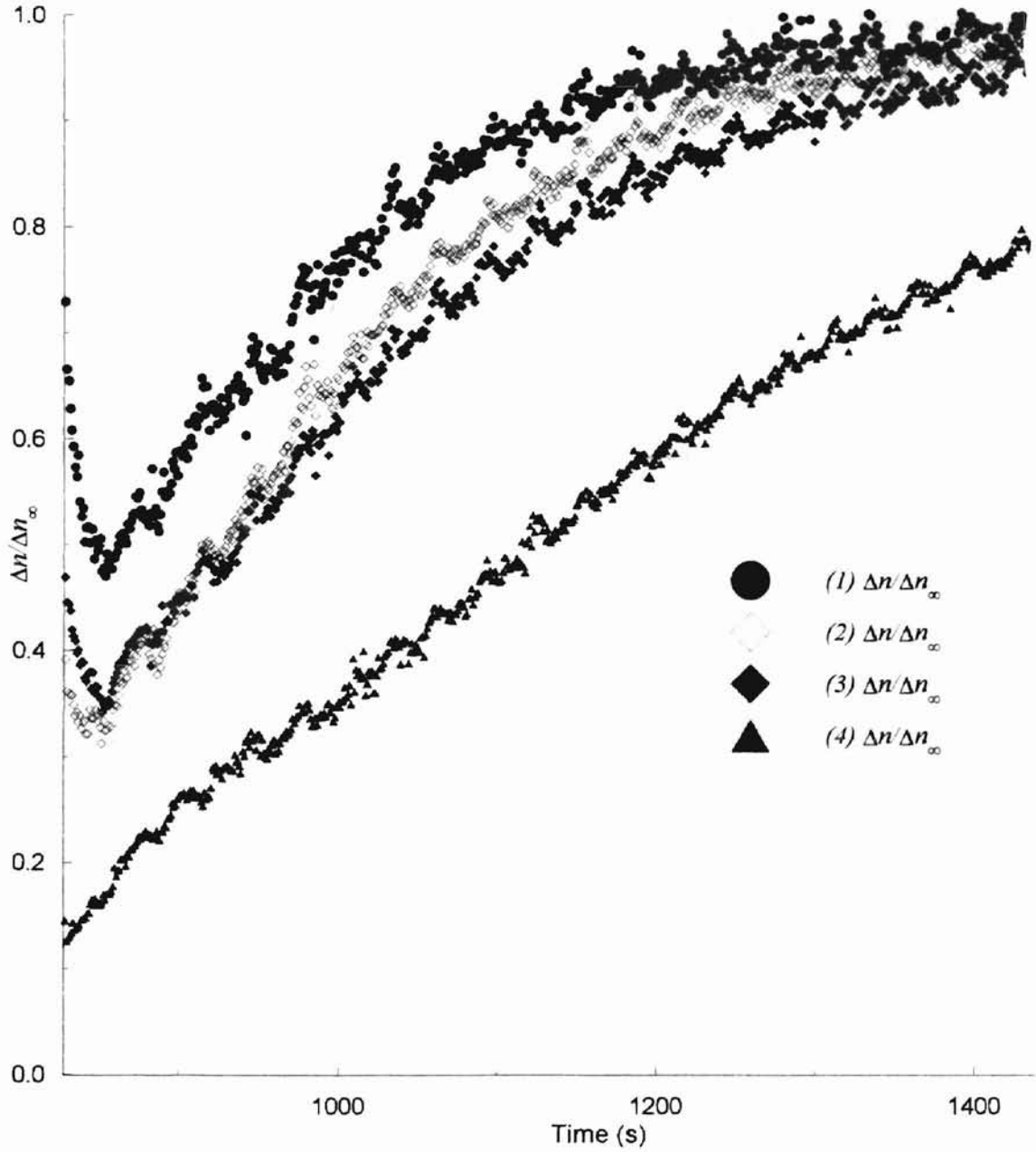

Figure 4.2 Relative Birefringence at the Four Locations
for Experiment 12 (Table 4.D)

§ 4.1(c) n and k Values, Onset of Crystallization and Initial Rate of Crystallization

Isolating the optical activity in the form of birefringence, at each location in the manner described in § 4.1(b), could impart useful information regarding the initial stage of crystallization, the onset of crystallization, and the n and k values.

In Figure 4.3a, b, c, d , the relative birefringence curves $(\Delta n/\Delta n_\infty)$ are plotted. The initial decrease in $\Delta n/\Delta n_\infty$ is due to the peak shown in Figure 3.19 for location (1) for which no logical explanation could be given. Since this feature affects the birefringence curve for less than 200 sec, it was disregarded in the procedure to obtain the values of n and k. The time interval over which $\Delta n/\Delta n_\infty$ approaches unity was ~2500 sec. This was the duration considered to obtain the values of n and k. Using the method of curve fitting to $(1-\Delta n/\Delta n_\infty)$, the n and k values for the four locations for the experiment in Table 4.G were obtained. Table 4.H shows the values obtained at four locations from top to bottom (Table 4.D, Experiment 12). The results show the values of n ~1. The k values show a decrease within the same order of magnitude. However, for this experiment, since the sample was not insulated, the temperature difference could have caused the differences in the values of k.

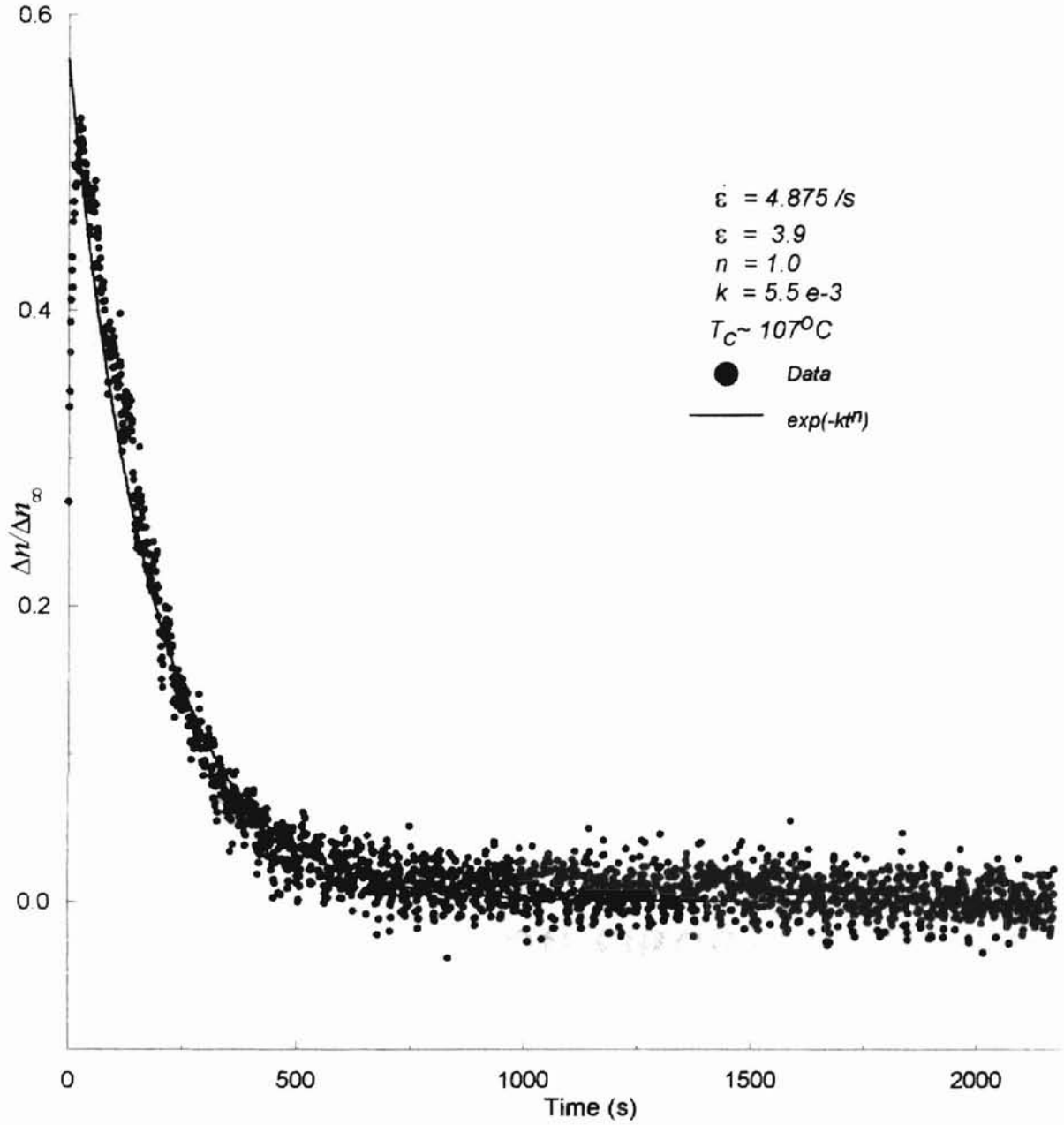

Figure 4.3a Regression Curves for Avrami Equation at Location (1)

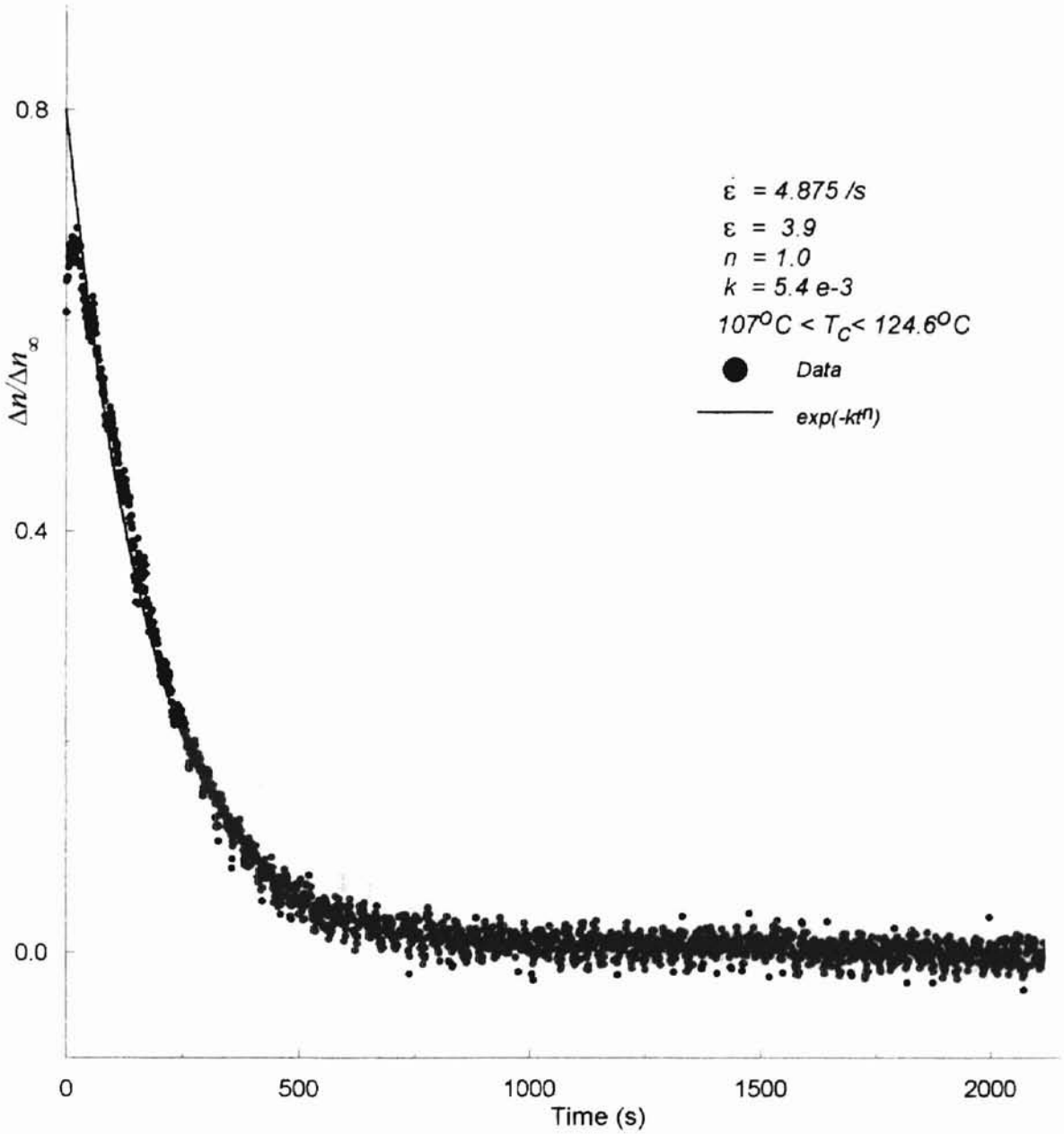

Figure 4.3b Regression Curves for Avrami Equation at Location (2)

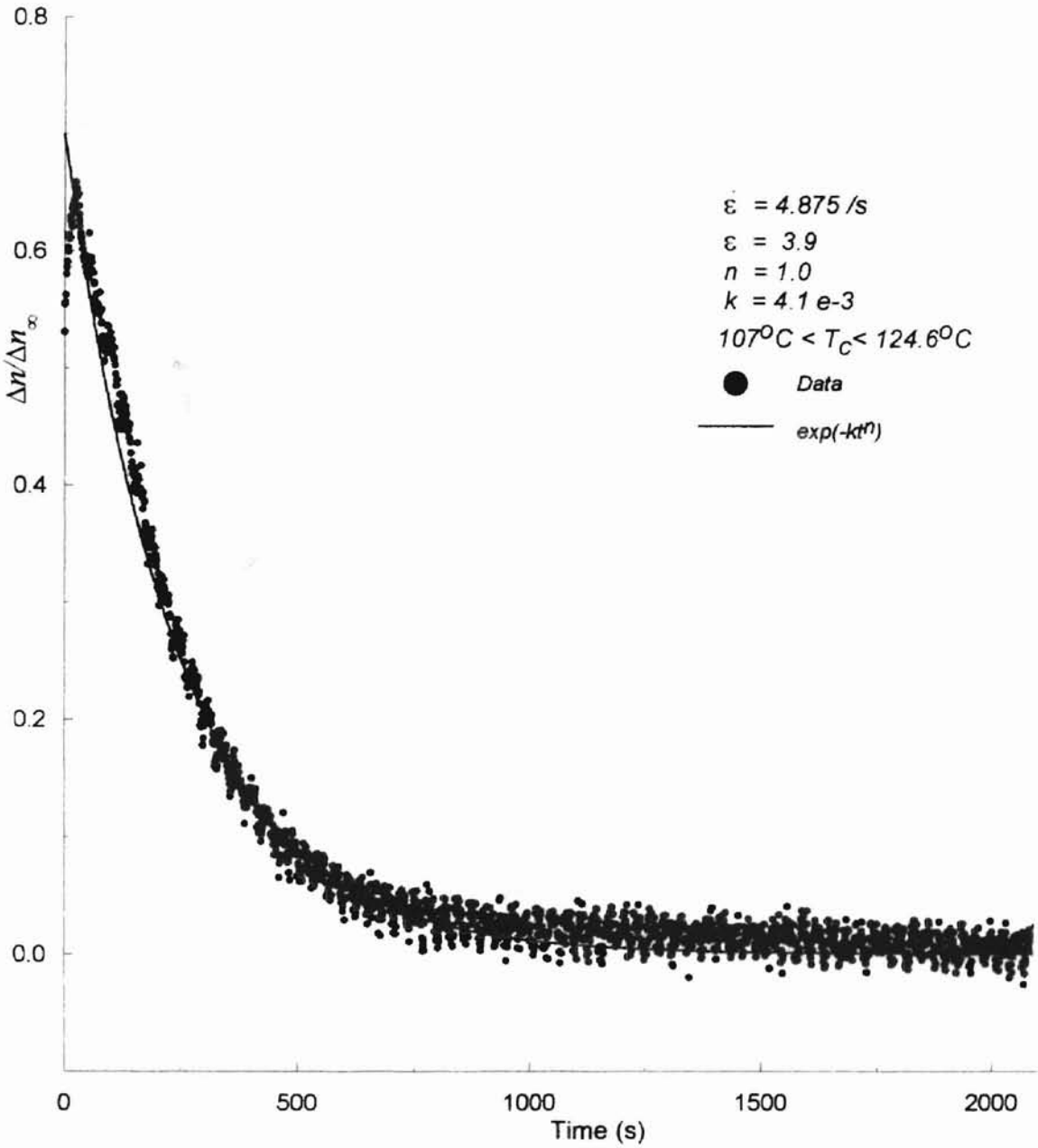

Figure 4.3c Regression Curves for Avrami Equation at Location (3)

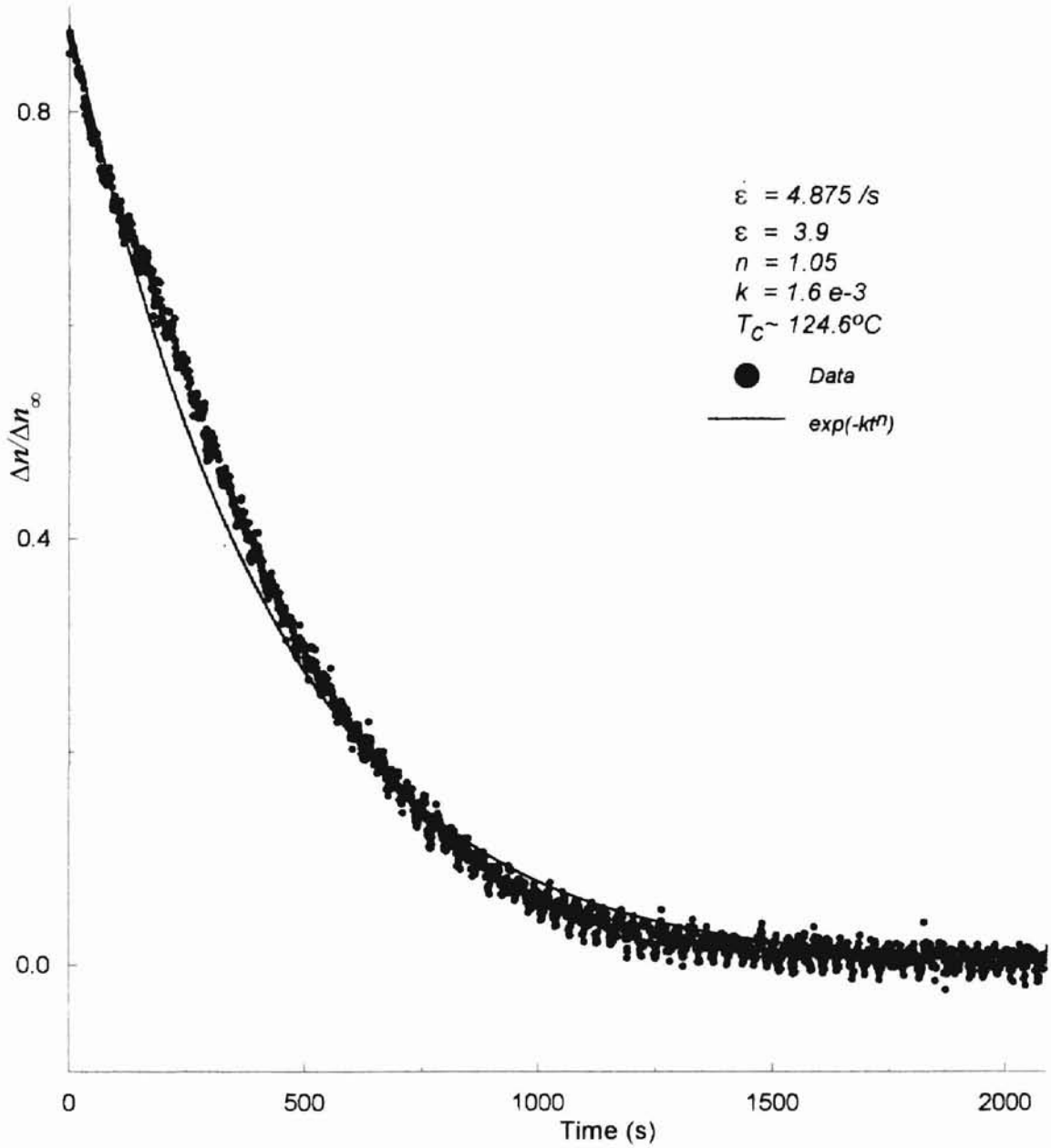

Figure 4.3d Regression Curves for Avrami Equation at Location (4)

TABLE 4.H

n and k Values for the Experiment in Table G
(Experiment **12**: Table 4.D, APPENDIX C)

Location on Sample from Top to Bottom	n	k (sec^{-n})
(1)	1.0	0.0055
(2)	1.0	0.0054
(3)	1.0	0.0041
(4)	1.05	0.0016

In order to establish how the birefringence plots could be used to estimate the time of onset of crystallization at each location of observation, each birefringence curve could be regressed to fit the form of the Avrami curve with $n = 1$, as obtained from Table 4.H:

$$\frac{\Delta n}{\Delta n_{\infty}} = 1 - e^{-kt}, \qquad (4.1)$$

where k is the characteristic time constant proportional to the rate at which the maximum value of $\Delta n/\Delta n_{\infty}$ could be reached. Figure 4.4 shows the regression curves along with the $\Delta n/\Delta n_{\infty}$ plots at each location. The regression curves when extrapolated to intercept the 'Time' axis yield the time of the onset of anisotropic behavior at a given location. In Figure 4.5 the regression curves in Figure 4.4 are re-plotted for clarity. The reference

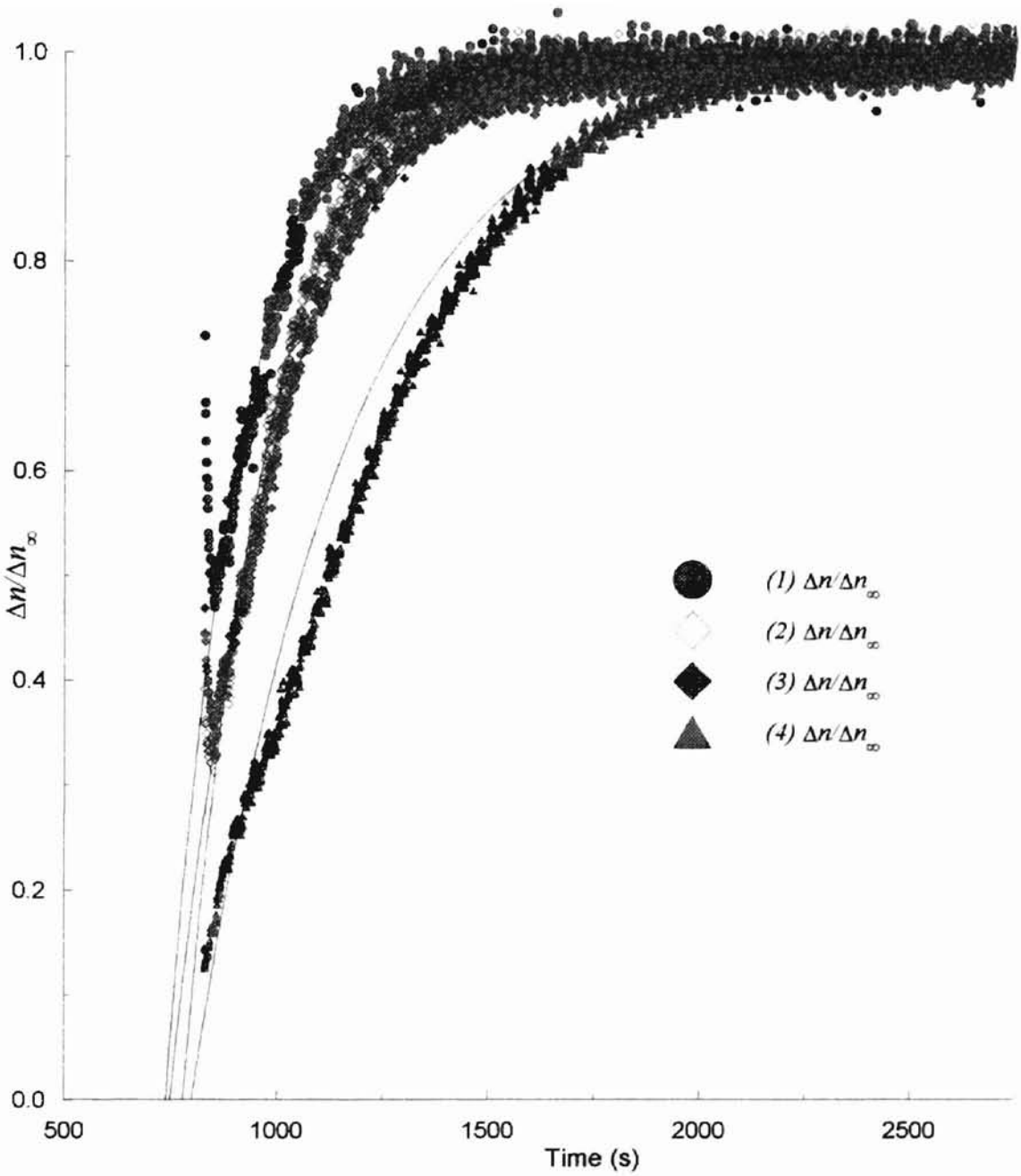

Figure 4.4 Regression Curves for Relative Birefringence Plots at Each Location for Experiment 12 (Table 4.D)

time with respect to which the time of the onset of crystallization was determined was, the time at which the thermostat was reset from 134 °C to 124.6 °C.

From Figure 4.5, information could also be obtained regarding the initial slope of crystallization and its variation with time. Table 4.I indicates that although crystallization at location (3) started earlier than at (2), the initial slope at location (2) was larger than at (3). The initial slope for the observation points decreased from top to bottom. Furthermore, the values of k indicate that the overall rate of crystallization is larger at the top than at the bottom.

Combining the information in Table 4.G, Table 4.I and Table 4.F, it could be concluded that the rate of crystallization was higher in the upper region of the sample where the sample was significantly thicker, than at the bottom where the sample was thin. This is in agreement with the observations made by Schultz[21] about the crystallization in bulk being more rapid than in samples of small thickness.

TABLE 4.I

Information Regarding the Onset of Crystallization and Initial Slope for Experiment **12** (Table 4.D, APPENDIX C)

Location from Top to Bottom	k (sec^{-1})	Onset of Crystallization, t_c Strain Applied at 13.83 (minute)	$d(\Delta n/\Delta n_\infty)/dt$ (sec^{-1}) Initial Slope at $\Delta n/\Delta n_\infty = 0.267$
(1)	0.0055	12.33	4.81e-3
(2)	0.0054	13.00	4.30e-3
(3)	0.0041	12.50	3.44e-3
(4)	0.0027	13.33	2.32e-3

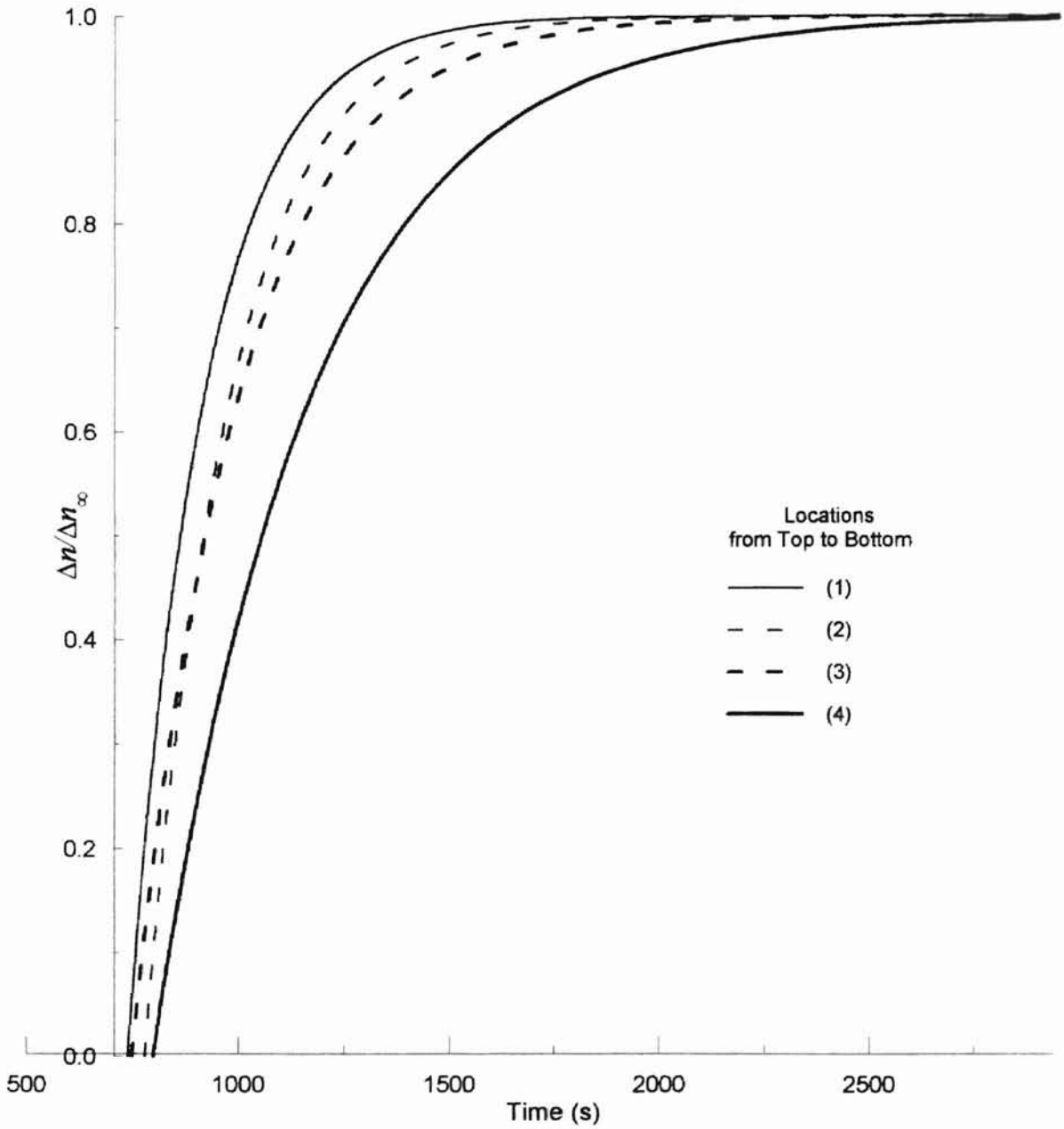

Figure 4.5 Regressed Relative Birefringence at Four Locations in Figure 4.4

Values of induction time at the four positions were also determined using Figure 4.5. From Table 4.J, it can be seen that, the induction time, τ, shows a increasing trend from the top of the sample to the bottom. The temperature was found to increase from the top to the sample to the bottom. The trend of τ increasing with temperature (with the exception of location (3), agrees with the observations made by Lednický and Muchová[19] and Wang and Lui[20].

TABLE 4.J

Induction Time (τ) at four locationson the Sample for Experiment **12** (Table 4.D, APPENDIX C)

Location	Induction Time, τ		
	t when T_c is reached (s)	t_c (s)	$\tau = t_c - t$ (s)
(1)	720	740	20
(2)	720	780	60
(3)	720	750	30
(4)	720	800	80

*t_c represents the time of the onset of crystallization.

The discussion demonstrates that important information regarding characteristics of flow-induced crystallization could be obtained. The induction time is primarily useful

in determining the initial time of crystallization. Thus simplifying the retardance curves by eliminating the thickness the sample, could be used to study several properties of FIC.

§ 4.1(d) Strain and Rate of Strain

Characterization of FIC also relies on the rate of strain and the total strain experienced by the sample. The non-uniform deformation discussed in §4.1(c) introduces error in the measurement of the total strain and subsequently, the rate of strain. The following discussion assesses the sources of error in the measurement of the total strain.

Kakani[7] observed the video recording to determine the distance between the foil edges on either side of the sample window. The separation between the edges at the cessation of flow was *l*. The actual total strain was then calculated using Equation (3.18). The experimentally determined strain was then divided by $\mathbf{t}_{th}$, the time obtained from the X-Language using Equation (3.16). In the calculation of ε_{actual}, Kakani assumed that the portion of the sample wrapped in the aluminum foil adhered to the foil and did not stretch. In the present work, however, it was noted that the portion of the sample beneath the edge of the foil outlining the exposed area was affected by the flow field. Therefore, the foil around the edges of the exposed window was peeled off to determine the actual value of *l*.

Table 4.K shows the input parameters of the X-Language commands which governed the rotating action of the Compumotor. Strain (ε_{th}) and the rate of strain ($\dot{\varepsilon}_{th}$)

TABLE 4.K

Calculation of Elongation and Rate of Strain from the X-Language Commands

Experimental Run	**D** (step)	**V** (rev/sec)	**t** (sec)	ε_{th}	$\dot{\varepsilon}_{th}$ (sec^{-1})
1	2500	0.025	4.0	3.594	0.899
2	2500	0.050	2.0	3.594	1.797
3	2500	0.040	2.5	3.594	1.438
4	2500	0.040	2.5	3.594	1.438
5	2500	0.100	1.0	3.594	3.594
6	2500	0.200	0.5	3.594	7.188
7	2500	0.500	0.2	3.594	17.97
8	2500	0.400	0.25	3.594	14.38
9	2525	0.050	2.02	3.630	1.797
10	2600	0.040	2.6	3.740	1.438
11	2525	0.500	0.202	3.630	17.97
12	3000	0.200	0.6	4.313	7.188
13	2700	0.040	2.7	3.88	1.438
14	3000	0.300	0.4	4.313	10.78
15	2750	0.200	0.55	3.953	7.188

were calculated from the variables **D**, **V**, and **t**, and were called theoretical values of strain and rate of strain. The total strain had values ranging from 3.5 to 4.4.

The actual values of ε and $\dot{\varepsilon}$ were calculated using the sample after the experiment was completed. The video tapes showed that the duration of the applied flow field extended beyond the time specified by the X-Language commands. This could be attributed to the continued rotation of the rollers despite the X-Language command to stop the rollers. Thus in majority of the cases listed in Table 4. G, $t_{th} < t_{actual}$, where t_{actual} was determined from the video recording. Table 4.L shows that ε_{actual} ranges from ~ 2.6 to ~ 4.1, for a set of experiments conducted in this work, with the average value of ε_{actual} over all the entries being 3.3. In most cases, $\varepsilon_{actual} < \varepsilon_{th}$.

The effect of change in time duration, and the total strain, on the rate of strain using Kakani's data was estimated as follows. In the experiments listed in Table 4.D, each of the samples were found to have elongated by approximately 2 mm under the foil, from the edge on either side of the window. Since the temperature gradient along the height of these sample were the same as in Kakani's experiments listed in Table 4.A, the same extension was assumed beneath the foil for Kakani's samples. Therefore, 4 mm were added to the total extension in Kakani's samples. Likewise, t_{th} used by Kakani to calculate $\dot{\varepsilon}$ was less than t_{actual} as was noted in the experiments listed in Table 4.L and Table 4.D. In Table 4.L, for most cases of $t_{th} > 1$ sec, $t_{actual} - t_{th} > 1$ sec. Therefore, for $t_{th} > 1$ sec in Kakani's experiments, t_{actual} was estimated by adding 1 sec. From Table 4.L, for $t_{th} < 1$ sec, an increase of at least 27% (run **15**) was observed. Thus, as a conservative assumption, 25% was added to Kakani's values of $t_{th} < 1$ sec to obtain t_{actual} . The results

TABLE 4.L

Experimental and Theoretical Values of Strain and Rate of Strain

Experimental Run	t_{th} (sec)	t_{actual} (sec)	ε_{th}	ε_{actual}	$\dot{\varepsilon}_{th}$ (sec^{-1})	$\dot{\varepsilon}_{actual}$ (sec^{-1})
1	4.0	5.5	3.594	3.74	0.899	0.604
2	2.0	4.5	3.594	3.03	1.797	0.658
3	2.5	3.5	3.594	2.71	1.438	0.774
4	2.5	3.5	3.594	2.62	1.438	0.749
5	1.0	1.1	3.594	3.38	3.594	3.073
6	0.5	0.7	3.594	3.07	7.188	4.386
7	0.2	0.46	3.594	3.14	17.97	6.828
8	0.25	0.5	3.594	3.52	14.38	7.04
9	2.02	3.0	3.630	3.35	1.797	1.117
10	2.6	2.6	3 740	3.18	1.438	1.223
11	0.202	0.46	3.630	2.85	17.97	6.196
12	0.6	0.8	4.313	3.9	7.188	4.875
13	2.7	3.5	3.88	2.72	1.438	0.777
14	0.4	0.67	4.313	3.81	10.78	5.687
15	0.55	0.7	3.953	4.07	7.188	5.814

in Table 4.M show that the percent differences, though mostly below 12%, could be as high as ~60%. The cases with high percent differences are those, for which t_{th} ~ 1s. Table 4.M indicates that, the error induced cannot be neglected in certain cases. Since the compumotor did not function as desired, in this investigation, a correlation between the k values and the rate of strain could not be studied. The difference between the actual and the X-Language rate of strain becomes significant in case of comparison with the model developed by Mendes[6], as will be discussed in § 4.4.

In conclusion of § 4.1, the improvements in the method of conducting the birefringence experiments and data analysis can be summarized as follows. A set of fifteen experiments listed in Table 4.D were conducted which corrected for the timing of the application of the flow in Kakani's experiments. A second set of eight experiments (Table 4.E) were performed in which the temperature gradient along the height of the sample was minimized to obtain consistent values of k within an experiment. One experiment from Table 4.D (run **12**) was chosen to demonstrate the effect of thickness change on crystallization kinetics. Although the thickness problem could not be solved because of the inherent floatation of HDPE melt on Silicone oil, important information could be obtained from the analysis regarding the onset of crystallization and induction time. The information gained from all the experiments conducted in this investigation marked a significant improvement in the methods used by Kakani.

TABLE 4.M

Estimation of the Values of Strain and the Rate of Strain Applying the New Method to Kakani's Data, and Comparison with the Values Obtained by Kakani[7]

Experiment	Kakani's Method			New Method			%Diff in
APPENDIX D[7]	ε	t(s)	$\dot{\varepsilon}(s^{-1})$	ε	t(s)	$\dot{\varepsilon}(s^{-1})$	$\dot{\varepsilon}$
D1	3.80	5.00	0.76	4.2	6.00	0.70	8.2
D2	3.60	5.00	0.72	4.0	6.00	0.67	7.2
D3	2.90	10.0	0.29	3.3	11.0	0.30	3.4
D4	3.40	2.00	1.70	3.8	3.00	1.27	29
D5	3.35	1.99	1.68	3.75	3.00	1.25	29.4
D6	3.20	10.0	0.32	3.6	11.0	0.33	3.1
D7	4.00	1.00	4.00	4.4	2.00	2.20	58
D8	3.30	1.00	3.30	3.7	2.00	1.85	56.3
D9	3.20	20.0	0.16	3.6	21.0	0.17	6.1
D10	4.06	19.3	0.21	4.46	20.0	0.22	4.7
D11	3.60	22.5	0.16	4.0	23.0	0.17	6.1
D12	3.80	1.00	3.80	4.2	2.00	2.10	57.6
D13	2.47	0.74	3.36	2.87	0.93	3.10	8.0
D14	2.25	0.67	3.38	2.65	0.84	3.15	7.0
D15	3.61	0.80	4.51	4.01	1.00	4.00	12.0
D16	3.00	0.50	5.97	3.4	0.63	5.40	10.0
D17	2.37	0.50	3.95	2.77	0.63	4.40	11.0
D18	3.03	0.50	6.06	3.43	0.63	5.44	11.0
D19	2.44	0.60	4.06	2.84	0.75	3.79	7.00

*ε from Kakani's data was increased by 0.4

* t > 1s was increased by 1s; t < 1s was increased by 25%

§ 4.2 Avrami Exponents in the Literature

Fractional values of the Avrami exponent, n and significant deviation of the values from the ideal values have been cited in literature (Chapter II). Many research groups, such as those discussed in Chapter II, attribute the variable values of n to the spatial constraints and secondary crystallization. The following discussion illustrates a comparison between the various values of n found in the literature, and those calculated in this work.

Isothermal studies on quiescent crystallization in poly(phenylene sulfide) (PPS), were conducted by Auer *et al.*,[50] and yielded values of n between 2.5 and 2.7. n was unaffected by T_c. However, monitoring the crystallization for a longer duration of time (~ 5 minutes, as opposed to 10 sec) n was observed to decrease to ~ 1.5-1.7. The lower range of values at longer time was attributed to secondary crystallization. Secondary crystallization was also reported to be responsible for fractional values of n, by Sakaguchi[23] and Ding and Spriuell[17]. Studies on the crystallization of PET by Sakaguchi[23], showed the average value of n to be ~ 1.5, independent of T_c. Ding and Spriuell[17], in their experiments with PP, arrived at an average value of n~3.5. Lambrigger[25] used a modified form of the Avrami equation to obtain the value of n as 3.6, at various values of T_c (170 K, 175 K, and 190 K). In the present investigation, it was observed that the values of n at four locations on a sample, held at different T_c's, showed no significant variation despite an equilibrium temperature gradient of ~17 °C along the height of the sample (Table 4.D, Table 4.E), in agreement with Lambrigger's observations.

He and Zoller[24] demonstrated that crystallization in disk shaped samples of PP and Nylon 66, was primary and gave consistent values of n (1.4 - 1.7), independent of the pressure. Schultz[21] explained the reason of $n < 2$ (the Avrami exponent for disk shaped crystal formation) as due to the constraint imposed by the thickness of the sample. In this work, experiments **1**, **7**, **8**, **9**, **10** and **11** listed in Table 4.C, showed a slight decrease in n from the thicker top region of the sample, to the thinner lower region, in agreement with the observation of He and Zoller[24] and the explanation provided by Schultz[21].

Tree[51] studied flow-induced crystallization of HDPE for elongational deformation. The Avrami exponents obtained were between ~2.0 and ~2.4 for temperatures between 135 °C to 155 °C. This is consistent with the expected value of n as 2 from the Avrami equation for planar crystallization. Planar crystallization of PPS was studied by He and Zoller[24] in which the samples were compressed to 5-6 mm thick disks. The treatment changed the growth pattern from spherulitic to tetrahedrons, discs, and tubes, leading to the values of n between 1and 2. Avrami exponents listed in Table 4.A using the method in this work show values and between 1 and 2, although the expected value is 1, for uniaxial crystallization. The reasoning presented by He and Zoller[24] could be used to explain the behavior of n in Table 4.A. Prior to the deformation, quiescent crystallization may have commenced disklike growth of crystals, which subsequently changed to uniaxial growth after the elongational flow was applied, giving values of n between 2 and 1.

§ 4.3 Avrami Coefficients and Crystallinity in the Literature

The Avrami coefficient, k has been found, in this work, to be sensitive to variations in temperature, and the rate of crystallization. Various research groups also, have established that k is a function of temperature, unlike n, which remains more or less constant for a fixed T_c.

Sakaguchi[23] has shown the dependence of k on T_c for PET. k was been described as a rate constant of overall crystallization. As T_c was raised above 180 °C, the k values decreased (Figure 2.13b). The overall crystallization was also shown to decrease with increase in T_c . Therefore, the rate of crystallization and T_c affected the values of k. Similar results were observed in this investigation. The values of k in Table 4.D and Table 4.E showed a decrease from locations at top to the locations situated in the lower half the sample. The equilibrium temperature measured at each location, established a rise in temperature from top to bottom. The case study of experiment number 12 (Table 4.I, Table 4.D), shows decreasing k values with temperature, for locations from the top to the bottom of the sample. The slow rise of crystallinity at lower regions of the sample in Figure 4.5 compared with the rapid increase at the top, also supports the functional dependence of k on the rate of crystallization.

Avrami plots at various T_c for Nylon-66, from the data obtained by He and Zoller[24] (Figure 2.11a, b) indicated a decreasing trend in the values of k by one order of magnitude $O(1)$, for a rise in temperature by ~2 °C from 282 °C. Crystallization of PP showed the k value to decrease sharply from 1.5×10^{-4} to 3.8×10^{-47}, for a rise in temperature from 154.8 °C to 173.7 °C (Figure 2.11a). Flow-induced crystallization in a

tubular flow geometry, studied by Spevacek and McHugh,[43] on HDPE and PP showed a decrease of $O(4)$ in the values of k for supercooling expressed as $T_m^o/(T\Delta T)\cdot 10^3$, ranging from 14 to 42 (Figure 2.23b). In the present study, the magnitude of the decrease in k values with temperature, was not as drastic as was observed by He and Zoller[24], and Spevacek and McHugh.[43] However, for a temperature variation of less than 2 °C along the height of the sample, in experiments **1**, **4**, **5**, and **8** listed in Table 4.E, the values showed a decreasing trend within the same order of magnitude. Auer *et al.*[50], also showed that as crystallization temperature increased, the values of k decreased. The results showed that for a range of 10-15 °C, the k values decreased by $O(1)$ or $O(2)$.

Hammami *et al.*[52] also demonstrated that, at a constant rate of undercooling the crystallinity showed significant decrease with temperature. This is in agreement with the observation in this investigation that the intensity plots for the bottom of the sample in several cases show more than one sinusoidal cycle and in some cases show intensity changes till the end of the experimental duration (three hours). The observation indicated that crystallinity was lower at the bottom of the sample than at the top where crystallinity was greater. The observation is evident especially for the experiments in Table 4.E.

The discussion in this section indicates that the values of k decrease with the temperature of crystallization, and crystallinity is lower at the locations where the temperature is higher than other regions on the sample.

§ 4.4 Comparison With the Model by Mendes[6]

Mendes[6] developed a model to describe the formation of extensional flow-induced crystals in polymers. The bead rod model discussed briefly in § 2.3(b), was deemed as the most appropriate model that would describe the experimental observations on flow-induced crystallization in this work. Therefore, a comparison was drawn between the experimental results and the results obtained from the model.

In the Mendes model, the bead-rod representation of a polymer molecule was used to describe crystallization kinetics. Figure 4.6 shows the data obtained from the simulation, as well as the curve obtained by the analysis using the new method (§ 4.1(a)). The strain rate, 0.29 s^{-1} and the duration of strain, 10s, were taken form data obtained by Kakani[7], given in Table 4.B. $\dot{\varepsilon}$ and t were among the input parameters for the simulation. The results obtained showed the value of n to be 1.05 and k as 0.033, whereas from Kakani's data, n and k were 1.12 and 0.0008, respectively. Figure 4.7 shows the Avrami plots of Kakani's data and data generated from simulation. A qualitative agreement between the experiment and the theory could be seen in terms of both displaying exponential curves for relative crystallinity.

The difference in the values of the Avrami parameters arise, despite the qualitative agreement between the experiment and the model, due to the following reasons. Simulations with input parameters $\dot{\varepsilon}$ and t, chosen from Table 4.B and Table 4.D, barring the case shown in Figure 4.6, either yielded results with no physical meaning or made the simulation unstable. This was recognized as being due to the simulation being able to take only low values of strain rate ($0 < \dot{\varepsilon} \leq 1$ /s), and duration of strain ($0 <$

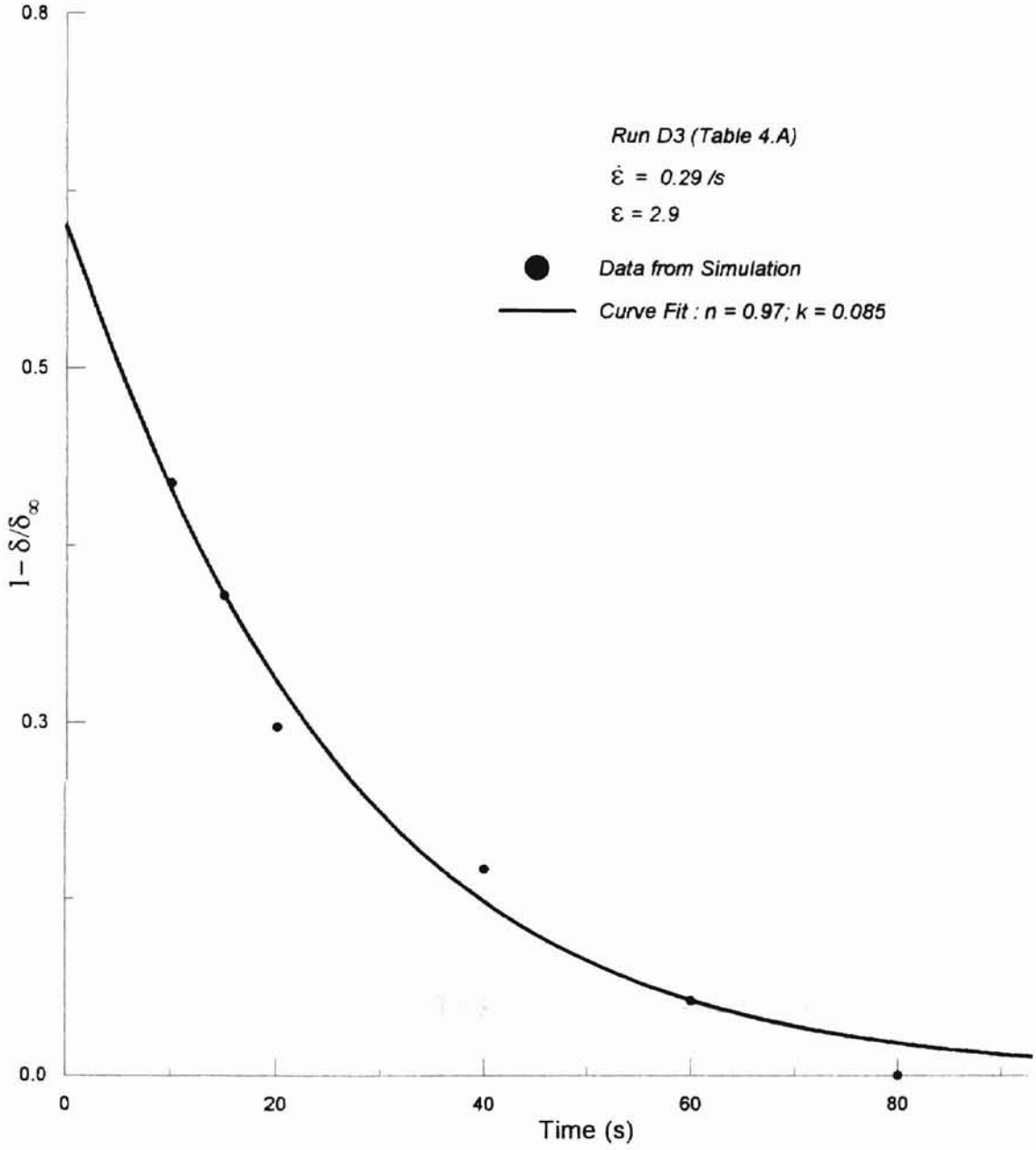

Figure 4.6 Non-Linear Form of Avrami Equation for Data Generated by Simulation[6]

$t \leq 5$ s) (Figure 2.24). On the other hand, the equation in the X-Language command was configured so as to obtain a large value of strain (> 3). As a result, suitable range of the two parameters for simulation could not be achieve simultaneously. Moreover, there an inherent estimated difference of ~ 10% between the rotational speed of the clamps, and the linear local speed of the sample[35].

Another source of discrepancy between the results model and the experiment is the value of λ, the relaxation time constant. The expression for relaxation of molecules after the cessation of flow is given by Bushman and McHugh[47] as an empirical formula

$$\delta = \delta_1 e^{-t/\lambda} + \delta_2 \quad , \tag{4.2}$$

where, δ is the instantaneous retardance, δ_1 and δ_2 are constants, and λ is the relaxation time. Equation (4.2) was used to fit the data during the relaxation period[47]. Although, the simulation generated by Mendes[6] did not show a relaxation period, λ was used in the development of the model. Another definition of relaxation time constant is[45]

$$\lambda = \frac{\zeta N(N+1)L^2}{72kT} = \frac{\zeta L^2}{12kT} \quad , \tag{4.3}$$

N being the number of beads associated with a molecule, k the Boltzmann constant, L the distance between two adjacent beads of the molecule, and ζ the friction coefficient. In the model,[6] the hydrodynamic drag force includes ζ; however, λ is not calculated using Equation (4.3). The value of λ = 30s used in the generalized diffusion Equation (2.51) was obtained from literature.[6]

On the experimental front, the values of $\dot{\varepsilon}$ shown in Table 4.A were obtained using the X-Language commands and did not represent the true value. The true value of

$\dot{\varepsilon}$ may lead to a different set of n and k values. For the experimental data Figure 4.7, T_c, was different throughout the height of the sample. Although T_c v °C (T_c used in the model), at the bottom edge of the sample, the locations t birefringence were chosen at random in Table 4.A. The deformation of the sa non-uniform. The aspects were overlooked in the model. Hence, the qu disagreement between the experiment and the model.

§ 4.5 A Study of FIC using Linear Dichroism in HDPE Melt

Dichroism is an aid to study molecular orientation in various mater birefringence. Birefringence, causes a phase difference between the two perp components of velocity of light due to the anisotropy of the material, whereas d determines the degree of anisotropy in the material from the absorption o mutually perpendicular directions. In general, materials predominantly birefr not display dichroism and vice versa[11]. However, certain materials can be bi and strongly dichroic, but in different frequency ranges of the spectrum[11]. birefringence, dichroism was also used in this investigation to observe a extensional flow-induced crystallization.

§ 4.5(a) Data Analysis and Discussion

Figure 4.8 shows a typical intensity graph as the outcome of the experim experimental set up resulted in the formation of two images of the observation w

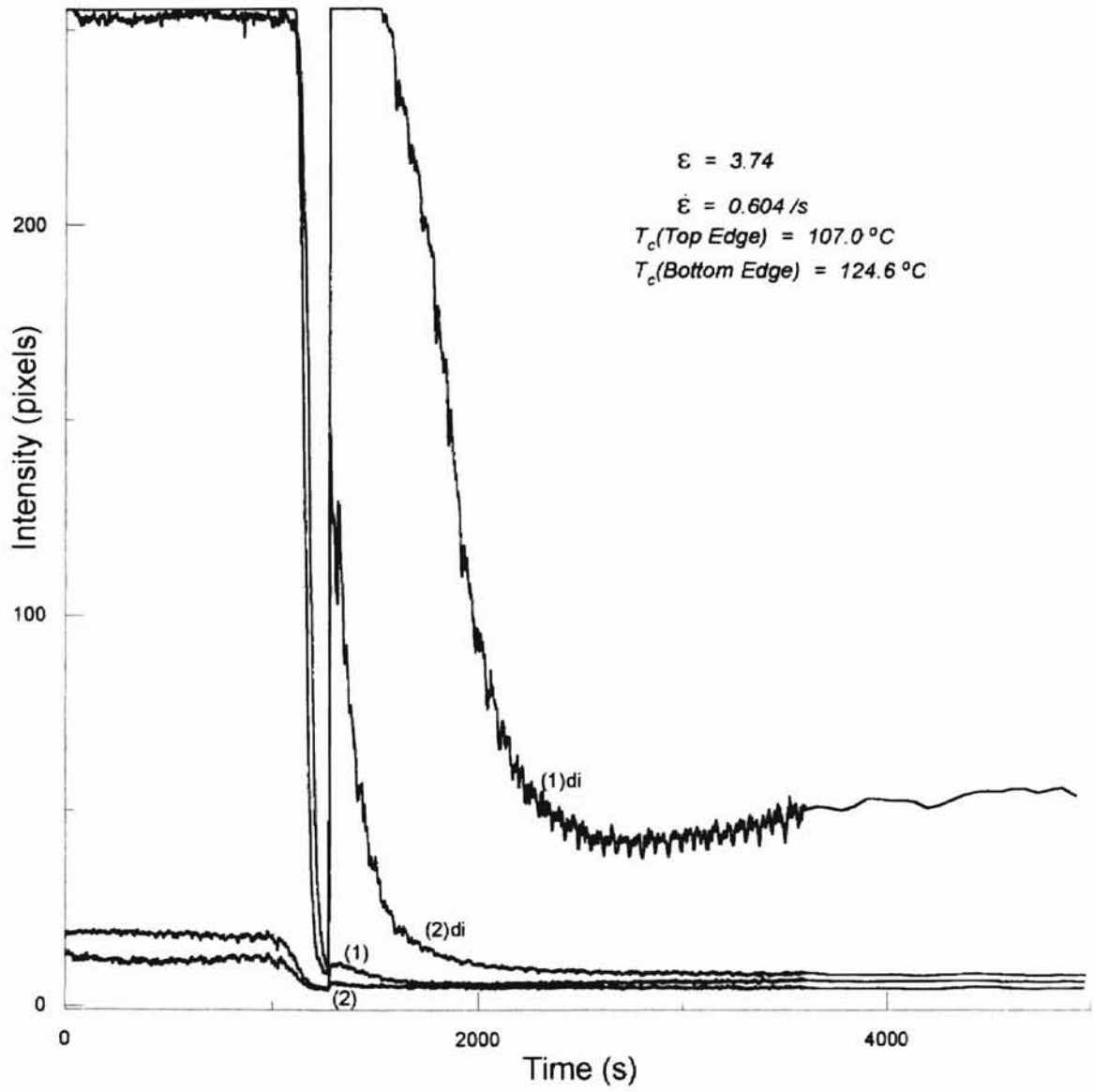

Figure 4.8 Dichroism and Birefringence Intensity as a Function of Time at Locations (1) and (2); 'di' stands for Dichroism

the sample on the monitor. The image displaying low intensity was due to the crossed polarizers in the path of the incident beam. Intensity for two locations on this image, (1) and (2) displayed low pixel values at $t = 0$, which decreased further at the onset of crystallization and increased to form a small intensity peak, due to birefringence in sample when the strain was applied. The magnitude of intensity of this image was approximately lower by a factor of 6 than in the experiments exclusively for birefringence measurements. The beam B, however, initially had a high intensity displaying the maximum pixel value of 255, dropping abruptly to values comparable to pixel values of beam A, at the onset of crystallization. After the flow-field was applied, the intensity increase due to the preferred orientation of molecules in the sample. The locations, (1) and (2) were chosen to study the development of orientation in the microstructure of the sample.

Equations (3.29) and (3.30) were used to calculate the values of the absorbance, A_e and extinction coefficient, κ. Figure 4.9 shows the values of A_e and κ for each of the locations, (1) and (2). The observations made are listed as follows:

(i) Location (2) had lower intensity for both beam A and beam B, compared with that of location (1) indicating that absorption of light was stronger at location (2). Consequently, higher values of A_e and κ related to absorption were observed compared to the A_e and κ at location (1).

(ii) The A_e and κ curves for the location with lower intensity, *i.e.*, location (2), had considerably more noise with respect to the A_e and κ values of location (1). This behavior is attributed to the argument of the natural logarithm in both A_e and κ,

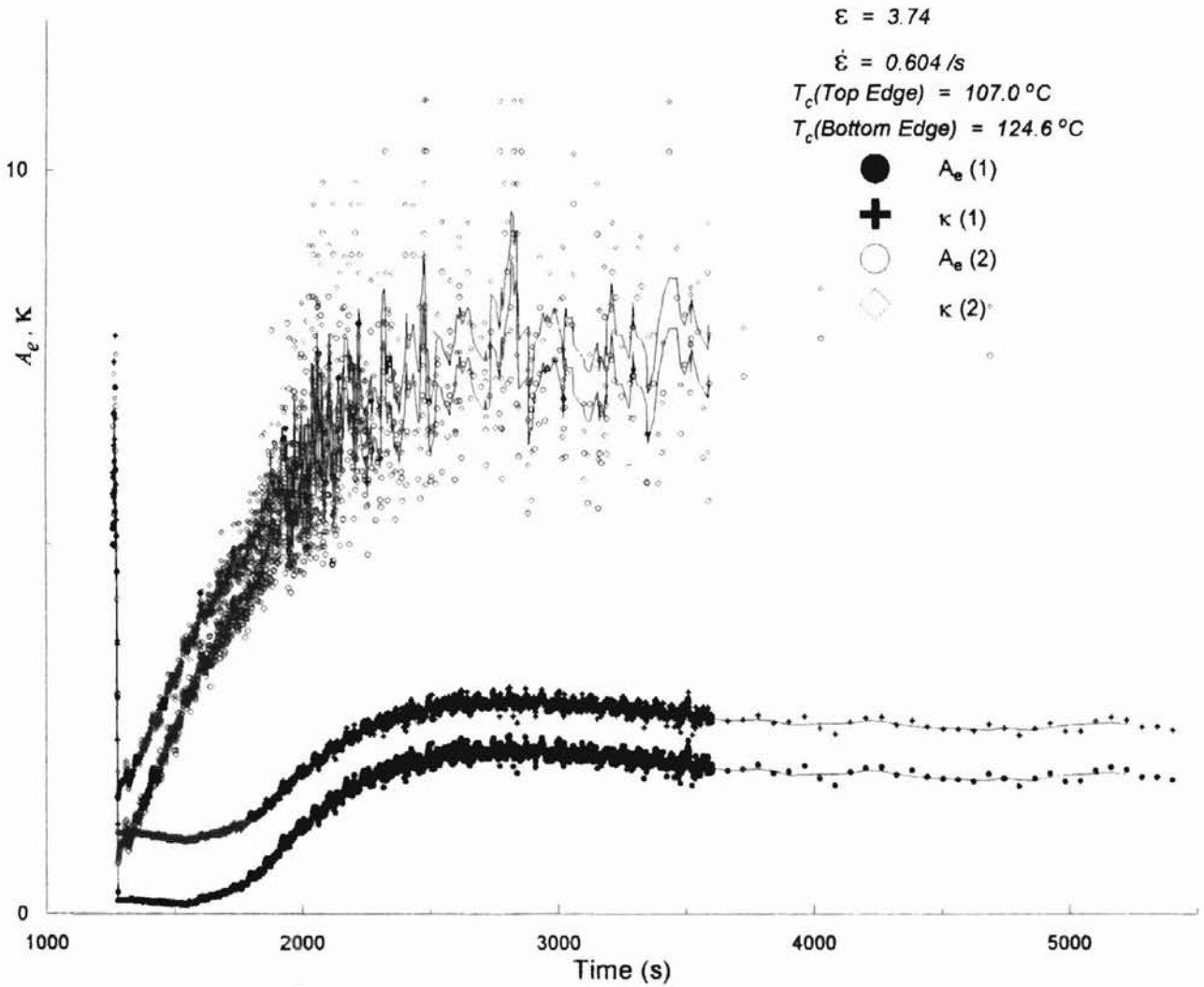

Figure 4.9 Absorptivity (A_e), and Kappa (κ) Versus Time for Dichroism Experiment in Figure 4.9

respectively. As natural logarithm function is more sensitive to smaller magnitude of the argument, than larger, the A_e and κ curves due to lower intensity are observed to obtain values which deviate about a smoothly varying mean value of A_e and κ, more than at location (1).

(iii) Intensity and absorption are inversely related to each other. Since intensity has an inverse functional dependence on coefficient a according to

$$I = I_o e^{-at} \quad , \tag{4.10}$$

which in turn, is a function of the extinction coefficient of the material, it could be deduced that as intensity rises, A_e and κ decrease, and vice versa (Figure 4.8 ,4.10).

(iv) The profile of κ has larger values compared with the profile of A_e at the same location. This is due to κ being a function of e^{A_e}.

McHugh *et al.*[47] performed experiments with HDPE to study flow-induced crystallization using dichroism (§ 2.3(c)). The schematic of the optical train is shown in Figure 2.25. Figure 2.26a shows that the intensity of beam A[47] remained constant for the most of the deformation (~50s), and monotonically decreased after the cessation of flow. Likewise, the intensity of beam B decreased following the cessation. However, a speculation of the setup of the optical train shows that the intensities of both the beams are subject to changes simultaneously, as the molecular orientation varies with time due to flow-induced crystallization. In the case of beam A, a deformation along x_1 would cause molecular alignment in the direction of the flow. This would result in transmission of light with **E**-vector along x_2. However, the analyzer was set to 0° with respect to x_1, indicating a considerable lowering of intensity. In Figure 2.26a, however, the intensity

was shown to have a maximum value during deformation. After the cessation of flow, the relaxation process would be marked by a rise in intensity. Beam B, as against beam A would qualify for the intensity curve in Figure 2.26a.

In this work, beam B did not have an analyzer as in the beam B of Figure 2.25, yet the intensity variations observed did not display a monotonically decreasing trend. Instead, the intensity decreased and attained a constant value, or the decrease was followed by a further increase to signify the ongoing crystallization. Beam A also displayed simultaneous variations in intensity, although the changes of beam B were more clearly visible with respect to those in beam A. Figure 4.10 shows a plot of difference in extinction coefficient of the two perpendicular components. The values of $\Delta n'$ are one order of magnitude greater than the values sited in Figure 2.26b.

Friedenberg *et al.*[34], studied the orientation of monolayers of a rod-like polymer, PcPS, dispersed in docosanoic acid, or arachidyl alcohol caused by an applied flow field, using a four-roll mill[47,51,1] (§ 2.3(c)). The results are shown in Figure 2.27b. Although the values of $\Delta n'$ obtained, are of the same order of magnitude as in this investigation, they were found to be less than the latter. The high values of $\Delta n'$ obtained in this work is due to unequal intensities for the beams A, and B. Beam A was intercepted by a polarizer and an analyzer. The transmitted light of beam A was significantly reduced by the simultaneous action of dichroism and birefringence. Since the value of κ was calculated using the transmitted intensities of B and A, the ratio of B to A was large compared to the ratio for the optical train used by Bushman and McHugh[47].

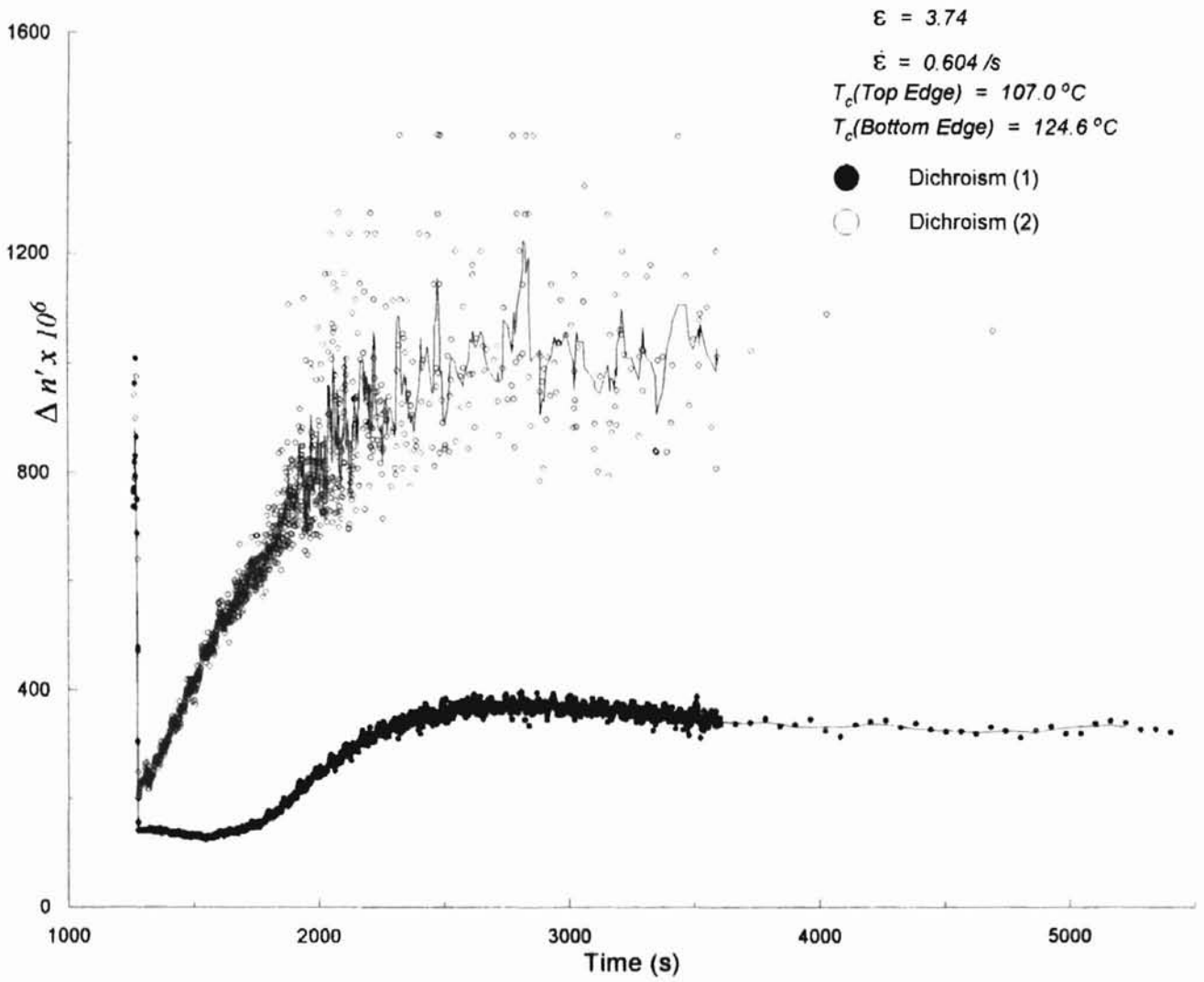

Figure 4.10 Dichroism ($\Delta n'$) at Locations (1) and (2) in Figure 4.10

Comparison between $\Delta n'$ obtained by Friedenberg *et al.*[34] and McHugh *et al.*[42] showed that the former is greater than the latter by $O(1)$. The explanation lies in the polarity of the molecules. PcPS molecules being strongly polar, become dichroic as the molecules align themselves along the flow field, while HDPE molecules comprising the polymeric melt, in this work were non-polar. The essential feature to observe dichroism is the existence of molecules or clusters of molecules which are ionic or polar in nature.

The observations indicate that a curve with high values of intensity in time, results in a well defined curve for κ. However, curves with lower intensity values, due to absorption by the polymer molecules, contain the important information regarding orientation of the molecules. From Figure 4.10, it can be seen that location (2) displays a scatter in the values of κ compared with location (1). Further processing of the data at location (2) to fit a model to characterize flow-induced crystallization would result in inconsistent results. Thus, for non-polar materials like HDPE, analysis of FIC by the method of birefringence would give more conclusive results than by using dichroism. On the contrary, if the material under study were polar, the method of dichroism would befit the analysis of FIC, as was studied by Friedenberg *et al.*[34]

The analysis of birefringence data depends on several factors which had been overlooked in the earlier analysis procedure. This chapter demonstrated the effect of these factors on the analysis of flow-induced crystallization in HDPE. The results obtained were comparable to results found in literature. Another method to study FIC is through dichroism measurements. However, it was demonstrated in this chapter that dichroism is not as effective as birefringence in characterizing FIC in HDPE. A

theoretical model developed by Mendes was also discussed briefly in its comparison with the experimental results.

CHAPTER V

SUMMARY AND CONCLUSIONS

The work in this investigation was a sequel to the experimental studies on flow-induced crystallization conducted by Kakani.[7] The lack of reproducibility of Kakani's results was due to the incorrect assumptions in the data analysis. However, the corrected results of Kakani's experiments showed a qualitative match with the model proposed by Mendes.[6] FIC was also studied using dichroism, in order to determine the usefulness of this approach to characterize FIC in HDPE.

The overall achievements in this investigation can be comprehensively stated as follows:

(i) Kakani's methods of data analysis were examined in detail to understand the effect of the assumptions on the results (Chapter III).

(ii) In the birefringence measurements, Kakani's intensity data were re-analyzed (§ 3.3 (b)). The discontinuous jump in the retardance curve shown in Figure 3.8 was removed to give a continuous smooth curve. The linear form of the Avrami equation was replaced by its non-linear form to obtain a reasonable estimate of the values of the Avrami exponent and coefficients.

(iii) A method to estimate the thickness of the sample, which could be a factor contributing to the incorrect results, was developed (§ 3.3(b.3)). As a check to

validity of this method, the original intensity pattern was reproduced using this method.

(iv) The procedure of performing the experiment was modified to give more consistent results than the results obtained earlier.[7]

(v) From the literature review and the experiments performed, a thermal gradient along the height of the sample was identified as an important factor affecting the magnitude of the k values. A housing of insulation was constructed to achieve a much smaller thermal gradient.

(vi) The values of n were found to be ~ 1, in accordance with the theoretical value predicted by the Avrami equation for uniaxial crystallization. The values were also independent of temperature variations in the different regions of the sample.

(vii) The retardance curves obtained experimentally were generated using the model developed by Mendes.[6] A qualitative agreement was obtained between the model and the experiment.

(viii) A new experimental method of studying FIC was developed using dichroism along with birefringence. Values of difference in extinction coefficients in mutually perpendicular directions were determined using the equations developed as shown in Appendix-A.

§ 5.1 Sources of Error

Several sources of error which could be considered for future investigation in FIC are discussed in this section.

§ 5.1(a) Design of Experimental Setup

The tank, which formed a part of the extensional rheometer used in this investigation, was made of aluminum. Aluminum could be replaced by Pyrex glass to provide better insulation to the system. Another reason to replace aluminum with Pyrex glass in this system would be to increase the heating efficiency of the system. The housing should be completely encased in glass wool sheets to ensure the required thermal insulation.

Instead of using a tank of large dimensions (72 x 35 x 16 cm.), a tank of smaller dimensions could be constructed. This would decrease the amount of Silicone oil required to immerse the sample.

Rectangular observation windows 20 cm. long, rather than the circular windows 2.5 cm in diameter, would give a complete view of the sample as it elongates. This may be considered a requirement, since in most experiments, the elongation of the sample was more than 2.5 cm., *i.e.*, the actual length of the deformation was beyond the field of vision of the camera.

The motor used to rotate the rotary clamps, was connected to one of pulleys. The operation of the motor results in the rotation of this pulley; hereafter the momentum is conveyed to four other pulleys that are responsible for the elongation of the sample. This causes a delay in the rotation of the clamps due to inertia. Thus, a command to terminate rotation also causes a similar lag. Another inherent problem with the extensional rheometer is the inefficient transfer of momentum from one roller to another.

The intensity of the plane polarized light ($I_o/2$), without the interception of the beam by the sample, was estimated to have a pixel value of 280. The VCR could only record up to 255 as the pixel value. The number of pixel values could also be affected by the 'contrast' and the 'brightness' knob on the VCR, if the settings varied from one experiment to another. To avoid the induced error, the source of light could be replaced by a He-Ne laser (~543 nm), or and Argon-ion laser (~514 nm)[54], and a photomultiplier tube could be used as the detector.

§ 5.1(b) Measurement of Total Strain

The volume of the unwrapped region on the sample could be written as $V = l \times h \times L$ where l, h, and L are the length, height, and the thickness of the portion of sample exposed as the window of observation. The sample window can be considered as being divided into n (not the Avrami exponent) equal segments. The initial length and the thickness of each segment can be named as, l_{oi} and L_{oi} , respectively. Assuming that the strain does not significantly affect the height of the sample, and that the volume of the window remains constant throughout the deformation, the quantity ($l \times L$) is constant for a particular experimental run. Therefore l and L are inversely proportional to each other. Regions close to the edge of the window bordering the foil showed that L_{oi} was unaffected by the applied strain. Consequently l_{oi} for the segment also becomes invariant. Therefore, for the segments close to the aluminum foil bordering the sample window,

$$\Delta l = l_o - l_{oi} = 0 \qquad \Rightarrow \qquad \varepsilon_i = (l_o - l_{oi})/\, l_{oi} = 0 .$$

Here l_o is the length of the segment after the cessation of the applied flow field, and ε_i the resulting strain. The method used by Kakani[7] and in the present investigation to calculate total strain, ε is

$$\varepsilon = \frac{l - l_o}{l_o} = \frac{(l_1 + l_2 + \cdots + l_n) - (l_{o_1} + l_{o_2} + \cdots + l_{o_n})}{(l_{o_1} + l_{o_2} + \cdots + l_{o_n})}$$

$$= \frac{(l_1 - l_{o_1}) + (l_2 - l_{o_2}) + \cdots + (l_n - l_{o_n})}{(l_{o_1} + l_{o_2} + \cdots + l_{o_n})} = \frac{(l_x - l_{o_x}) + (l_{x+1} - l_{o_{x+1}}) + \cdots + (l_{n-x} - l_{o_{n-x}})}{(l_{o_1} + l_{o_2} + \cdots + l_{o_n})}$$

where $x > 1$ and $\varepsilon_i \approx 0 \quad \forall \quad i < x$.

$$\therefore \qquad \varepsilon = \frac{\sum_{i\,=\,x;\,x\,>\,1}^{n-x} (l_i - l_{o_i})}{\sum_{i=1}^{n} (l_{o_i})} \qquad (5.1)$$

A suggested method to calculate the actual value of ε is:

$$\varepsilon = \frac{l_x - l_{o_x}}{l_{o_x}} + \frac{l_{x+1} - l_{o_{x+1}}}{l_{o_{x+1}}} + \cdots + \frac{l_{n-x} - l_{o_{n-x}}}{l_{o_{n-x}}}$$

or

$$\varepsilon_{actual} = \sum_{i=x;x>1}^{n-x} \frac{l - l_{o_i}}{l_{o_i}} \; . \qquad (5.2)$$

Comparison of Equation (5.1) with Equation (5.2) shows that $\varepsilon_{actual} > \varepsilon$. For the suggested method of calculation of the total strain, a method will have to be devised to demarcate segments before the elongation takes place, and to trace the lines of separation after the elongation.

§ 5.1(c) Sample

The HDPE sample used in this work, had a value of 6.5 for the melt flow index (MFI). Due to the large value of MFI, the sample in its melt state had a tendency to float, causing the upper part of the sample to be thicker than the lower region. The polyethylene samples used by Meissner *et al.*[35], had values of MFI between 1.5 and 1.7. Choosing samples with low values of MFI, could minimize the error in analysis caused by floatation of the sample.

§ 5.1(d) Experimental Setup for Dichroism Measurements

The experimental setup for dichroism in Figure 3.1 shows prisms used as beam splitters and reflectors. However, the prisms also led to the scattering of the transmitted light resulting in tremendously reduced intensity of the beam passing through the analyzer. A partially silvered mirror could be used as a replacement to reduce the light scattering. All other prisms could be replaced by fully silvered mirrors.

For future studies, a method could be devised to produce uniformly deformed samples under the influence of a flow field. Then, by implementing the suggestions discussed above, reproducibility of the results on crystallization kinetics could be attained. In conclusion, this thesis is a comprehensive study of the most important factors which determine the reproducibility of the experiments in flow-induced crystallization.

REFERENCES

1. Guy, R. Kirk, "A Study Of Flow Induced Crystallization In Two Phase Polymer Melts", Ph.D. Thesis (Chemical Engineering), University of Illinois, Urbana, Illinois (1992).

2. Grulke, E. A., "Polymer Process Engineering", Prentice - Hall, (1994).

3. Avrami, M., 'Kinetics of Phase Change. III, Granulation, Phase Change, and Microstructure', Journal of Chemical Physics, **9**, 177-184, (1941).

4. Avrami, M., 'Kinetics of Phase Change. II, Transformation-Time Relations for Random Distribution of Nuclei', Journal of Chemical Physics, **8**, 212-224, (1940).

5. Avrami, M., 'Kinetics of Phase Change. I, General Theory', Journal of Chemical Physics, **7**, 1103-1112, (1939).

6. Mendes, L. J., "Mechanistic Kinetic Modeling of Flow-Induced Crystallization in Semicrystalline Polymers", Ph.D. Thesis (Chemical Engineering), Oklahoma State University, Stillwater, Oklahoma (1998).

7. Kakani, M., "An Experimental Study Of Flow Induced Crystallization In High Density Polyethylene And Polypropylene", M. S. Thesis (Chemical Engineering) Oklahoma State University, Stillwater, Oklahoma (1996).

8. Hecht, E., "Optics", Addison-Wesley Publishing Company, 1990.

9. Born, M. and Wolf, E, "Principles of Optics", Pergamon Press, 1959.

10. Kishbaugh, A. J., "The Rheo-Optics of Shear-Thickening and Structure Formation in Polymer Solution", Ph.D. Thesis (Chemical Engineering), University of Illinois, Urbana, Illinois (1992).

11. Pedrotti, F. L., and Pedrotti, L. S., 'Introduction to Optics', Prentice Hall, 1987.

12. Fincham, W. H. A., and Freeman, M. H., 'Optics', Butterworth & Co (Publishers) Ltd., Ninth ed., 1980.

13. Marentette, J. M. and Brown, G. R., '1. Birefringence and Morphology', Journal of Chemical Education, **70**, 435, (1993).

14. Vesely, D., 'The Development of Spherulite Morphology in Polymers', Journal of Macromolecular Science - Physics, **B35(3 & 4)**, 411-425, (1996).

15. Shroff, R., Prasad, A., and Lee, C., 'Effect of Molecular Structure on Rheological and Crystallization Properties of Polyethylenes', Journal of Polymer Science. Part B, Polymer Physics, **34**, 2317, (1996).

16. Sutton, S. J., Vaughan, A. S., and Bassett, D. C., 'On the Morphology and Crystallization Kinetics of Monodisperse Polyethylene Oligomers Crystallized From the Melt', Polymer, **37**, 5735-5738, (1996).

17. Ding, Z. and Spruiell, J. E., 'An Experimental method for Studying Nonisothermal Crystallization of Polymers at Very High Cooling Rates.' Journal of Polymer Science. Part B, Polymer Physics, **34**, 2783, (1996).

18. Fu, Q., Chiu, F.-C., McCreight, K. W., Guo, M., Tseng, W. W., Cheng, S. Z. D., Keating, M. Y., Hsieh, E. T., and DesLauriers, P. J., 'Effects of the Phase-Separated Melt on Crystallization Behavior and Morphology in Short Chain Branched Metallocene Polyethylenes', Journal of Macromolecular Science - Physics, **B36(1)**, 41, (1997).

19. Lednický, F., and Muchová, M., "Quantitative Evaluation of Early - Stage Growth Kinetics of Heterogeneously Nucleated Spherutlites: Has the Nucleation Induction Time a Nonzero Value?", Journal of Macromolecular Science - Physics, **B34**, 75-85 (1995).

20. Wang, C., and Liu, C. R., "Transcrystallization of Polypropylene on Carbon Fibers", Polymer, **38**, 4715-4718, (1997).

21. Schultz, J. M. 'Effect of Specimen Thickness on Crystallization Rate', Macromolecules, **29**, 3022-3024, (1996).

22. Lambrigger, M., 'Avrami Master Curves for Isothermal Polymer Crystallization', Polymer Journal, **29**, 188, (1996).

23. Sakaguchi, Y., "Modification of Crystallization Properties of Poy(ethylene Teraphthalate) by Copolymerization with Arylate-Units III. Bisphenol - A - and Bisphenol - S - Containing Copolymers", Polymer Journal, **28**, 874-879, (1996).

24. He, J., and Zoller, P., "Crystallization of Polypropylene, Nylon-66 and Poly (ethylene Teraphthalate) at Pressures to 200 Mpa: Kinetics and Characterization of Products", Journal of Polymer Science: Part B: Polymer Physics, **32**, 1049-1067 (1994).

25. Lambrigger, M., 'Evaluation of Data on the Kinetics of Isothermal Polymer Crystallization : Part II', Polymer Engineering and Science, **37**, 460, (1997).

26. Hinrichs, V., Kalinka, G., and Hinrichsen G., 'An Avrami-Based Model for the Description of the Secondary Crystallization of Polymers', Journal of Macromolecular Science - Physics, **B35(3&4)**, 295, (1996).

27. Zachariades, A. E., and Logan, J. A., "The Melt Anisotropy of Ultrahigh-Molecular-Weight Polyethylene", Journal of Polymer Science: Polymer Physics Edition, **21**, 821-830, (1983).

28. Bremner, T., and Rudin, A., "Persistence of Regions with High Segment Density n Polyethylene Melts", Journal of Polymer Science: Part B: Polymer Physics, **30**, 1247-1260, (1992).

29. Sakellarides, S. L., and McHugh, A. J., "Oriented Structure Formation During Polymer Film Extrusion", Polymer Engineering and Science, **25**, 1179-1187, (1985).

30. Titomanlio, G., and Marrucci, G., "Capillary Experiments of Flow Induced Crystallization of HDPE", AIChE Journal, **36**, 13-18, (1990).

31. van der Vegt, A. K., and Smit, P. P. A., "Crystallization Phenomena in Flowing Polymers", Advances in Polymer Science and Technology, Society of Chemical Industry (Ed.), Monograph **26**, London, 313-326, (1967).

32. Southern, J. H., and Porter, R. S., "Melting Behavior of Polyethylene Crystallized in a Pressure Capillary Viscometer", Journal of Applied Polymer Science, **10**, 1135-1143, (1972).

33. Tree, D. A., "Crystallization Kinetics Of Polymer Melts in Extensional Flow", M. S. Thesis (Chemical Engineering), University of Illinois, Urbana, Illinois (....).

34. Friedenberg, M. C., Fuller, G. G., Frank, C. W., and Robertson, C. R., "In Situ Optical Studies of Flow-Induced Orientation in a Two-Dimensional Polymer Solution", Macromolecules, **29**, 705-712, (1996).

35. Meissner, J., Raible, T., and Stephenson, S. E., 'Rotary Clamp in Uniaxial Extensional Rheometry of Polymer Melts', Journal of Rheology, **25**, 1-28, (1981).

36. Southern, J. H., and Porter, R. S., "The Properties of Polyethylene Crystallized Under the Orientation and Pressure Effects of a Pressure Capillary Viscometer", Journal of Applied Polymer Science, **14**, 2305-2317, (1970).

37. Desai, P., and Abhiraman, A. S., "Fundamental Aspects of Stress, Deformation, and Phase Transitions in Crystallizable Polymers: Experiments with Poly(ethylene terephthalate) in Uniaxial Stress Fields", Journal of Polymer Science: Polymer Physics Edition, **26**, 1657-1675 (1988).

38. Desai, P., and Abhiraman, A. S., "Crystallization in Oriented Poly (ethylene Terephthate) Fibres. I. Fundamental Aspects", Journal of Polymer Science: Polymer Physics Edition, **23**, 653-674 (1985).

39. Eder, G., Janeschitz-Kriegl, H., and Liedauer, S., "Influence of Flow on the Crystallization kinetics of Polymers", Progress in Colloid and Polymer Science, **87**, 129-131, (1992).

40. Jerchow, P. and Janeschitz-Kriegl, H., 'The Role of Long Molecules and Nucleating Agents in Shear Induced Crystallization of Isotactic Polypropylenes', International Polymer Processing, **12**, 72, (1997).

41. McHugh, A. J., Tree, D. A., Pornnimit, B., and Ehrenstein, G. W., "Flow-Induced Crystallization and Self-Reinforcement During Extrusion", International Polymer Processing, VI, **3**, 208-211, (1991).

42. McHugh, A. J., Guy, R. K., and Tree, D. A., "Extensional Flow-Induced Crystallization of a Polyethylene Melt", Colloid and Polymer Science, **271**, 629-645, (1993).

43. McHugh, A. J., and Spevacek, J. A., "The Kinetics of Flow-Induced Crystallization from Solution", Journal of Polymer Science: Part B: Polymer Physics, **29**, 969-979, (1991).

44. Siddiquee, M. S., "Production of High Strength Polymers Through Flow-Induced Crystallization", M. S. Thesis (Chemical Engineering) Oklahoma State University, Stillwater, Oklahoma (1992).

45. Bird, R. B., Curtiss, C. F., Armstrong, R. C., and Hassager, O., 'Dynamics of Polymeric Liquids', Vol 2, 2nd ed., John Wiley & Sons, Inc., (1987).

46. Tsai, T. C., "Modeling And Optimization of Flow induced Crystallization in Polymer Processing", Ph.D. Thesis (Chemical Engineering), Oklahoma State University, Stillwater, Oklahoma (1997).

47. Bushman, A. C.and McHugh, A. J., 'Transient Flow-Induced Crystallization of a Polyethylene Melt', Journal of Applied Polymer Science, **64**, 2165-2176, (1997).

48. Quantum Chemical Corporation, USI Division, 11500 Northlake Drive, Cincinnati, OH 45249, 1994.

49. Kalogrianitis, S. G., and van Egmond, J. W., 'Full Tensor Optical Rheometry of Polymer Fluids', Journal of Rheology, **41**, 343-364, (1997).

50. Auer, C., Kalinka, G., Krause, Th., and Hinrichsen, G., "Crystallization Kinetics of Pure and Fiber-Reinforced Poly (phenylene Sulfide)", Journal of Applied Polymer Science, **51**, 407-413, (1994).

51. Tree, D. A., "Crystallization Kinetics Of Polymer Melts in Extensional Flow", Ph.D. Thesis (Chemical Engineering), University of Illinois, Urbana, Illinois (1990).

52. Hammami, A., Spruiell, J. E., and Mehrotra, A. K., "Quiescent Nonisothermal Crystallization Kinetics of Isotactic Propylenes", Polymer Engineering and Science, **35**, 797-804, (1995).

53. Janeschitz-Kriegl, H., 'Polymer Solidification by Crystallization Under Heat Transfer and Flow Coniditions', Progress in Colloid and Polymer Science, 87, 117-127, (1992).

54. Fuller, G. G., "Optical Rheometry of Complex Fluids", Oxford University Press, (1995).

APPENDICES

APPENDIX A1

TRANSMISSION INTENSITY

The optical train shown in Figure A1 is a schematic diagram of the optical train shown in Figure 2.25. The polarizer and the analyzer were ±45° with respect to the $x_{\perp}$ axis, and 90° with respect to each other. The polymer sample was placed between the polarizer and the analyzer. If the sample were perfectly aligned in the $x_{\parallel}$ direction, the polarizer and the analyzer would be ±45° with respect to the polymer polarization axis ($x_{\perp}$), respectively.

The electric field vector, $\mathbf{E}_P$, for the transmitted light through the polarizer can be written as:

$$\mathbf{E}_P = \mathbf{E}cos\theta \quad , \tag{A1.1}$$

where θ is the polarization angle between the polarizer and the reference axis, $x_{\perp}$. Using Mallus law the transmitted intensity can be written as:

$$I_P = |\mathbf{E}_P|^2 = |\ \mathbf{E}\ cos\theta\ |^2 = |\mathbf{E}|^2\ cos^2\theta = I_o\ cos^2 45° \tag{A1.2}$$

Similarly, the transmitted intensity through the sample and the analyzer can be written as follows:

$$I_S = |\mathbf{E}_S\ |^2 = |\ \mathbf{E_P}\ cos45°\ |^2 = |\ \mathbf{E_P}\ |^2\ cos^2 45° = I_o\ cos^4 45° \tag{A1.3}$$

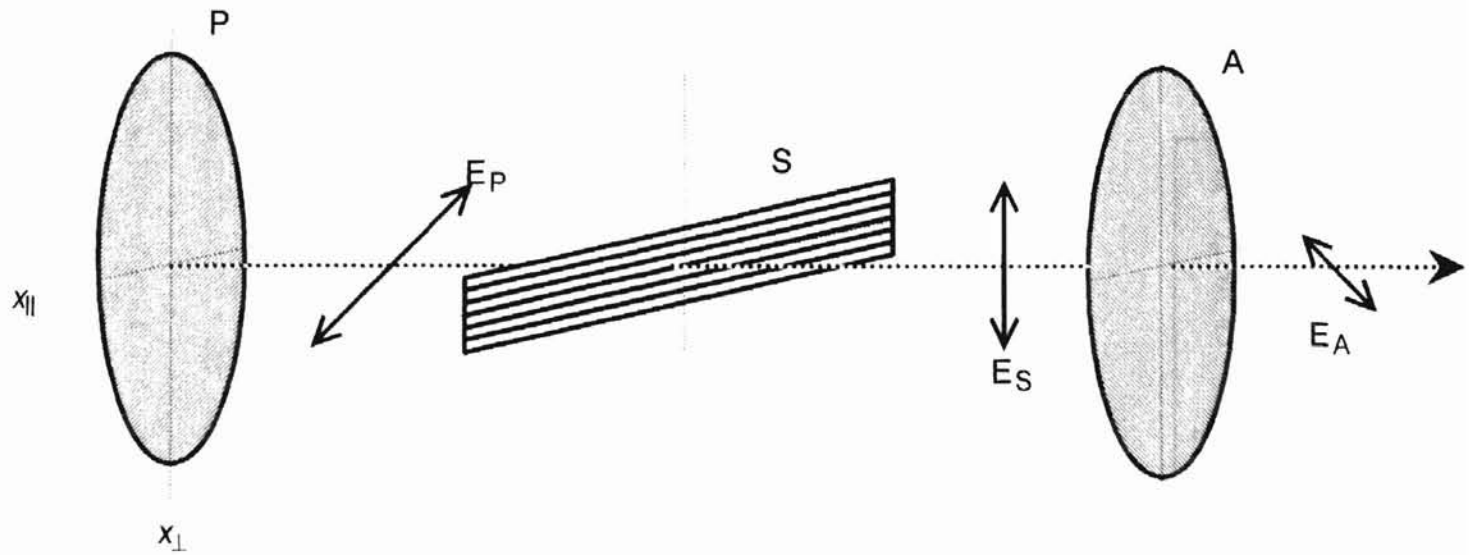

Figure A1 Electric Field Vector, **E** as Transmitted Though a Polarizer, P, Perfectly aligned Sample, S and Analyzer, A

$$I_A = |\mathbf{E}_A|^2 = |\mathbf{E}_S \cos 45° |^2 = |\mathbf{E}_S|^2 \cos^2 45° = I_o \cos^6 45° \tag{A1.4}$$

Therefore, the transmitted intensity through the complete optical train as a unit is:

$$I_A = I_o \cos^6 45° = I_o \left(\frac{1}{\sqrt{2}}\right)^6$$

$$\boxed{I_A = I_o \cos^6 45° = \frac{I_o/2}{2}} \tag{A1.5}$$

APPENDIX A2

ABSORBANCE AND EXTINCTION COEFFICIENT

Refractive index associated with a material composed of two components, *viz.*, the real component and the imaginary component:

$$\tilde{n} = n + i \quad n' \tag{A2.1}$$

The real component n is the factor affecting the phenomenon of birefringence, whereas the imaginary part n' is responsible for the dichroic behavior displayed by a material. n' is called the extinction coefficient and is proportional to the absorption coefficient of the material expressed as

$$I = I_o e^{-\alpha L}$$

where α is the absorption coefficient of the material, L is the path length of light through the material (thickness) and I_o is the incident intensity on the material.

From Mueller matrices[23], transmittance for the optical path including the polarizer and the analyzer (fig. 3.15) causing birefringence in the polymeric material is given by :

$$\frac{I_b}{I_0} = \frac{e^{-} A_e}{4} \left(cosh \quad \kappa - cos \quad \delta \right) sin^2[2(\alpha - \chi)] \quad . \tag{A2.2}$$

The optical path without the analyzer (fig. 3.3) yields transmittance expressed as

$$\frac{I_d}{I_0} = \frac{e^{-A_e}}{2}\left(\cosh\ \kappa - \sinh\ \kappa\ \cos[2(\alpha-\chi)]\right) \quad , \tag{A2.3}$$

where A_e and κ are the absorbance, and a quantity similar to retardance δ that compares the extinction coefficients in two perpendicular directions, respectively, given as:

$$A_e = \frac{\pi L}{\lambda_0}\left(n'_{\perp} + n'_{\parallel}\right)$$

and

$$\kappa = \frac{\pi L}{\lambda_0}\left(n'_{\perp} - n'_{\parallel}\right) \quad .$$

In equations (A.2) and (A.3) α is the angle between the optic axis of the sample and the polarization axis, and χ is angle between the reference frame (in this case the frame of the laboratory). In the present work, $\alpha = 45°$; $\chi = 0°$. Equation. (A.2) and (A.3) become

$$\frac{I_b}{I_0} = \frac{e^{-A_e}}{4}\left(\cosh\ \kappa - \cos\ \delta\right) \quad , \tag{A2.2'}$$

$$\frac{I_d}{I_0} = \frac{e^{-A_e}}{2}\left(\cosh\ \kappa\right) \tag{A2.3'}$$

Writing eq. (A.2') and (A.3') explicitly, the following set is obtained.

$$\frac{I_b}{(I_0/2)} = \frac{e^{-A_e}}{2}\left(\frac{e^{\kappa}+e^{-\kappa}}{2}\right) - \frac{e^{-A_e}}{2}\left(\cos\ \delta\right) \tag{A2.4}$$

$$\frac{1}{2}\frac{I_d}{(I_0/2)} = \frac{e^{-A_e}}{2}\left(\frac{e^{\kappa}+e^{-\kappa}}{2}\right) \tag{A2.5}$$

Subtracting eq. (A.4) from eq. (A.5)

$$\frac{\left(\frac{I_d}{2} - I_b\right)}{(I_0/2)} = \frac{e^{-A_e}}{2}\left(cos\ \ \delta\right) \quad . \tag{A2.6}$$

Rearranging eq. (A.6)

$$e^{-A_e} = \frac{\left(\frac{cos\ \ \delta}{2}\right)}{\frac{1}{(I_0/2)}\left(\frac{I_d}{2} - I_b\right)}$$

Solving for A_e yields

$$\boxed{A_e = ln\left(\frac{(I_o/2)(cos\delta)/2}{\left(I_d/2 - I_b\right)}\right)} \quad . \tag{A2.7}$$

Adding eq. (A.4) and eq. (A.5)

$$\frac{1}{(I_0/2)}\left(I_b + \frac{I_d}{2}\right) = e^{-A_e}\left(\frac{e^{\kappa} + e^{-\kappa}}{2}\right) - \frac{e^{-A_e}}{2}\left(cos\ \ \delta\right)$$

Rearranging,

$$2e^{A_e}\left(\frac{\left(I_b + \frac{I_d}{2}\right)}{(I_0/2)} + cos\ \ \delta\right) = \left(\frac{e^{2\kappa} + 1}{e^{\kappa}}\right) \quad . \tag{A2.8}$$

Naming the left hand side **B** and rearranging eq. (A.8)

$$e^{2\kappa} - \mathbf{B}e^{\kappa} + 1 = 0 \tag{A2.9}$$

or

$$x^2 - \mathbf{B} \cdot x + 1 = 0 \ , \tag{A2.10}$$

where $e^{2\kappa} = x$. Eq. (A.10) is in the form of quadratic equation and can be solved for x as

$$x = \frac{\mathbf{B} \pm \sqrt{\mathbf{B}^2 - 4}}{2} \quad . \tag{A2.11}$$

Solving for κ and discarding the negative solution,

$$\boxed{\kappa = ln\{\frac{\mathbf{B} \pm \sqrt{\mathbf{B}^2 - 4}}{2}\}} \quad . \tag{A2.12}$$

APPENDIX - B

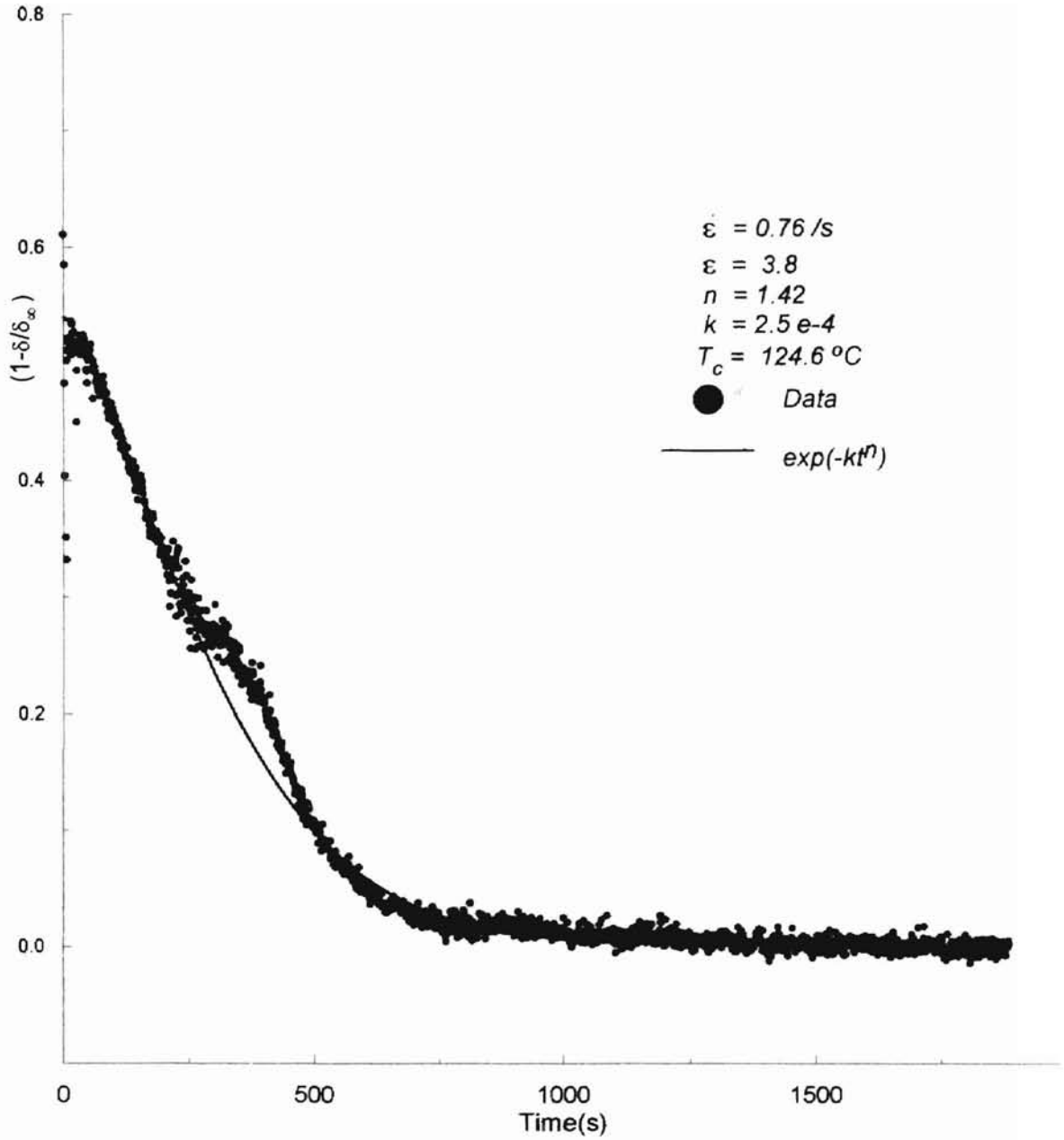

Figure B.1 Avrami Equation Using Kakani's Data in Figure D.1[7]

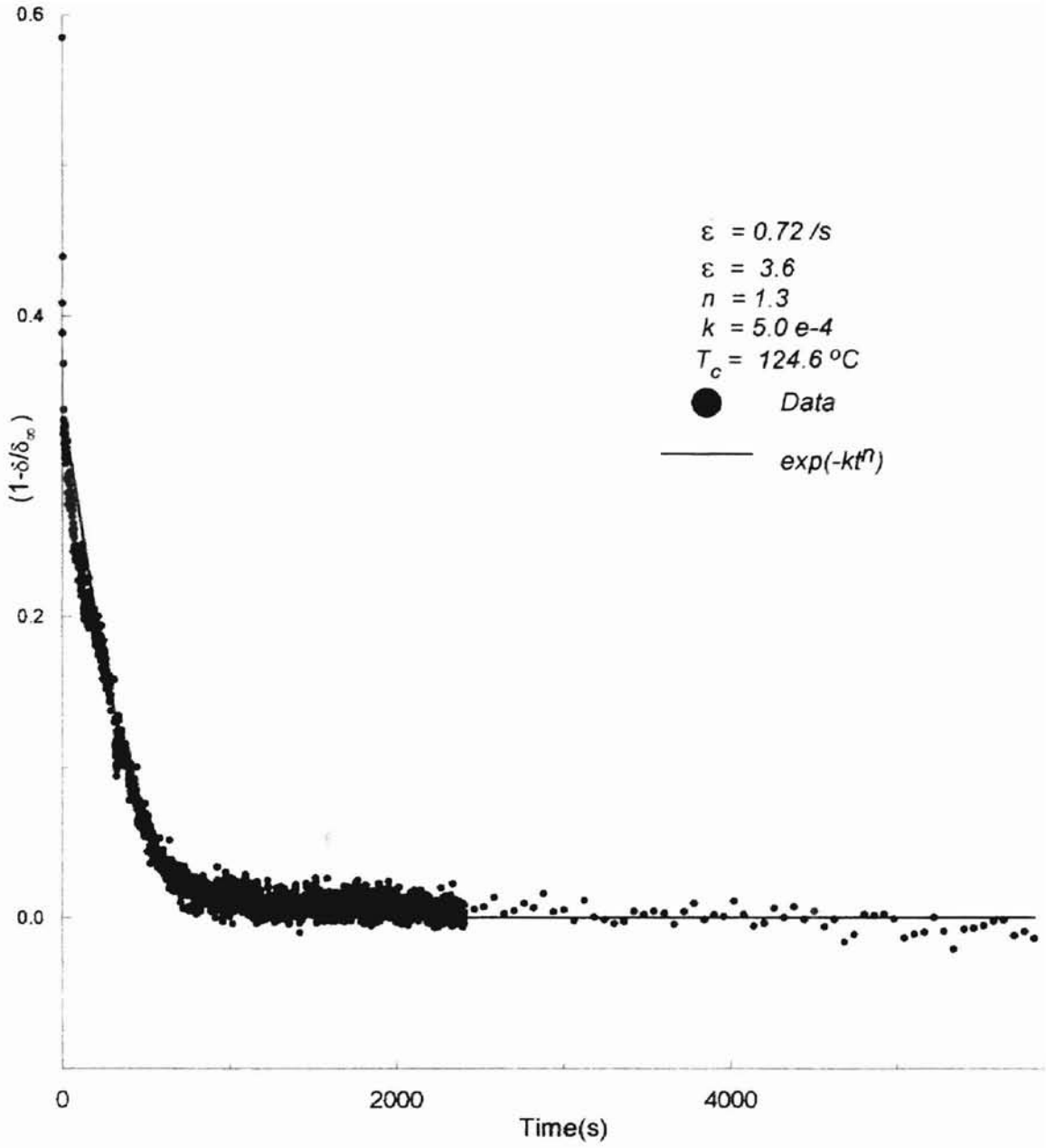

Figure B.2 Avrami Equation Using Kakani's Data in Figure D.2[7]

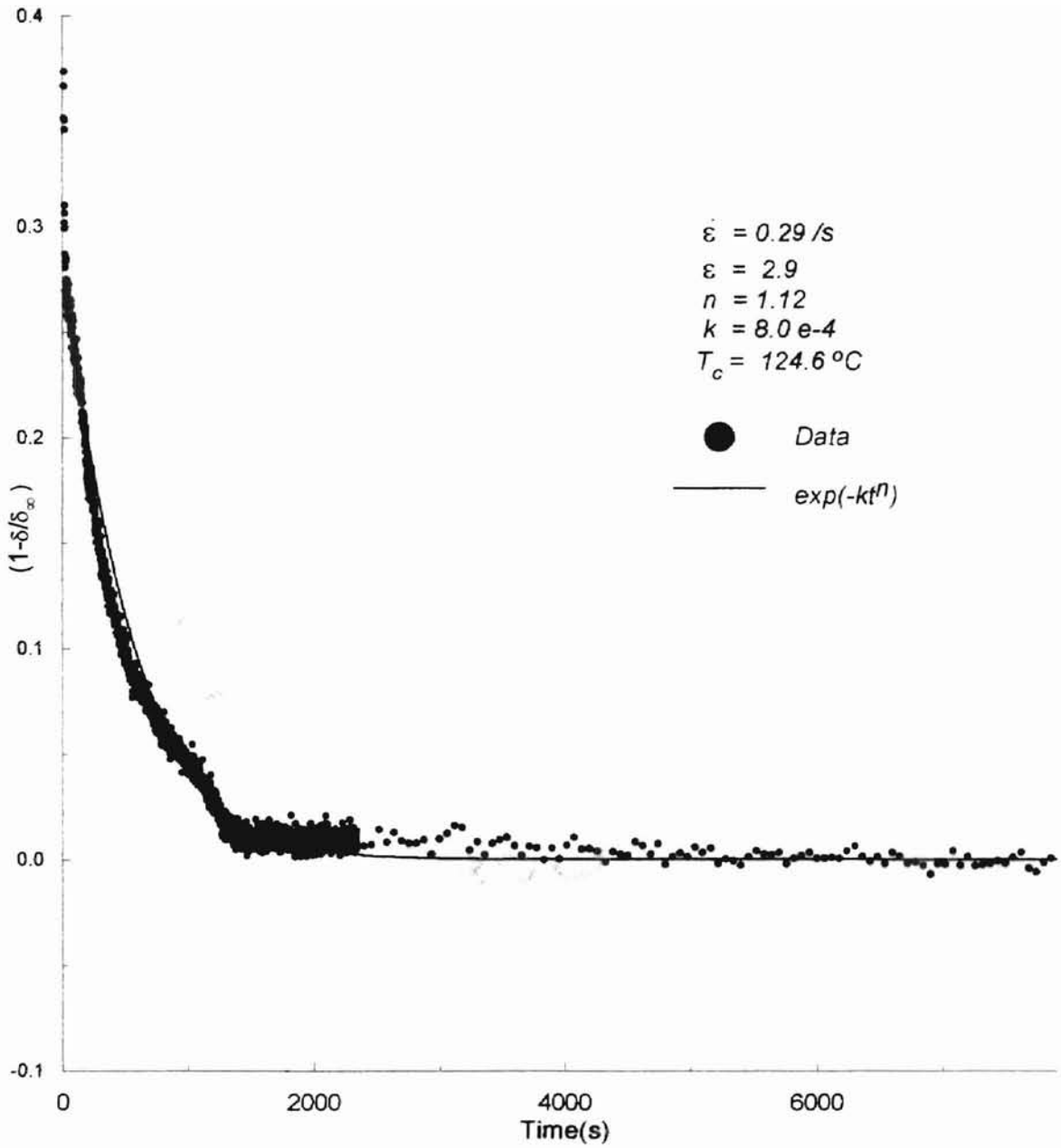

Figure B.3 Avrami Equation Using Kakani's Data in Figure D.3[7]

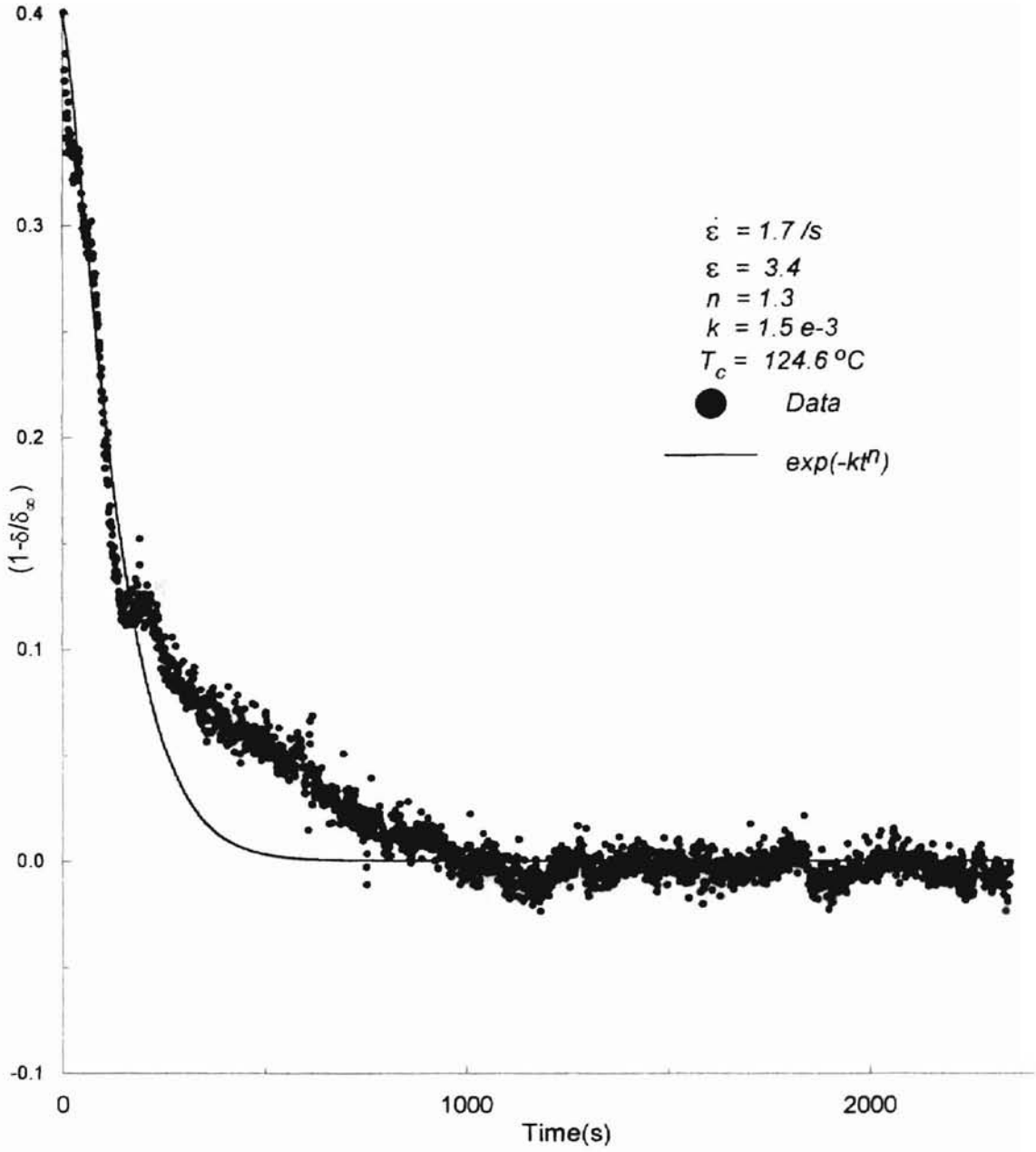

Figure B.4 Avrami Equation Using Kakani's Data in Figure D.4[7]

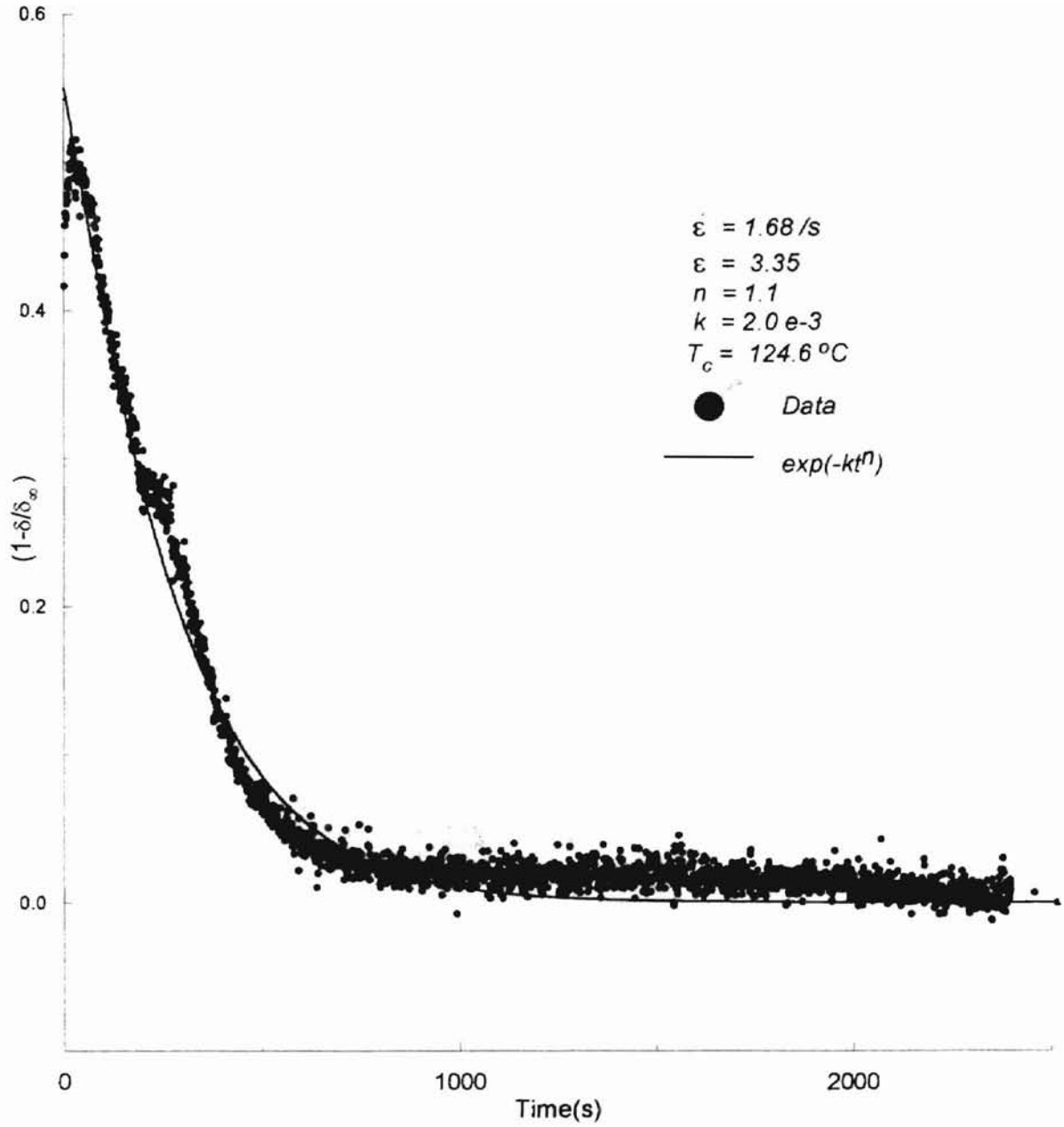

Figure B.5 Avrami Equation Using Kakani's Data in Figure D.5[7]

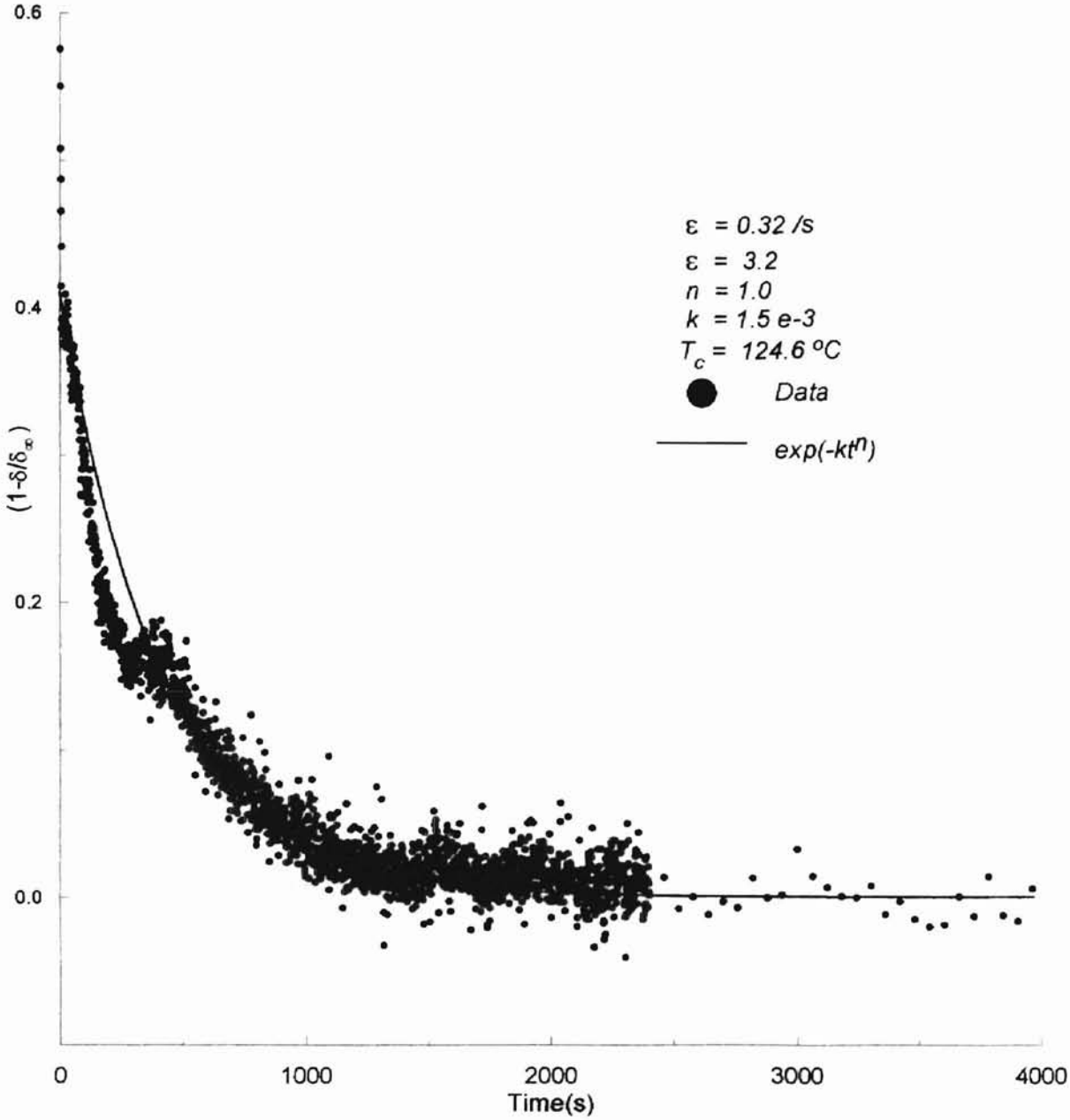

Figure B.6 Avrami Equation Using Kakani's Data in Figure D.6[7]

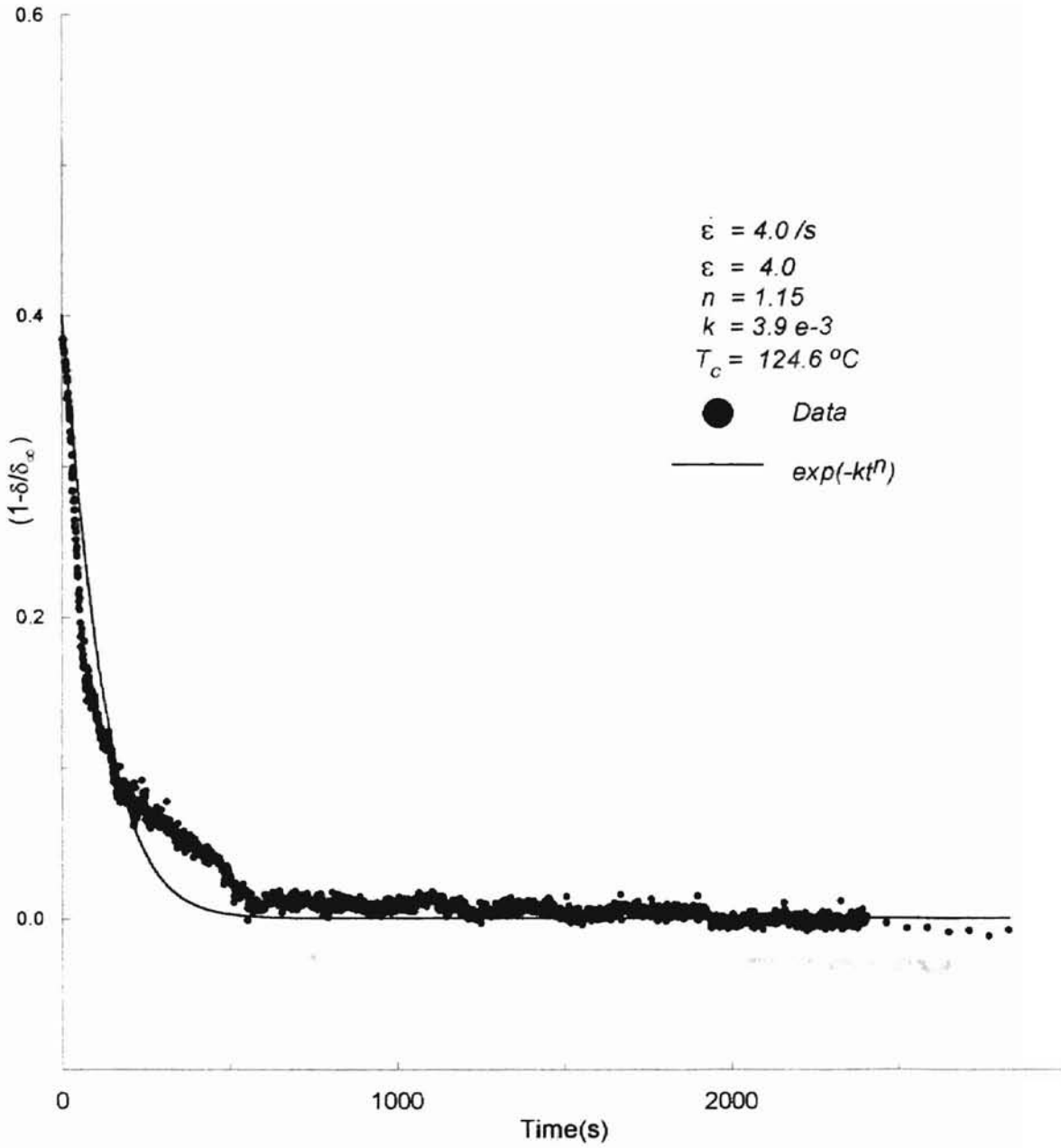

Figure B.7 Avrami Equation Using Kakani's Data in Figure D.7[7]

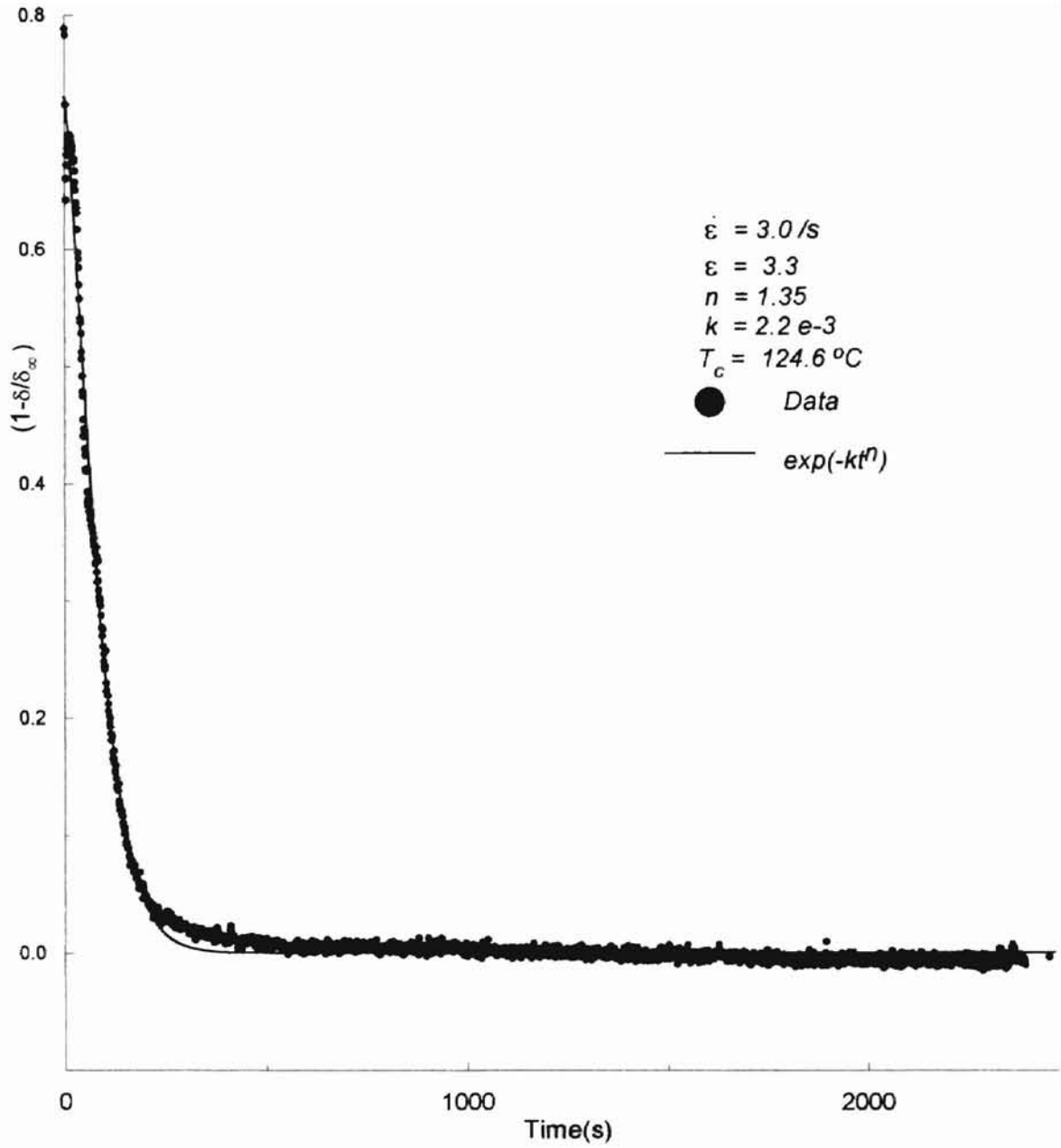

Figure B.8 Avrami Equation Using Kakani's Data in Figure D.8[7]

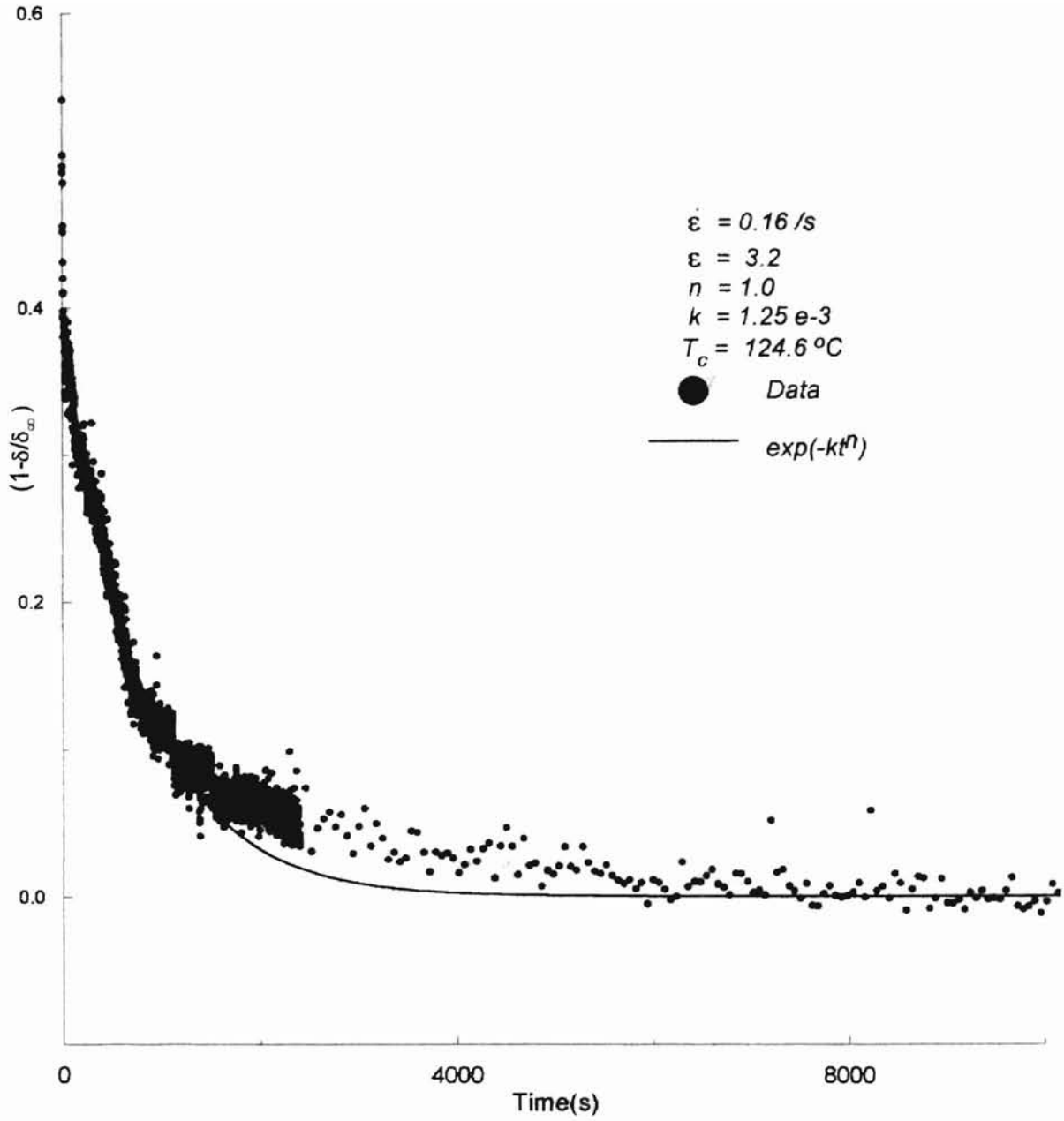

Figure B.9 Avrami Equation Using Kakani's Data in Figure D.9[7]

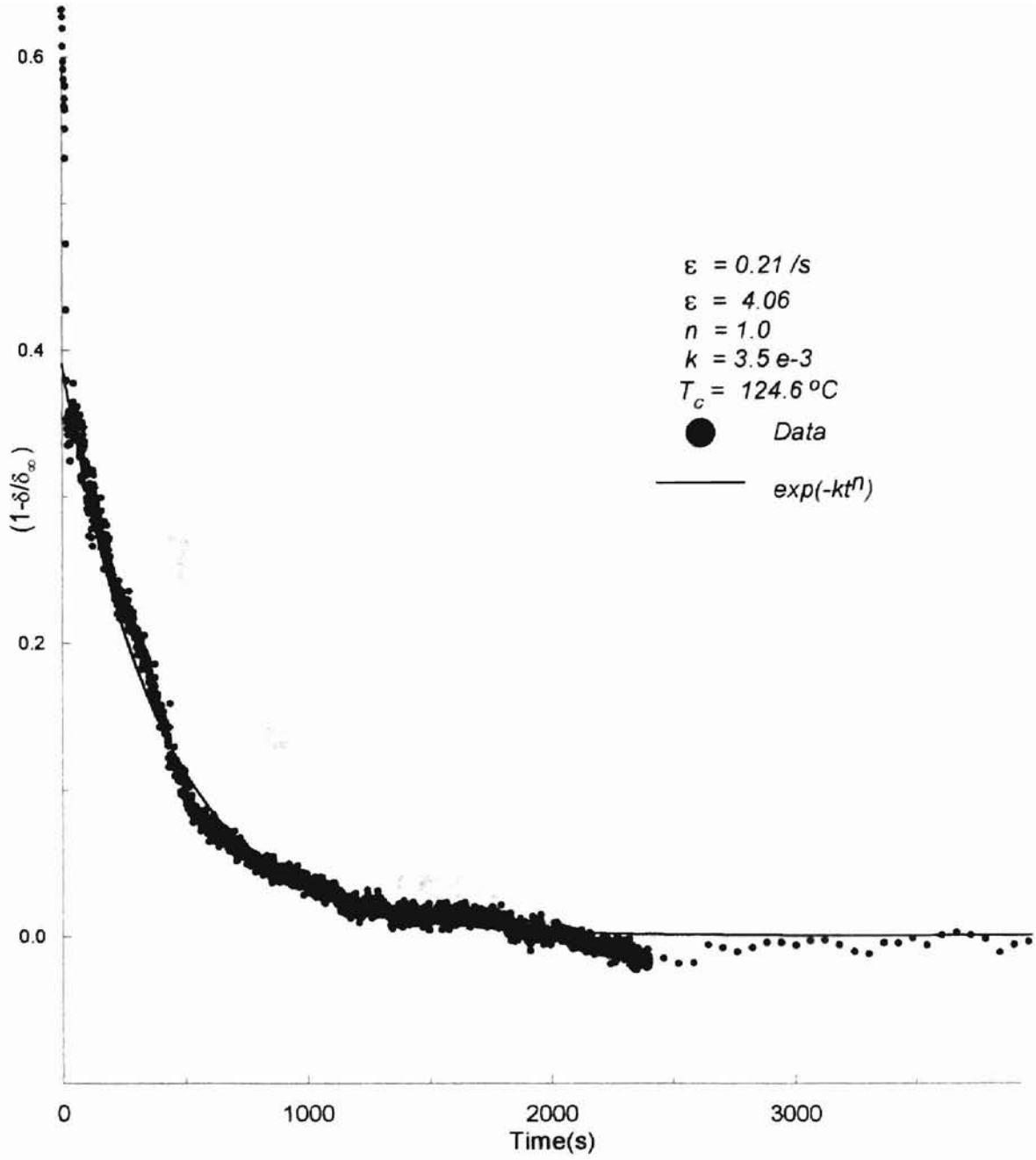

Figure B.10 Avrami Equation Using Kakani's Data in Figure D.10[7]

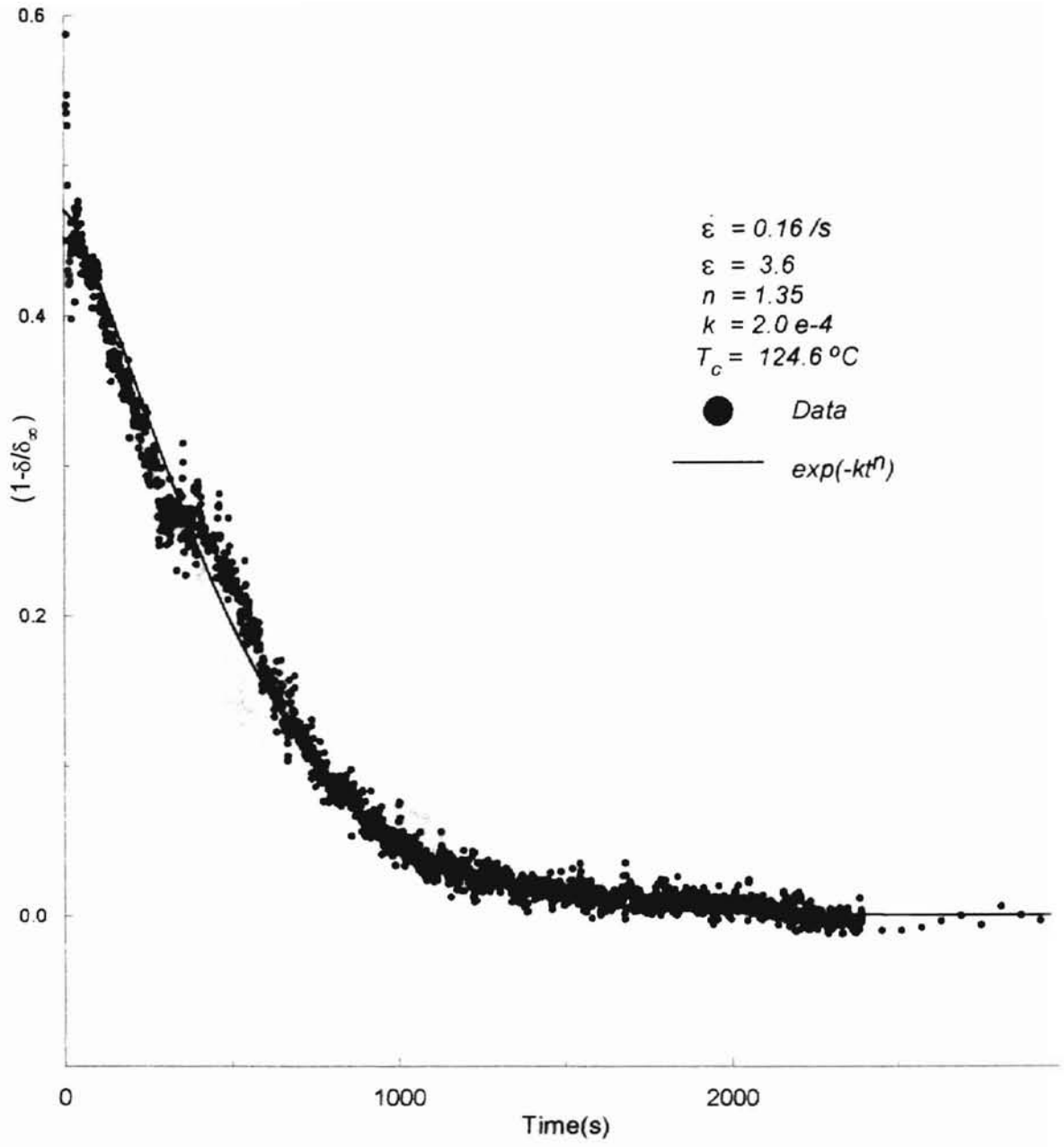

Figure B.11 Avrami Equation Using Kakani's Data in Figure D.11[7]

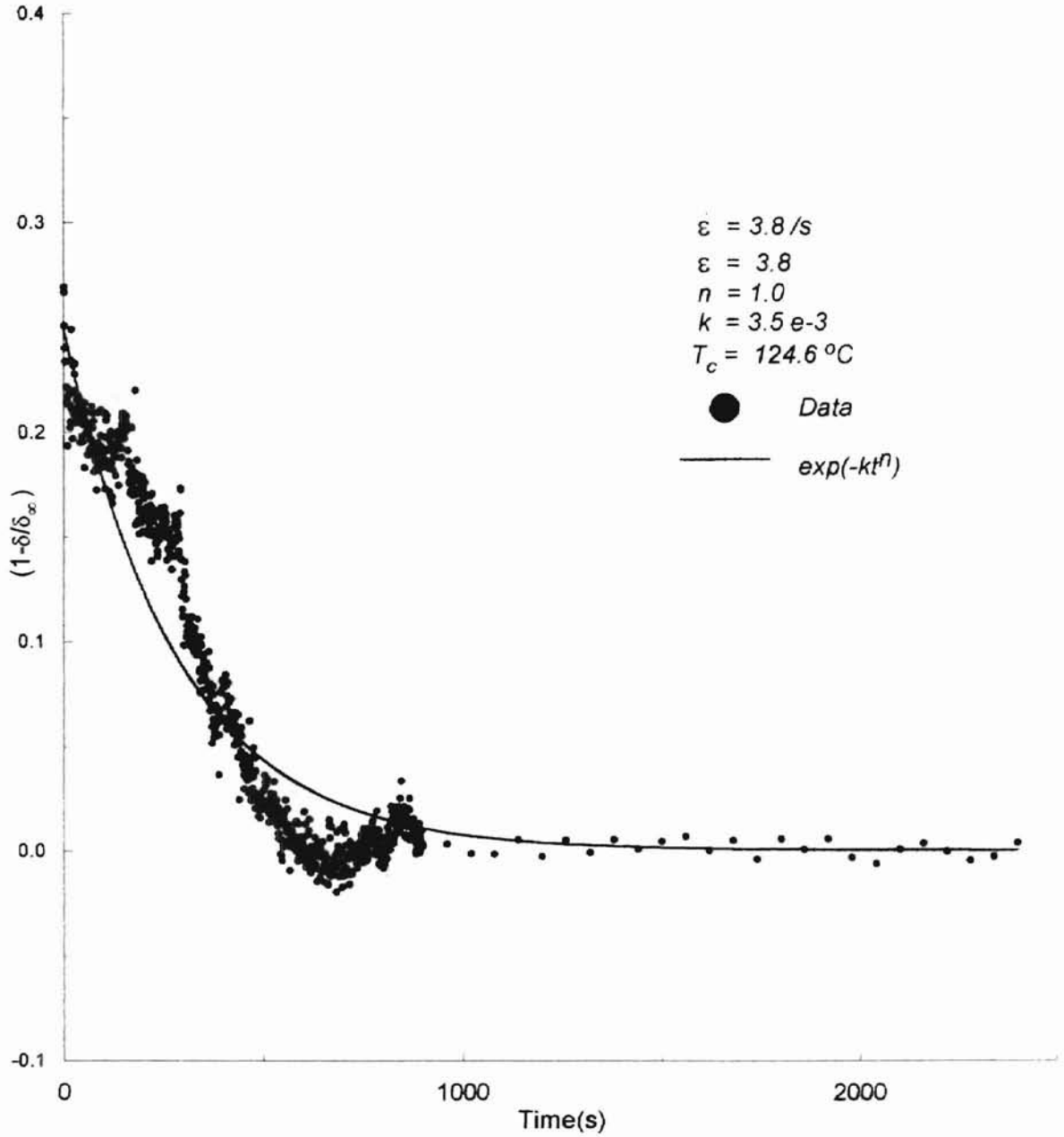

Figure B.12 Avrami Equation Using Kakani's Data in Figure D.12[7]

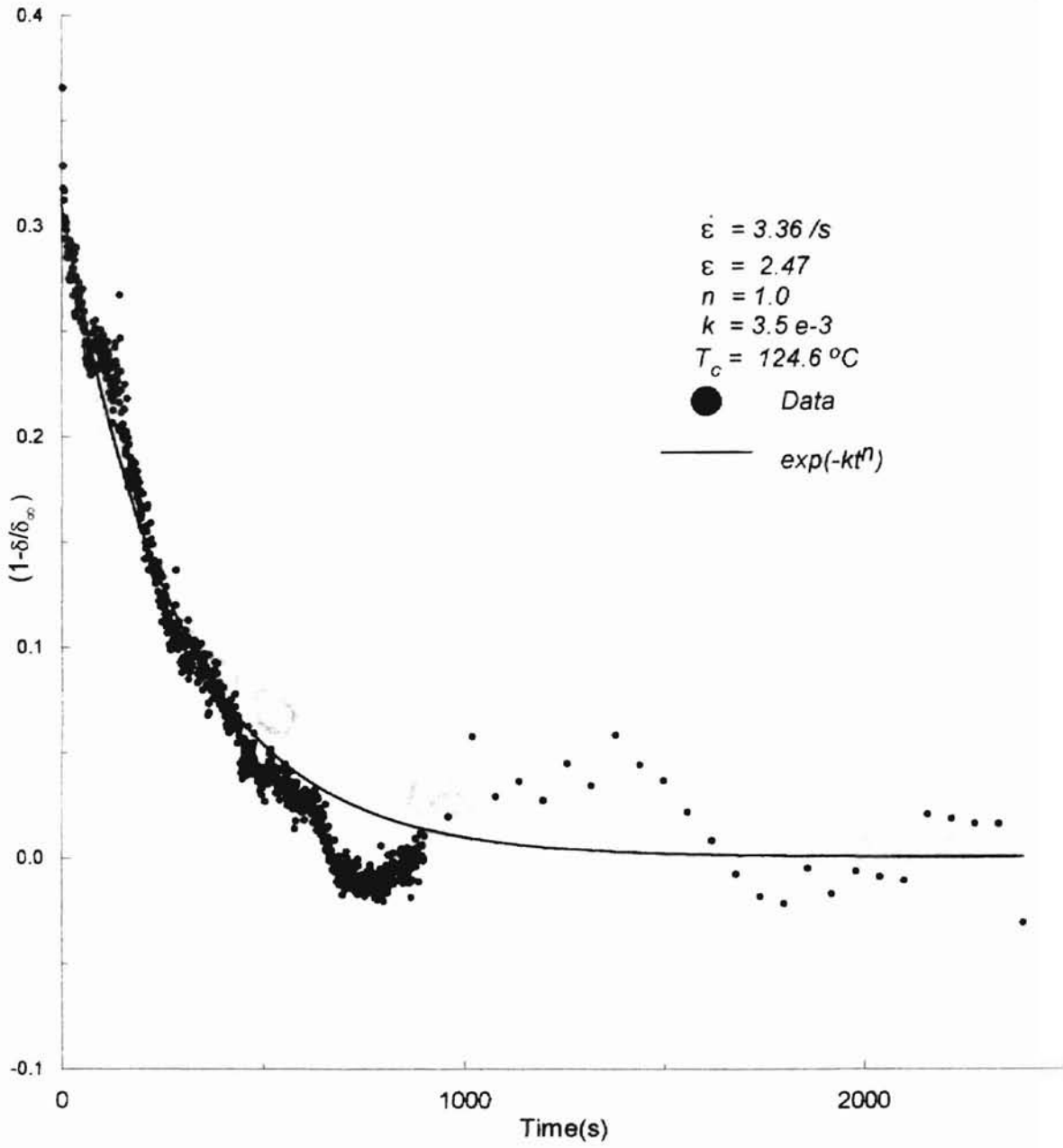

Figure B.13 Avrami Equation Using Kakani's Data in Figure D.13[7]

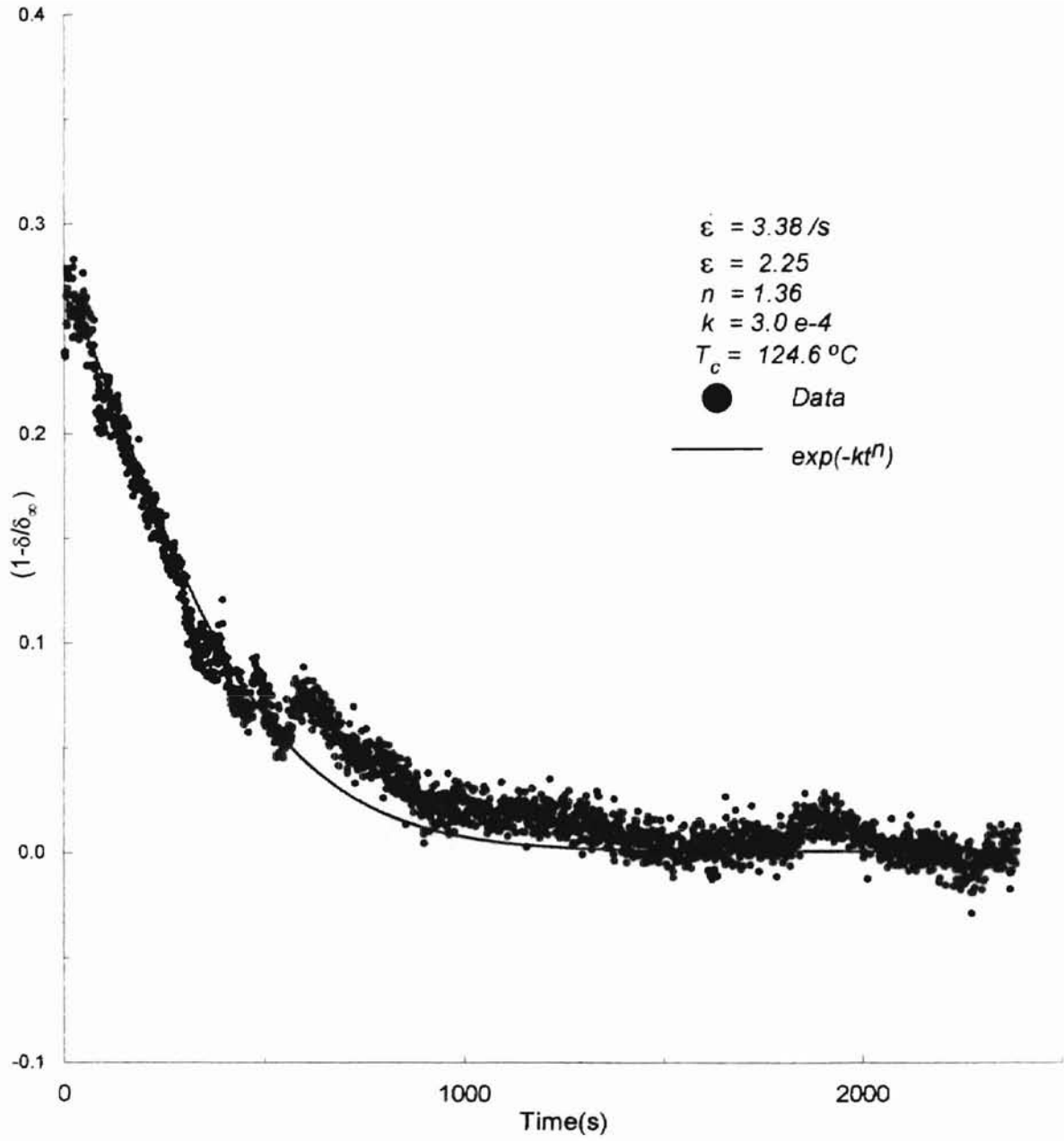

Figure B.14 Avrami Equation Using Kakani's Data in Figure D.14[7]

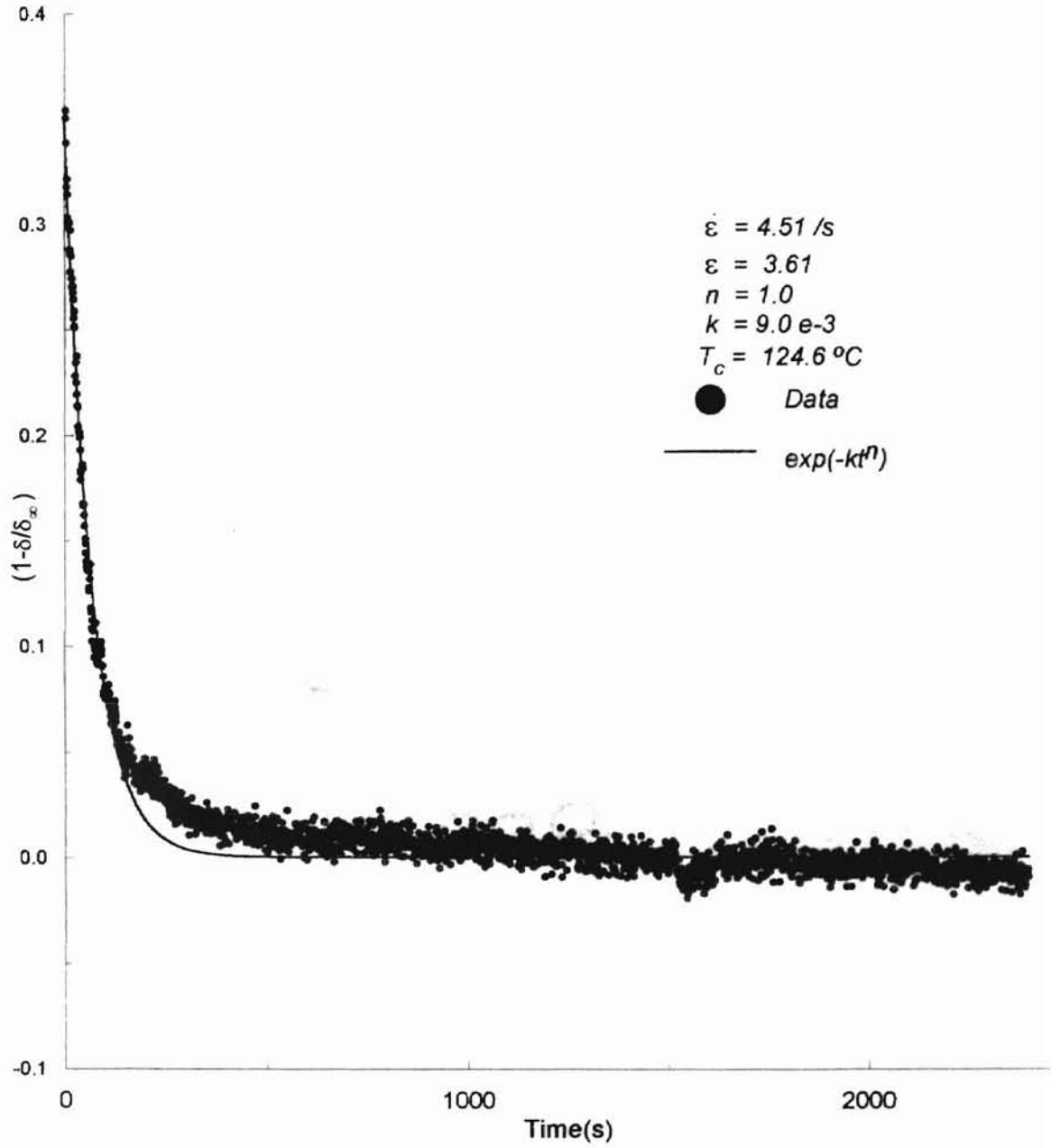

Figure B.15 Avrami Equation Using Kakani's Data in Figure D.15[7]

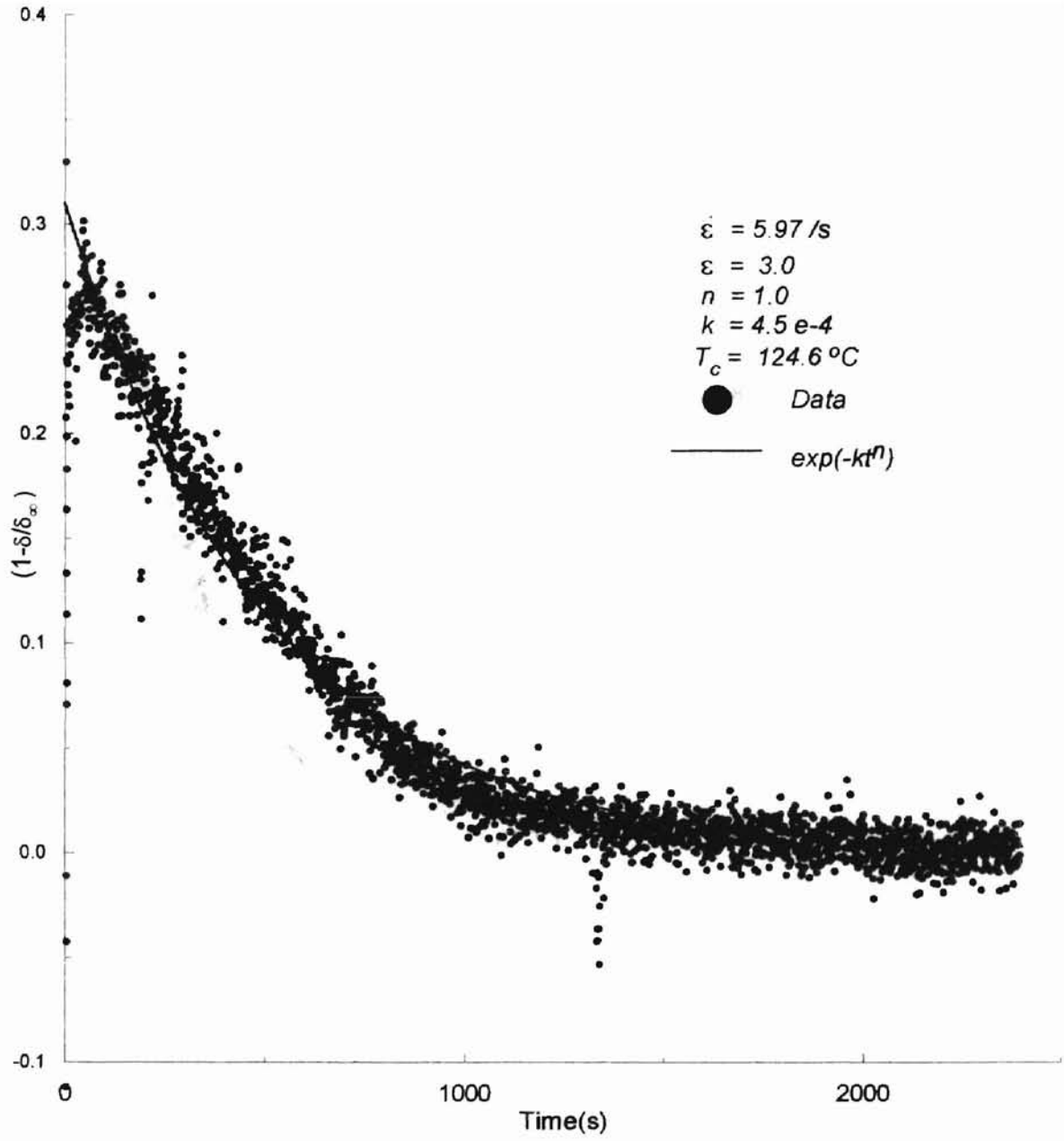

Figure B.16 Avrami Equation Using Kakani's Data in Figure D.16[7]

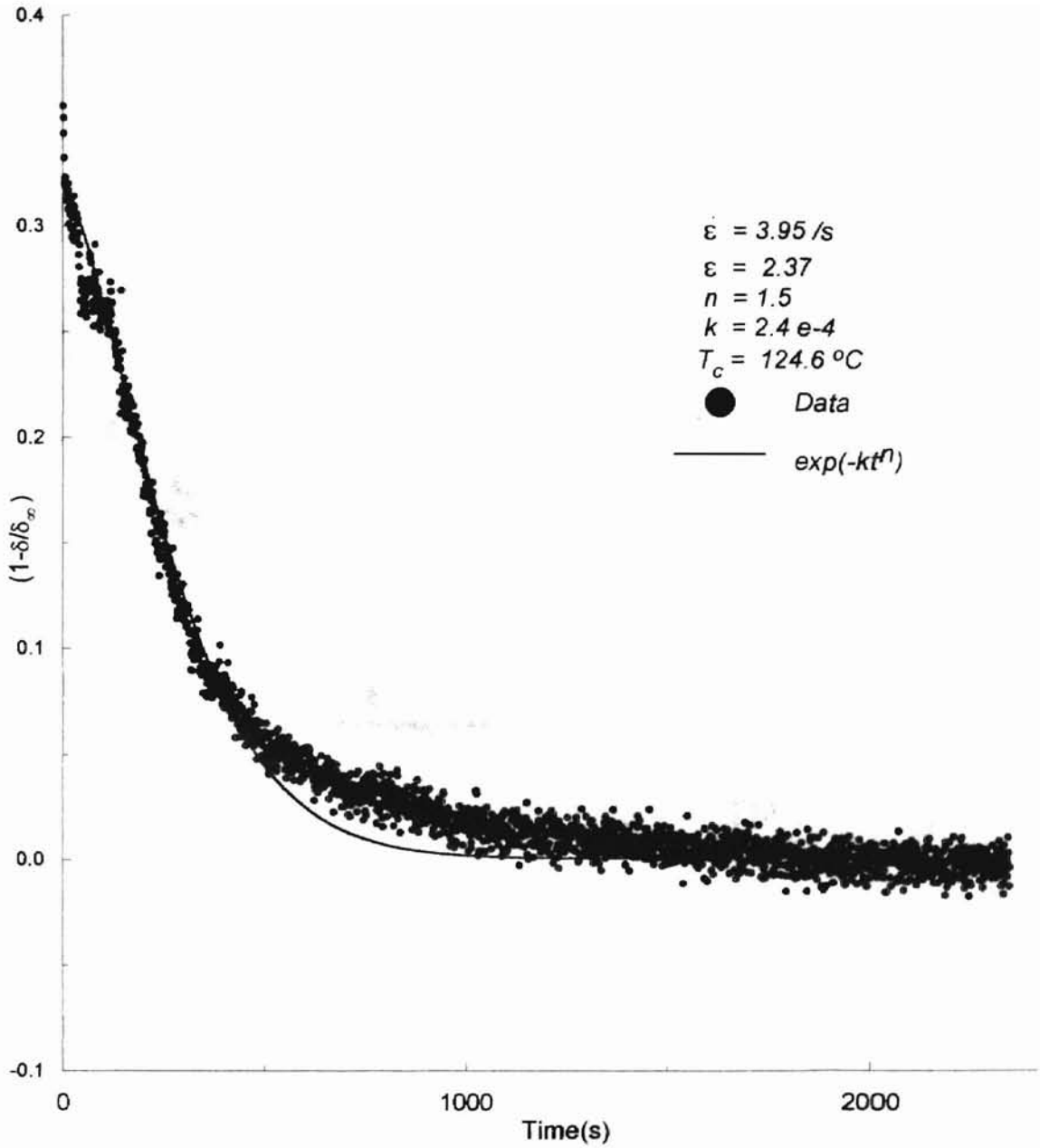

Figure B.17 Avrami Equation Using Kakani's Data in Figure D.17[7]

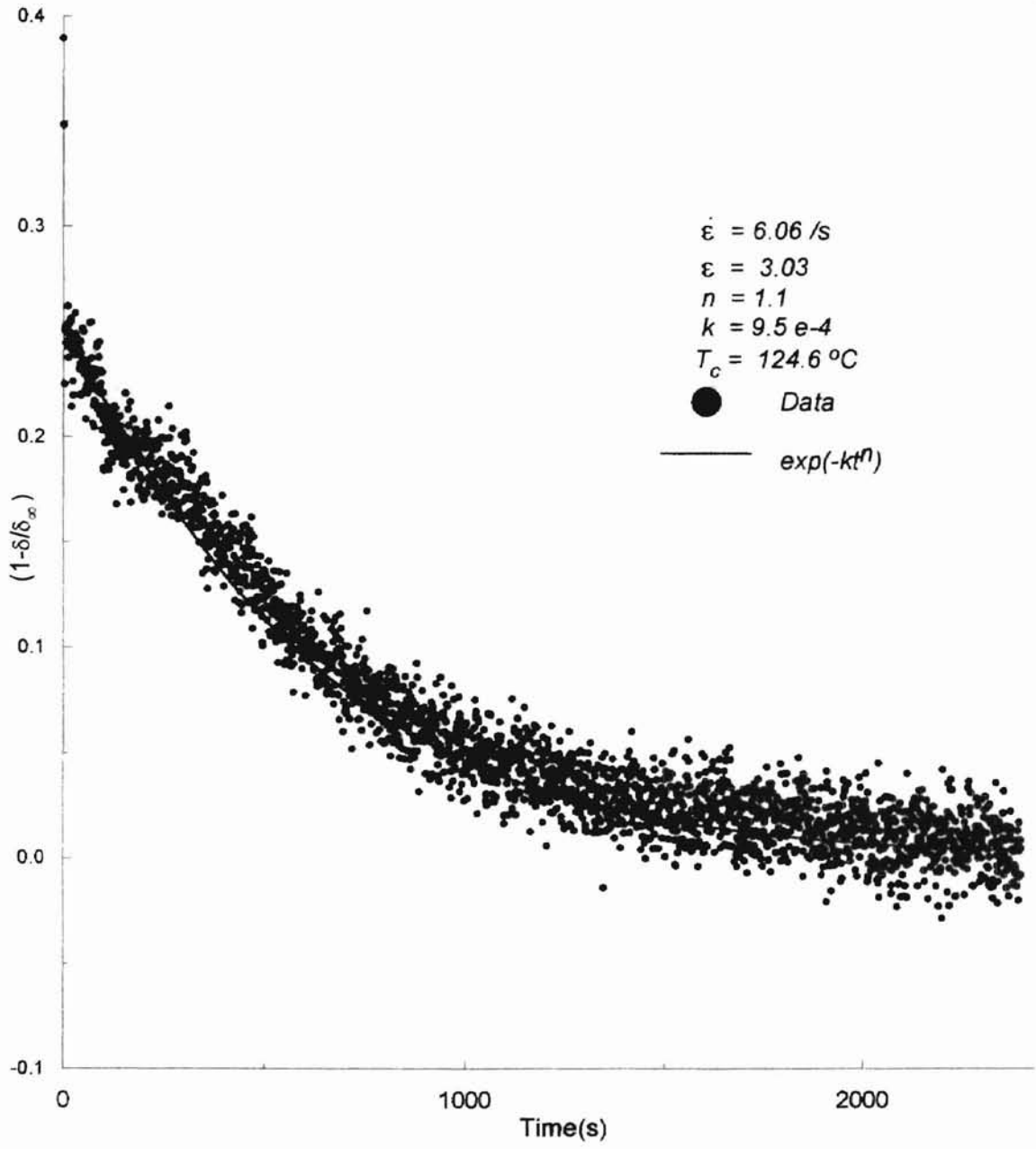

Figure B.18 Avrami Equation Using Kakani's Data in Figure D.18[7]

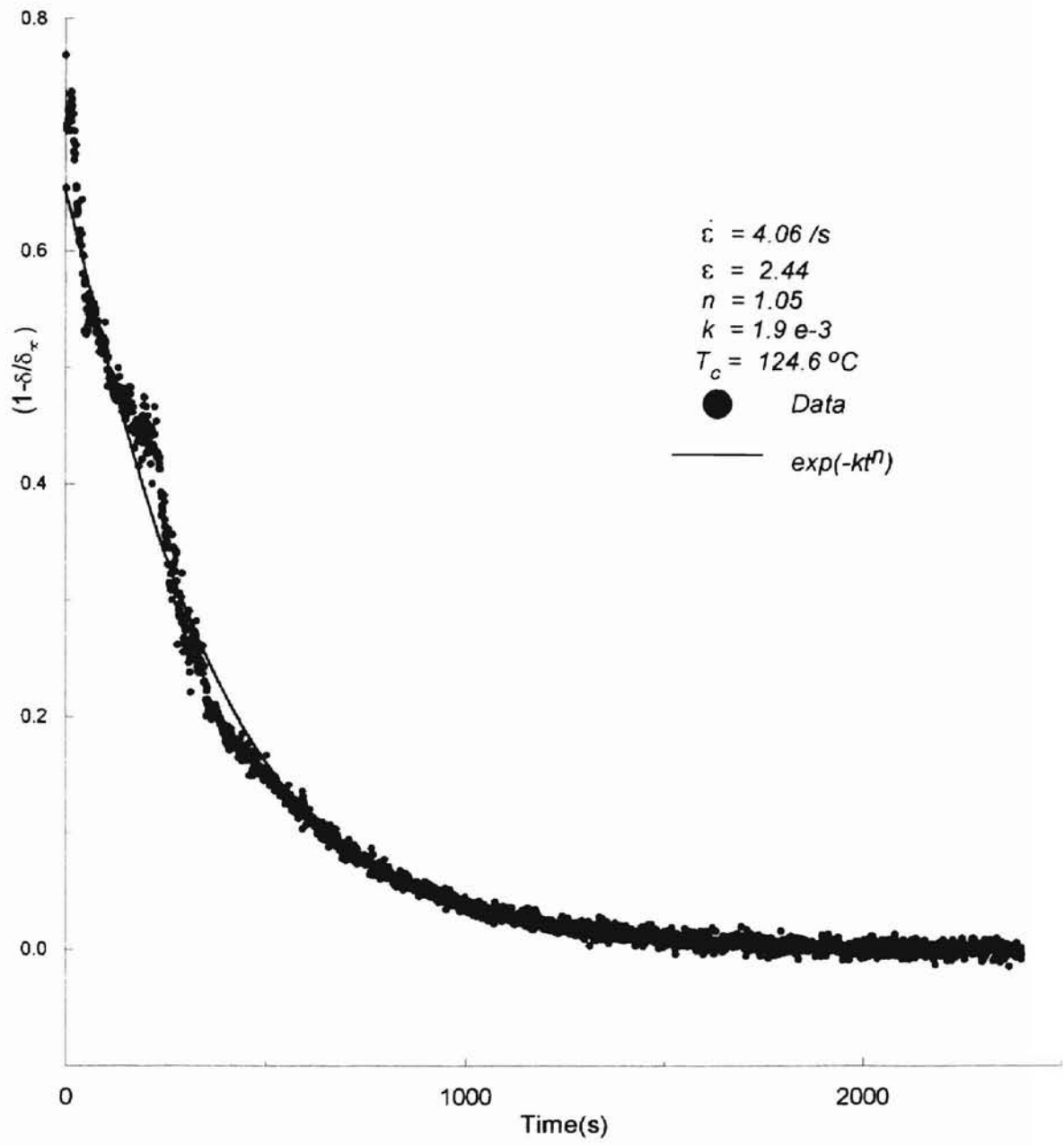

Figure B.19 Avrami Equation Using Kakani's Data in Figure D.19[7]

APPENDIX - C

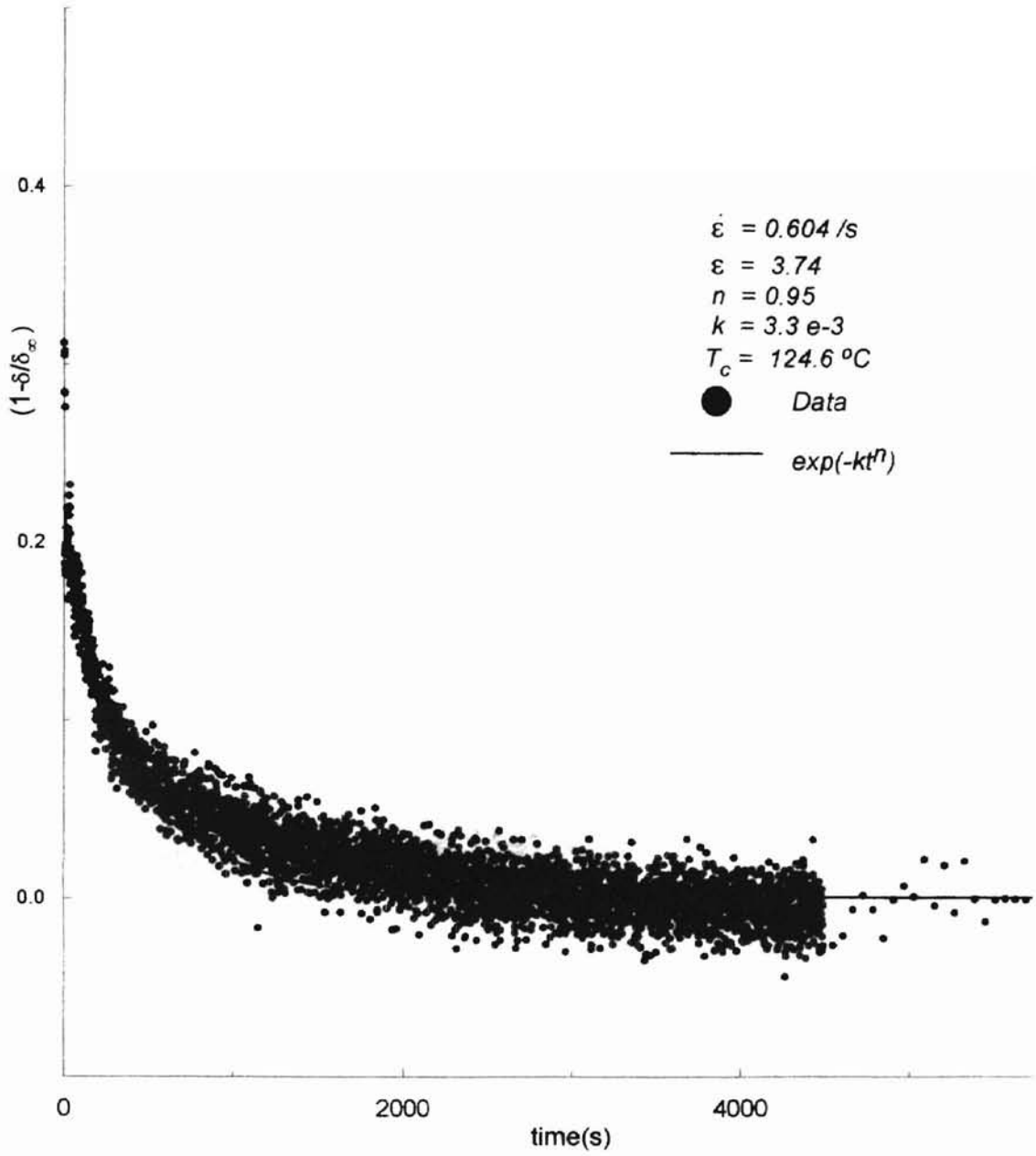

Figure C.1 Avrami Equation for Experiment 1 in Table 4.D

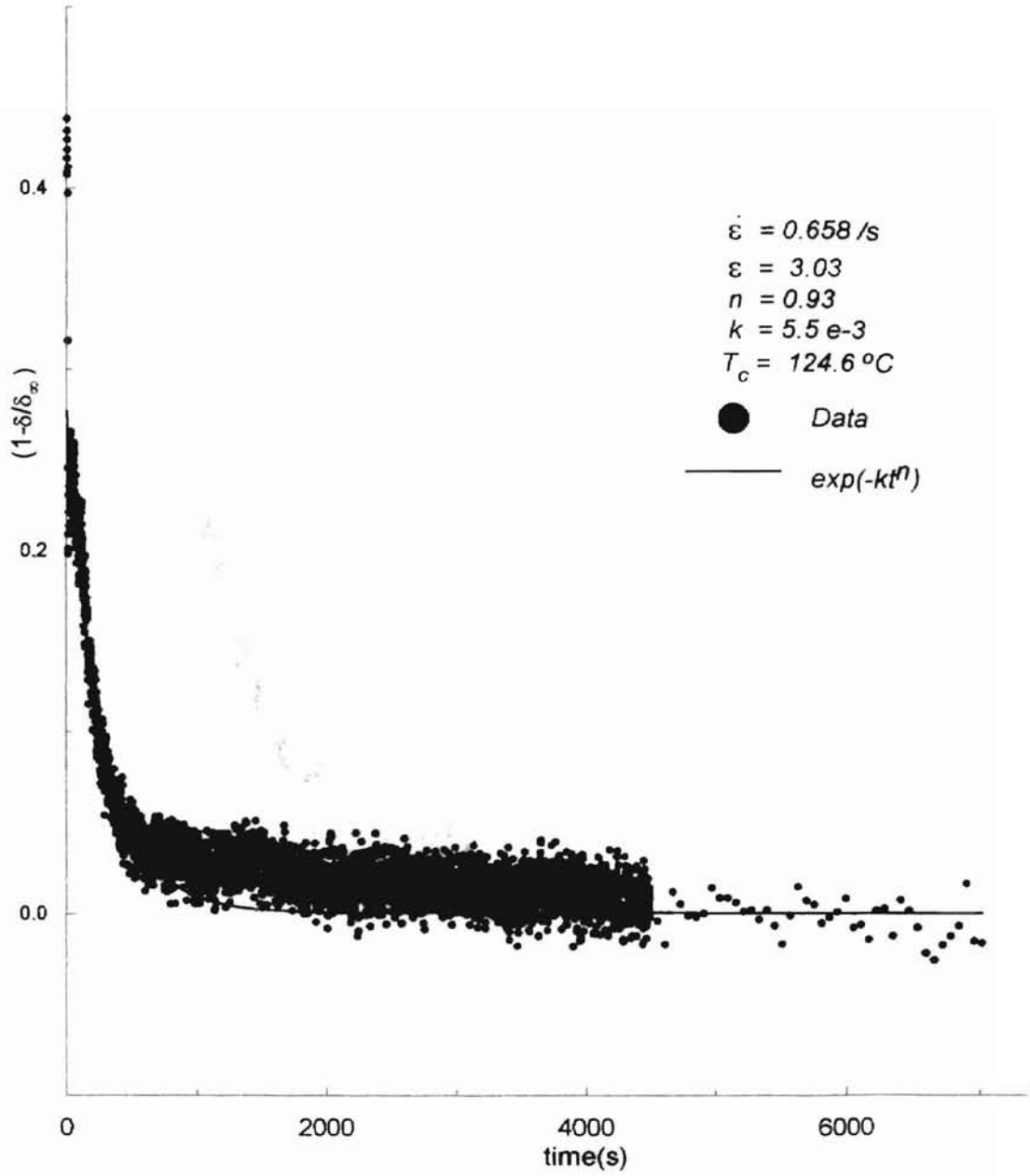

Figure C.2 Avrami Equation for Experiment 2 in Table 4.D

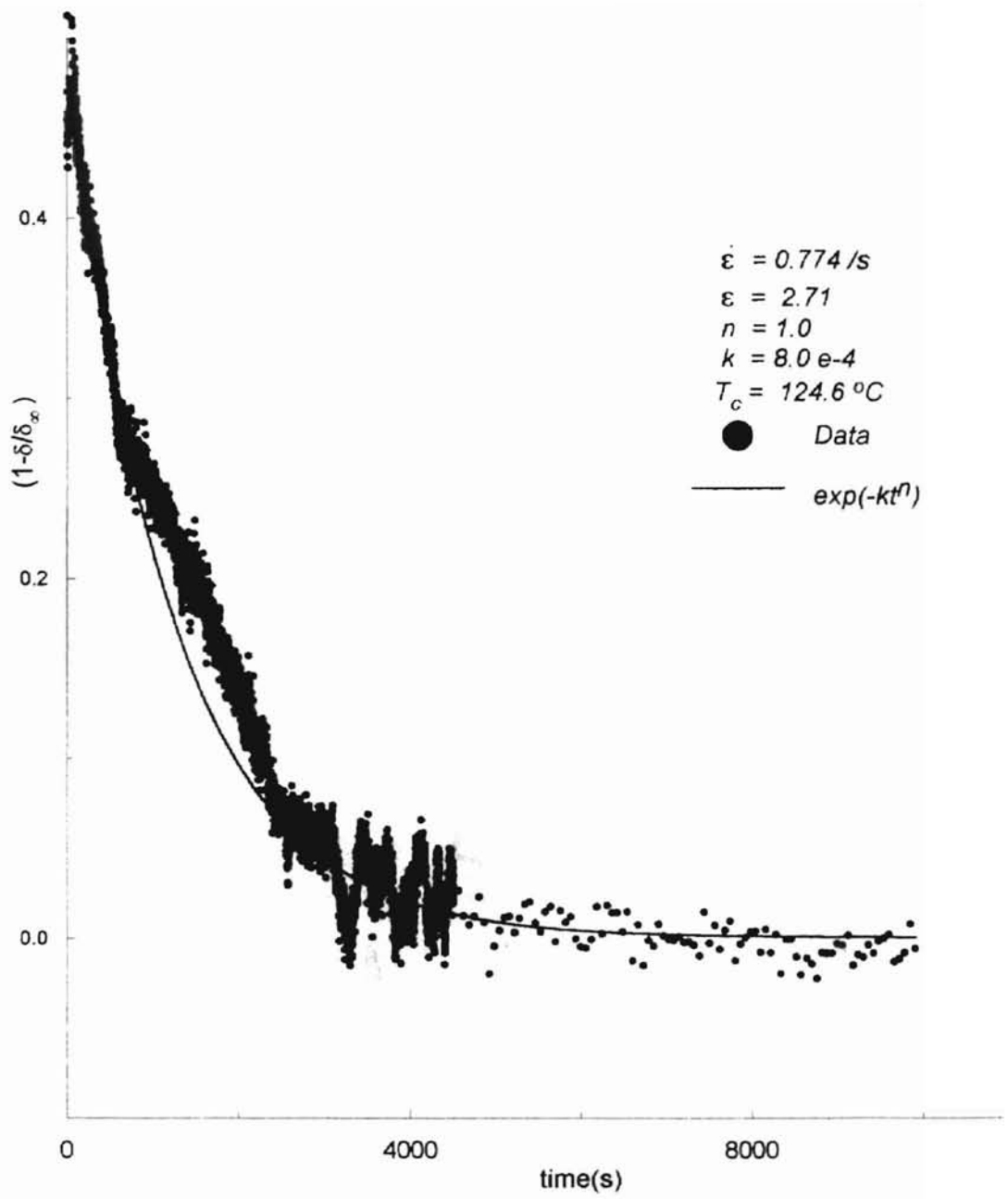

Figure C.3 Avrami Equation for Experiment 3 in Table 4.D

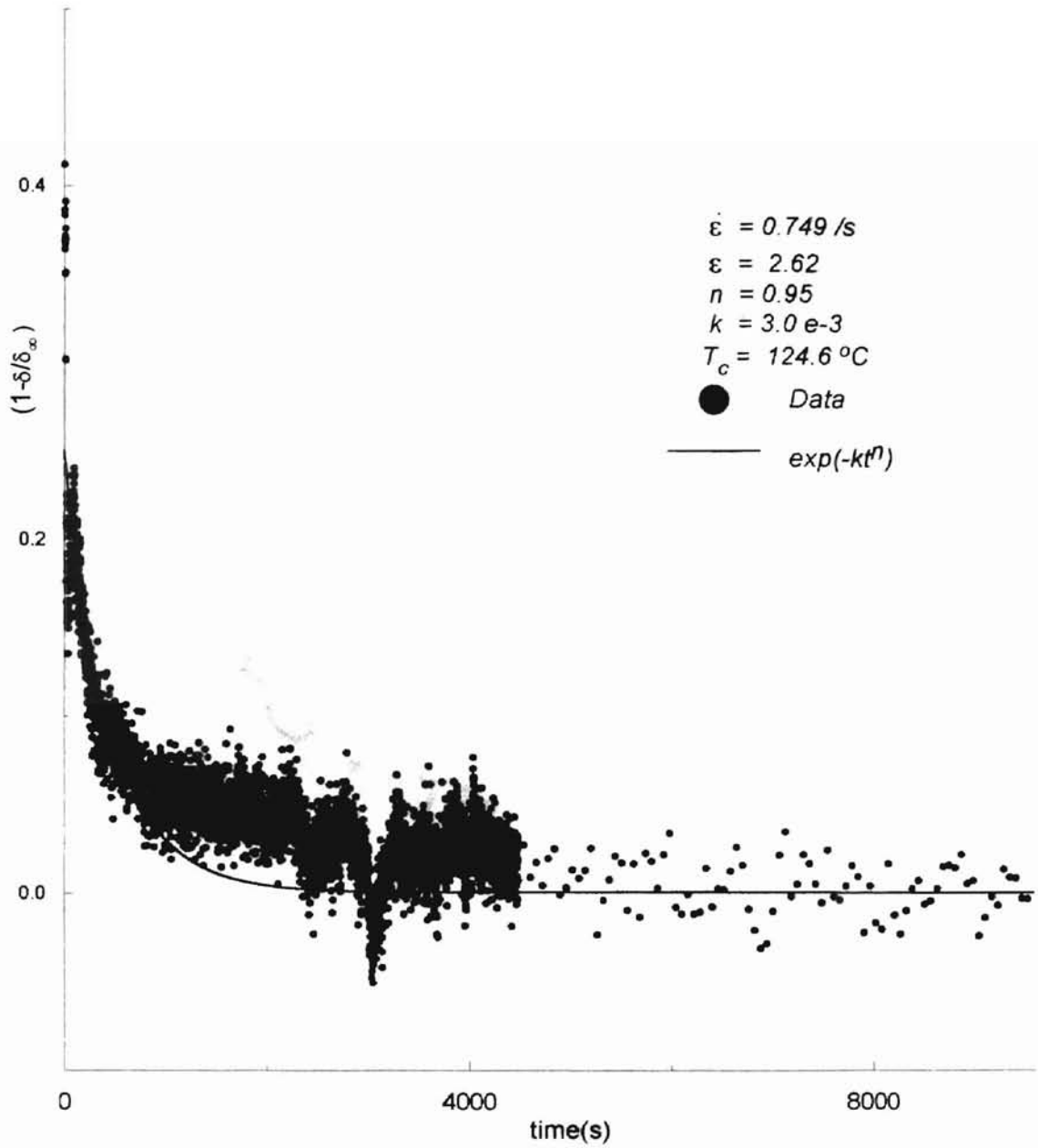

Figure C.4 Avrami Equation for Experiment 4 in Table 4.D

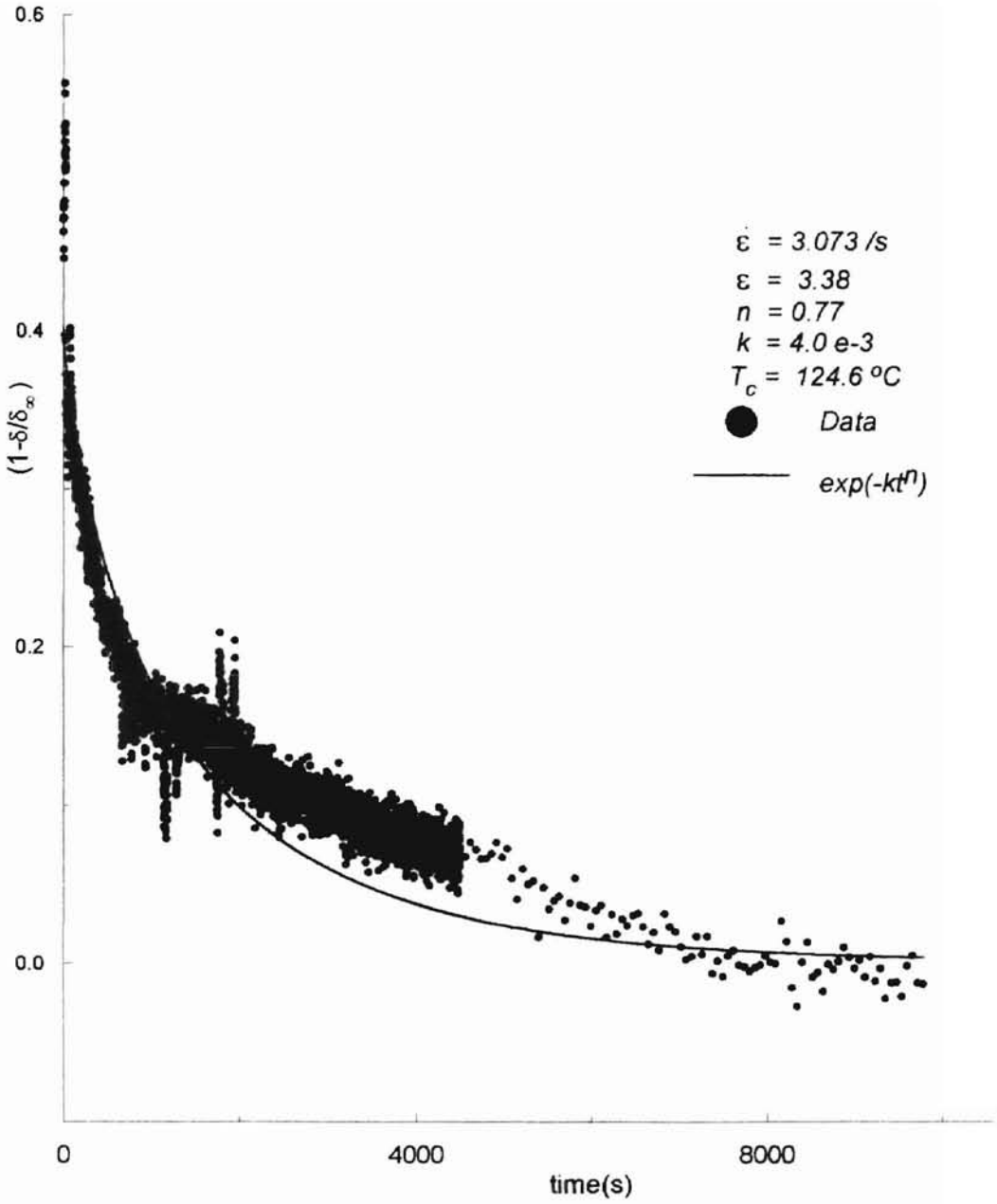

Figure C.5 Avrami Equation for Experiment 5 in Table 4.D

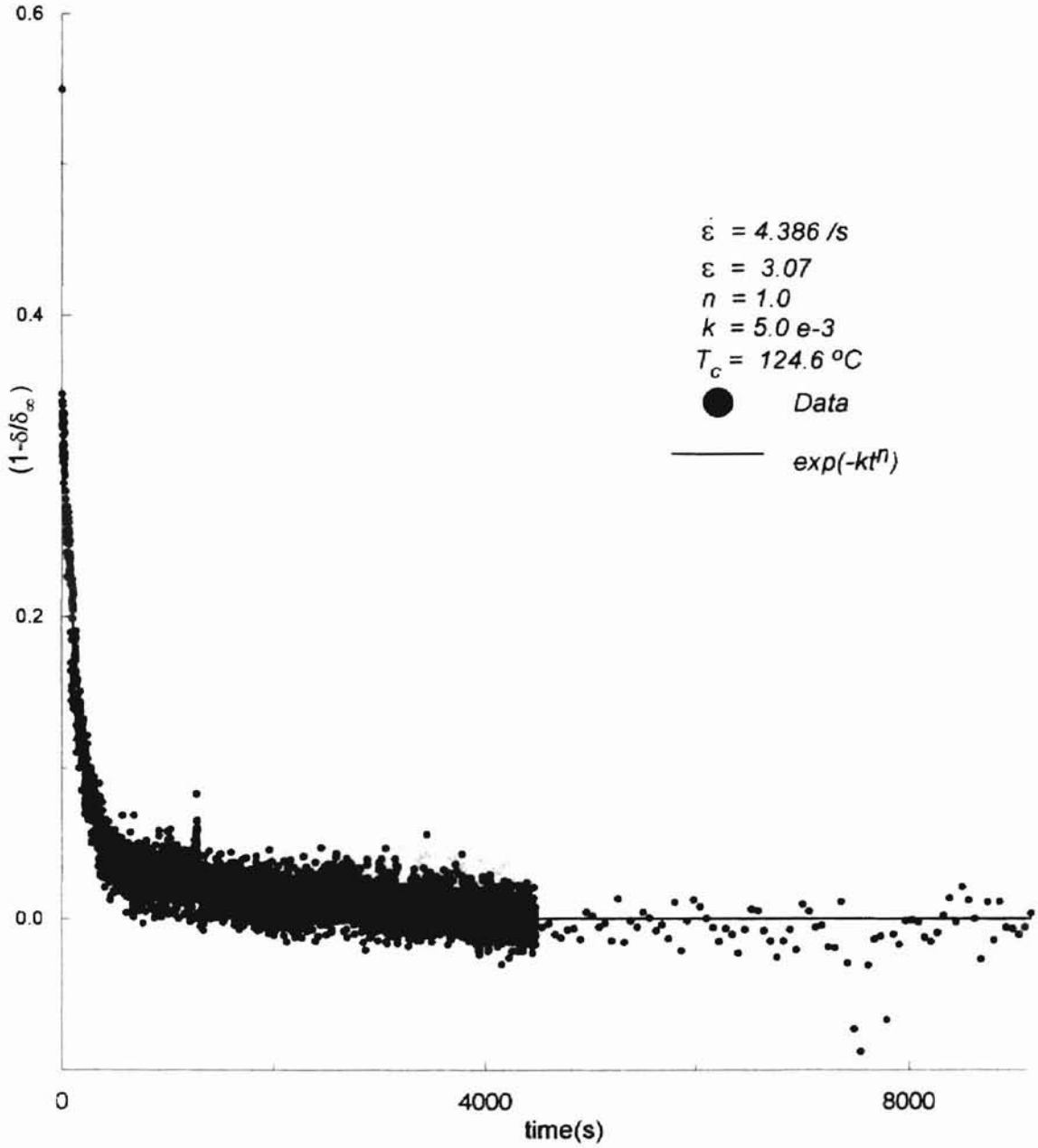

Figure C.6 Avrami Equation for Experiment 6 in Table 4.D

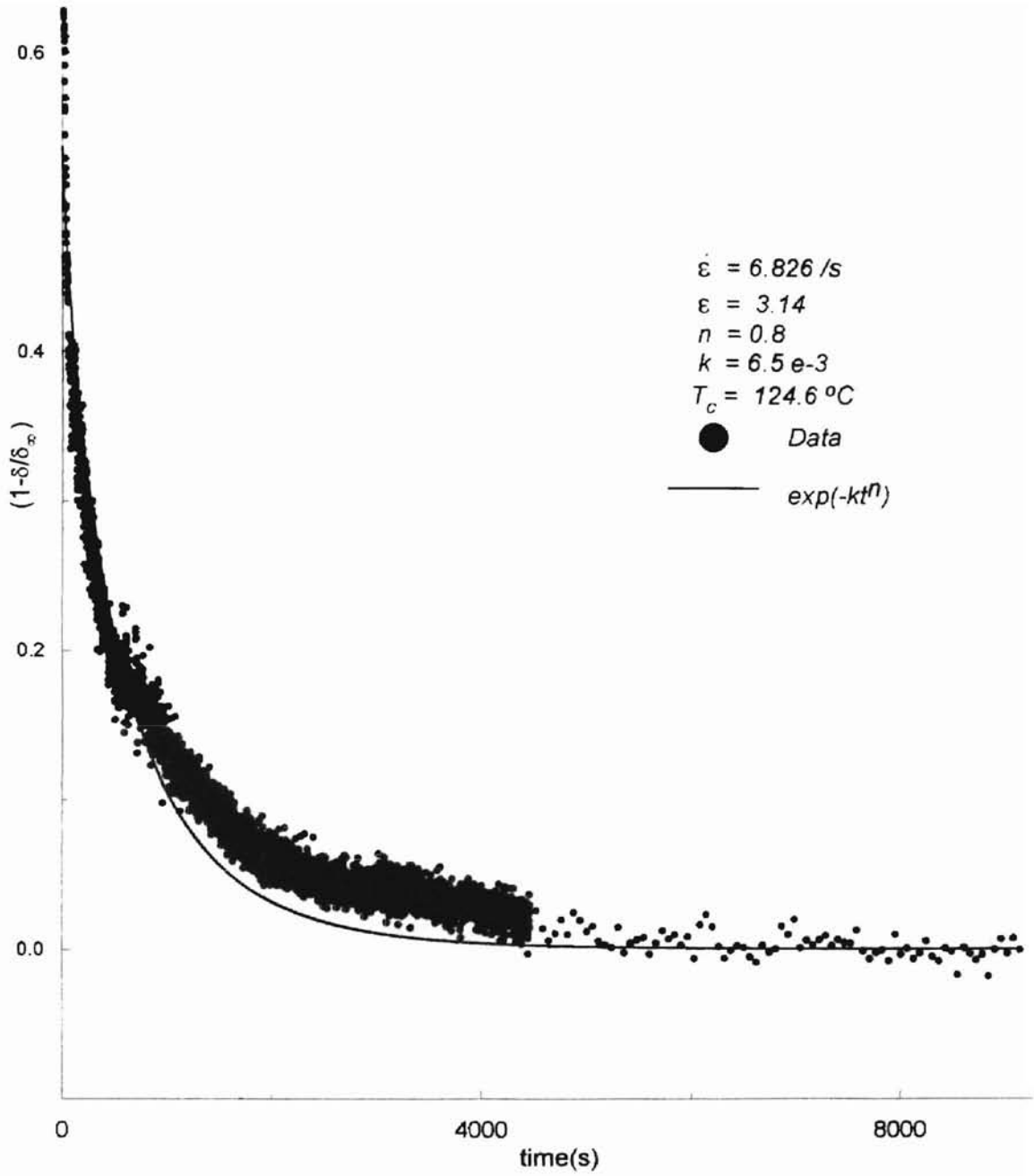

Figure C.7 Avrami Equation for Experiment 7 in Table 4.D

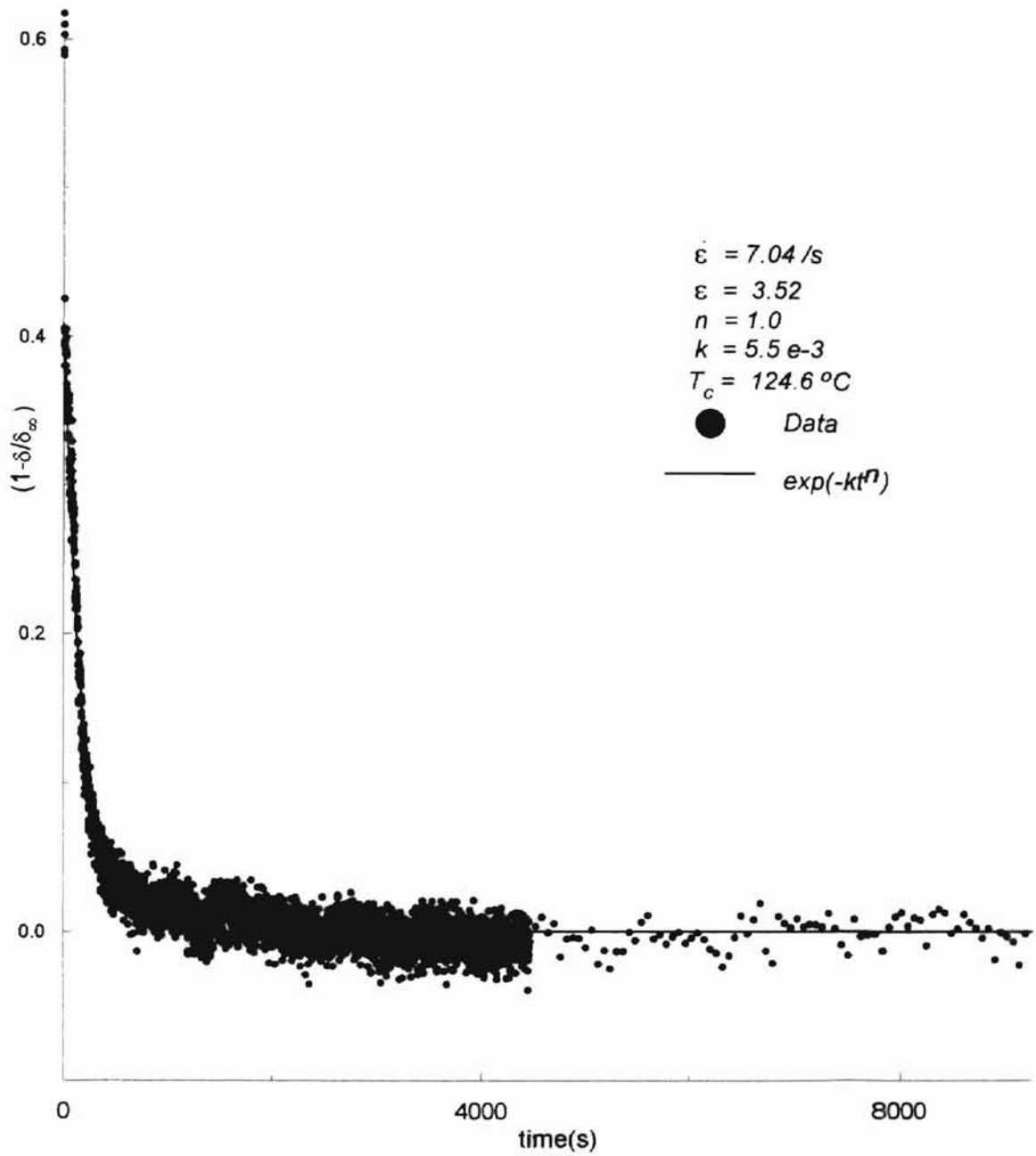

Figure C.8 Avrami Equation for Experiment 8 in Table 4.D

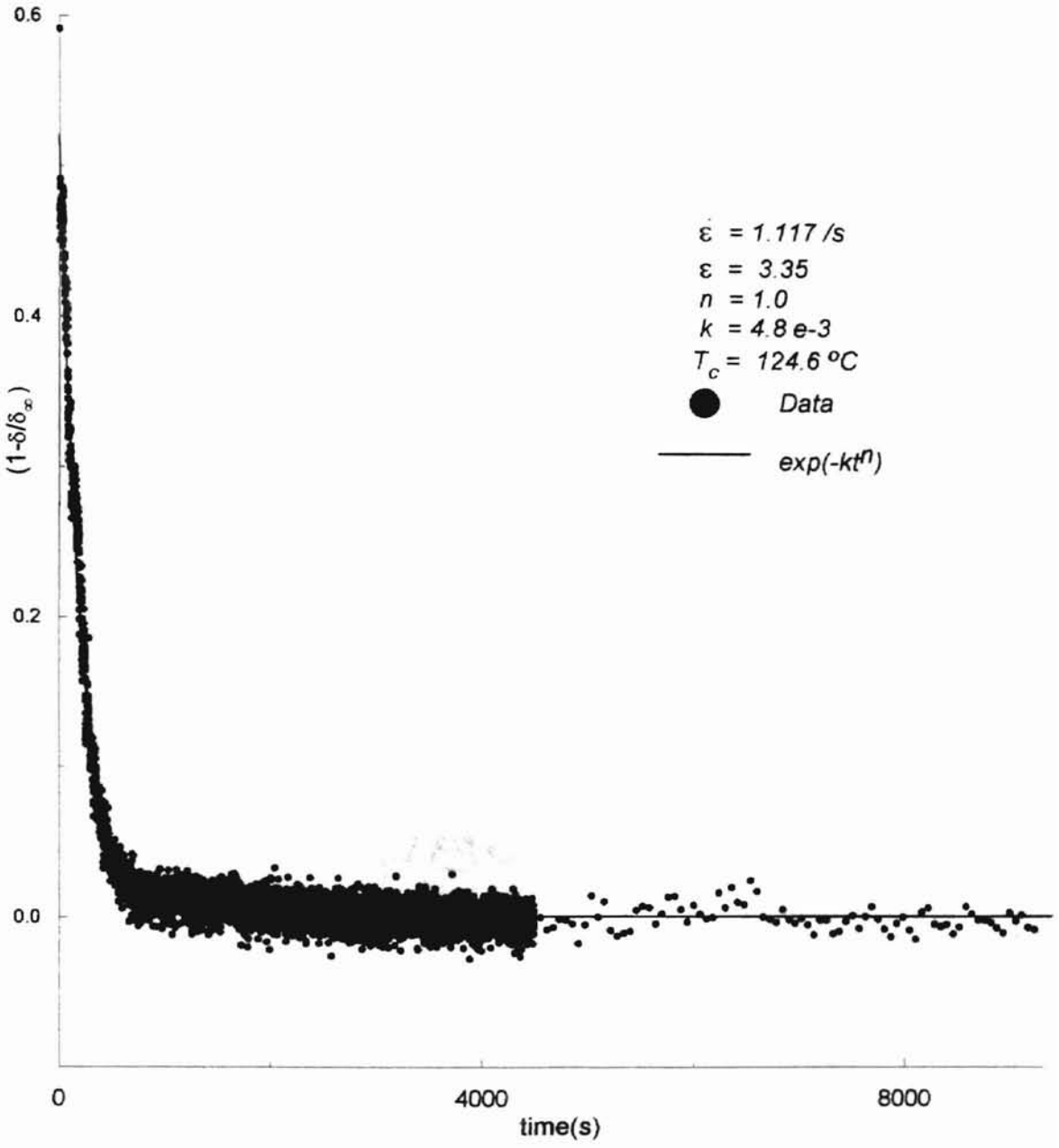

Figure C.9 Avrami Equation for Experiment 9 in Table 4.D

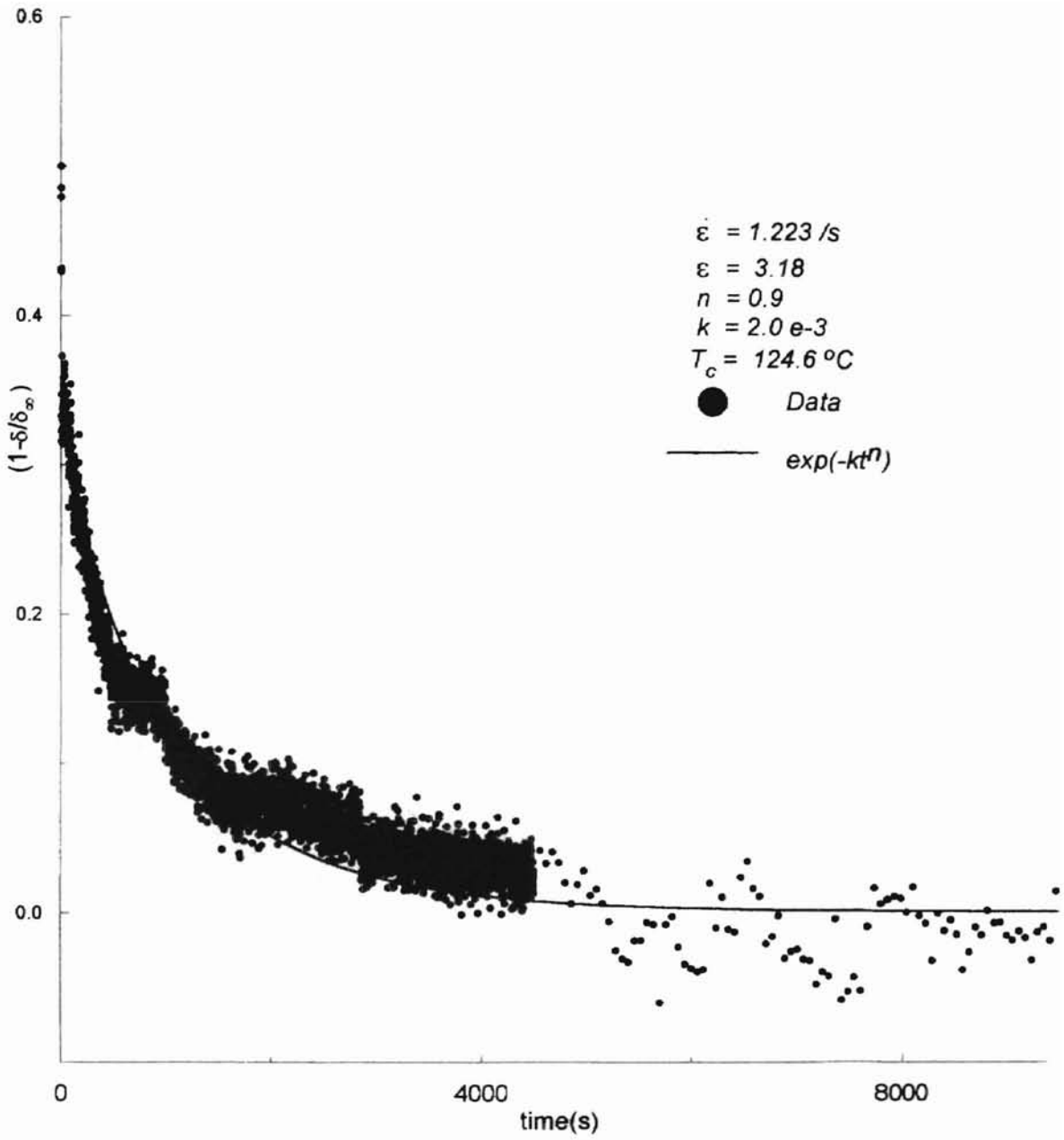

Figure C.10 Avrami Equation for Experiment 10 in Table 4.D

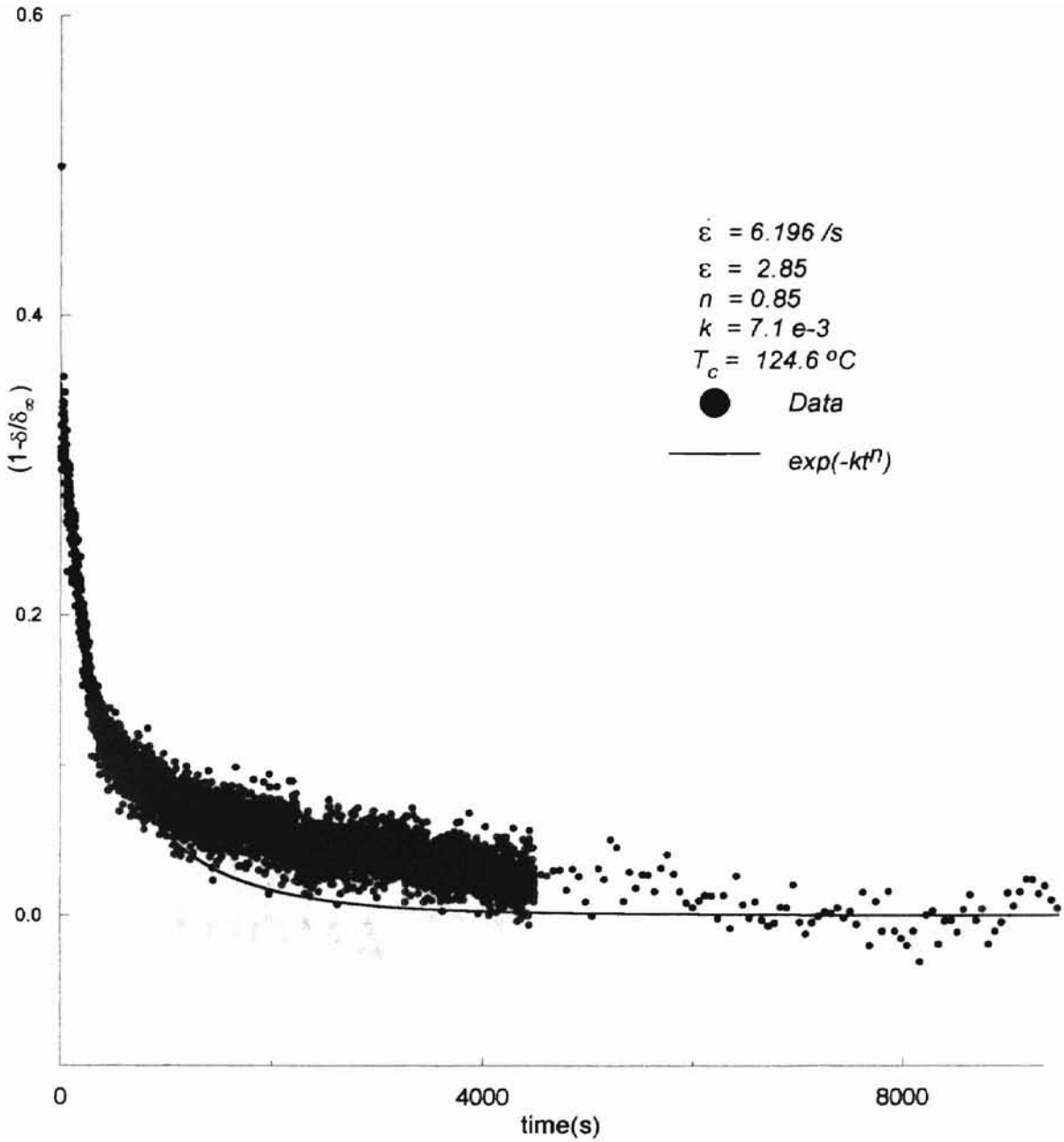

Figure C.11 Avrami Equation for Experiment 11 in Table 4.D

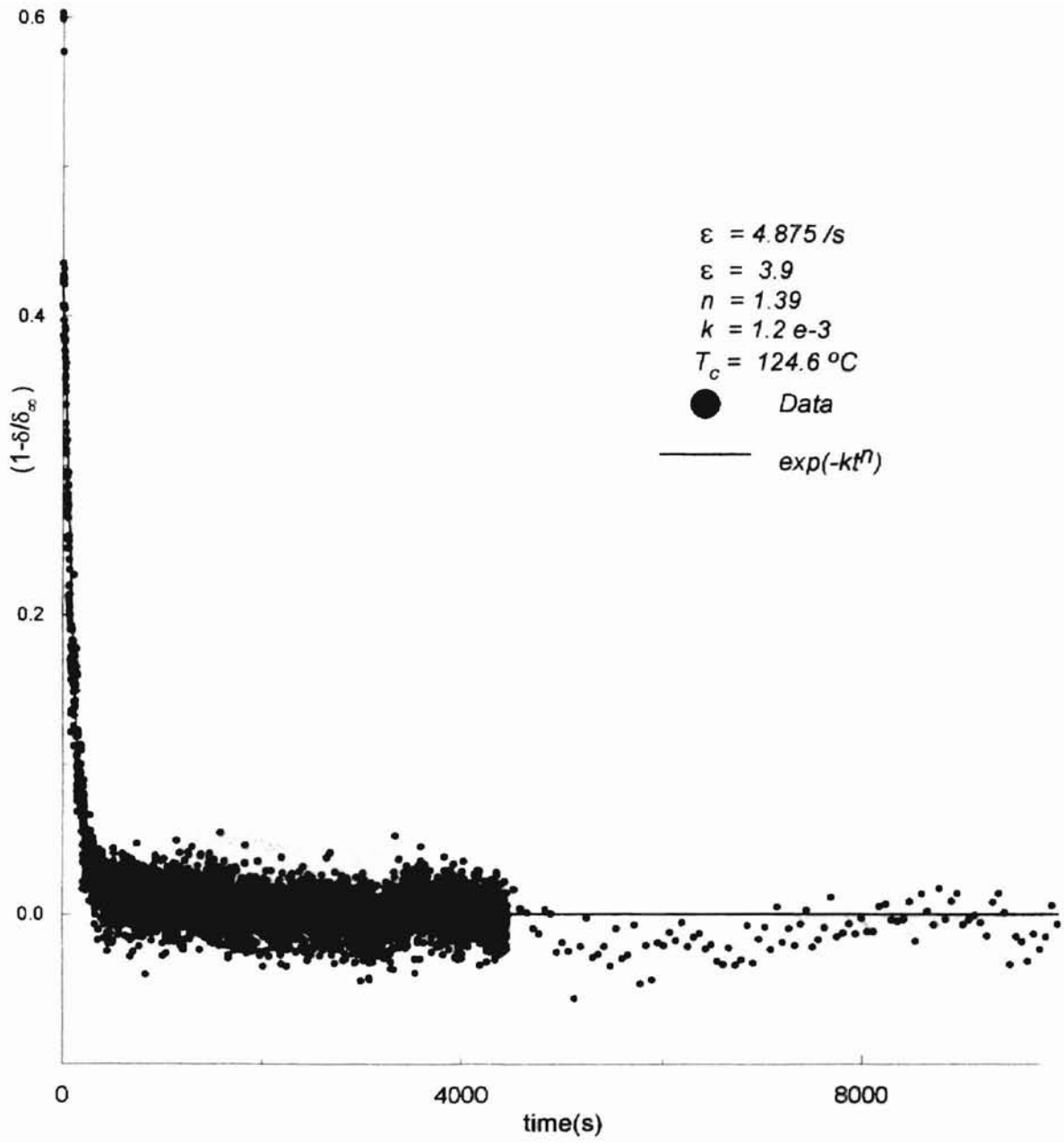

Figure C.12 Avrami Equation for Experiment 12 in Table 4.D

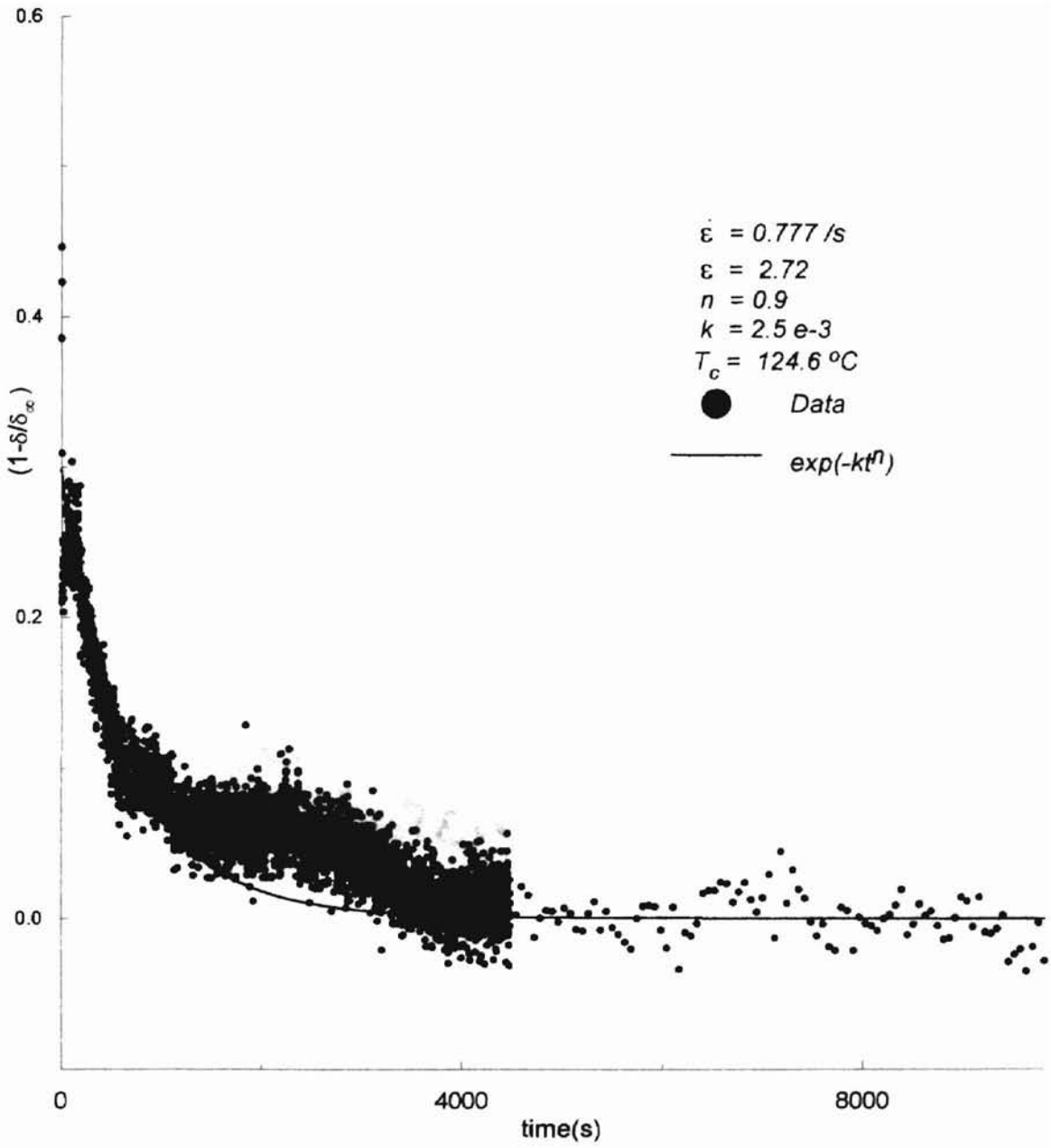

Figure C.13 Avrami Equation for Experiment 13 in Table 4.D

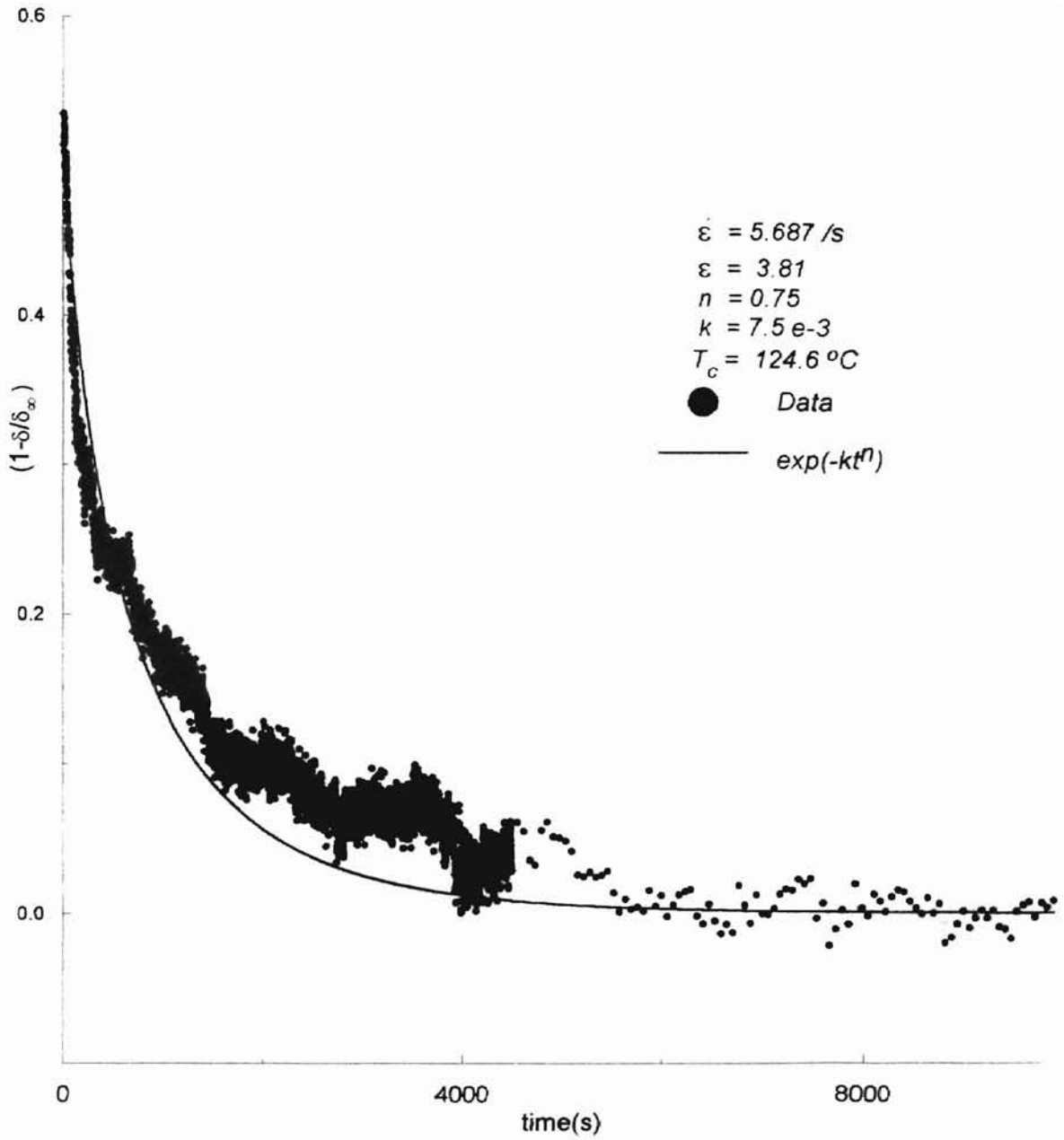

Figure C.14 Avrami Equation for Experiment 14 in Table 4.D

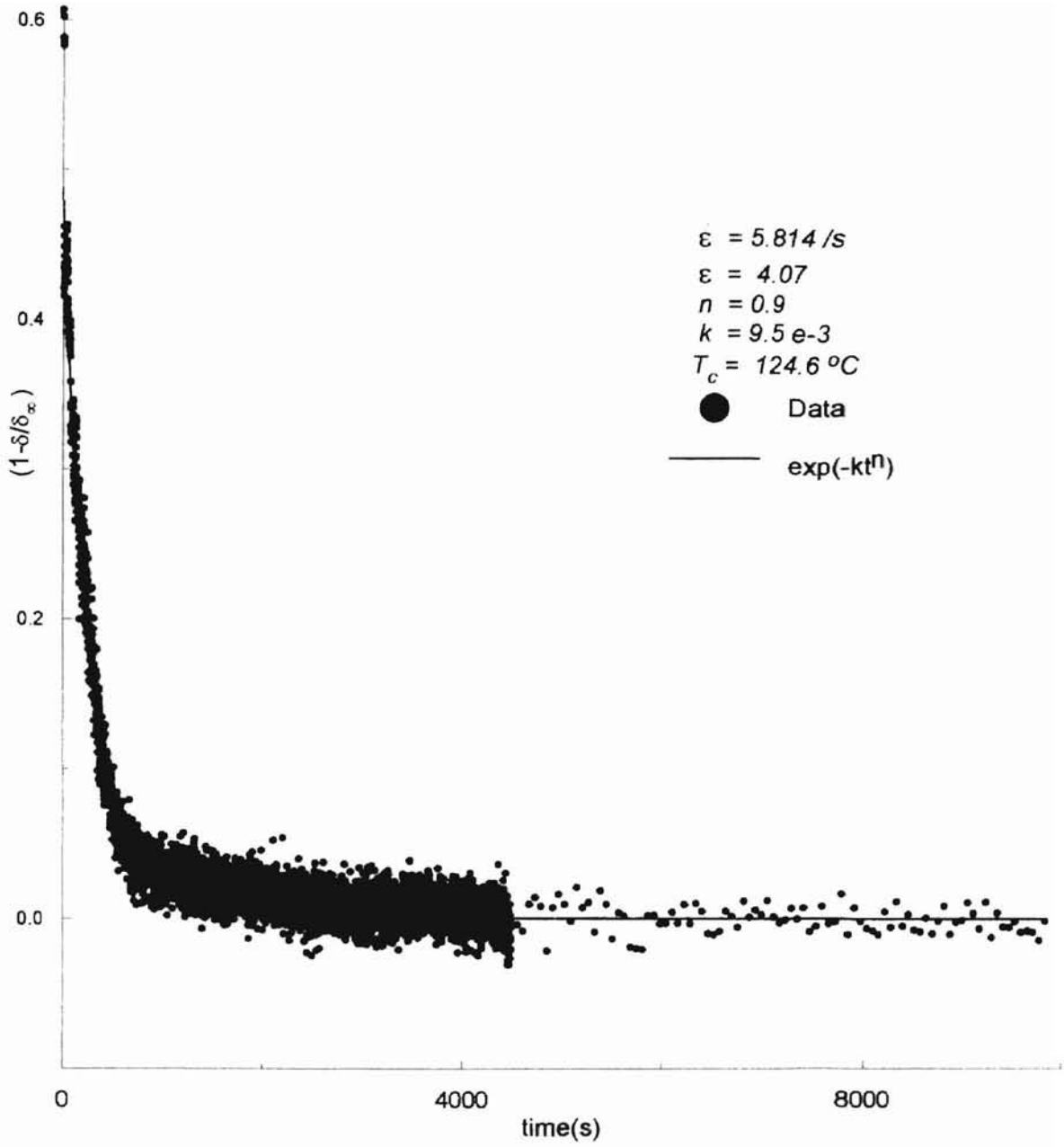

Figure C.15 Avrami Equation for Experiment 15 in Table 4.D

APPENDIX - D

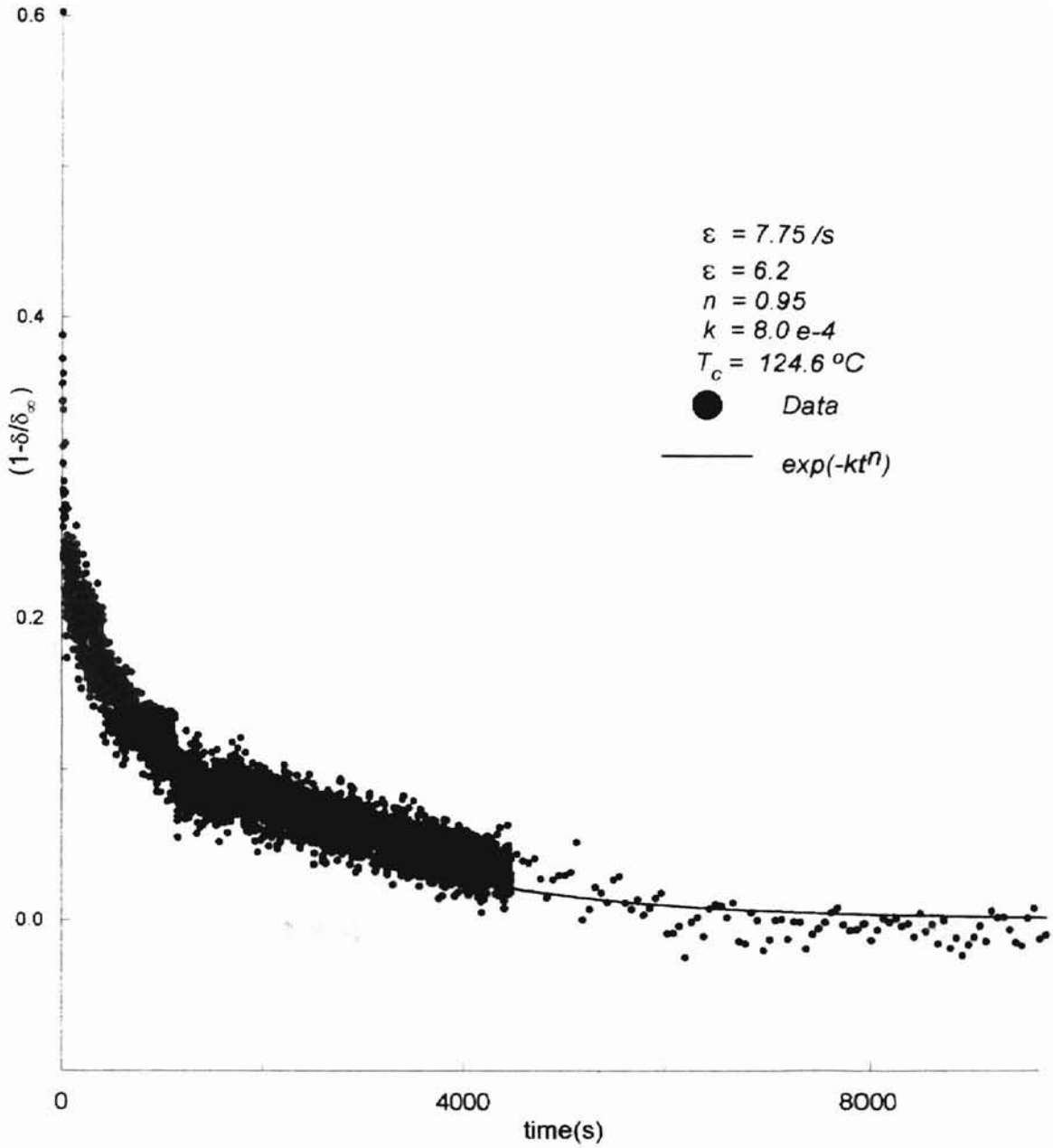

Figure D.1 Avrami Equation for Experiment 1 in Table 4.E

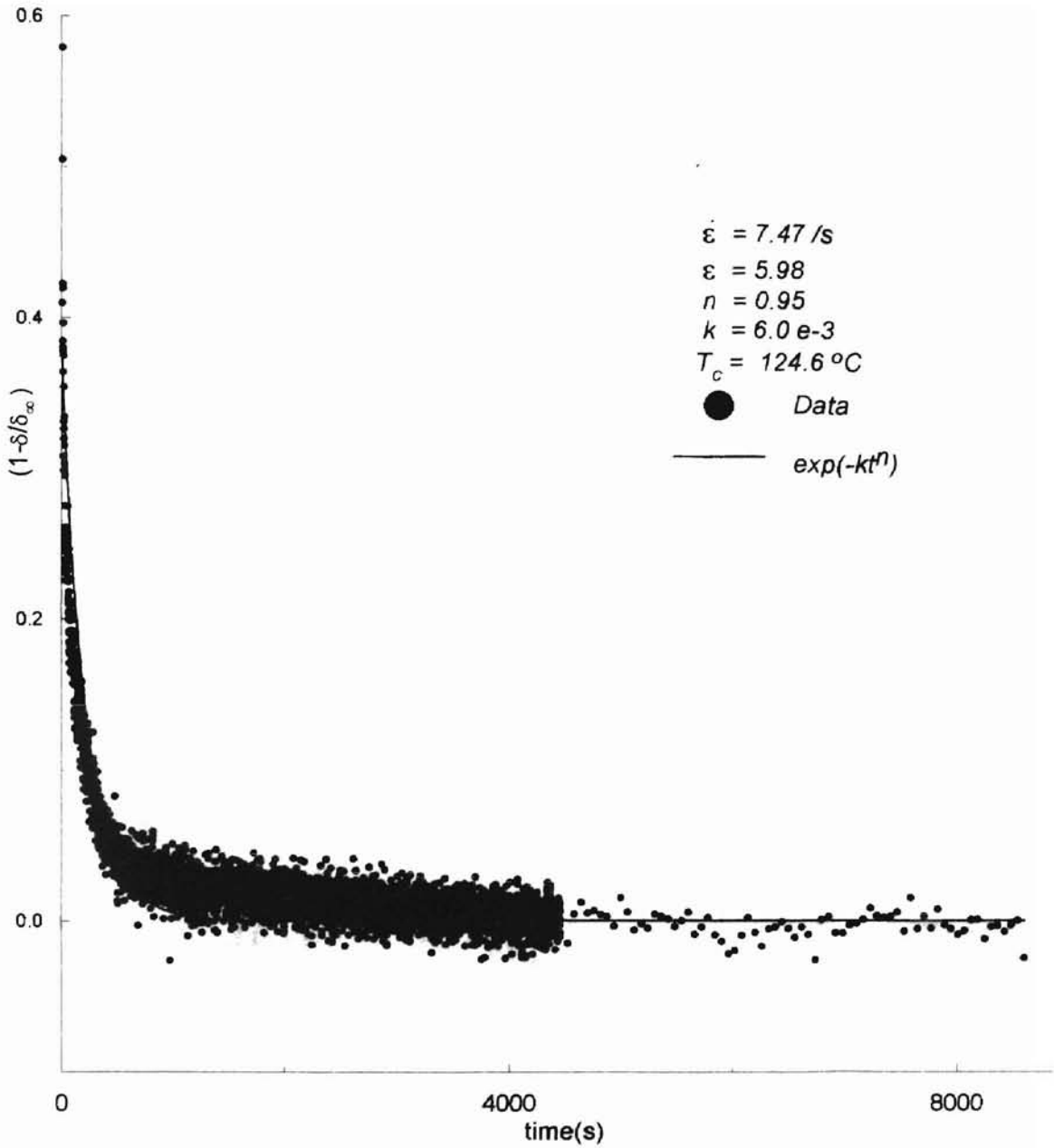

Figure D.2 Avrami Equation for Experiment 2 in Table 4.E

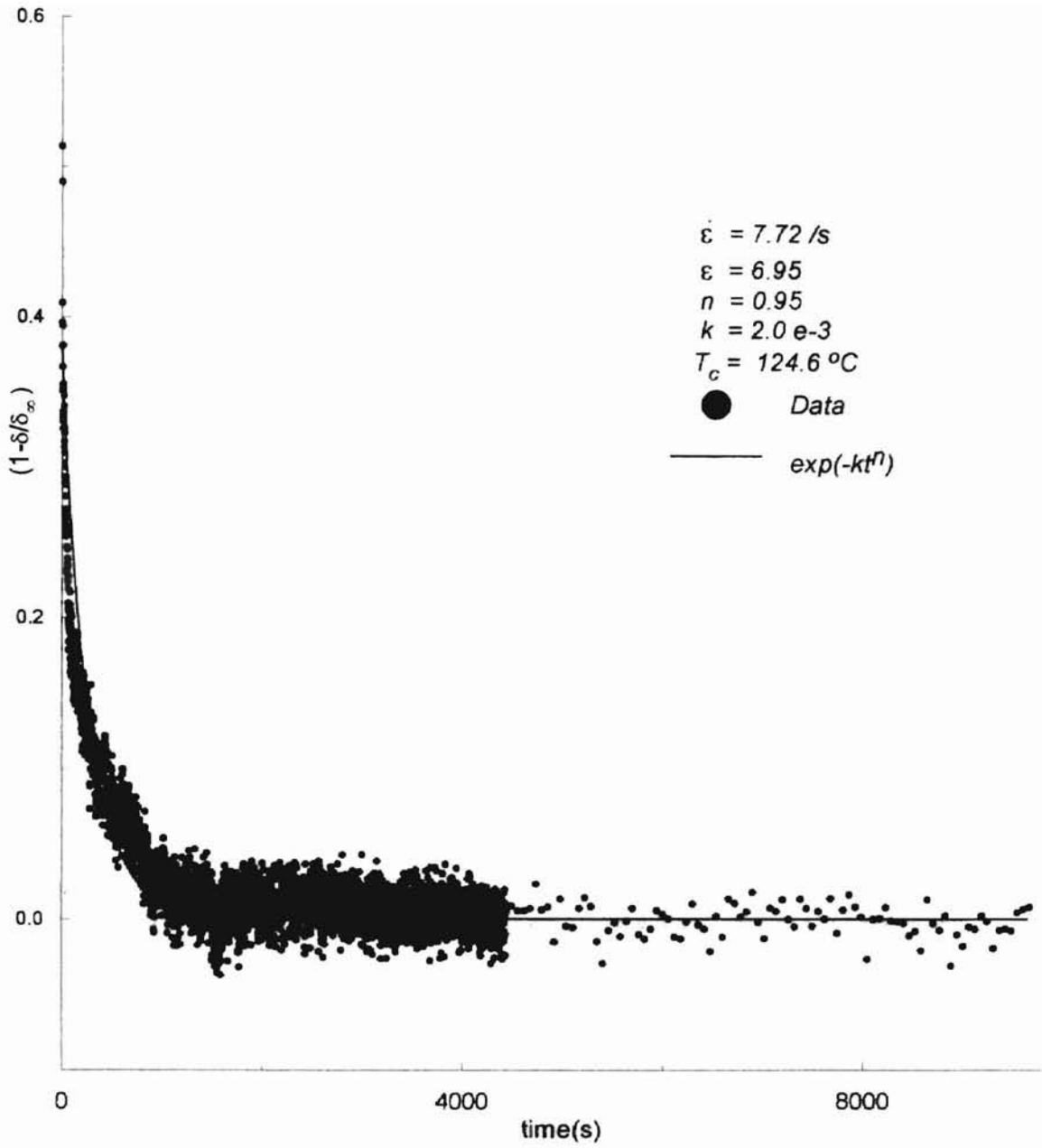

Figure D.3 Avrami Equation for Experiment 3 in Table 4.E

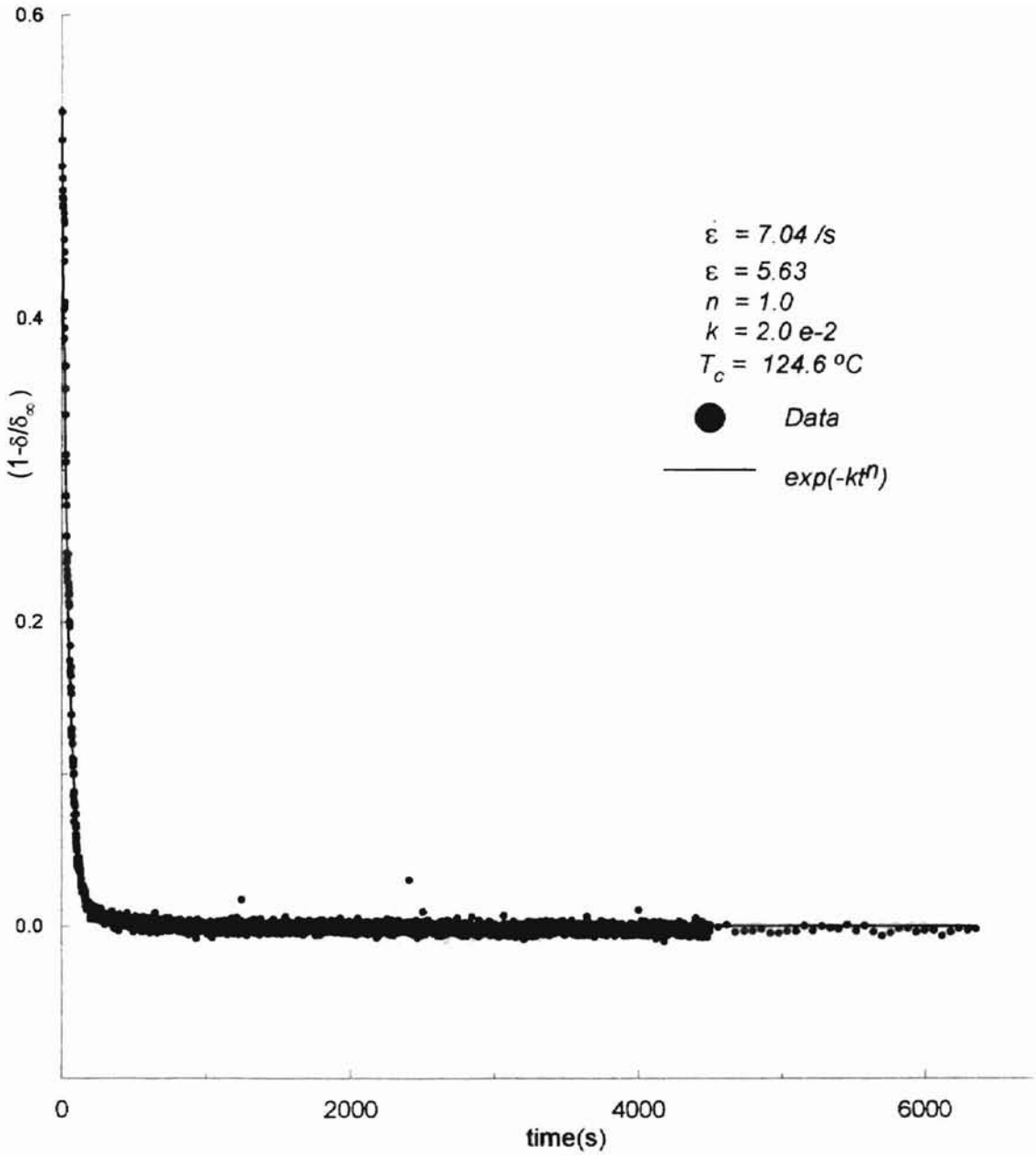

Figure D.4 Avrami Equation for Experiment 4 in Table 4.E

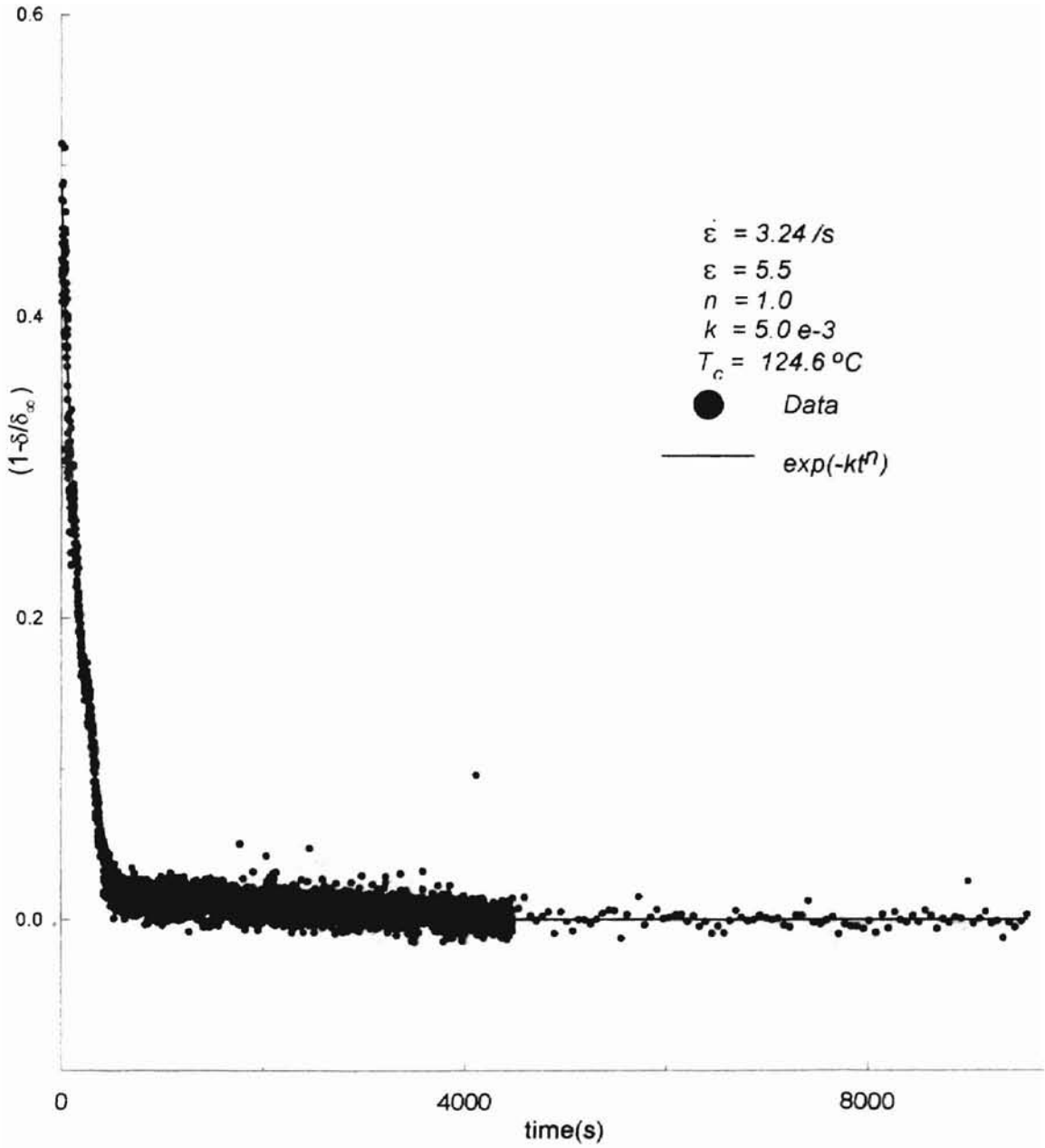

Figure D.5 Avrami Equation for Experiment 5 in Table 4.E

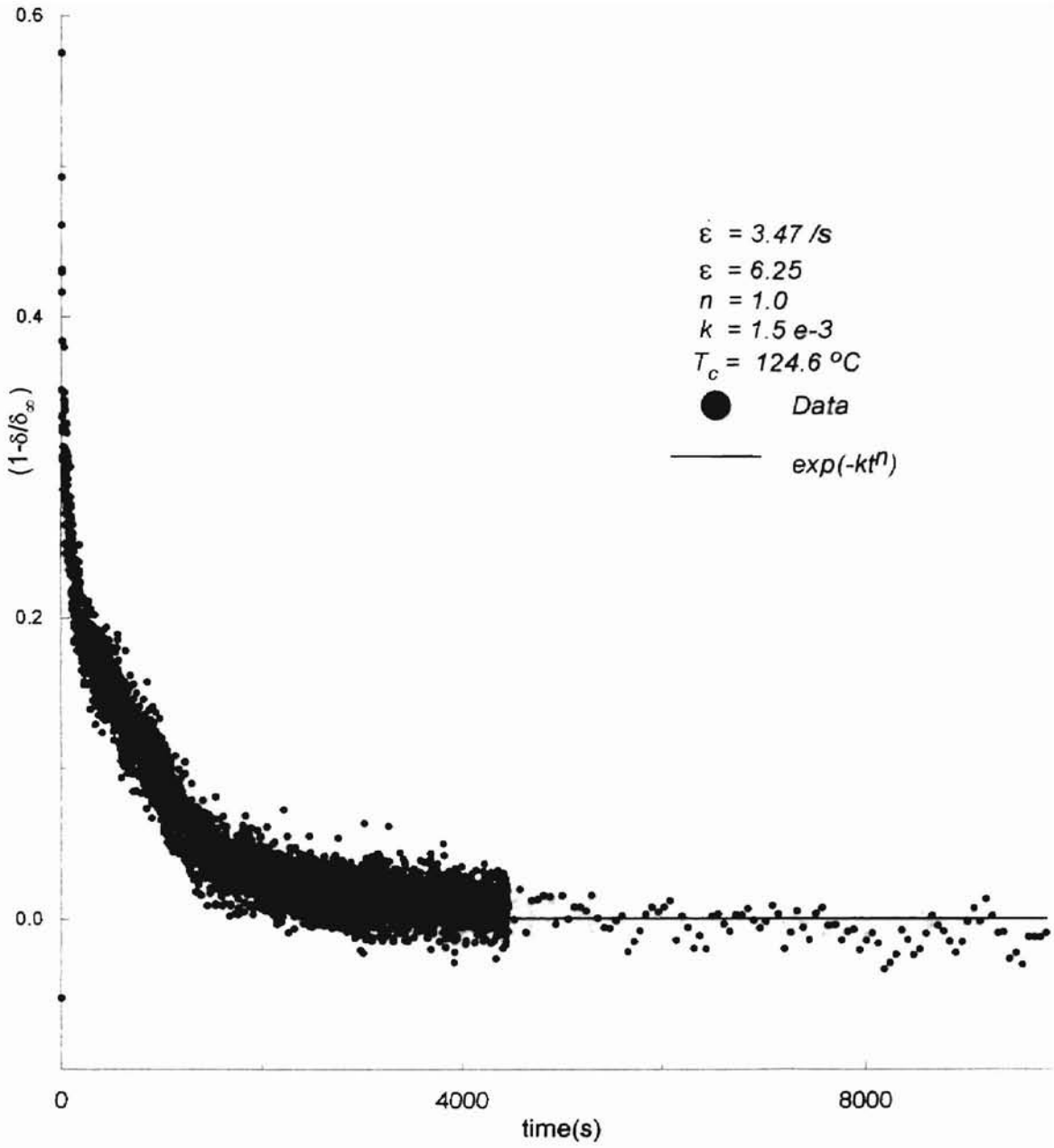

Figure D.6 Avrami Equation for Experiment 6 in Table 4.E

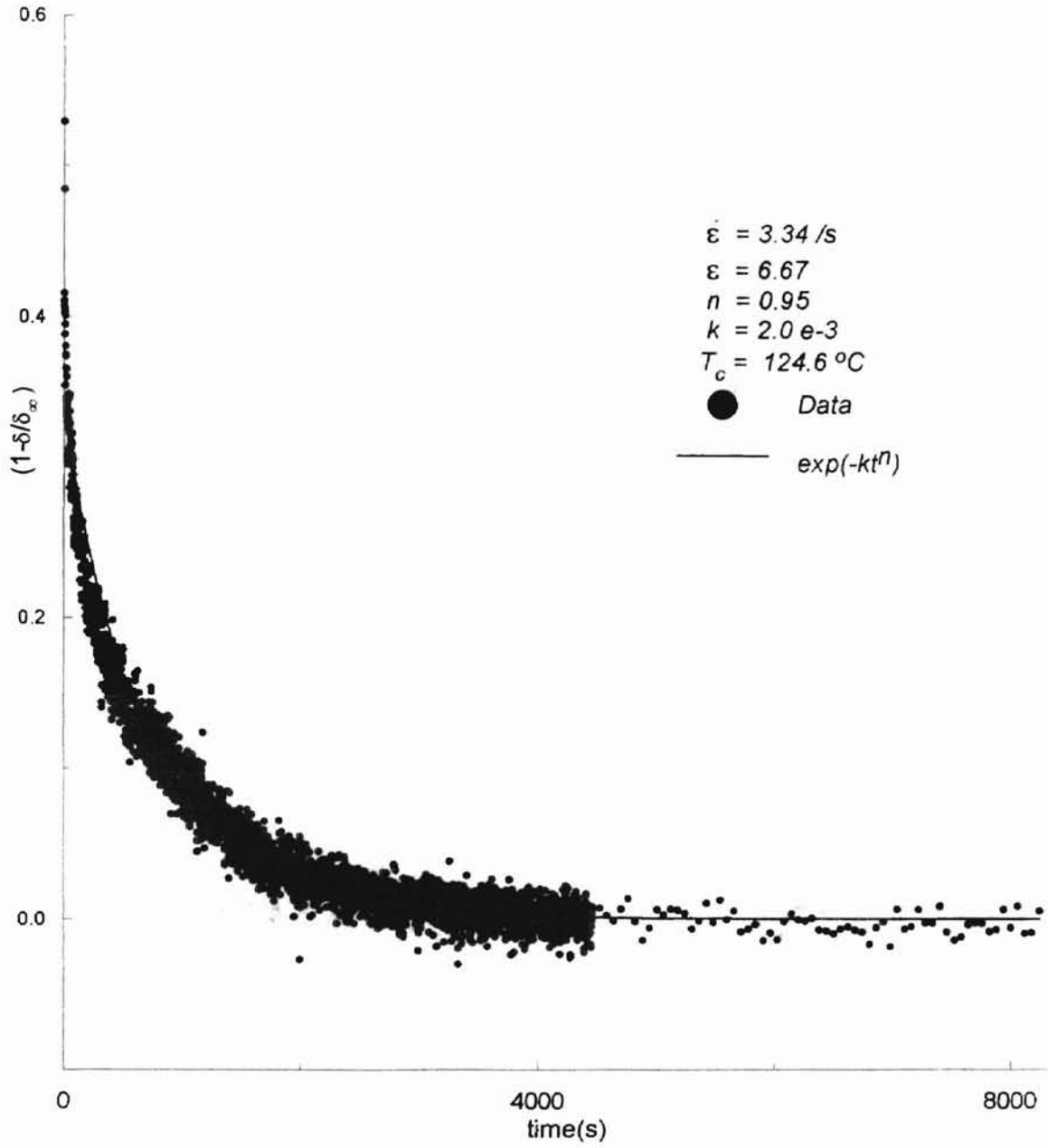

Figure D.7 Avrami Equation for Experiment 7 in Table 4.E

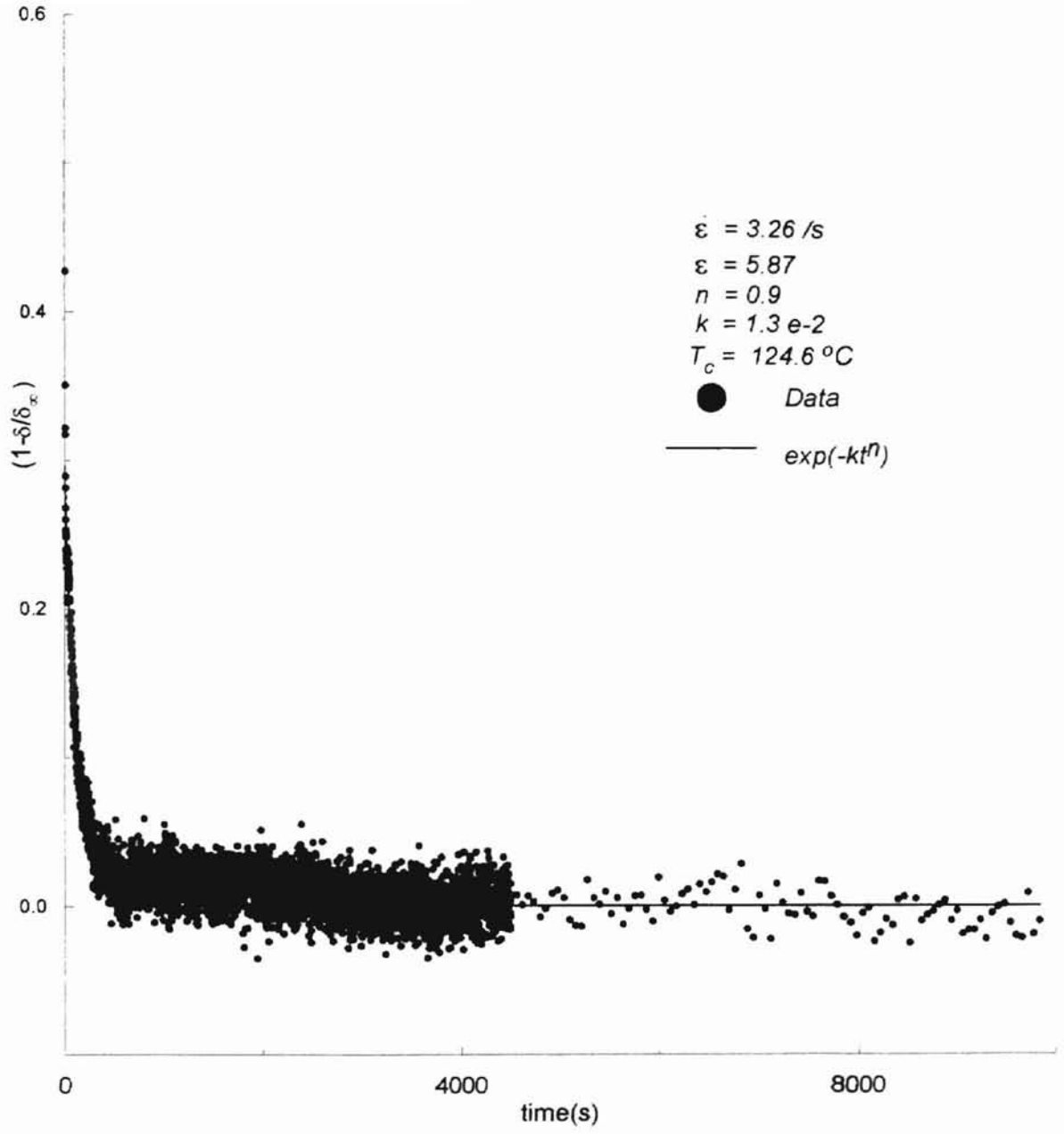

Figure D.8 Avrami Equation for Experiment 8 in Table 4.E

APPENDIX - E

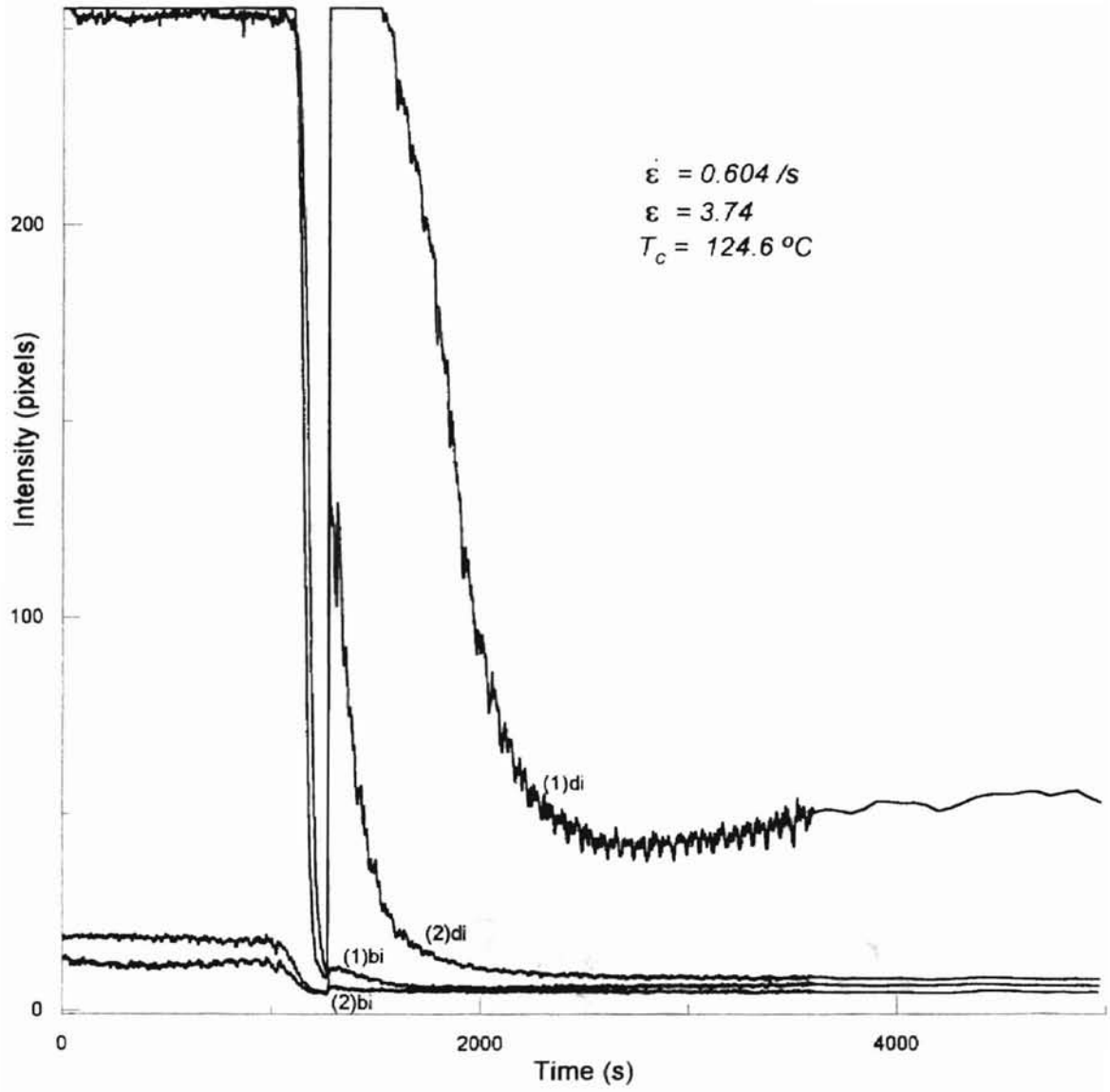

Figure E.1a Dichroism and Birefringence Intensity versus Time at Locations (1) and (2); 'di' and 'bi' stand for Dichroism and birefringence, respectively

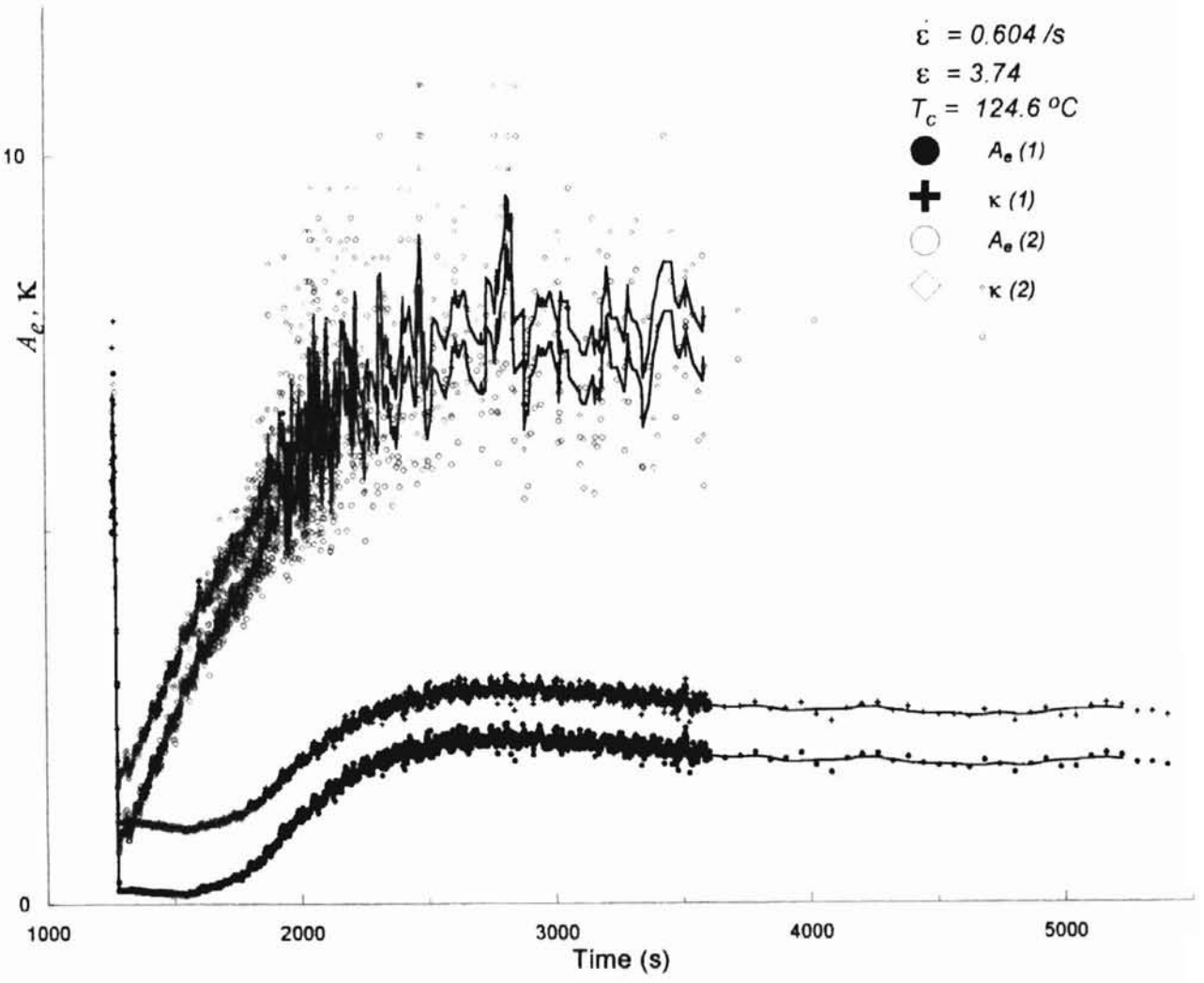

Figure E.1b Absorptivity (A_e), and Kappa (κ) Versus Time for Figure E.1a

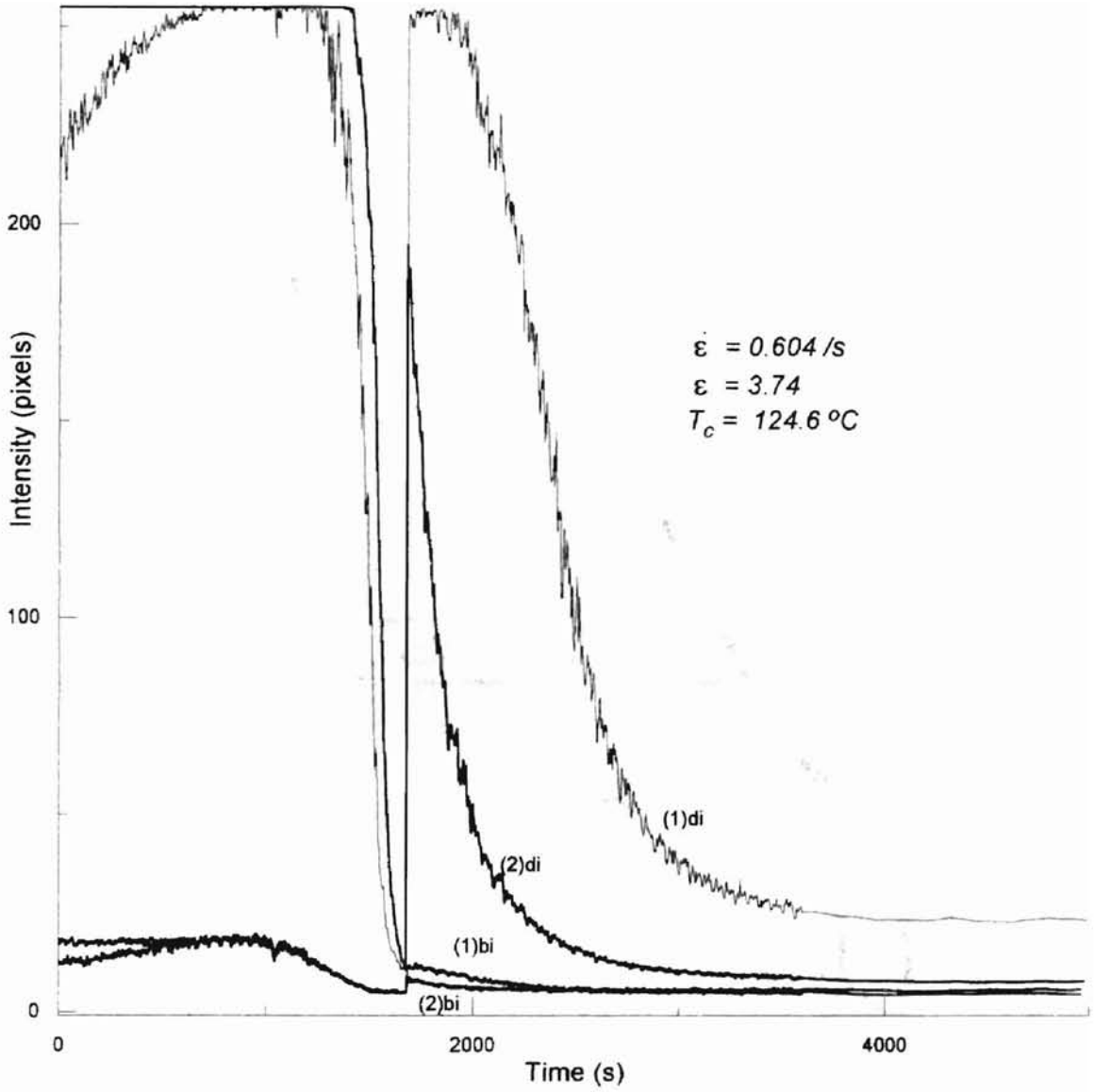

Figure E.2a Dichroism and Birefringence Intensity Versus Time at Locations (1) and (2); 'di' and 'bi' Stand for Dichroism and Birefringence, Respectively

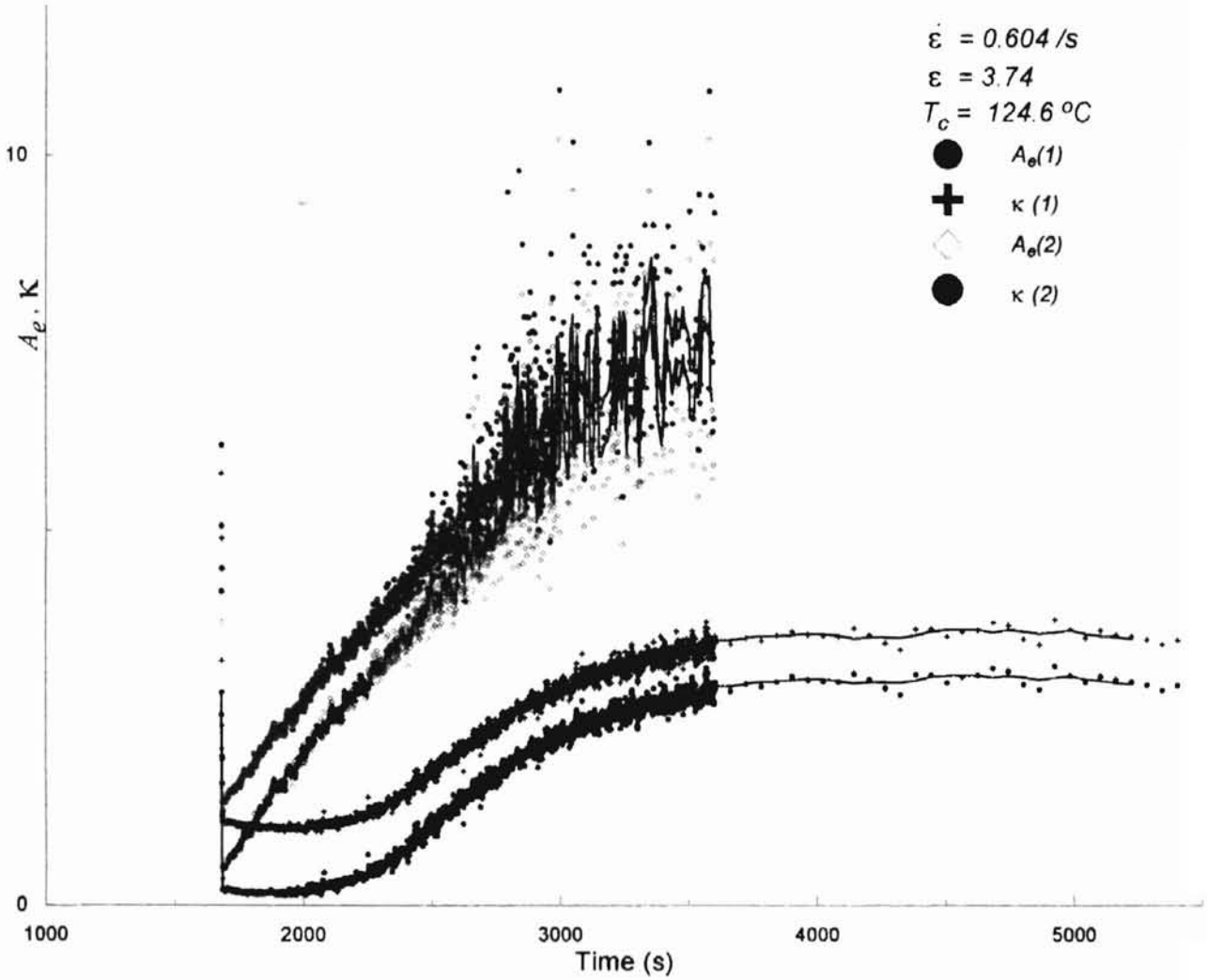

Figure E.2b Absorptivity (A_e), and Kappa (κ) Versus Time for Figure E.2a

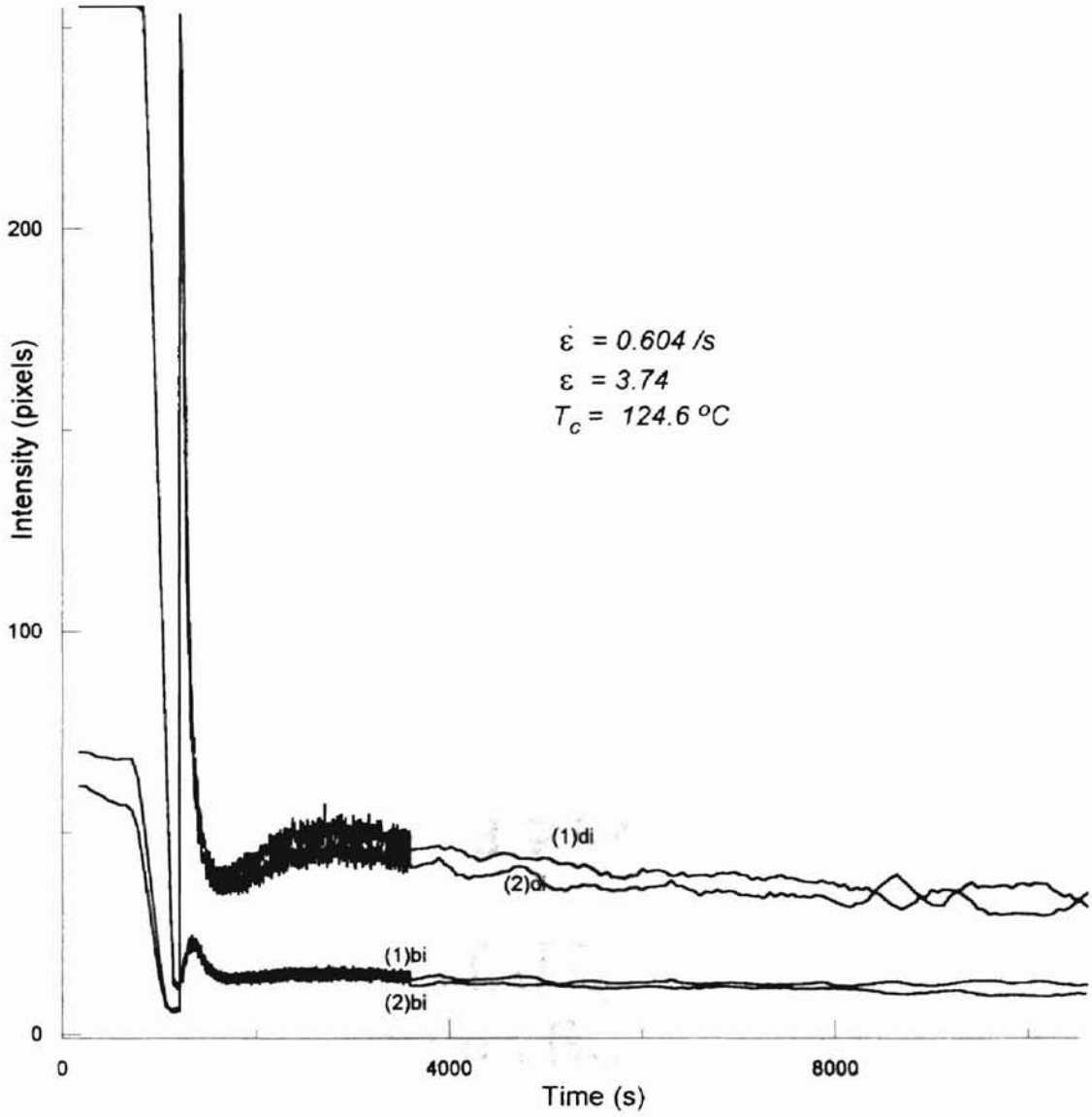

Figure E.3a Dichroism and Birefringence Intensity Versus Time at Locations (1) and (2); 'di' and 'bi' Stand for Dichroism and Birefringence, Respectively

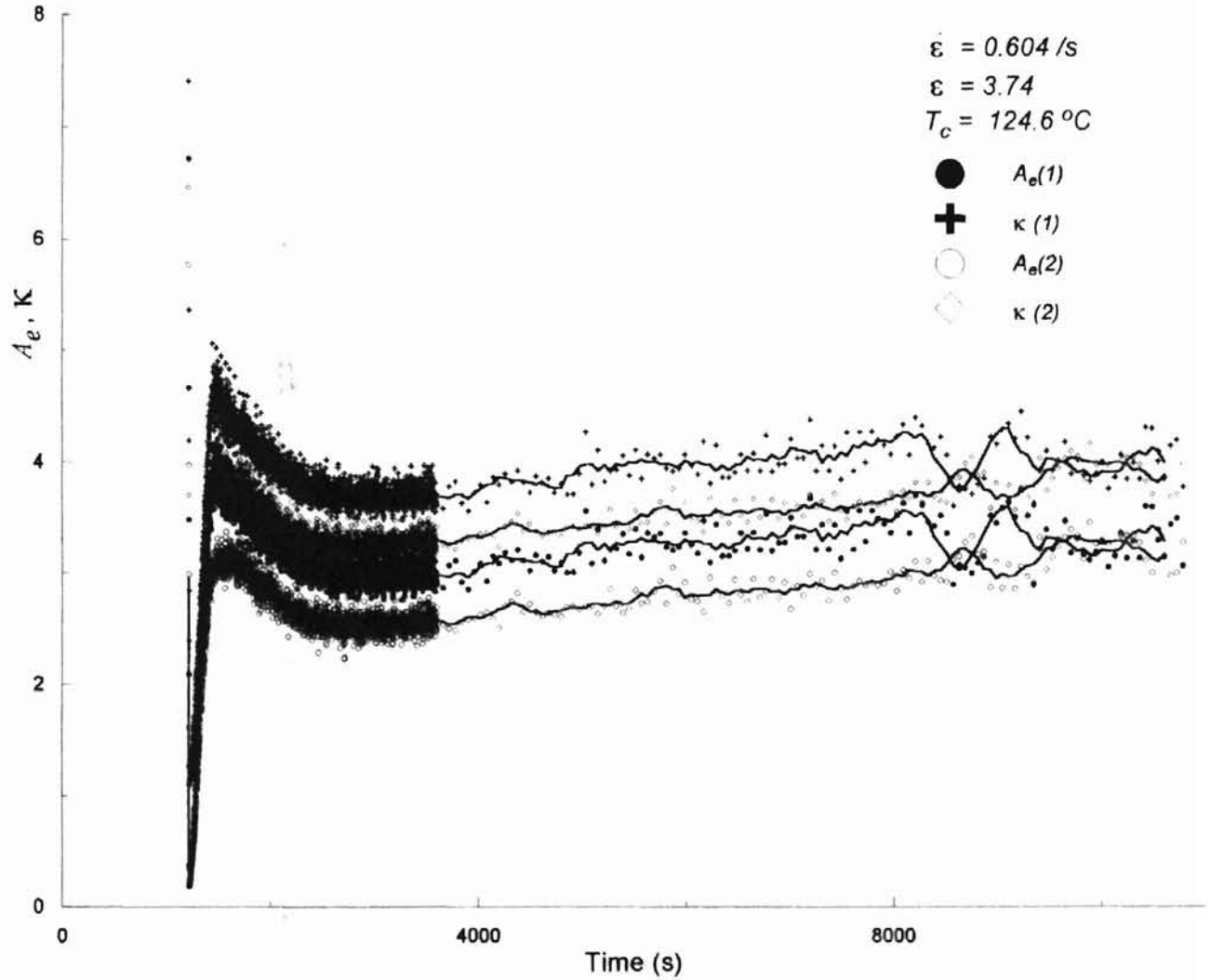

Figure E.3b Absorptivity (A_e), and Kappa (κ) Versus Time for Figure E.3a

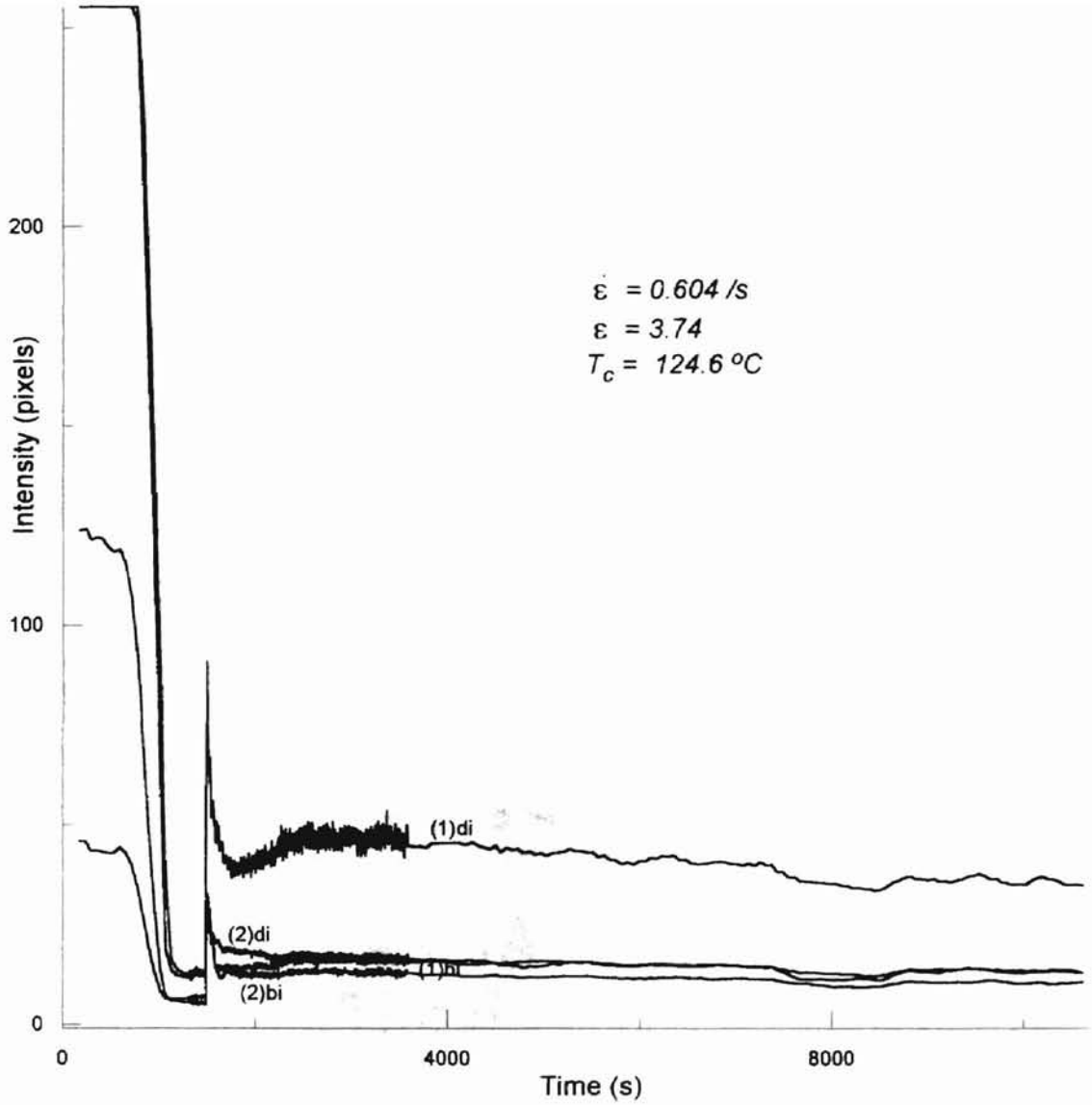

Figure E.4a Dichroism and Birefringence Intensity Versus Time at Locations (1) and (2); 'di' and 'bi' Stand for Dichroism and Birefringence, Respectively

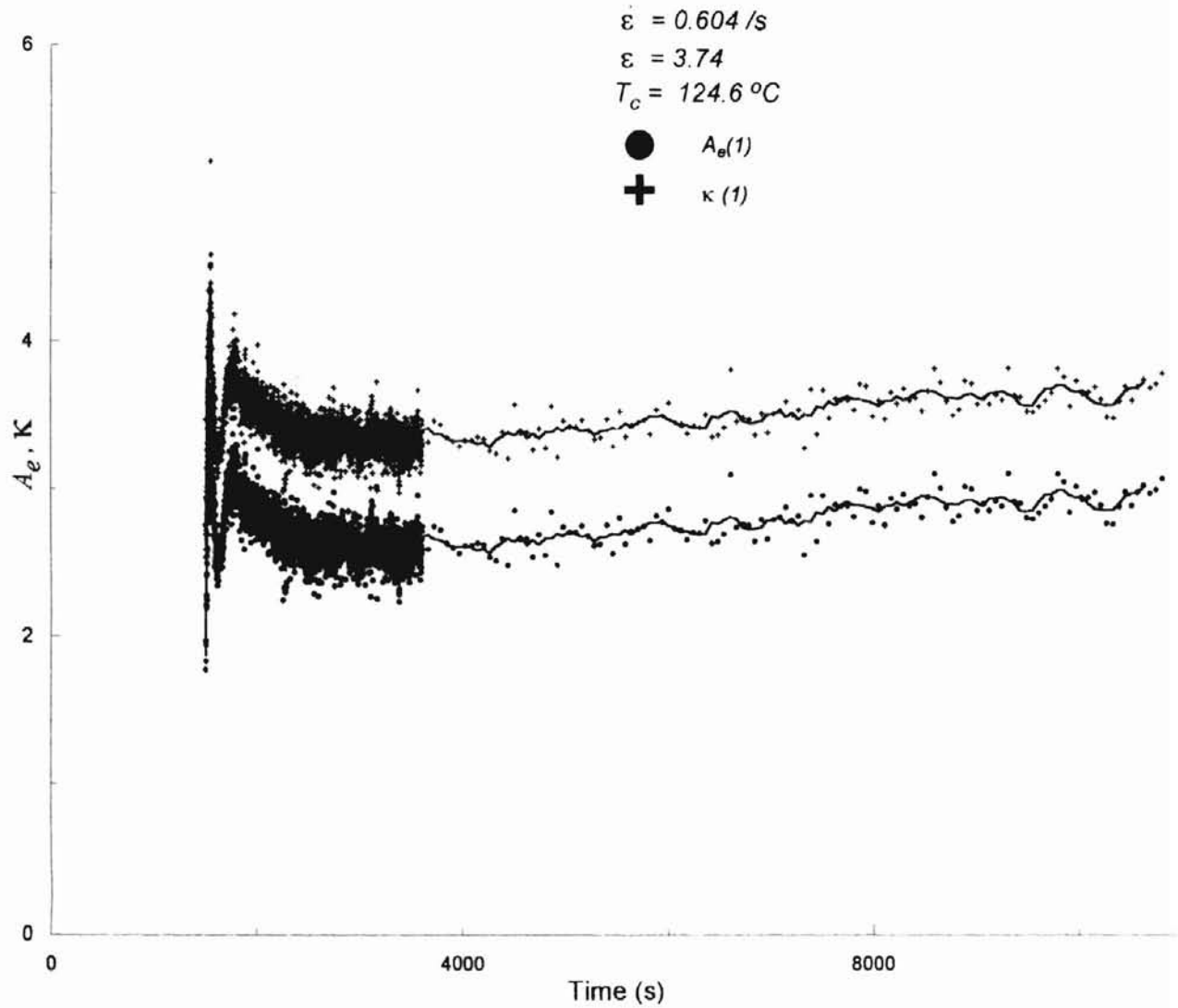

Figure E.4b Absorptivity (A_e), and Kappa (κ) Versus Time for Figure E.4a

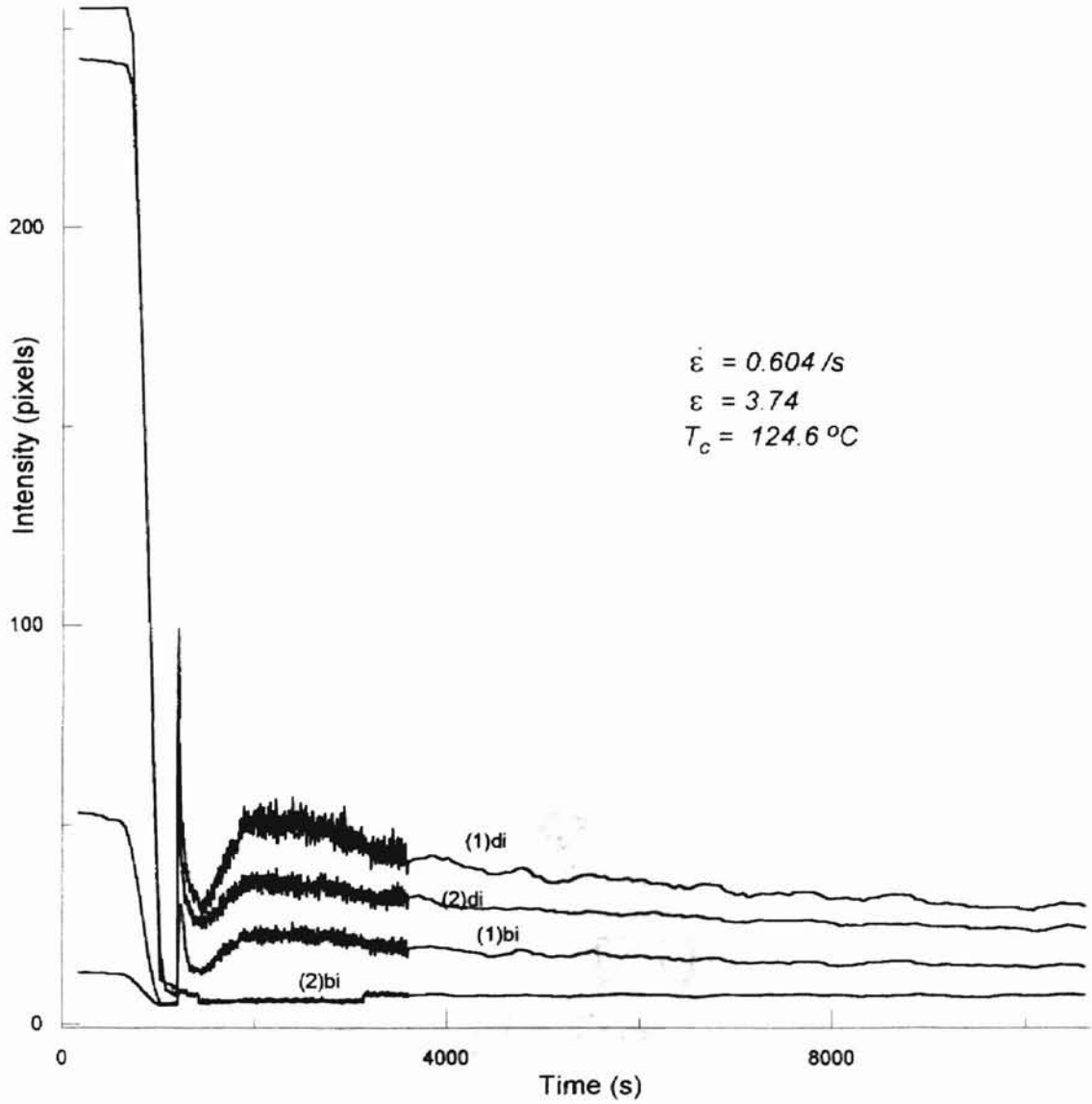

Figure E.5a Dichroism and Birefringence Intensity Versus Time at Locations (1) and (2); 'di' and 'bi' Stand for Dichroism and Birefringence, Respectively

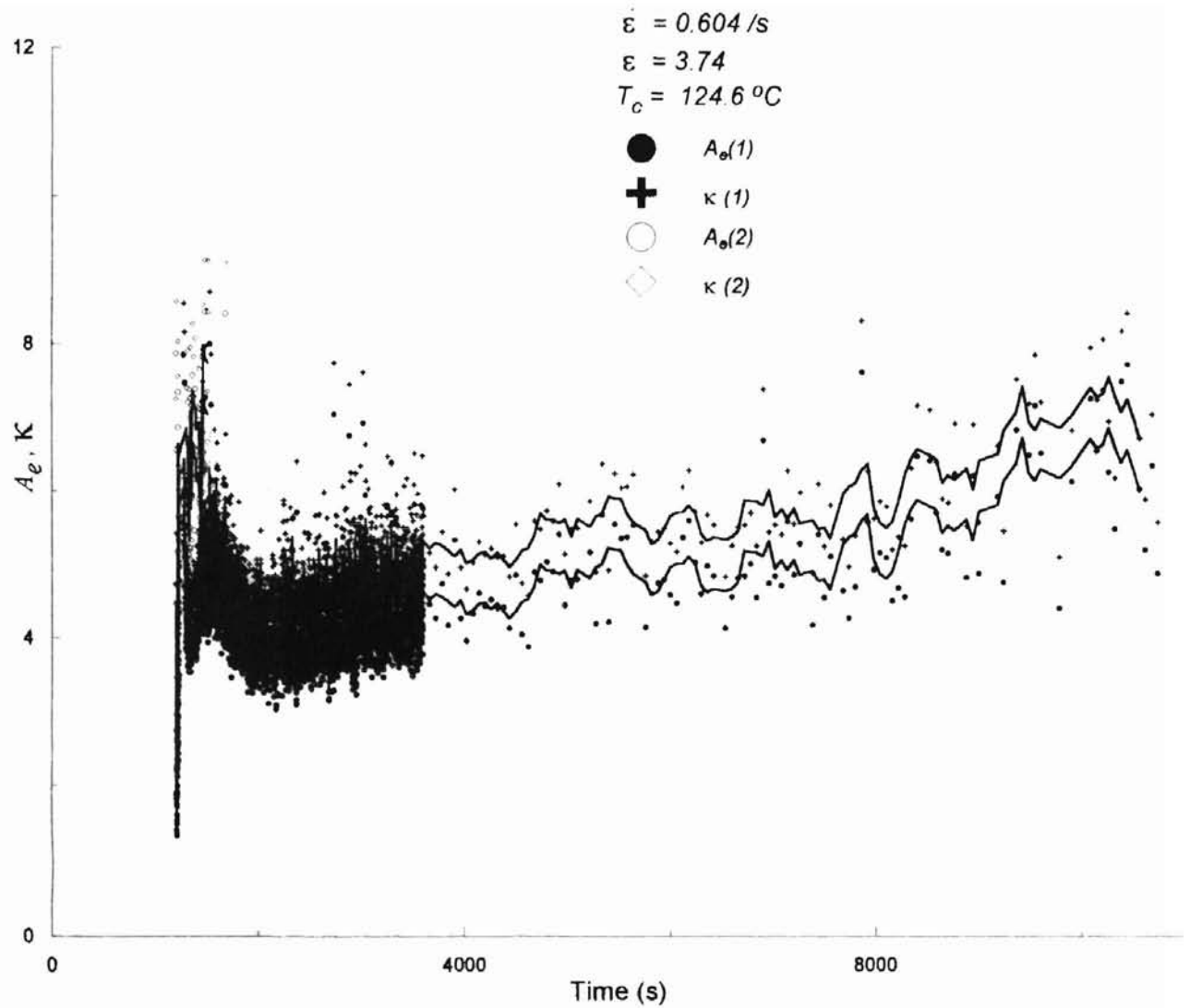

Figure E.5b Absorptivity (A_e), and Kappa (κ) Versus Time for Figure E.5a

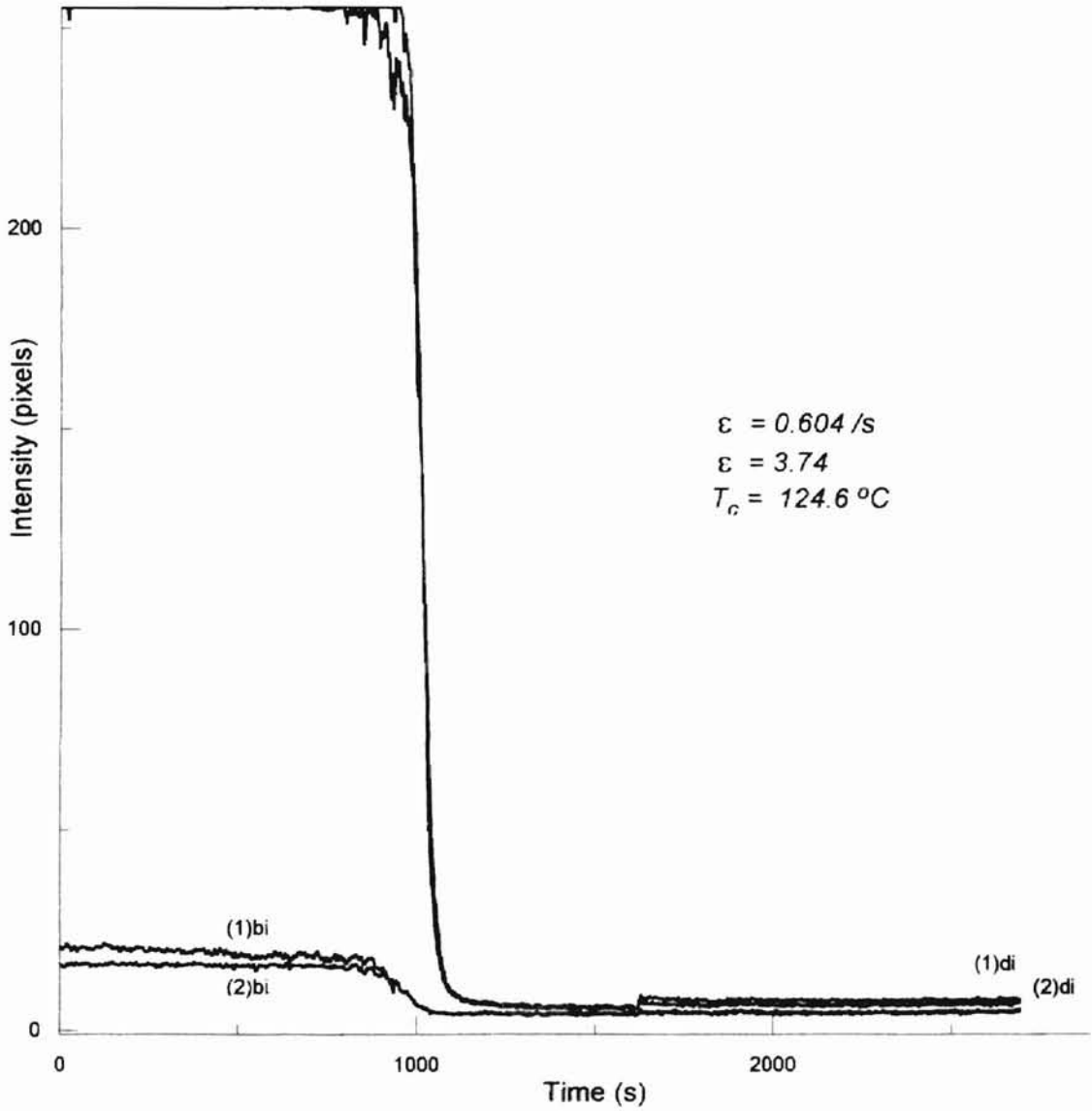

Figure E.6a Dichroism and Birefringence Intensity Versus Time at Locations (1) and (2); 'di' and 'bi' Stand for Dichroism and Birefringence, Respectively

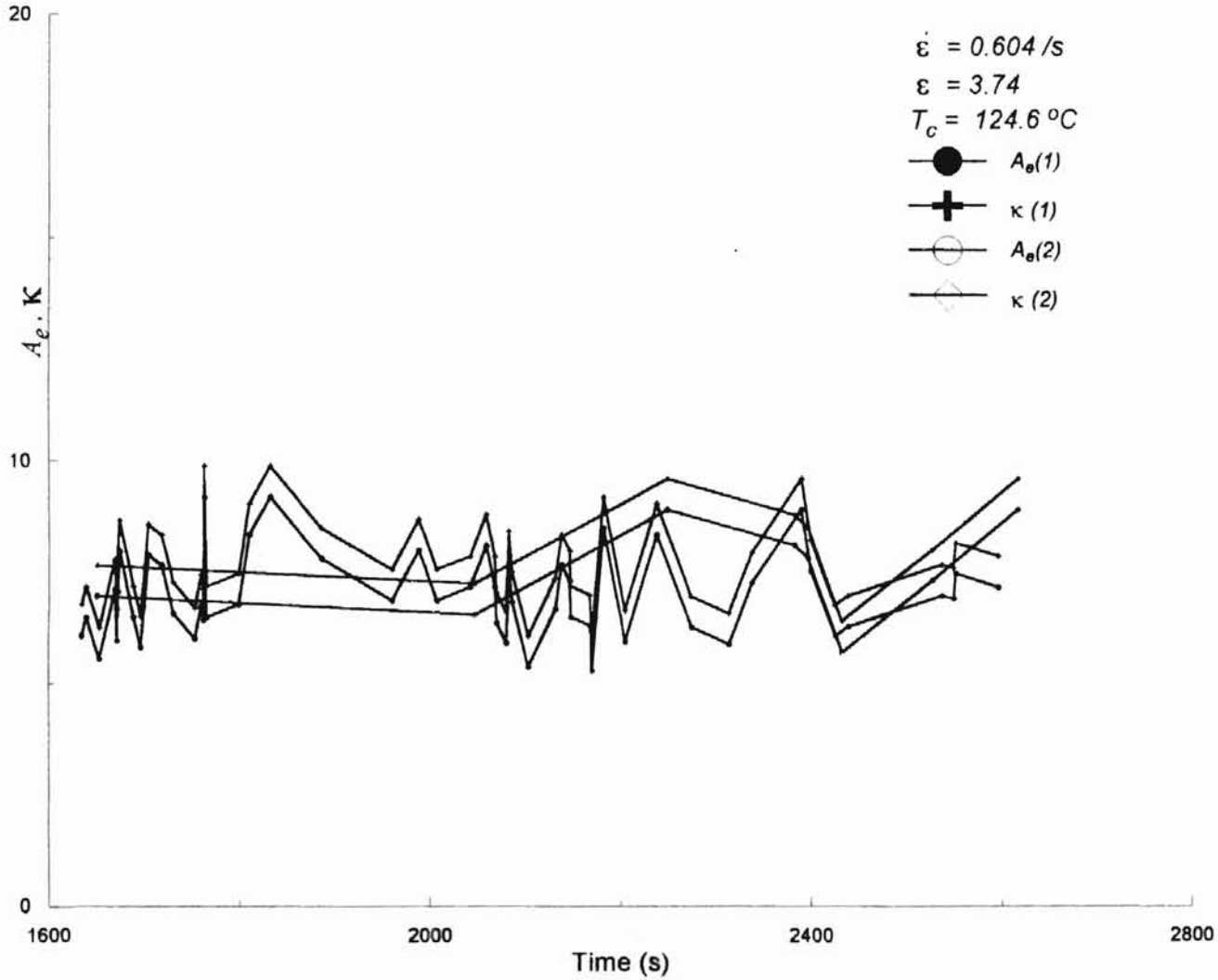

Figure E.6b Absorptivity (A_e), and Kappa (κ) Versus Time for Figure E.6a

VITA

Sheena Jacob

Candidate for the Degree of

Mater of Science

Thesis: FACTORS AFFECTING EXTENSIONAL FLOW-INDUCED CRYSTALLIZATION IN HIGH DENSITY POLYETHYLENE

Major Field: Chemical Engineering

Biographical:

Personal Data: Born in Ernakulam, Kerala, India, on April 1, 1963, the daughter of Jacob George and Omana Jacob.

Educational: Graduated from Birla Balika Vidyapeeth, Pilani, Rajasthan, India, June 1981; received Bachelor of Science (Honors) degree in Physics from Panjab University, Chandigarh, India, June 1984; received Master of Science (Honors) degree in Physics from Panjab University, Chandigarh, India, June 1986; received Master of Science degree in Physics from Oklahoma State University, December 1995; completed requirements for the Master of Science degree at Oklahoma State University, May 2000.

Professional Experience: Teaching Assistant, Department of Physics, Oklahoma State University, August 1993 to May 1995, August 1997 to December 1997; Teaching Assistant, School of Chemical Engineering, Oklahoma State University, January 1995 to July 1997; Research Assistant, School of Chemical Engineering, Oklahoma State University, August 1995 to May 1997; Engineer, Nomadics, Inc., Stillwater, Oklahoma, July 1999 to Present.